Microstructure and High Temperature Mechanical Properties of Ni and Co Based Alloys Fabricated by Electron Beam Melting

By
Shihai SUN

Department of Materials Processing,

Graduate School of Engineering, Tohoku University

A thesis submitted to Tohoku University for the degree of Doctor of philosophy

January, 2015

Microstructure and High Temperature Mechanical Properties of Ni and Co Based Alloys Fabricated by Electron Beam Melting

By

Shihai SUN

Department of Materials Processing,

Graduate School of Engineering, Tohoku University

Approved by:

Professor **Akihiko CHIBA** (Supervisor)

Department of Materials Processing, Tohoku University

Professor **Ryosuke KAINUMA**

Department of Metallurgy, Tohoku University

Professor **Kyosuke YOSHIMI**

Department of Materials Science, Tohoku University

Associate Professor **Yuichiro KOIZUMI** (Research Advisor)

Department of Materials Processing, Tohoku University

Contents

Abstract

Electron beam melting (EBM) is the most advanced 3D printing technology of metal, which can produce any 3D structures with high density (>99.9%) from metal powders by scanning a high-power electron beam to melt metal powder selectively along a series of 2D slices of a 3D object repeatedly, layer by layer. EBM has been attracting wide attention because of its ability to be applied to advanced metal alloys, such as Ni-based superalloys, Co-based alloys, Ti-alloys, for applications such as aerospace engine parts and biomedical orthopedic implants, which are mostly difficult to be formed by conventional processes. However, only limited has been known about the microstructures of EBM-built products, which should greatly affect the properties of alloys.

Because of the uniqueness of EBM process, in particular, (i) directional solidification by scanning electron beam, and (ii) successive stacking of layered 2D slices, it was anticipated that the microstructure and accordingly the mechanical properties of EBM-built products, depend on its orientation with respect to the electron-scanning direction and the stacking direction (i.e. build direction). Hence, the main purposes of my Ph.D study were to elucidate the build direction dependence of microstructures and the mechanical properties of Ni-based superalloy and Co–based alloy, which are typical alloys at which the EBM is being targeted.

Inconel718 alloy and Co–28Cr–6Mo–0.23C–0.17N alloy rods were fabricated by EBM with cylindrical axes deviating from the build-direction by 0°, 45°, 55°, and 90°. The microstructures were investigated by SEM, electron probe micro-analyzer (EPMA), electron backscattering diffraction (EBSD) and TEM. Tensile and creep properties of samples with various build directions were evaluated to investigate the effect of anisotropic microstructure on mechanical property.

The main findings about microstructure and mechanical properties of Inconel 718 alloy fabricated by EBM with various build directions are as follows:

1) Single crystal-like structure of Inconel 718 alloy with <001> orientation in build direction can be obtained by the EBM process, which suggests crystal orientation can be controlled by selecting the oriented direction relative to the build direction, thus the mechanical properties can be controlled as a result.

2) Precipitate amount was dependent on the build height because the early-built part was kept at high temperature for longer time when waiting for the fabrication of the latter-built part, which would have more precipitates. However, inhomogeneous distribution of precipitates in the build height can be solved by subsequent solution treatment without changing the preferential crystal orientation.

3) 55°-sample exhibited smaller minimum creep rate than the samples with other build directions, which suggests that creep resistance of component can be improved if the loading direction is parallel to the <111> orientation direction.

4) [001] variant of metastable γ''-Ni_3Nb ($D0_{22}$, bct) will dissolve into the matrix in 0°- and 90°-samples (<001> orientation) after creep deformation, but all the γ'' variants can be kept in 45°- and 55°-samples (<011> and <111> orientations) because the stress state difference for the γ'' variants in the samples with different build directions. This result can explain why the minimum creep rate in 0°-sample is much higher than that in 55°-sample in the same stress.

The main findings about microstructure and mechanical properties of Co-Cr-Mo alloy fabricated by EBM with various build directions are as follows:

1) Single crystal-like structure of Co-Cr-Mo alloy with metastable γ-fcc phase can be obtained by the EBM process, whose <001> orientation was parallel to the build direction. This result demonstrates the ability of EBM used to produce single-crystal like structure of material with cubic structure.

2) Phase transformation from γ-fcc to ε-hcp may occur in bottom part of the sample with high build height in the EBM process because of long post-built time in the bottom part. The grain structure throughout the height of EBM-built object can not be homogenized by simple aging treatment. It is suggested that the conditions of heat treatment to homogenize the microstructure should be determined by taking into

account the thermal history during the post-melt period of the EBM process especially when the solid-solid transformation is sluggish. The reverse phase transformation may be a possible way to solve the inhomogeneous microstructure problem in Co-Cr-Mo alloy.

3) Isothermal martensitic transformation or diffusive transformation from metastable γ-fcc to stable ε-hcp can be selected by choosing heat treatment temperature, by which the grain texture and resultant mechanical property can be controlled.

Chapter1

1. Introduction

1.1 Additive manufacturing

Additive manufacturing (AM) technologies, also known as “3D printing”, fabricate the three-dimensional (3D) parts directly from computer-aided design (CAD) models by adding materials selectively to the substrate along a series of two-dimensional (2D) slices of 3D parts, layer by layer [1-6]. They can be used to produce aerospace part [7-10], verify structure design [1], make the prosthesis [11,12] and even build a house. Compared with traditional subtractive manufacturing (i.e. machining process including turning, milling, planning, grinding drilling and the like), AM can reduce raw material usage, shorten part production period, save manufacturing cost and produce the part with extremely complex geometric (such as conformal cooling channel and cellular structure). Therefore, AM offers particular benefit to the aerospace, automotive field, and biomedical field. Though powder metallurgy technology can fabricate relatively complex parts with good mechanical properties in a short period of time, the use of molds limits the manufacturing of the shapes with inner feature where a two part mold must be used, as well as the active powders which will react with the mold. Therefore, AM technologies are most promising among the fabrication technologies in the future.

AM equipment appeared in the late 1980s, there has been lots of AM equipment at the market though 20 year development. The typical AM equipment [1] is summarized in Table1-1. According to the state of starting material used, AM process can be divided into the following four broad categories [1,2]: (1) liquid (2) filament/paste (3) powder and (4) solid sheet. The layer creation principles of the AM processes are summarized in Table 2. And the schematic of typical AM processes are shown in Fig.1-1-Fig.1-7 [13-21]. One layer of feedstock can be created by the liquid vat (Fig.1-1) or powder-bed (Fig.1-2, Fig.1-3), or direct deposition from the nozzle with the powder (Fig.1-4) or liquid (melted filament) (Fig.1-5, Fig.1-6) state, or addition of the thin sheet (Fig.1-7). The liquid feedstock will be selectively photopolymerized by the laser or ultra violet (Fig.1-1), the powder feedstock from the powder bed will be selectively sintered or melted by the laser beam (Fig.1-2) or electron beam, or selectively boned with the binders(Fig.1-3), powder feedstock from the nozzle will be melted by the laser beam (Fig.1-4), the wired feedstock will be welded by electric arc (Fig.1-6) or electron beam, and thin sheet will be cut by the laser beam (Fig.1-7) or turning tools. The 3D build process can be achieved by moving the deposition head and/ or the substrate using a computer-controlled translation stage, gantry and/or multi-axis robotic system. Because of the principle difference for adding the material to the substrate, the available materials are restricted in each AM process. Among the AM processes, the most attractive and complex ones are the additive manufacturing for metals.

1.2 Additive manufacturing for metals

Major additive manufacturing for metals are SLM [9,22-28], EBM [8,29-34], electron beam free form fabrication (EBFFF) [35], LENS [36-39], electric arc welding [40-42] and ultrasonic additive manufacturing (UAM) [43-45]. In the LENS, EBFFF and electron arc welding process, the material is directly deposited on the workpiece. The component precision is low because the material delivery amount is very difficult to control, but large geometry size is available. Compared with the deposition process, the powder bed process can produce the component with high precision, and the unmelt powders can be recycled, which can save the feedstock. But the component geometry size is limited by the powder bed. Though the ultrasonic additive manufacturing can produce the component with high precision but machining is necessary in each build layer, which will decrease the productivity. Therefore, the powder bed based additive manufacturing with electron beam or laser beam as heat source are considered as the most cutting edge 3D printing technology for the metals.

The comparison between EBM and SLM are shown in Table1-2 [1,33]. Compared with SLM, EBM has several superiorities as following. Firstly, the EBM has the higher powder, which can make it possible to produce the high melting point metals or alloys with high density. Secondly, higher scanning speed of EBM can reduce the production period. Thirdly, the component is produced in a vacuum environment in the EBM process, which can avoid the material oxidation and improve the component quality. In addition, the preheating process is necessary in EBM process, which can relieve the residual strain in the component and make EBM be more suitable to produce the component with thin parts. The purpose for preheating will be explained in detail in the next section.

1.3 Electron beam melting

The schematic of EBM equipment is shown in Fig.1-8. It consists of electron gun system, vacuum system, powder delivery system, and control system. The maximum power of electron gun is 3.5 kW at a voltage of 60 kV and the energy density is over 102 kW/cm^2. The beam diameter can be focused down to about 100 μm by changing the beam focus offset (Fig.1-9). The build chamber has a nominal vacuum of around10^{-4} torr, and usually helium gas will be filled to the chamber to reach the vacuum of around10^{-2} torr during the melting, which was used to facilitate the build cooling and thermal stability. The powders are loaded in two hoppers, and they are spread to the build platform by the rake. The motion of the electron beam and platform are all controlled by the computer.

The powder type (such as gas atomized powder and plasma rotating electrode processed powder), diameter distribution and flowability will affect the quality (such porosity, unmelt particle) of the build part and the resultant mechanical property. Full density component is easy to be obtained from the plasma rotating electrode processed powder [39,46], which can avoid the residual gas in the powder being involved in the component during the melting process. Generally, the diameter of the powder used for EBM process is in the range of 45 to 150 μm, and bimodal size distribution is preferred [33,47], which can form closely packed layer, contributing to melting and reducing the porosity. Flowability of the powders is affected by density (or compressibility) cohesive strength, wall friction, van der Waals and electrostatic forces on the powder particles, surface tension and interlocking characteristics determined by the particle sizes, size distribution and particle morphology [33]. Flowability improves significantly with sphericity of powders, and is worse for irregular, crushed powders.

The fabrication process is as following. A 3D CAD model to be built is firstly divided into a series of 2D slices with the equal thickness by computer program. Then the file will be transmitted to EBM equipment, and analyzed by the computer control system. Underneath the build part, there is often an additional support part, which is used to avoid deformation of the build part during the fabrication owing to weaken strength of the light sintered powders for supporting effect. In addition, the support part can avoid the element diffusion from the substrate to the build part, which will change the microstructure of the build part. During the EBM process, a layer of powder is raked on the build bed at first, then the powders on the layer will be preheated to 0.5-0.8 of melting temperature with defocused beam to slightly sinter. After that, the desired 2D area will be melted by the focused beam. As shown in Fig.1-10, usually in the melting step, the electron beam is firstly scanned along the perimeter of 2D area for two circuits (the number of turns can be changed according to the requirement), which is called “contour process”. Then the electron beam scans the interior of the 2D area with a snake shape, which is called “hatching process”. The build parameter such as beam current, beam focus offset and line offset in the contour process and hatching process are usually different because of the different thermal conduction condition in the edge and interior of the scanning area. After completion of one layer, the whole powder bed is lowered down 50~100 μm (depending on the powder size and size distribution) and a new layer of powder is raked on the building zone. The processing sequence is repeated until the component is completed. The detail illustration of the EBM process can refer to the video animation published by Oak Ridge National Laboratory [21].

The preheating process is unique to EBM process, and its effects are as following:

1) Sintering the precursor powders to improve the conductivity of powder to help the electrons flow out of the build bed.
2) Minimizing thermal gradient to reduce the internal stress in the build part.
3) Maintaining a uniform temperature in the build part.

1.4 Research status of electron beam melting

EBM has been applied to numerous advanced metal alloys, such as Ti-alloys [7,8,48-58], Ni-based superalloys [10,29,59-61], Co-based alloys [31,34,62,63], Stainless steel [64], and Cu-alloys [65,66], for applications such as aerospace engine parts, automotive gearbox parts and biomedical orthopedic implants, which are mostly difficult to be formed by conventional processes. The following sections will introduce the microstructures and mechanical properties of three major materials investigated in the previous studies on EBM.

1.4.1 Microstructure of Ti-6Al-4V alloy fabricated by EBM

Ti–6Al–4V is the material which is the most extensively investigated by EBM, because of its wide application in aerospace and biomedical fields. Widmanstätten microstructure (acicular α-plate) similar to wrought counterpart can form in the as-EBM-built cylindrical sample with 1.2 cm in diameter and 6.8 cm in the length [50], and acicular α-plate thickness on the bottom build part (~1 cm from the bottom) was larger than that on the top build part (~1 cm from the top) because of higher cooling rate at the bottom part. The grains with α′ martensite and particulate β can form in the cell ligament part of as-EBM-built open cellular foam with a higher cooling rate [51]. The microstructure across the build height can be categorized into the following three regions. The first region is at the bottom part with the height about 500 μm from the stainless substrate. This region consists of equiaxed grains with single β phase because of the diffusion of β stabilizing elements, such as Cr, Fe and Ni to the build part from the stainless [49]. This part is very brittle, which is helpful to remove the build part from the stainless substrate. The second region is above the chemical composition transition part. This region consists of equiaxed parent β grains, whose orientation near <001> will grow into columnar grains at the subsequent build process. The third region is the columnar parent β grains, which will transform into α or α′ depending on the cooling rate [49].

Though the orientation of acicular α-plate is random in the final sample, the <001> orientation of columnar parent β grains were found to be parallel to the build direction in the interior of bulk section by reconstruction of β phase from electron backscatter diffraction (EBSD) data of α phase [7,49]. The columnar parent β grains were indicated to be related to the melt pool elongated in the stacking direction [7]. Near the surface layer, the growth direction of the columnar grains deviated from the stacking direction because of the lateral heat loss, which should be considered in the sample with thin thickness [7]. In the junction position from thick part to thin part, the columnar grain growth will break off when the wall thickness of the thin part was less than 1 mm [7]. In the junction position from thin part to thick part, the grains with <001> orientation near build direction in the thin part would extend to the thick part and grow coarsely, restraining the growth of grains with other orientation [7].

Build defect, such as porous (unmelted or unsintered) zones, impurity inclusions and gas bubbles from the trapped argon gas in the gas atomized powders can appear in the EBM-built samples [30]. The unmelted or unsintered zones appeared usually because of the interrupt of electron beam caused by charge accumulation in the powders, and improper usage of build parameter, such as line offset, focus offset and scanning speed. The impurity inclusions, such as oxide particle, came from the initial or recycled powders, which can cause beam tripping, leaving a defect in the build sample. Even though the build parameter has been optimized, the spherical voids can be still embedded in the build matrix. The reason is the gas bubble with low pressure can not overcome the melt surface tension of Ti–6Al–4V. These gas voids can be prominently eliminated by the standard hot isostatic pressing (HIP) treatment at 900 ℃ for 2 h under 0.1 GPa pressure [30], but residual void can be still found in the sample after the HIP treatment. Gaytan et al. [30] indicated that the residual gas void would not affect the mechanical property because of their small size and a little amount.

Because of the high saturated vapor pressure of Al element, there is the possibility of Al loss during the EBM process. And also the Ti–6Al–4V powders may be excessively oxidized for the recycling usage. However, Gaytan et al. [3027] indicated that the chemical composition and grain size distribution of recycled Ti–6Al–4V powders did not change significantly for up to 40 cycles of recycling usage, but the Al content would reduce about 10-15% in the build component. Juechter et al. [48] investigated the effect of energy input and scanning speed on heat affected zone and alloy composition. They indicated that the heat affected zone increased linearly with scanning speed at constant line energy because the heat from previous lines can be used for melting at high scanning speed. The Al content would decrease notably at higher line energy and scanning speed, because higher line energy and scanning speed will cause higher surface temperatures and larger melt pools. The Al content on each of the build layer would decrease with increasing the build height because the low diffusivity of Al can not homogenize the Al content in the melt with evaporation loss on the melt surface.

1.4.2 Microstructure of Inconel 718 fabricated by EBM

Inconel 718 is a kind of precipitate hardening nickel based superalloy, containing significant amounts of Fe, Cr and minor amounts of Nb, Mo Ti and Al, primarily strengthened by γ″ (Ni_3Nb, $D0_{22}$) and complementary by γ′ ($Ni_3(Al, Ti, Nb)$, $L1_2$) [67].

The volume fraction of γ″ and γ′ in the peak aged condition are about 15% and 4% [68], respectively. δ phase (Ni_3Nb, $D0_a$) [69-71] also often appears in the matrix, which nucleate preferentially at grain boundaries. Inconel 718 combines good corrosion resistance and high temperature strength with excellent weldability and often used as turbine disk, cryogenic storage tanks, and pipes in nuclear reactor [9,39,72]. There have been trials to fabricate Inconel 718 products by EBM.

Strondl et al. [29] investigated the microstructure of EBM-built Inconel 718 without any post-build heat treatment at the first. The single crystal-like microstructure with <001> orientation parallel to the build direction was found in the as-EBM-built Inconel 718. The plate-shape γ″ precipitate with 5-10 nm in diameter could be observed in the as-EBM-built sample, keeping the following orientation relationship with the γ matrix: $(001)_{\gamma''} // \{001\}_{\gamma}$; $[100]_{\gamma''} // [010]_{\gamma}$. The spherical shape γ′ precipitate was found to be only 2-5 nm in diameter because of high cooling rate during EBM process. Spherical shaped (Ti,Nb)(C,N,B) precipitate with B1 structure was observed to be aligned discontinuously along the build direction with 5-10 μm in the sample[29,60]. The plate-like δ-Ni_3(Nb,Ti) phase with a length less than 10 μm and thickness of around 100 nm was aligned along the build direction, keeping the following orientation relationship with the γ matrix: $\{010\}_{\delta} // (111)_{\gamma}$; $\langle 100\rangle_{\delta} // \langle 110\rangle_{\gamma}$ [60]. In addition, hexagonal Laves phase $(Ni,Fe,Cr)_2(Nb,Mo,Ti)$ and topologically close-packed (TCP) σ phase (FeCr) could also be found in the as-EBM-built samples [60].

Evidence of incipient melting, i.e., partial remelting of previous layers when a new powder layer on top was melt by the electron beam, was observed in the EBM-built sample [29]. Incipient melting causes the chemical inhomogeneity and the uneven distribution of the precipitates and would be detrimental to the mechanical property. Therefore, incipient melting should be avoided by choosing the proper parameters in the EBM process.

Because the early-built part will be reheated when new layer powder on the top is preheated and melted by the electron beam melting, the early-built part will be kept at high temperature until the completion of the build process. Therefore, the microstructure in the early-built part may change as in the heat treatment process. In the research carried out by Strondl et al. [29,60], the distribution of precipitate type (δ phase or Laves phase) along the build height was not indicated.

1.4.3 Microstructure of Co-Cr-Mo alloy fabricated by EBM

Co–Cr–Mo alloy is often used as the orthopedic implant (such as hip and knee joint) material because of its high strength, excellent wear resistance, good corrosion resistance and biocompatibility[49,51,73,74]. ε-hcp phase is stable at room temperature and γ-fcc is stable at high temperature. γ-fcc phase can exist at room temperature by addition of carbon [75] and nitrogen[76-78]. Gaytan et al. [31] investigated Co–Cr–Mo alloy fabricated by EBM for the biomedical application for the first time. The columnar grains formed in the as-EBM-built sample with solid geometry (cylindrical or rectangular block component). $Cr_{23}C_6$ carbides were found to align along the build-direction (*z* axis) in the grains with about 2 μm intervals owing to unidirectional solidification. However, the zigzag-like carbide pattern can also be observed in the sample, which may be caused by the rotation of electron beam scanning direction for 90 ° on every layer during the preheating and melting process. Numerous stacking faults were observed in the γ-fcc matrix by TEM. On the bottom part of the as-EBM-built knee component, numerous equiaxed grains were observed beside the columnar grains. And the carbide arrangement did not correspond to the build direction anymore.

Gaytan et al. also investigated the effect of annealing heat treatment on the microstructure of EBM-built knee component, which includes initial HIP at 1200 ℃ for 4 h in Ar atmosphere of 10^3 bar and following homogenizing treatment at 1220 ℃ for 4 h in Ar atmosphere, followed by cooling at 75 ℃ / min. The columnar grains formed in the EBM process were replaced by the equiaxed grains (about 42 μm) and annealing twins after the annealing process. And the carbides reduced significantly because of the high annealing temperature. However, the stacking faults still existed with the similar feature as that in the as-EBM-built samples.

The microstructures of the Co–26Cr–6Mo–0.2C alloys fabricated by EBM have been observed only by optical microscopy to examine the carbide array and by transmission electron microscopy (TEM) for relatively local, lattice-defect structures. As mentioned above, the phase constitution and grain structures, including the crystal orientation distribution (i.e., texture), should also be examined in order to understand the relationship between the microstructural and mechanical properties.

1.4.4 Mechanical properties of EBM-built materials

Fig.1-11 shows the mechanical properties of three major materials found in the studies on the EBM-built materials [9,31,50,60]. It suggests that the mechanical properties of EBM-built parts are comparable or superior to those of the wrought counterparts. The detailed mechanical properties of the EBM-built materials are as following.

For Ti–6Al–4V alloy, the hardness was higher on the bottom than that on the top because finer α-plate formed on the bottom part [50]. And also the hardness was higher on the strut part of cellular structure foam than that on the bulk build component because α′ martensite formed on the strut part with higher cooling rate [51]. The yield stress of Ti–6Al–4V would decrease when the preheating temperature was higher than 680 ℃ [49], because α plate thickness will increase when the preheating temperature was larger than 680 ℃. The HIP treatment (at 920 ℃ for 2 h under the pressure of 100 MPa, followed by a cooling rate of 6±2 ℃ to room temperature) for the EBM-built Ti–6Al–4V will decrease the yield and tensile strength significantly, but increase the elongation a little [49]. These were caused by the coarsening of the microstructure during the HIP treatment.

For Inconel 718, the strength in the build direction was similar to that in the direction perpendicular to the build direction. However, the elongation and area reduction were much lower in the build direction than that in the direction perpendicular to the build direction. This was thought to be caused by the local elongated void in the build direction [60], which would decrease the cohesion between the successive build layers. The strength of the EBM-built Inconel 718 will be improved, but the elongation will be decreased after the heat treatment which consists of initial solution treatment at 1000 ℃ for 1 h, followed by rapid cooling, and two aging hardening treatments. The first aging treatment is at 718 ℃ for 8 h, followed by furnace cooling to 621 ℃ in 2 h, and second aging treatment is at 621 ℃ for 18 h, followed by air cooling.

For Co–Cr–Mo alloy, the hardness of strut part of cellular structure sample was about 25% higher than that in bulk build sample because the higher volume fraction of carbide formed in the strut part with higher cooling rate [31]. Kircher R.S. [62] investigated the mechanical properties of the samples parallel and perpendicular to the build direction before and after heat treatment. The as-EBM-built sample was very brittle, with elongation of 5% in the direction perpendicular to the build direction while only elongation of 0.8% in the build direction. Though the constituent phase was not indicated in tensile test sample, the worse elongation in the build direction should be caused by the partially transformed ε-hcp phase from single γ-fcc in the early-built part, which will be kept at high temperature for long time during the EBM process for the high build height. While the sample for tensile test in the direction perpendicular to the build direction can be single γ-fcc phase because of its short time at high temperature during the EBM process for the low build height. The samples with HIP (1185 ℃ for 4 h in Ar atmosphere of 172.4 MPa) and homogenizing treatment (1190 ℃ for 4 h in Ar atmosphere followed by cooling at 75 ℃/min) exhibited mechanical properties independent of orientation. Compared with the as-EBM-built samples, the yield stress decreased but the ultimate tensile strength (UTS) could be kept after HIP and homogenization treatment. In addition, the elongation of the samples parallel to the build direction or perpendicular to the build direction could increase to 30 % after the HIP and homogenization treatment. In the fatigue test for the samples with heat treatment exhibited higher fatigue stress after 10 million cycle stress in the direction perpendicular to the build direction.

These mechanical property researches about EBM-built materials are focused on the properties at room temperature, which are too limited for the component with high temperature application. And also the effect of constituent phase, crystal orientation, precipitate, and grain boundary on mechanical property should be investigated systematically to promote their practical application.

1.5 Objective of this study

Because of the uniqueness of EBM process, in particular, (i) directional solidification by scanning electron beam, and (ii) successive stacking of layered 2D slices, it is anticipated that the microstructure and accordingly the mechanical properties of EBM-built products, depend on its orientation with respect to the electron-scanning direction and the stacking direction (i.e. build direction). Hence, the main purpose of my study is to elucidate the build direction dependence of microstructures and the mechanical properties of Ni-based superalloy and Co–based alloy, which are typical alloys at which the EBM is being targeted.

Table 1-1. The typical additive manufacturing equipment in the market

AM Equipment	Abbreviation	Company	Country
Stereolithography Apparatus	SLA®	3D Systems	United States
Selective Laser Sintering	SLS®	3D Systems	United States
Laser Engineered Net Shaping	LENS®	Optomec	United States
Direct Metal Deposition	DMD®	POM group	United States
Three-Dimensional Printing	3DP™	Z Corporation	United States
Fused Deposition Modeling	FDM	Stratasys	United States
Laminated Object Manufacturing	LOM™	Cubic Technologies	United States
Direct Metal Laser Sintering	DMLS	Electro Optical Systems (EOS)	Germany
Selective Laser Melting	SLM	MCP-HEK Tooling GmbH	Germany
Electron beam melting	EBM®	Arcam AB	Sweden

Table 1-2. Summary of additive manufacturing process

State of starting material	Process	Layer creation technique	Phase change	Typical materials
Liquid	Stereolithography (SL)	Laser curing liquid layer	Photopoly-merization	Photopolymers (acrylates, epoxies, colorable resins), ceramic suspension
	Multi-Jet Modeling (MJM)	Ink-jet printing	Cooling & Photopoly-merization	Photopolymers, waxes
Filament / paste	Fused Deposition Modeling (FDM)	Continuous extrution & deposition	Solidification by cooling	Thermoplastics (ABS, polycarbonate, elasomer) and wax
	Electric Arc Welding (EAW)	Deposition of melting wire	Solidification by cooling	Metal
	Freeze-form Extrusion Fabrication (FEF)	Continuous extrution	Solidification by cooling	Ceramic paste
Powder	Selective Laser Sintering (SLS)	Laser scanning powder layer	Partial melting & solidification	Thermoplastics, waxes, metals with binder, ceramics and sand with binder
	Selective Laser Melting (SLM)	Laser scanning powder layer	Full melting & solidification	Metals
	Electron beam melting (EBM)	Electron beam scanning powder layer	Full melting & solidification	Metals
	Direct Metal Deposition (DMD)	On-demand powder injection and melted by laser	Full melting & solidification	Metals
	Three-dimensional printing (3DP)	Binder droplet deposition onto powder layer	No phase change	Polyer, metals, ceramic
Solid sheet	Laminated Object Manufacturing (LOM)	Binder connecting & laser cutting	No phase change	Paper, plastic, metal
	Ultrasonic Additive Manufacturing (UAM)	Ultrasonic friction welding & machining	No phase change	Metal

Table 1-3. Comparison between electron beam melting and selective laser melting

	Electron beam melting（EBM）	Selective laser melting (SLM
Equipment	EBM A2 (Arcam AB,Sweden)	EOSINT M 280 (EOS)
Heat source	Electron beam (W filament)	Yb-fibre laser
Build dimension (W×D×H)	200x200x350	250x250x325
Largest power1	3500 W	400 W
Beam size	0.2-1.0 mm	0.1-0.5 mm
Largest scanning speed	8000 mm/s	7 m/s
Building speed	15-22 mm3/s	2-8 mm3/s
Building atmosphere	Imputing He (10-3mbar) after high vacuum(10-5 mbar)	Ar or N2
Preheating temperature	(0.5-0.8) Tm (Tm:Melting temperature(K))	~90

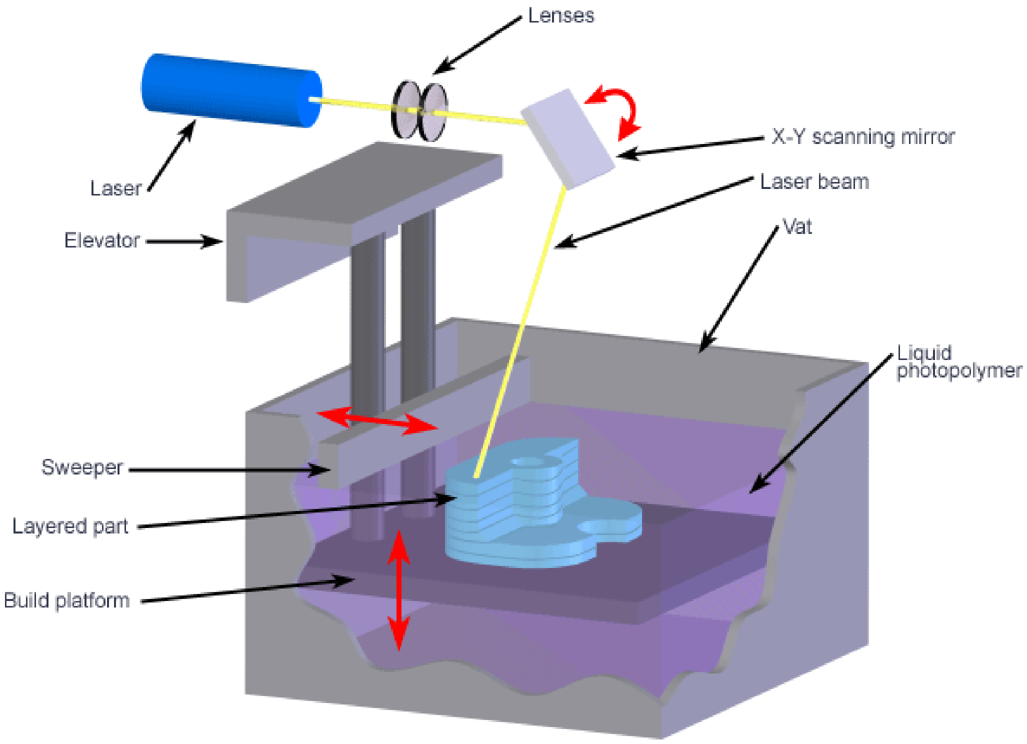

Fig.1-1. Schematic of Stereolithography Apparatus (SLA) [13,14]

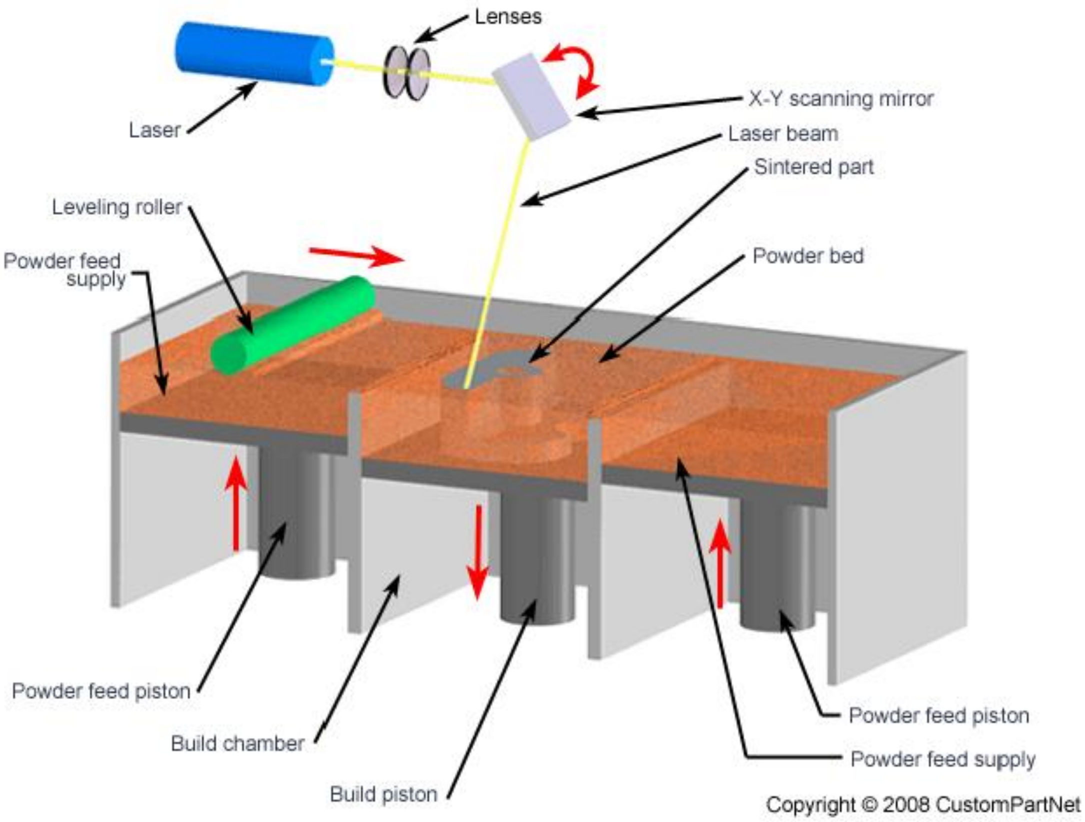

Fig.1-2. Schematic of Selective Laser Sintering (SLS) [13,15]

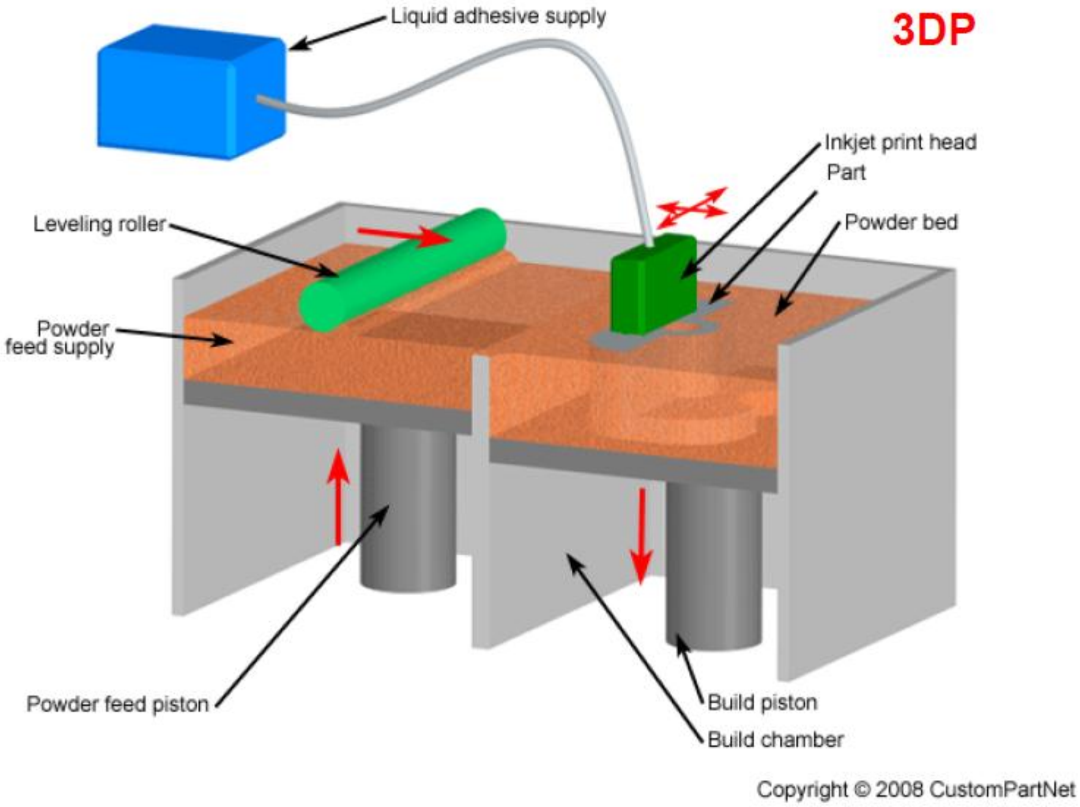

Fig.1-3. Schematic of Three-dimensional Printing (3DP) [13,16]

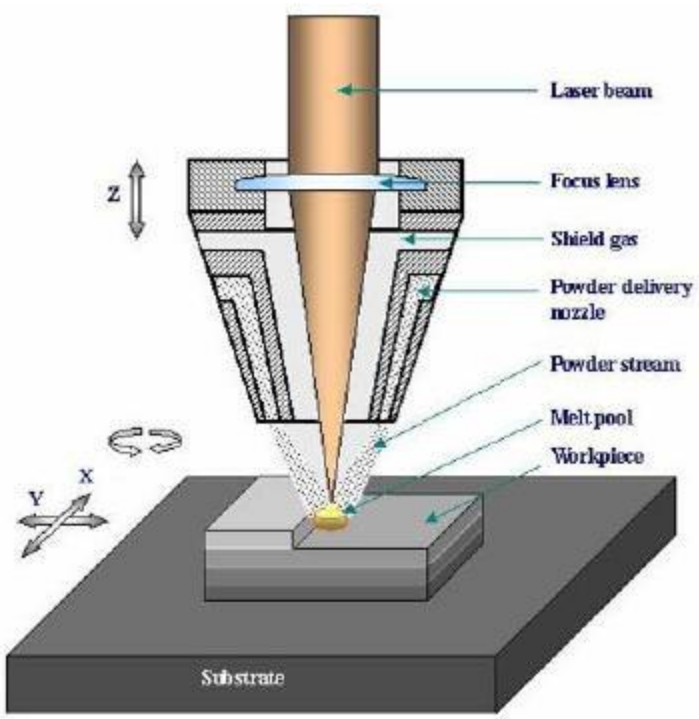

Fig.1-4. Schematic of Direct Metal Deposition (DMD) [17]

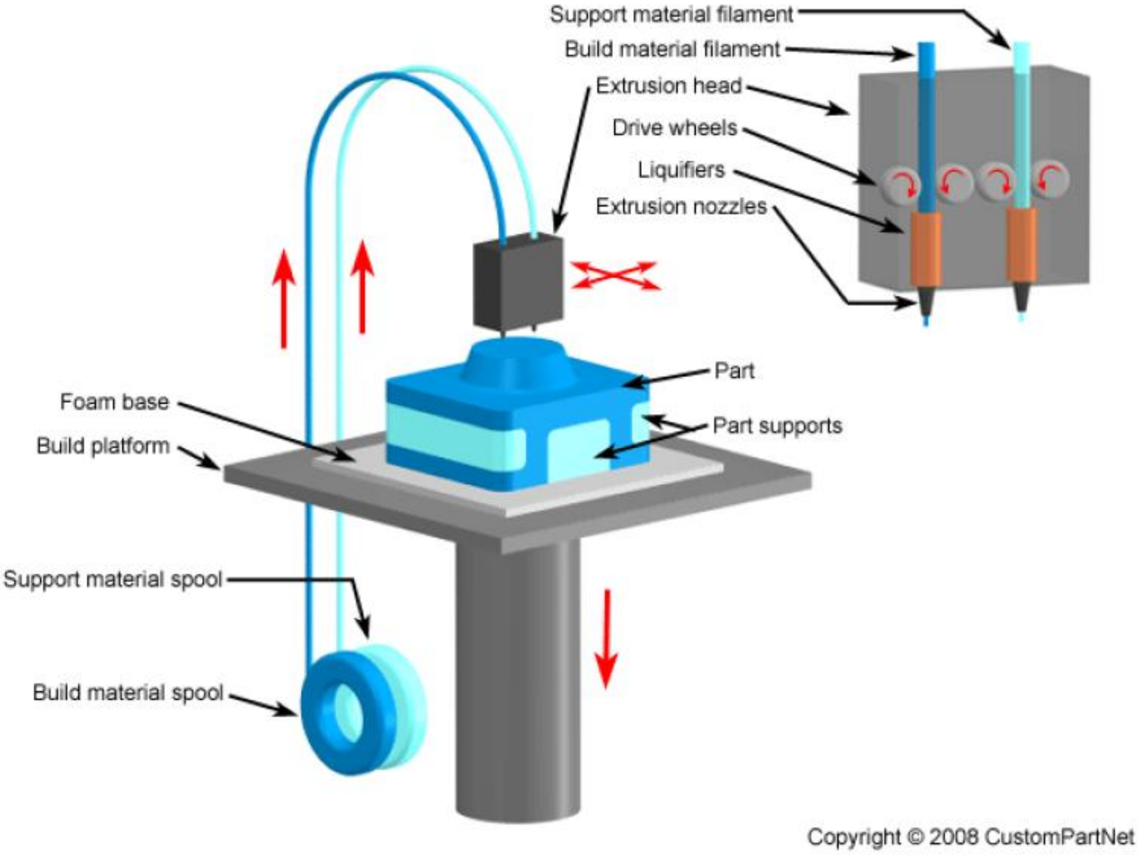

Fig.1-5. Schematic of Fused Deposition Modeling (FDM) [13,18]

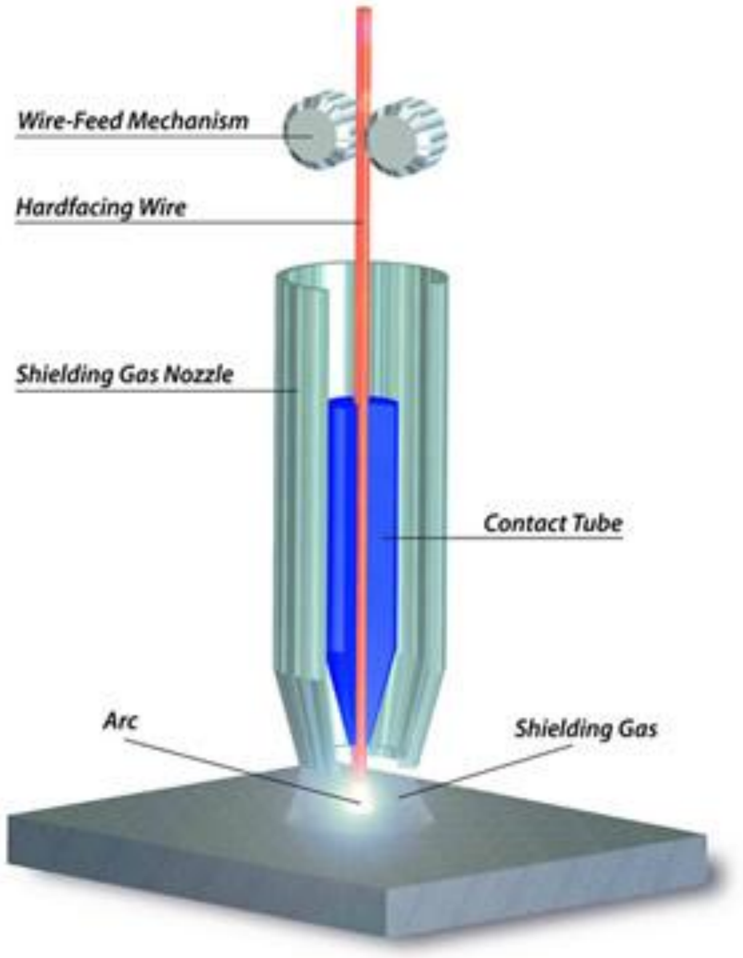

Fig.1-6. Schematic of Electric Arc Welding (EAW) [19]

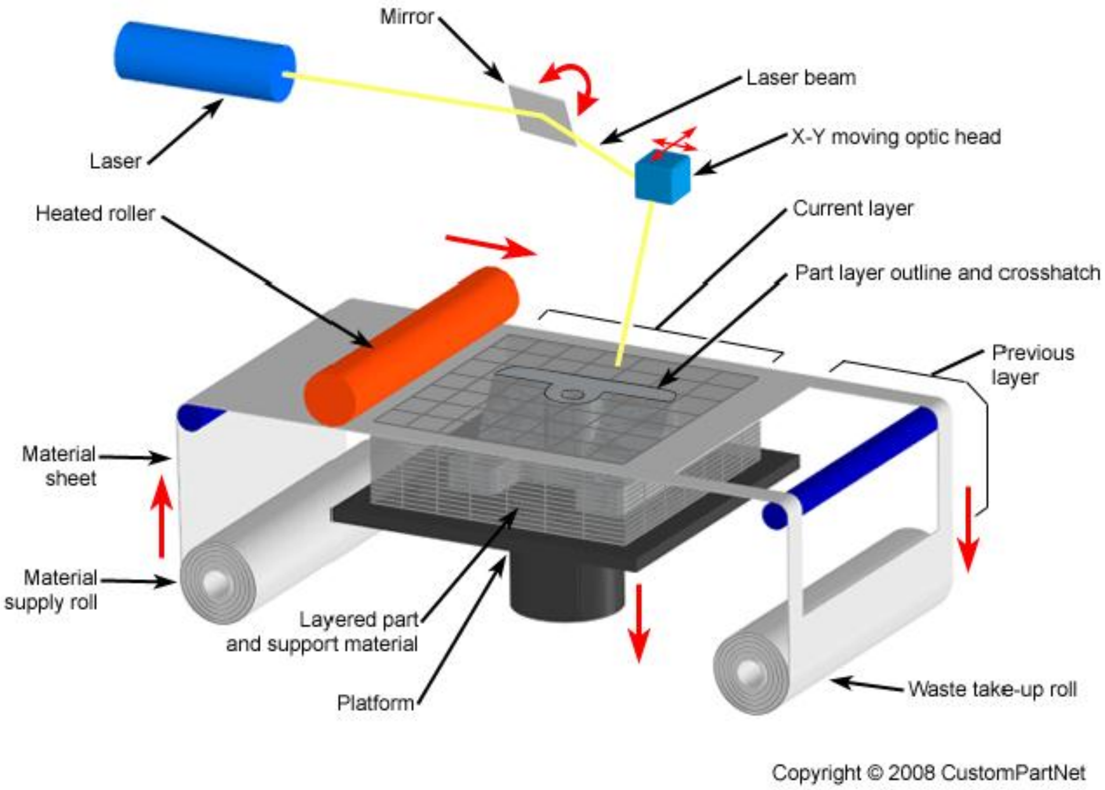

Fig.1-7. Schematic of Laminated Object Manufacturing (LOM) [13]

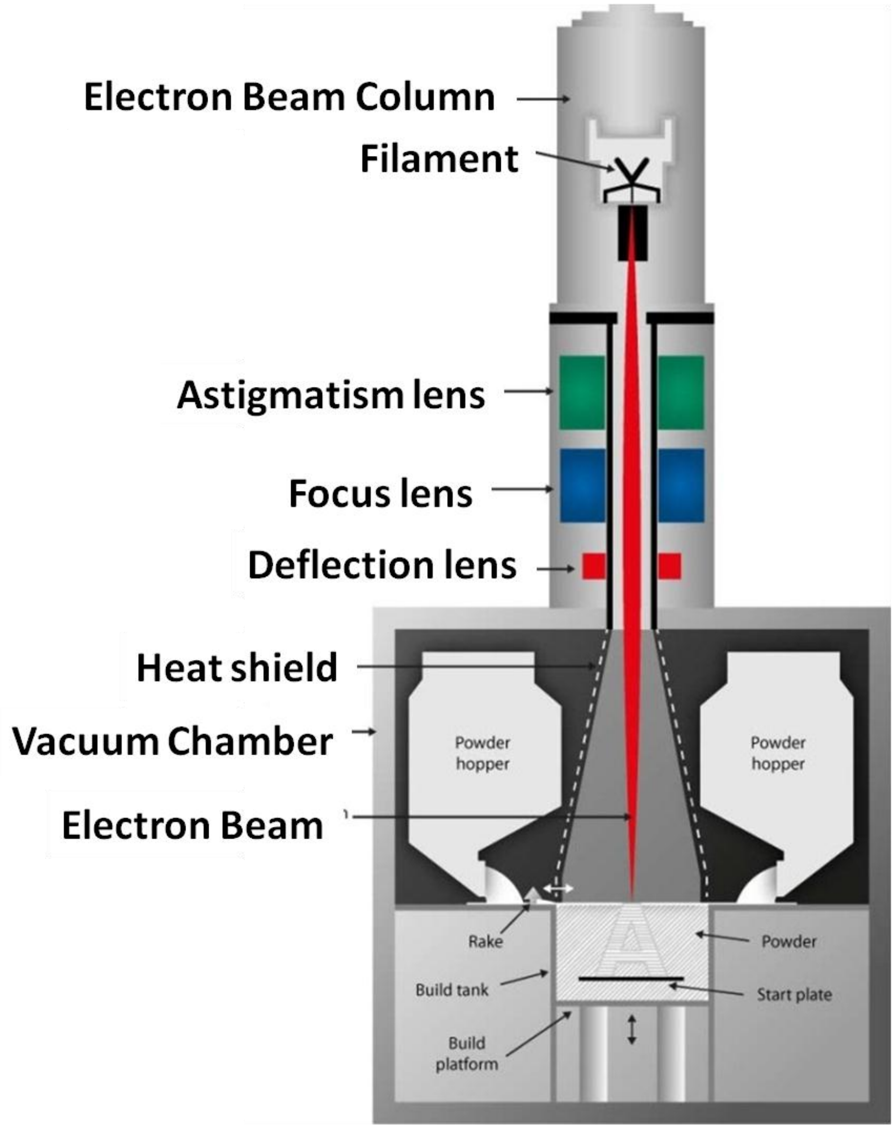

Fig.1-8. Schematic of Electron Beam Melting (EBM) [20,21]

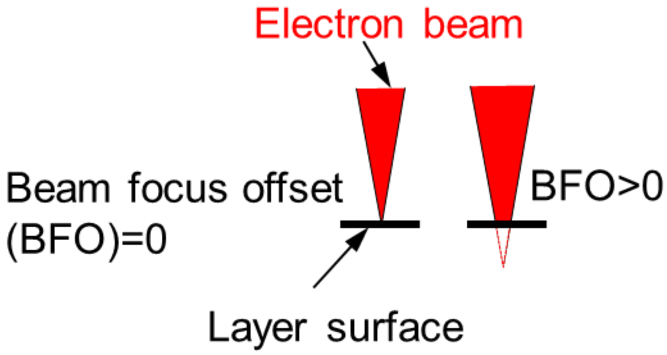

Fig.1-9. Schematic of the effect of beam focus offset on the beam size.

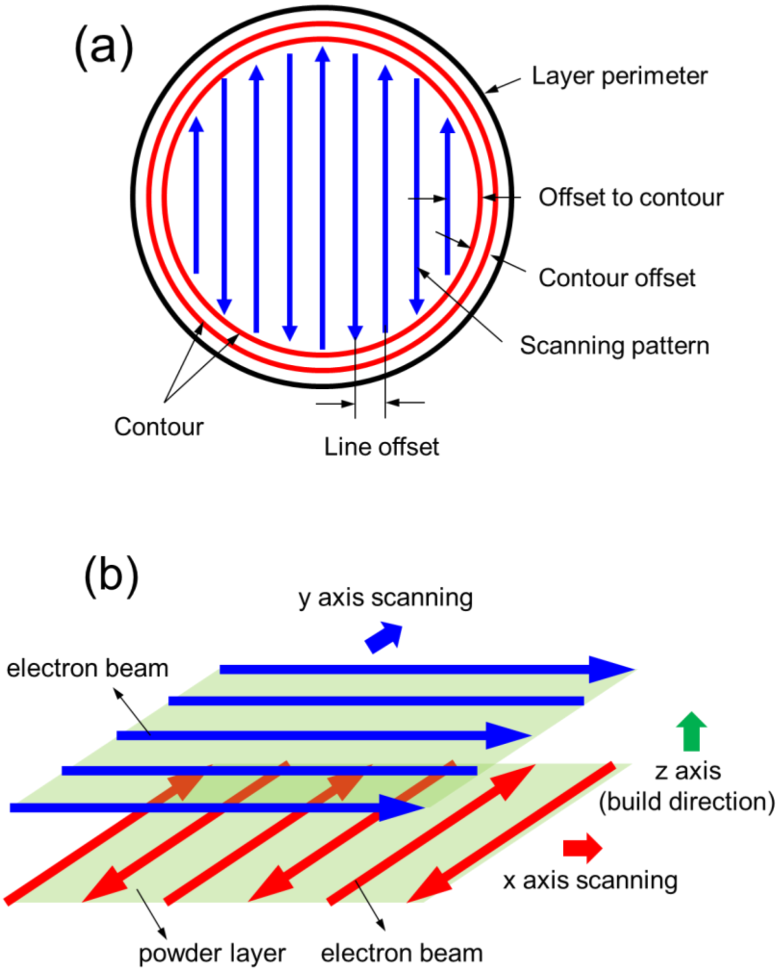

Fig.1-10. Scanning strategy of electron beam during melting process. (a) Scanning path on one layer. The electron beam scans the contour part at first, then scans the interior in the next. (b) Scanning direction on the neighboring layers. The scanning directions are perpendicular to each other on the neighboring layer, in order to homogenize the temperature in the build area.

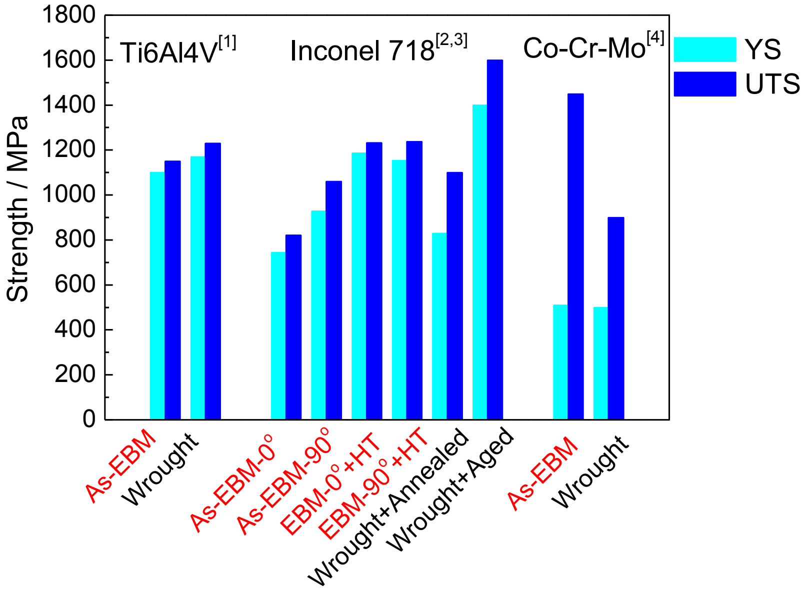

Fig.1-11. Mechanical property comparison between EBM-built material and wrought counterpart.

References

[1] C. K. Chua, K. F. Leong, and C. S. Lim, “Rapid Prototyping: Principles and Applications”. World Scientific, 2010, p. 512.

[2] N. N. Guo and M. C. Leu, “Additive Manufacturing:Technology, Applications and Research Needs,” *Frontiers of Mechanical Engineering*, vol. 8, no. 3, pp. 215–243, May 2013.

[3] K. V. Wong and A. Hernandez, “A Review of Additive Manufacturing,” *ISRN Mechanical Engineering*, vol. 2012, 2012.

[4] M. Vaezi, H. Seitz, and S. Yang, “A Review on 3D Micro-additive Manufacturing Technologies,” *The International Journal of Advanced Manufacturing Technology*, vol. 67, no. 5–8, pp. 1721–1754, Nov. 2012.

[5] P. A. Kobryn, N. R. Ontko, L. P. Perkins, and J. S. Tiley, “Additive Manufacturing of Aerospace Alloys for Aircraft Structures,” *Air Force Research Lab Wright-patterson Afb Oh Materials and Manufacturing Directorate*, pp. 1–14, May 2006.

[6] W. E. Frazier, “Metal Additive Manufacturing: A Review,” *Journal of Materials Engineering and Performance*, vol. 23, no. 6, pp. 1917–1928, Apr. 2014.

[7] A. A. Antonysamy, J. Meyer, and P. B. Prangnell, “Effect of Build Geometry on the β-grain Structure and Texture in Additive Manufacture of Ti6Al4V by Selective Electron Beam Melting,” *Materials Characterization*, vol. 84, pp. 153–168, Oct. 2013.

[8] L. E. Murr, S. M. Gaytan, A. Ceylan, E. Martinez, and J. L. Martinez, “Characterization of Titanium Aluminide Alloy Components Fabricated by Additive Manufacturing Using Electron Beam Melting,” *Acta Materialia*, vol. 58, no. 5, pp. 1887–1894, 2010.

[9] K. N. Amato, S. M. Gaytan, L. E. Murr, E. Martinez, P. W. Shindo, J. Hernandez, S. Collins, and F. Medina, “Microstructures and Mechanical Behavior of Inconel 718 Fabricated by Selective Laser Melting,” *Acta Materialia*, vol. 60, no. 5, pp. 2229–2239, Mar. 2012.

[10] L. E. Murr, E. Martinez, X. M. Pan, S. M. Gaytan, J. A. Castro, C. A. Terrazas, F. Medina, R. B. Wicker, and D. H. Abbott, “Microstructures of Rene 142 Nickel-based Superalloy Fabricated by Electron Beam Melting,” *Acta Materialia,* vol. 61, no. 11, pp. 4289–4296, Jun. 2013.

[11] L. E. Murr, S. M. Gaytan, F. Medina, H. Lopez, E. Martinez, B. I. Machado, D. H. Hernandez, L. Martinez, M. I. Lopez, R. B. Wicker, and J. Bracke, “Next-generation Biomedical Implants Using Additive Manufacturing of Complex, Cellular and Functional Mesh Arrays,” *Philosophical transactions. Series A, Mathematical, physical, and engineering sciences*, vol. 368, no. 1917, pp. 1999–2032, Apr. 2010.

[12] L. E. Murr, S. M. Gaytan, E. Martinez, F. Medina, and R. B. Wicker, “Next Generation Orthopaedic Implants by Additive Manufacturing Using Electron Beam Melting,” *International Journal of Biomaterials*, vol. 2012, 2012.

[13] S. Aarnio, “Rapid Prototyping,” 2010. [Online]. Available: http://www3.hamk.fi/metnet/Documents/RAPID PROTOTYPING_COTTBUS_2010.pdf.

[14] “Stereolithography.” [Online]. Available: http://www.youtube.com/watch?v=eJ7s-1XvDFw&feature=related.

[15] “Selective Laser Sintering.” [Online]. Available: http://www.youtube.com/watch?v=ShX_qXSTj_E&feature=related.

[16] “Three-dimensional Printing.” [Online]. Available: http://www.youtube.com/watch?v=uAt2xD1L8dw.

[17] M. ALIAKBARI, “Additive Manufacturing:State-of-the-Art, Capabilities, and Sample Applications with Cost Analysis,” Kungliga Tekniska Högskolan, 2012.

[18] “Fused Deposition Modeling.” [Online]. Available: http://www.youtube.com/watch?v=oYLjyI5honM&feature=related.

[19] Kennametal Stellite, “MIG Weld Deposition.” [Online]. Available: http://stellite.com/ProductsServices/HardfacingAlloys/WeldingProcesses/MIGWeldDeposition/tabid/324/Default.aspx.

[20] Arcam AB, “Arcam Q10.” [Online]. Available: http://www.arcam.com/wp-content/uploads/Arcam-Q10.pdf.

[21] O. R. N. Laboratory, “Electron Beam Melting.” [Online]. Available: https://www.youtube.com/watch?v=M_qSnjKN7f8.

[22] F. Abe, K. Osakada, M. Shiomi, K. Uematsu, and M. Matsumoto, “The Manufacturing of Hard Tools from Metallic Powders by Selective Laser Melting,” *Journal of Materials Processing Technology*, vol. 111, no. 1–3, pp. 210–213, Apr. 2001.

[23] L. Thijs, F. Verhaeghe, T. Craeghs, J. Van Humbeeck, and J. P. Kruth, “A Study of the Microstructural Evolution during Selective Laser Melting of Ti–6Al–4V,” *Acta Materialia*, vol. 58, no. 9, pp. 3303–3312, May 2010.

[24] Z. Wang, K. Guan, M. Gao, X. Li, X. Chen, and X. Zeng, “The Microstructure and Mechanical Properties of Deposited-IN718 by Selective Laser Melting,” *Journal of Alloys and Compounds*, vol. 513, pp. 518–523, Feb. 2012.

[25] L. E. Murr, S. M. Gaytan, D. A. Ramirez, E. Martinez, J. Hernandez, K. N. Amato, P. W. Shindo, F. R. Medina, and R. B. Wicker, “Metal Fabrication by Additive Manufacturing Using

Laser and Electron Beam Melting Technologies,” *Journal of Materials Science & Technology*, vol. 28, no. 1, pp. 1–14, Jan. 2012.

[26] L. Thijs, K. Kempen, J.-P. Kruth, and J. Van Humbeeck, “Fine-structured Aluminium Products with Controllable Texture by Selective Laser Melting of Pre-alloyed AlSi10Mg powder,” *Acta Materialia*, vol. 61, no. 5, pp. 1809–1819, Mar. 2013.

[27] A. Takaichi, Suyalatu, T. Nakamoto, N. Joko, N. Nomura, Y. Tsutsumi, S. Migita, H. Doi, S. Kurosu, A. Chiba, N. Wakabayashi, Y. Igarashi, and T. Hanawa, “Microstructures and Mechanical Properties of Co-29Cr-6Mo Alloy Fabricated by Selective Laser Melting Process for Dental Applications,” *Journal of the mechanical behavior of biomedical materials*, vol. 21, pp. 67–76, May 2013.

[28] B. Vrancken, L. Thijs, J.-P. Kruth, and J. Van Humbeeck, “Microstructure and Mechanical Properties of a Novel β Titanium Metallic Composite by Selective Laser Melting,” *Acta Materialia*, vol. 68, pp. 150–158, Apr. 2014.

[29] A. Strondl, R. Fischer, G. Frommeyer, and A. Schneider, “Investigations of MX and γ'/γ'' Precipitates in the Nickel-based Superalloy 718 Produced by Electron Beam Melting,” *Materials Science and Engineering: A*, vol. 480, no. 1–2, pp. 138–147, May 2008.

[30] S. M. Gaytan, L. E. Murr, F. Medina, E. Martinez, M. I. Lopez, and R. B. Wicker, “Advanced Metal Powder Based Manufacturing of Complex Components by Electron Beam Melting,” vol. 24, no. 3, 2009.

[31] S. M. Gaytan, L. E. Murr, E. Martinez, J. L. Martinez, B. I. Machado, D. A. Ramirez, F. Medina, S. Collins, and R. B. Wicker, “Comparison of Microstructures and Mechanical Properties for Solid and Mesh Cobalt-Base Alloy Prototypes Fabricated by Electron Beam Melting,” *Metallurgical and Materials Transactions A*, vol. 41, no. 12, pp. 3216–3227, Aug. 2010.

[32] D. A. Ramirez, L. E. Murr, S. J. Li, Y. X. Tian, E. Martinez, J. L. Martinez, B. I. Machado, S. M. Gaytan, F. Medina, and R. B. Wicker, “Open-cellular Copper Structures Fabricated by Additive Manufacturing Using Electron Beam Melting,” *Materials Science and Engineering: A*, vol. 528, no. 16–17, pp. 5379–5386, Jun. 2011.

[33] L. E. Murr, E. Martinez, K. N. Amato, S. M. Gaytan, J. Hernandez, D. A. Ramirez, P. W. Shindo, F. Medina, and R. B. Wicker, “Fabrication of Metal and Alloy Components by Additive Manufacturing: Examples of 3D Materials Science,” *Journal of Materials Research and Technology*, vol. 1, no. 1, pp. 42–54, Apr. 2012.

[34] S. H. Sun, Y. Koizumi, S. Kurosu, Y. P. Li, H. Matsumoto, and A. Chiba, “Build Direction Dependence of Microstructure and High-temperature Tensile Property of Co–Cr–Mo Alloy Fabricated by Electron Beam Melting,” *Acta Materialia*, vol. 64, pp. 154–168, Feb. 2014.

[35] K. M. Taminger and R. A. Hafley, “Electron Beam Freeform Fabrication for Cost Effective Near-Net Shape Manufacturing” .

[36] M. L. Griffith, D. M. Keicher, C. L. Atwood, J. A. Romero, J. E. Smugeresky, L. D. Harwell, and D. L. Greene, “Free Form Fabrication of Metallic Components Using Laser Engineered Net Shaping (LENS^{TM}).” *Proceedings of the Solid Freeform Fabrication Symposium*, Austin, TX, pp. 125–131, 1996.

[37] R. P. MUDGE and N. R. WALD, “Laser Engineered Net Shaping Advances Additive Manufacturing and Repair.” *Welding Journal-New York*, vol. 86, no. 1, pp. 44–48, 2007.

[38] “Laser Engineered Net Shaping.” [Online]. Available: http://www.sandia.gov/mst/pdf/LENS.pdf.

[39] H. Qi, M. Azer, and A. Ritter, “Studies of Standard Heat Treatment Effects on Microstructure and Mechanical Properties of Laser Net Shape Manufactured INCONEL 718,” *Metallurgical and Materials Transactions A*, vol. 40, no. 10, pp. 2410–2422, Aug. 2009.

[40] B. Baufeld, O. Van Der Biest, and R. Gault, “Additive Manufacturing of Ti–6Al–4V Components by Shaped Metal Deposition : Microstructure and Mechanical Properties,” *Materials and Design*, vol. 31, pp. S106–S111, 2010.

[41] J. Ding, P. Colegrove, J. Mehnen, S. Ganguly, P. M. Sequeira Almeida, F. Wang, and S. Williams, “Thermo-mechanical Analysis of Wire and Arc Additive Layer Manufacturing Process on Large Multi-layer Parts,” *Computational Materials Science*, vol. 50, no. 12, pp. 3315–3322, Jul. 2011.

[42] B. Baufeld, E. Brandl, and O. van der Biest, “Wire Based Additive Layer Manufacturing: Comparison of Microstructure and Mechanical Properties of Ti–6Al–4V Components Fabricated by Laser-beam Deposition and Shaped Metal Deposition,” *Journal of Materials Processing Technology*, vol. 211, no. 6, pp. 1146–1158, Jun. 2011.

[43] R. R. Dehoff and S. S. Babu, “Characterization of Interfacial Microstructures in 3003 Aluminum Alloy Blocks Fabricated by Ultrasonic Additive Manufacturing,” *Acta Materialia*, vol. 58, no. 13, pp. 4305–4315, Aug. 2010.

[44] M. R. Sriraman, S. S. Babu, and M. Short, “Bonding Characteristics during Very High Power Ultrasonic Additive Manufacturing of Copper,” *Scripta Materialia*, vol. 62, no. 8, pp. 560–563, Apr. 2010.

[45] R. J. Friel and R. A. Harris, “Ultrasonic Additive Manufacturing – A Hybrid Production Process for Novel Functional Products,” *Procedia CIRP*, vol. 6, pp. 35–40, 2013.

[46] X. Zhao, J. Chen, X. Lin, and W. Huang, “Study on Microstructure and Mechanical Properties of Laser Rapid Forming Inconel 718,” *Materials Science and Engineering: A*, vol. 478, no. 1–2, pp. 119–124, Apr. 2008.

[47] A. N. Arce, “Thermal Modeling and Simulation of Electron Beam Melting for Rapid Prototyping on Ti6Al4V Alloys,” North Carolina State University, 2012.

[48] V. Juechter, T. Scharowsky, R. F. Singer, and C. Körner, “Processing Window and Evaporation Phenomena for Ti–6Al–4V Produced by Selective Electron Beam Melting,” *Acta Materialia*, vol. 76, pp. 252–258, Sep. 2014.

[49] S. S. Al-Bermani, M. L. Blackmore, W. Zhang, and I. Todd, “The Origin of Microstructural Diversity, Texture, and Mechanical Properties in Electron Beam Melted Ti-6Al-4V,” *Metallurgical and Materials Transactions A*, vol. 41, no. 13, pp. 3422–3434, Aug. 2010.

[50] L. E. Murr, E. V Esquivel, S. A. Quinones, S. M. Gaytan, M. I. Lopez, E. Y. Martinez, F. Medina, D. H. Hernandez, E. Martinez, J. L. Martinez, S. W. Stafford, D. K. Brown, T. Hoppe, W. Meyers, U. Lindhe, and R. B. Wicker, “Microstructures and Mechanical Properties of Electron Beam-Rapid Manufactured Ti–6Al–4V Biomedical Prototypes Compared to Wrought Ti–6Al–4V,” *Materials Characterization*, vol. 60, no. 2, pp. 96–105, 2008.

[51] L. E. Murr, S. M. Gaytan, F. Medina, E. Martinez, J. L. Martinez, D. H. Hernandez, B. I. Machado, D. A. Ramirez, and R. B. Wicker, “Characterization of Ti–6Al–4V Open Cellular Foams Fabricated by Additive Manufacturing Using Electron Beam Melting,” *Materials Science and Engineering: A*, vol. 527, no. 7–8, pp. 1861–1868, Mar. 2010.

[52] O. Cansizoglu, O. Harrysson, D. Cormier, H. West, and T. Mahale, “Properties of Ti–6Al–4V Non-stochastic Lattice Structures Fabricated via Electron Beam Mmelting,” vol. 492, pp. 468–474, 2008.

[53] S. J. Li, L. E. Murr, X. Y. Cheng, Z. B. Zhang, Y. L. Hao, R. Yang, F. Medina, and R. B. Wicker, “Compression Fatigue Behavior of Ti–6Al–4V Mesh Arrays Fabricated by Electron Beam Melting,” *Acta Materialia*, vol. 60, no. 3, pp. 793–802, Feb. 2012.

[54] L. Yang, O. Harrysson, H. West, and D. Cormier, “Compressive Properties of Ti–6Al–4V Auxetic Mesh Structures Made by Electron Eeam Melting,” *Acta Materialia*, vol. 60, no. 8, pp. 3370–3379, May 2012.

[55] X. Y. Cheng, S. J. Li, L. E. Murr, Z. B. Zhang, Y. L. Hao, R. Yang, F. Medina, and R. B. Wicker, “Compression Deformation behavior of Ti – 6Al – 4V Alloy with Cellular Structures Fabricated by Electron Beam Melting,” vol. 16, pp. 153–162, 2012.

[56] S. Biamino, A. Penna, U. Ackelid, S. Sabbadini, O. Tassa, P. Fino, M. Pavese, P. Gennaro, and C. Badini, “Electron Beam Melting of Ti–48Al–2Cr–2Nb alloy: Microstructure and Mechanical Properties Investigation,” *Intermetallics*, vol. 19, no. 6, pp. 776–781, Jun. 2011.

[57] J. Hernandez, S. J. Li, E. Martinez, L. E. Murr, X. M. Pan, K. N. Amato, X. Y. Cheng, F. Yang, C. A. Terrazas, S. M. Gaytan, Y. L. Hao, R. Yang, F. Medina, and R. B. Wicker, "Microstructures and Hardness Properties for β-Phase Ti–24Nb–4Zr–7.9Sn Alloy Fabricated by Electron Beam Melting," *Journal of Materials Science & Technology*, vol. 29, no. 11, pp. 1011–1017, 2013.

[58] A. R. Rastkar and B. Shokri, "Surface Transformation of Ti–45Al–2Nb–2Mn–1B Titanium Aluminide by Electron Beam Melting," *Surface and Coatings Technology*, vol. 204, no. 11, pp. 1817–1822, Feb. 2010.

[59] W. J. Sames, K. a. Unocic, R. R. Dehoff, T. Lolla, and S. S. Babu, "Thermal Effects on Microstructural Heterogeneity of Inconel 718 Materials Fabricated by Electron Beam Melting," *Journal of Materials Research*, vol. 29, no. 17, pp. 1920–1930, Jul. 2014.

[60] A. Strondl, M. Palm, J. Gnauk, and G. Frommeyer, "Microstructure and Mechanical Properties of Nickel Based Superalloy IN718 Produced by Rapid Prototyping with Electron Beam Melting (EBM)," *Materials Science and Technology*, vol. 27, no. 5, pp. 876–883, May 2011.

[61] L. E. Murr, E. Martinez, S. M. Gaytan, D. A. Ramirez, B. I. Machado, P. W. Shindo, J. L. Martinez, F. Medina, J. Wooten, D. Ciscel, U. Ackelid, and R. B. Wicker, "Microstructural Architecture, Microstructures, and Mechanical Properties for a Nickel-Base Superalloy Fabricated by Electron Beam Melting," *Metallurgical and Materials Transactions A*, vol. 42, no. 11, pp. 3491–3508, Jun. 2011.

[62] R. S. Kircher, A. M. Christensen, and K. W. Wurth, "Electron Beam Melted (EBM) Co-Cr-Mo Alloy for Orthopaedic Implant Applications," in *Solid Freeform Fabrication Proceedings*, 2009, pp. 428–436.

[63] S. M. Gaytan, L. E. Murr, D. A. Ramirez, B. I. Machado, E. Martinez, D. H. Hernandez, J. L. Martinez, F. Medina, and R. B. Wicker, "A TEM Study of Cobalt-Base Alloy Prototypes Fabricated by EBM," *Materials Sciences and Applications*, vol. 02, no. 05, pp. 355–363, May 2011.

[64] H. B. Qi, Y. N. Yan, F. Lin, W. He, and R. J. Zhang, "Direct Metal Part Forming of 316L Stainless Steel Powder by Electron Beam Selective Melting," *Proceedings of the Institution of Mechanical Engineers, Part B: Journal of Engineering Manufacture*, vol. 220, no. 11, pp. 1845–1853, Jan. 2006.

[65] D. A. Ramirez, L. E. Murr, E. Martinez, D. H. Hernandez, J. L. Martinez, B. I. Machado, F. Medina, P. Frigola, and R. B. Wicker, "Novel Precipitate–Microstructural Architecture Developed in the Fabrication of Solid Copper components by Additive Manufacturing using Electron Beam Melting," *Acta Materialia*, vol. 59, no. 10, pp. 4088–4099, Jun. 2011.

[66] T. R. Mahale, "Electron Beam Melting of Advanced Materials and Structures," North Carolina State University, 2009.

[67] D. F. Paulonis, J. M. Oblak, and D. S. Duvall, “Precipitation in Nickel-Base Alloy 718,” *Trans. ASM (Amer. Soc. Metals)*, vol. 62, pp. 611-622, Jan. 1969.

[68] M. C. Chaturvedi and Y. Han, “Strengthening Mechanisms in Inconel 718 Superalloy,” *Metal Science*, vol. 17, no. 3, pp. 145–149, Mar. 1983.

[69] S. Azadian, L.Y. Wei, and R. Warren, “Delta Phase Precipitation in Inconel 718,” *Materials Characterization*, vol. 53, no. 1, pp. 7–16, Sep. 2004.

[70] M. Dehmas, J. Lacaze, A. Niang, and B. Viguier, “TEM Study of High-Temperature Precipitation of Delta Phase in Inconel 718 Alloy,” *Advances in Materials Science and Engineering*, vol. 2011, pp. 1–9, 2011.

[71] M. Sundararaman, P. Mukhopadhyay, and S. Banerjee, “Precipitation of the δ-Ni_3Nb Phase in Two Nickel Base Superalloys,” *Metallurgical Transactions A*, vol. 19, no. 3, pp. 453–465, Mar. 1988.

[72] P. L. Blackwell, “The Mechanical and Microstructural Characteristics of Laser-Deposited IN718,” *Journal of Materials Processing Technology*, vol. 170, no. 1–2, pp. 240–246, Dec. 2005.

[73] A. Chiba, K. Kumagai, N. Nomura, and S. Miyakawa, “Pin-on-Disk Wear Behavior in a like-on-like Configuration in a Biological Environment of High Carbon Cast and Low Carbon Forged Co–29Cr–6Mo Alloys,” *Acta Materialia*, vol. 55, no. 4, pp. 1309–1318, Feb. 2007.

[74] A. Chiba, N. Nomura, and Y. Ono, “Microstructure and Mechanical Properties of Biomedical Co–29Cr–8Mo Alloy Wire Fabricated by a Modified Melt-spinning Process,” *Acta Materialia*, vol. 55, no. 6, pp. 2119–2128, Apr. 2007.

[75] S. Kurosu, H. Matsumoto, and A. Chiba, “Isothermal Phase Transformation in Biomedical Co-29Cr-6Mo Alloy without Addition of Carbon or Nitrogen,” *Metallurgical and Materials Transactions A*, vol. 41, no. 10, pp. 2613–2625, Jun. 2010.

[76] Y. P. Li, J. S. Yu, S. Kurosu, Y. Koizumi, H. Matsumoto, and A. Chiba, “Role of Nitrogen Addition in Stabilizing the γ Phase of Biomedical Co–29Cr–6Mo Alloy,” *Materials Chemistry and Physics*, vol. 133, no. 1, pp. 29–32, Mar. 2012.

[77] K. Yamanaka, M. Mori, and A. Chiba, “Nanoarchitectured Co-Cr-Mo Orthopedic Implant Alloys: Nitrogen-Enhanced Nanostructural Evolution and Its Effect on Phase Stability,” *Acta Biomaterialia*, vol. 9, no. 4, pp. 6259–6267, Apr. 2013.

[78] K. Yamanaka, M. Mori, and A. Chiba, “Effects of Nitrogen Addition on Microstructure and Mechanical Behavior of Biomedical Co–Cr–Mo alloys,” *Journal of the Mechanical Behavior of Biomedical Materials*, vol. 29, pp. 417–426, Jan. 2014.

Chapter 2

2． Literature review of characteristic of electron beam melting

2.1 Introduction

Additive manufacturing, just as its name implies, produces the 3D object by adding its 2D slice features to a substrate layer by layer. In the EBM or SLM process, the powder in the region corresponding to the 2D slice feature will be selectively melted by electron beam (EB) or laser beam (LB). Therefore, the microstructure of the object fabricated by EBM or SLM is affected by the solidification of melt pool and the following post-built process. Because the selective melting of powders in EBM or SLM is similar to that in welding process, the solidification of the melt pool in EBM or SLM can be explained by analogy with those in the EB or LB welding process.

For the EB or LB welding process, the solidification direction is related to the melt pool geometry [1]. Generally, the shape of melt pool in metal welding is elliptical when beam travelling speed (V_t) is equal to solidification speed (R_s) (Fig.2-1a), and is tear drop shape when beam V_t is R_s (Fig.2-1b). When the melt pool is elliptical shape (Fig.2-1a) during the EBM process, curved-columnar will be formed because of the concaved temperature field. When the melt pool is tear drop shape (Fig.2-1b), the growth direction of the solidified grains will approach to the direction being perpendicular to the scanning direction, forming straight columnar grains.

According to the theory of solidification and crystal growth, the microstructure morphology is governed by the combination of temperature gradient (G) of liquid on the solid/liquid interface of melt pool and solidification speed (R) (Fig.2-2). The product of G and R (G•R) controls crystal growth mode (single crystal growth, cellular growth, dendritic growth or equiaxed crystal growth), and the ratio of G and R (G/R) controls the size and spacing of dendrites and cells [2]. For constant G, the solidification microstructure changes from cellular crystal (or single crystal) to dendritic crystal and finally equiaxed crystal with increasing R (i.e. decreasing G/R). At constant G_l/R, smaller G_l generates larger cellular size or spacing of dendrites.

The solidification condition of the melt pool is closely related to the processing parameter of EBM, which mainly includes beam current, beam focus offset, scanning speed, scanning route and line offset. Therefore, to control the solidification direction and microstructure morphology of EBM-built object, it is necessary to investigate the effect of build parameter on melt pool and establish the relationship between build parameter and microstructure.

2.2 Process map

Process map is a common method used to investigate the effect of build parameter on the microstructure of the object fabricated by AM. The build parameter considered in process map of AM mainly contains heat source power (P), heat source travel speed (V), material feed rate, existing temperature of the part being deposited onto (T_0) and feature geometry (local geometry of the part) [3]. A detail study of the process map can consider the build parameter such as the average powder size, beam spot size and preheating temperature. Beside the microstructure morphology, the issue such as residual stress [4,5] and Al evaporation in γ–TiAl [6] or Ti–6Al–4V [7] can be investigated by process map.

Though numerous parameters are considered in establishing process map, the most often used parameters are power and velocity (i.e. P and V). Fig. 2-3 shows an example process map research to obtain the dense microstructure of Ti–48Al–2Nb–2Cr fabricated by EBM [6]. Line energy (LE) is defined as

$$\mathrm{LE}=U*I/v\ , \tag{2.1}$$

where, U is acceleration voltage, which is fixed to 60 kV. I is the beam current, and v

is the deflection speed (i.e., scanning speed for melting). The criterion to judge the dense microstructure is process related porosity cannot be observed, which is large flaw embedded in the build part, as shown in the insert micrograph on the lower right corner of Fig. 2-3. The process related porosity is different from the powder related porosity, which is the gas bubble from the trapped argon gas in the gas atomized powders. The powder related porosity is very difficult to remove even by optimizing the build parameter. The minimum *LE* for the dense microstructure decreased with increasing deflection speed. The reason why higher *LE* is needed at lower deflection speed is that thermal loss from the melt pool to surrounding powders will become larger use of increased conduction time for heat loss at lower v. The higher the v is, the more the heat from the adjacent scanning line heated can be used to melt the powders in the neighboring scanning line. Therefore, less *LE* is needed at higher deflection speed**.** The time required for the beam to move from a position in the last pass to its neighboring position in the next parallel scanning line depends on the geometry of the build part. Therefore, the optimum *LE* and deflection velocity for obtaining pore-free object depends on the geometry of the object.

Because aluminum loss in the Ti–6Al–4V will change the microstructure and following mechanical properties, the process map is also used to investigate aluminum loss in the Ti–6Al–4V fabricated by EBM, as shown in Fig. 2-4 [7]. The aluminum content was measured by spark spectrometry. The aluminum loss decreased with decreasing *LE* at constant scanning speed, because the melt pool size and top surface temperature decreased with decreasing *LE*. Aluminum loss would increase with increasing scanning speed at constant *LE*, because the melt pool geometry and top surface temperature will increase at higher scanning speed. More heat loss from the previous scanning path could be used to melt the powders in the neighboring scanning path at higher scanning speed is the reason for the increased melt pool geometry and surface temperature.

Fig. 2-5 shows the schematic for the melt pool geometry and a process map for controlling the melt pool geometry of Ti–6Al–4V fabricated by EBFFF [3]. The temperature of the part being deposited onto is 576 ℃, and the ratio of molten material to total deposited material for melting is 0.77. Fig. 2-5(a) shows the schematic for melt pool geometry. A represents the largest bead cross section area perpendicular to the beam travelling direction, which is assumed to be a semi-circle and can reflect the melt pool size. d is the maximum effective melt pool depth, which is defined as

$$d=\sqrt{2A/\pi} \tag{2.2}$$

L is the distance between the maximum depth position and the melt pool trailing edge in the beam travelling direction. L/d can reflect the melt pool shape. The solid green, red and blue lines in Fig. 2-5(b) represent the P-V conditions generating the bead cross sections with 0.063 in^2, 0.031 in^2, and 0.016 in^2, respectively. The dashed lavender, turquoise and orange lines in Fig. 2-5(b) represent the P-V conditions generating the melt pool with constant L/d rate of 4, 6 and 8, respectively.

Combining solidification map with solidification rate and temperature gradient of the melt pool from finite element simulation, Gockel et al. [8] obtained the process map predicting the microstructure of Ti–6Al–4V fabricated by EBFFF, as shown in Fig. 2-6. The black curves represent the P-V conditions generating the constant grain size. The red dash curve is the P-V condition boundary of fully columnar grains and mixed grains (columnar grains and equiaxed grains), while the solid blue curve is the P-V condition boundary of mixed grains and fully equiaxed grains. Comparing Fig. 2-5(b) with Fig. 2-6, Gockel et al. [8] indicated that the constant melt pool area curves in Fig. 2-5(b) corresponded to the constant grain size curves in Fig. 2-6, and that constant shape (L/d) curves in Fig. 2-5(b) corresponded to the grain morphology curves (boundaries between mixed grains and fully columnar grains or equiaxed grains) in Fig. 2-6. Therefore, it is possible to control the solidification microstructure by controlling the melt pool geometry.

2.3 Melt pool analysis and simulation

To predict the solidification microstructure of the materials fabricated by the AM process, the cooling rates and temperature gradients of the melt pool are required to be known. However, they are very difficult to be measured directly. Therefore, analysis and simulation of melt pool with thermal conduction model is a possible way to obtain the cooling rates and temperature gradients of the melt pool.

2.3.1 Melt pool analysis with Rosenthal solution

3D Rosenthal solution is an analytical method which is used to investigate the temperature distribution on an infinite substrate on which a point heat source (such as arc, laser and electron beam) is moving [9]. This method was first applied in the arc welding process [10], but Vasinonta et al. [11] indicated that it was also possible to be applied in beam-based additive manufacturing process. Fig. 2-7 shows the 3D geometry model for Rosenthal solution analysis [9]. The absorbed powder is assumed to be proportional to the electron beam power, with a coefficient of α. The relative coordinate of the electron beam is (x_0, y_0, z_0), and the electron beam moving speed is V.

There are several assumptions for the analysis are as following [9]:

1) The heat source is considered as a point, and the effect of the beam diameter on the temperature distribution is neglected. This assumption is more reasonable when the melt pool is much larger than the beam diameter.
2) The model considers only the case where the point heat source moves along a single direction in an infinite half space. Here, the beam is assumed to move only in the x direction. Then the coordinate of the beam at the time of t is (x-Vt, y_0, z_0).
3) Only the heat conduction between the melt pool and the surrounding bulk geometry is considered. The radiation of the melt pool surface, convective heat transfer between the melt pool and surrounding environment, and convection flows in the melt pool are neglected because their effects on heat transfer can be

treated with the power absorption coefficient α.

4) The thermal physical properties, such as density, specific heat and thermal conductivity is independent of temperature.

Based on the above assumption, the relative temperature at any position can be calculated by the thermal conduction equation, and expressed as:

$$\bar{T}=\frac{\exp(-\bar{x}_0-\sqrt{\bar{x}_0^2+\bar{y}_0^2+\bar{z}_0^2})}{2\sqrt{\bar{x}_0^2+\bar{y}_0^2+\bar{z}_0^2}}\ , \tag{2.3}$$

where the relative coordinate $\bar{x}_0$, $\bar{y}_0$, and $\bar{z}_0$ are defined as:

$$\bar{x}_0=\frac{x_0}{(2k/\rho cV)},\bar{y}_0=\frac{y_0}{(2\mathrm{k}/\rho cV)},\text{ and }\bar{z}_0=\frac{z_0}{(2\mathrm{k}/\rho cV)}\ \text{, respectively.} \tag{2.4}$$

$\bar{T}$ given by the actual temperature is expressed as:

$$\bar{T}=\frac{T\text{-}T_0}{(\alpha Q/\pi k)(\rho cV/2k)}\ , \tag{2.5}$$

T_0, ρ, c, and k are the initial temperature, density, specific heat and the thermal conductivity of the substrate, respectively.

The relative cooling rate of the melt pool is given by

$$\frac{\partial\bar{T}}{\partial\bar{t}}=\frac{1}{2}\frac{\exp(-(\bar{x}\text{-}\bar{t})\text{-}\sqrt{(\bar{x}\text{-}\bar{t})^2+\bar{y}_0^2+\bar{z}_0^2})}{\sqrt{(\bar{x}\text{-}\bar{t})^2+\bar{y}_0^2+\bar{z}_0^2}}\times\left\{1+\frac{\bar{x}\text{-}\bar{t}}{\sqrt{(\bar{x}\text{-}\bar{t})^2+\bar{y}_0^2+\bar{z}_0^2}}+\frac{\bar{x}\text{-}\bar{t}}{(\bar{x}\text{-}\bar{t})^2+\bar{y}_0^2+\bar{z}_0^2}\right\}, \tag{2.6}$$

where $\frac{\partial\bar{T}}{\partial\bar{t}}$ given by the actual cooling rate is expressed as:

$$\frac{\partial\bar{T}}{\partial\bar{t}}=\left(\frac{2k}{\rho cV}\right)^2\left(\frac{\pi k}{\alpha QV}\right)\frac{\partial T}{\partial t}\ , \tag{2.7}$$

The dimensionless coordinate $\bar{x}$ in Eq.2.6 is defined as:

$$\bar{x}=\bar{x}_0+\bar{t}\ , \tag{2.8}$$

where $\bar{t}$ is expressed as

$$\bar{t}=t/(2k/\rho cV^2)\ . \tag{2.9}$$

The relative temperature gradient can be obtained by differentiating Eq.2.3 with relative coordinates, $\bar{x}_0$, $\bar{y}_0$, and $\bar{z}_0$, and the result is

$$|\nabla\bar{T}|=\sqrt{\left(\frac{\partial\bar{T}}{\partial\bar{x}_0}\right)^2+\left(\frac{\partial\bar{T}}{\partial\bar{y}_0}\right)^2+\frac{\partial\bar{T}}{\partial\bar{z}_0}}, \tag{2.10}$$

where

$$\frac{\partial \bar{T}}{\partial \bar{x}_0} = -\frac{\exp(-\bar{x}_0 - \sqrt{\bar{x}_0^2+\bar{y}_0^2+\bar{z}_0^2})}{2\sqrt{\bar{x}_0^2+\bar{y}_0^2+\bar{z}_0^2}} \times \left\{1 + \frac{\bar{x}_0}{\sqrt{\bar{x}_0^2+\bar{y}_0^2+\bar{z}_0^2}} + \frac{\bar{x}_0}{\bar{x}_0^2+\bar{y}_0^2+\bar{z}_0^2}\right\}, \tag{2.11}$$

$$\frac{\partial \bar{T}}{\partial \bar{y}_0} = -\frac{\bar{y}_0}{2} \frac{\exp(-\bar{x}_0 - \sqrt{\bar{x}_0^2+\bar{y}_0^2+\bar{z}_0^2})}{(\bar{x}_0^2+\bar{y}_0^2+\bar{z}_0^2)} \left(1 + \frac{1}{\sqrt{\bar{x}_0^2+\bar{y}_0^2+\bar{z}_0^2}}\right) , \tag{2.12}$$

and

$$\frac{\partial \bar{T}}{\partial \bar{z}_0} = -\frac{\bar{z}_0}{2} \frac{\exp(-\bar{x}_0 - \sqrt{\bar{x}_0^2+\bar{y}_0^2+\bar{z}_0^2})}{(\bar{x}_0^2+\bar{y}_0^2+\bar{z}_0^2)} \left(1 + \frac{1}{\sqrt{\bar{x}_0^2+\bar{y}_0^2+\bar{z}_0^2}}\right) . \tag{2.13}$$

The relative temperature gradient $|\overline{\nabla T}|$ given by the actual temperature gradient $|\nabla T|$ is expressed as:

$$|\overline{\nabla T}| = \left(\frac{2k}{\rho c V}\right)^2 \left(\frac{\pi k}{\alpha Q}\right) |\nabla T| \ . \tag{2.14}$$

The solidification velocity R obtained from the cooling rate $\frac{\partial T}{\partial t}$ is given by

$$R = \frac{1}{G} \frac{\partial T}{\partial t} \ . \tag{2.15}$$

To know cooling rate and temperature gradient at the melt pool boundary, the temperature T appearing in the above equations is taken as the melting point T_{m}.

Though thermophysical properties are considered to be independent of temperature and phase transformation latent heat is neglected in the Rosenthal solution, Bontha et al. [9] indicated that the cooling rate and temperature gradient calculated by Rosenthal solution for microstructure prediction was reasonable by comparing them with those derived by the finite element modeling (FEM).

Fig. 2-8 shows the Rosenthal solution for bulk Co–Cr–Mo alloy. The parameters for calculation are listed in Table 2-1. The calculation was carried out on the software of “Wolfram Mathematica 6.0”. The simulation result shows that the melt pool becomes narrow and shallow with increasing the beam travelling rate.

2.3.2 Melt pool numerical simulation by finite element modeling

Though Rosenthal solution is reasonable for the calculation of the cooling rate and temperature gradient of the melt pool, the effect of powder porosity and beam energy absorption on the melt pool geometry still can not be solved. Therefore, melt pool numerical simulation was widely investigated.

Shen et al.[12] investigated the effect of powder porosity and beam size on the temperature fields and melt pool geometries of Ti–6Al–4V by FEM based on the transient heat transfer model. Fig. 2-9 shows their results about the temperature fields and melt pool geometries in the cases where the heat conduct substrates are solid (Fig.2-9(a)) and porous with porosity of 30% (Fig.2-9(b)). The temperature contour around the melt pool is shown in the centers of Fig. 2-9(a,b), and the melt pool geometries (i.e. the temperature contour part with the temperature higher than the melting point) are shown in lower right corners of Fig. 2-9(a,b). Fig. 2-9(c) shows the temperature profile along the center line of the temperature contour from the beam center to the position with the initial preheating temperature of 750 ℃ behind the center position. Because the heat conductivity around the melt pool is almost uniform in the case of solid substrate, the melt pool shape tends to be elliptical (Fig. 2-9(a)) similarly to that derived by Rosenthal solution. In the case of powder layer substrate, the trailing part of the melt pool will dissipate more heat than the ahead part because the trailing part contact with already solidified part, which has higher heat conductivity than the porous substrate. Therefore, the melt pool shape tends to be tear drop shape (Fig. 2-9(b)). Also, the powder layer substrate will exhibit much larger melt pool geometry than the solid layer substrate because of the lower heat conductivity in the powder layer substrate. Owing to latent heat, the temperature profile along the center line of the temperature contour (Fig. 2-9(c)) exhibits a plateau, which is longer in the scanning direction in the powder layer substrate than in the solid substrate. The red dotted line shows the temperature profile result without considering the latent heat for comparison, which exhibits no plateau. With increasing the porosity of the powder layer, the melt pool changes from the tear drop shape to elliptical shape because of the increased adiabatic effect, and exhibits higher maximum temperature at higher porosity powder layer. With increasing the beam diameter, the melt pool depth will decrease owing to the decrease of energy density, which may cause the unmelt particles.

In the research of Shen et al., the powders are considered as a homogenous material with the effective properties. For an example, the thermal conductivity of the powders with some packing density is taken as the value of the solid material with the same density. However, in the actual situation, the thermal conductivity of the powder with some packing density is smaller than that of the solid material with the same density, because the contact between the powders is weaker than that in the porous solid. Therefore, the simulation result can only reflect the tendency of the melt pool geometry variation with changing the powder packing density. In addition, their consideration about the powder shrinkage from the solidification of melting just assumes the packing density of the powders, which is different from the actual situation of the powders with stochastic size. The factor results in that the numerical simulation result about the melt pool is always regular shape, being different from the experimental observation with accidental variable shape.

Körner et al. [13] investigated 2D melt pool cross section of Ti–6Al–4V in the EBM process by lattice Boltzmann model and compared them with the experimental results. The physical model in their research is shown in Fig. 2-10. This model considered numerical complex physical phenomena in the EBM, including the beam absorption in the powder bed and melt pool, melting and solidification of the melt pool, wetting of the powder particles with the melt pool liquid, diffusive and radiative heat conduction in the powders, diffusive and convective heat conduction in the melt pool, capillary effects, gravity, and powder arrangement on the raked layer with the same density, which are shown by the bold font in Fig. 2-10. In order to simplify the model, some physical phenomena are also neglected, such as solidification shrinkage, element vaporization, radiation of the beam, sintering of the powders, and Marangoni-convection, which are shown by the normal font in Fig. 2-10. The main conclusions in the research are as following:

1) Pronounced balling effect [14] can take place if the liquid metal does not wet the powder (i.e. the wetting angle is 180 °).
2) When the melt pool geometry is not much larger than the mean powder size, the melt pool will keep the round shape. But when melt pool geometry is

much larger than the mean powder size, the melt pool will present the semielliptical shape.

3) The melt pool geometry will become more and more defined (regular semielliptical shape) with increasing the powder particle packing density.
4) The melt pool geometry is strongly dependent on the local powder density and arrangement. The melt pool geometry may be different even though the powder density in the each raked layer.
5) The bead continuity mainly depends on the line energy, and does not change with the scanning speed at constant line energy. The beads along the scanning line will become continuous and closed packed consolidated line with increasing line energy. The process map for the bead continuity is shown in Fig. 2-11.

The process map for the bead continuity shown in Fig. 2-11 is closely related to the process map for density part shown in Fig. 2-3, because the discontinuous beads in the scanning line is a main reason for causing the porosity in the build part.

Rai et al.[15] indicated that fluid flow can widen the melt pool geometry of 304L stainless steel, Ti–6Al–4V, Tantalum, and Vanadium welded by the laser beam, because heat transfer can increase when flow convection is considered. Therefore, Jamshidinia et al. [16] investigated the effect of electron beam scanning speed, beam current and powder bed density on the temperature fields and melt pool geometries of Ti–6Al–4V by FEM based on 3D thermal-fluid flow model with the consideration of flow convection in the melt pool. At constant beam current condition (i.e. the constant powder, because the accelerate voltage is kept at 60 kV), with increasing the electron beam scanning speed, the melt pool will become narrow and long when seen from the top surface. This is because the line energy decreases with increasing electron beam scanning speed, which will result in lower temperature in the same volume of material. The melt pool in the thermal fluid flow model exhibited larger surface area (wider and longer size) than that in the pure thermal model. However, the melt pool depth and maximum temperature in the thermal fluid flow model were less than those in the pure thermal model. These results were caused by the fluid flow direction in the melt pool, as shown in Fig. 2-12. Fig. 2-12 show that the fluid flow formed a convection loop from the bottom to the surface in the depth direction, and formed a convection loop from the center to the edge on the melt pool surface. Therefore, the melt pool surface will be enlarged by the outward flow on the top surface, and the depth will be deceased by the upward flow in the depth direction, which will prevent the molten material penetration. Also, the fluid convection will decrease the local high temperature in the center of the melt pool, therefore, the maximum temperature in the thermal fluid flow model is less than those in the pure thermal model. Because the thermal conductivity of the powders increases with increasing the powder density, the heat dissipation from the molten pool center to the surrounding loose powders will become larger. As a result, the melt pool geometry will decrease with increasing the powder bed density.

2.4 Superiority of electron beam melting for microstructure control

Fig.2-13 shows the comparison between Inconel 718 microstructure predicted by process map of EBF^3 process and actual microstructure in electron beam melting process (EBM) in the same absorbed power and scanning velocity condition [17]. In the process map of EBF^3, the absorbed power (P) and scanning velocity (V) parameter range for fully columnar grains is very narrow. In the condition with the power of 3000 W and scanning speed of 1000 mm/s, the microstructure of Inconel 718 fabricated by EBM process is predicted to be equiaxed grains based on the process map of EBF3. However, the actual microstructure obtained by EBM process is single crystal-like microstructure. This result reveals that the P-V build parameter region for the columnar grains may be very wide in the EBM process. The condition difference to obtain columnar grains should be caused by the additional preheating process in EBM process. The preheating process will sinter the powder partly, which will change of thermal conductivity of the powder bed significantly. Therefore, the process map of Inconel 718 in the EBM process should be made separately.

In the current beam based AM processes for metals, the beam powder and scanning speed are largely different from each other. Fig.2-14 shows the maximum absorbed power and scanning velocity parameter ranges used for object fabrication in four commercial additive manufacturing equipments for metals. Among the four AM process, the EBM exhibits the largest P-V variation region. This means EBM is more suitable for microstructure control than the other AM process, because P and V are the main factors governing the microstructure.

Conclusions

1) Process map consisting of absorbed power and scanning speed can not only be used to investigate the microstructure morphology (porosity, grain size, gain morphology), but also the issue such as residual stress and Al evaporation in γ–TiAl and Ti–6Al–4V.
2) The microstructure of EBM-built object can be changed by changing the beam power and beam scanning speed.
3) By optimizing the simulation model with considering more physical phenomena, such as solidification shrinkage, Marangoni-convection, powder size and preheating temperature, the simulation result about melt pool will be much more accurate.
4) Electron beam melting can control the microstructure in wider range than the other additive manufacturing processes because of its much wider operation region of absorbed power and scanning velocity for object fabrication.

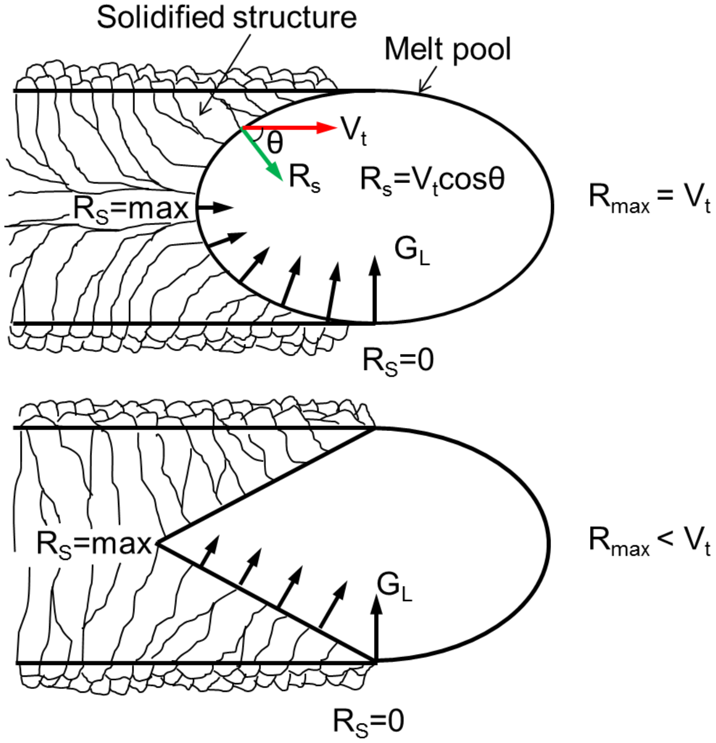

Fig.2-1 Microstructures around the melt pools with different beam travelling speed. (a) Low and moderate electron beam travelling speed for diverging grain growth, (b) high electron beam travelling speed for straight grain growth [1].

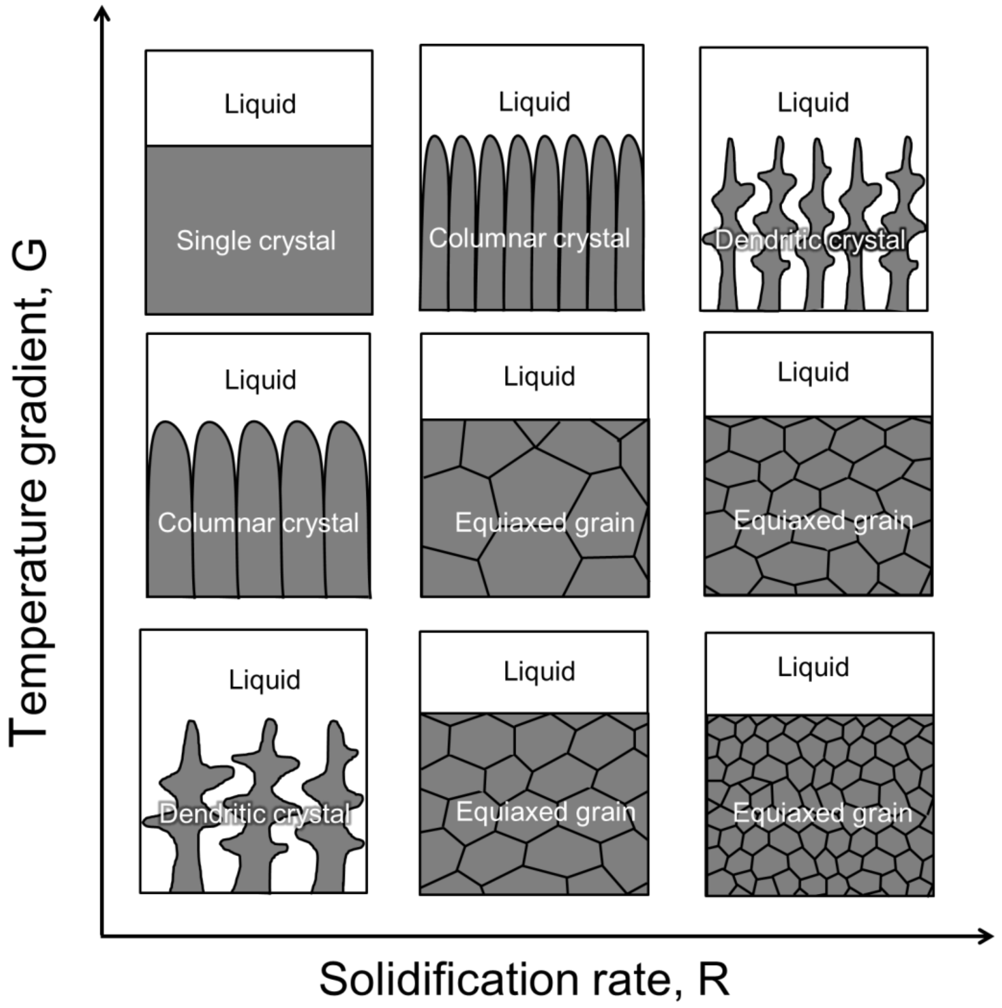

Fig.2-2 Solidification microstructure variation as a function of temperature gradient G and growth rate R.

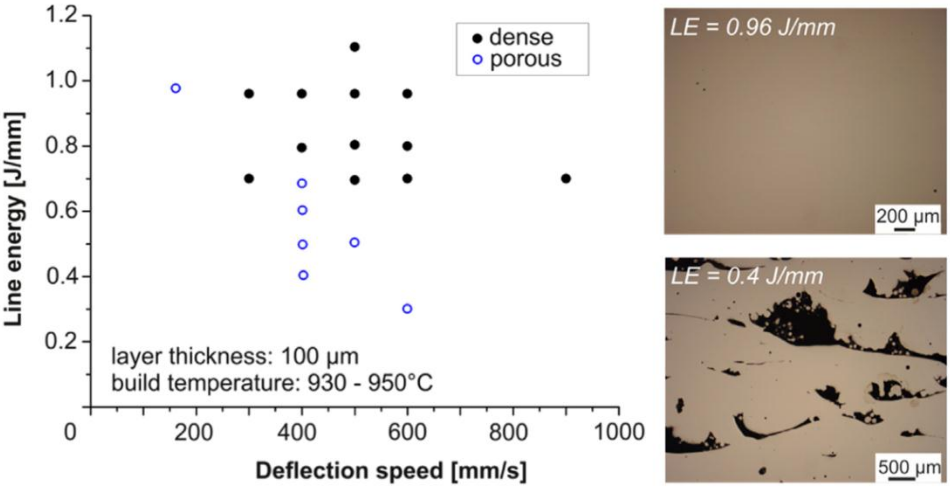

Fig.2-3 Process map to determine dense microstructure of Ti–48Al–2Nb–2Cr fabricated by EBM [6]. The insert micrographs on the upper right and lower right show the examples for dense microstructure and porous microstructures, respectively.

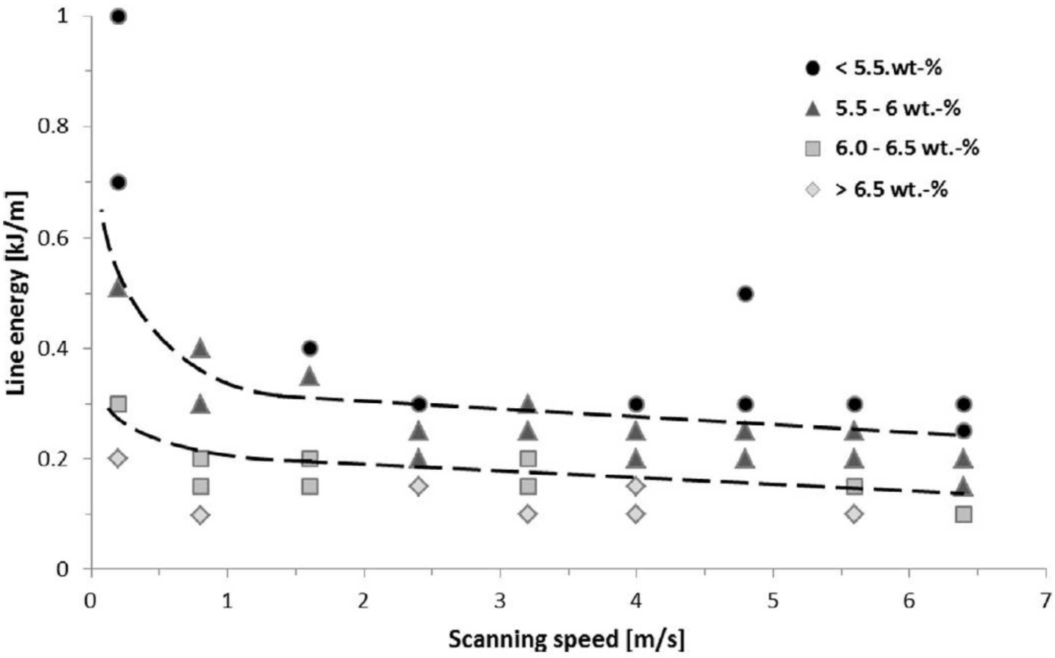

Fig.2-4 Process map research about aluminum loss of Ti–6Al–4V fabricated by EBM. The dashed line represents the dense and dimensionally stable parts at different line energy and scanning speed [7].

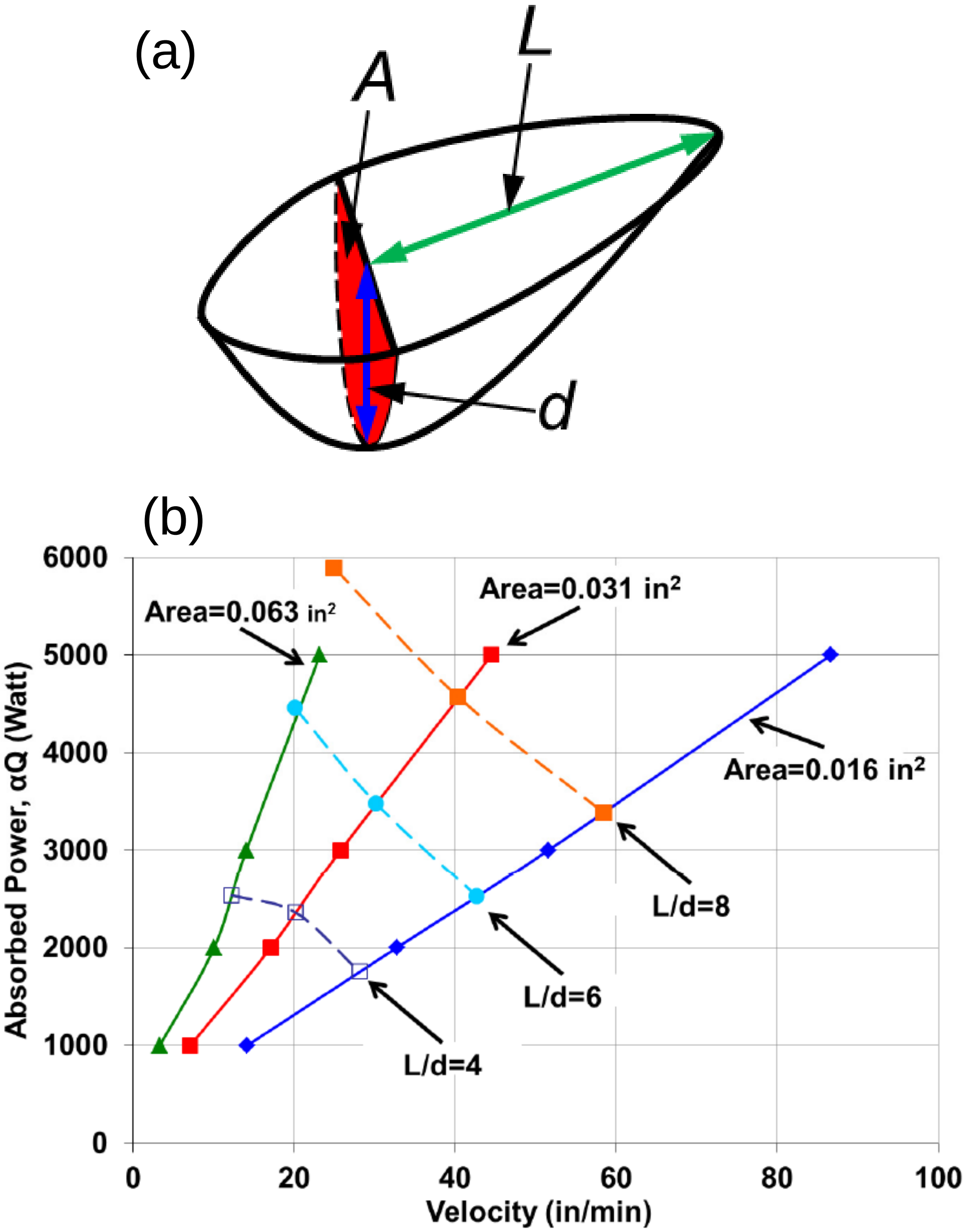

Fig.2-5 (a) Schematic for melt pool geometry. (b) Process map research about melt pool geometry of Ti–6Al–4V fabricated by EBFFF [3].

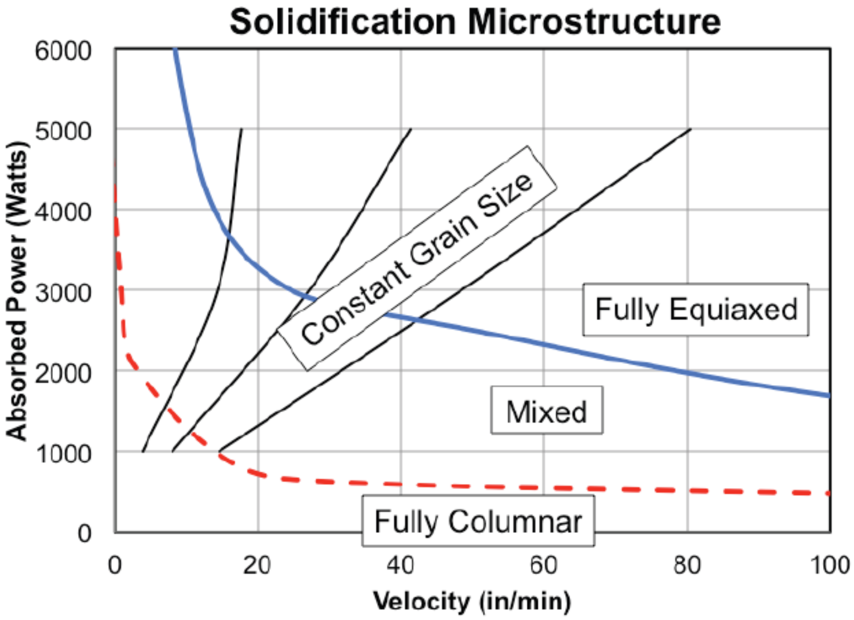

Fig.2-6 Microstructure process map of Ti–6Al–4V fabricated by EBFFF [8].

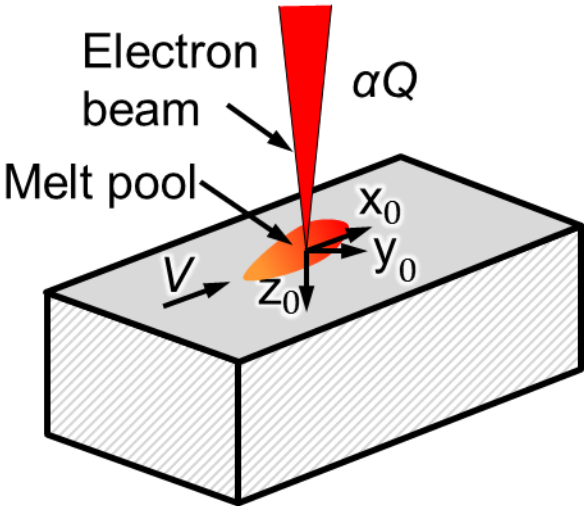

Fig.2-7 3D geometry model for Rosenthal solution analysis.

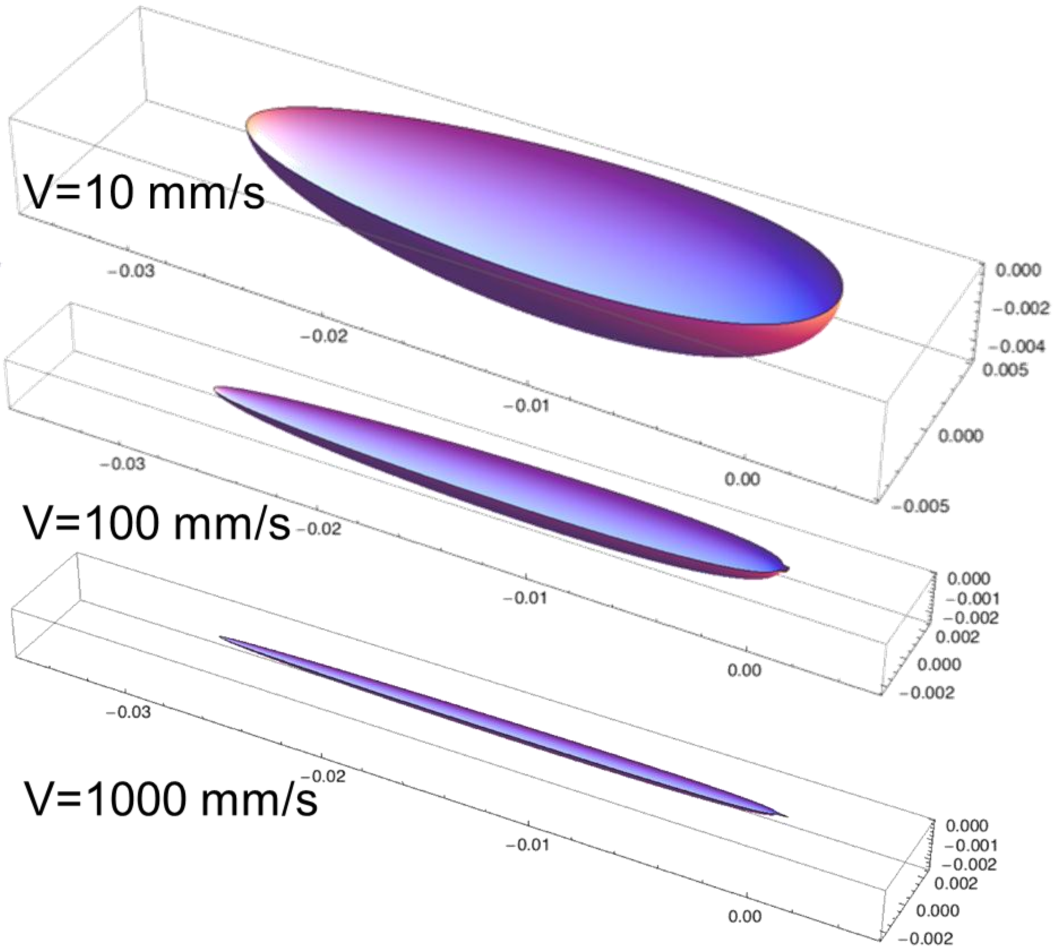

Fig.2-8 Rosenthal solution for bulk Co–Cr–Mo alloy with different scanning speeds.

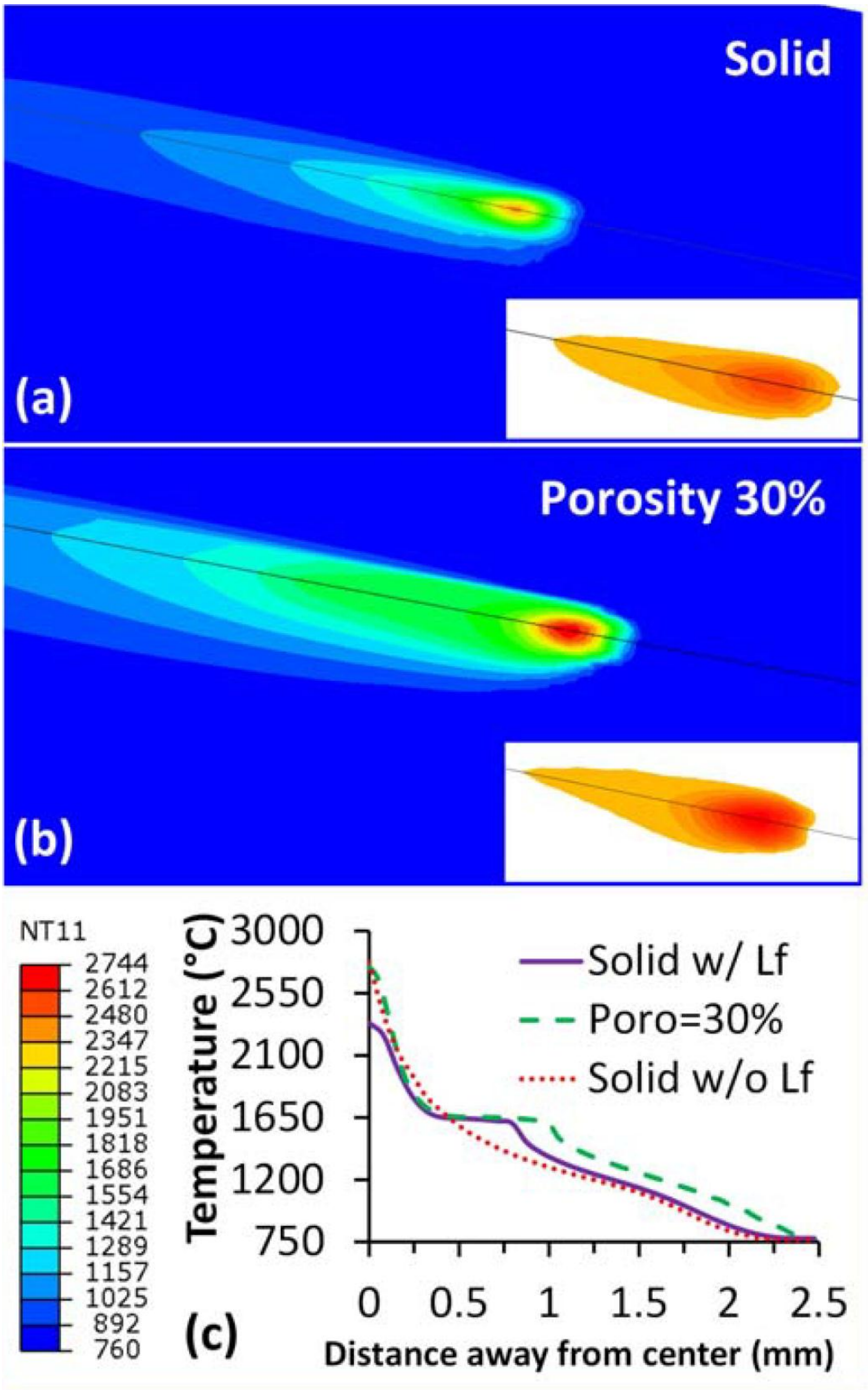

Fig.2-9 Temperature field and molten pool geometry comparison between the solid substrate and the powder substrate with the porosity of 30 %. [12]

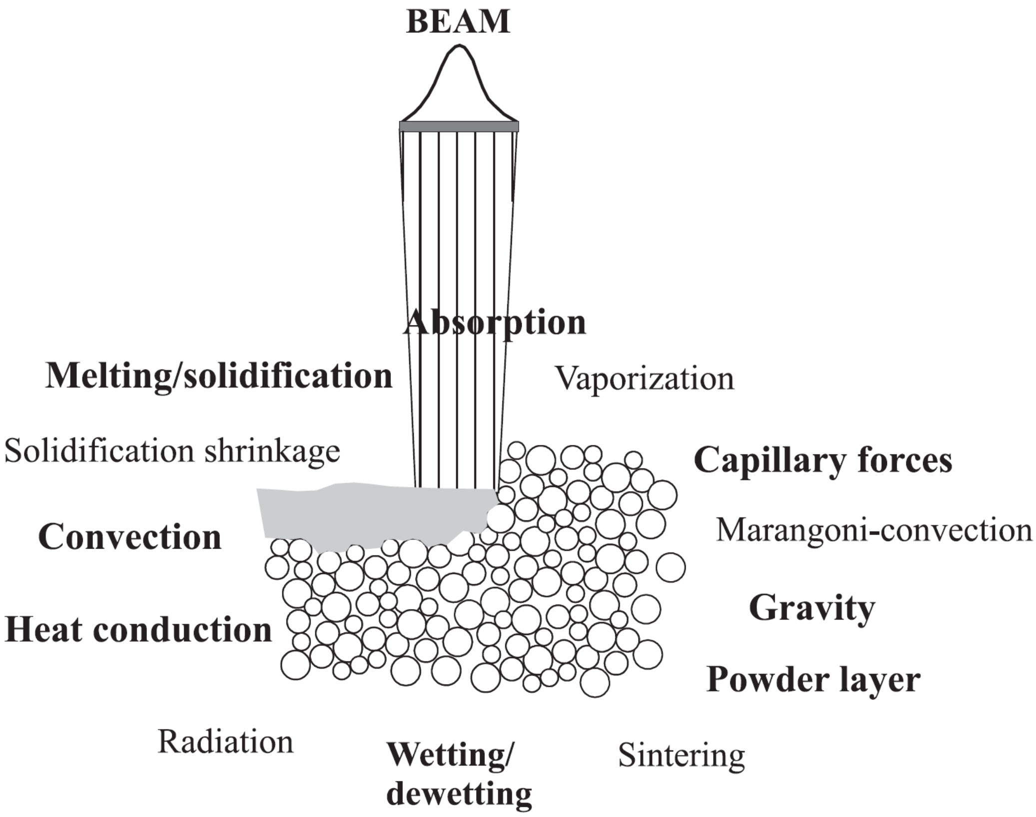

Fig.2-10 Physical model for simulation of EBM process [13] .

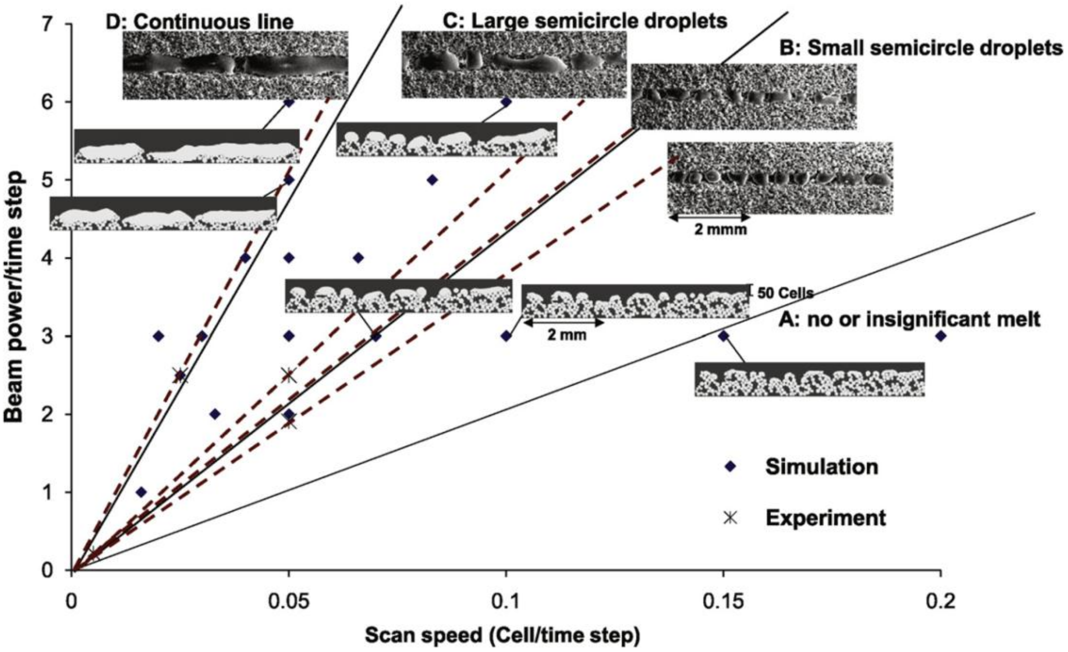

Fig.2-11 Process map for beads continuity of Ti–6Al–4V in EBM process [13] .

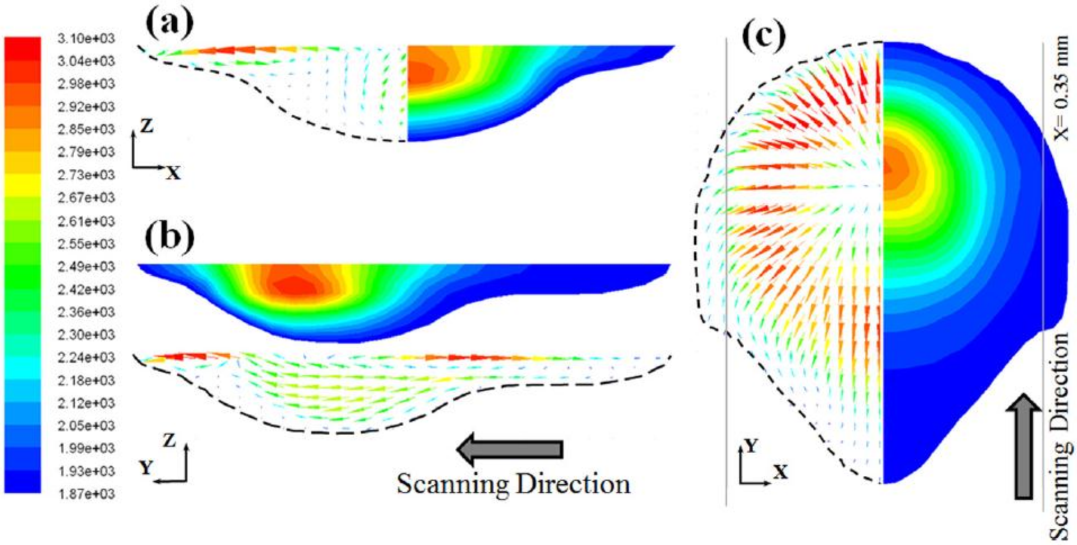

Fig.2-12 Temperature distribution and fluid convection in the melt pool. (a) view along the electron beam scanning direction (i.e. X-Z plane) at the position with Y axis intercept of 6mm (Corresponding to the maximum depth of the melt pool), (b) view normal to the electron beam scanning direction (i.e. Y-Z plane) at the position with X axis intercept of 0 mm, (c) top view (i.e. X-Y plane). [16]

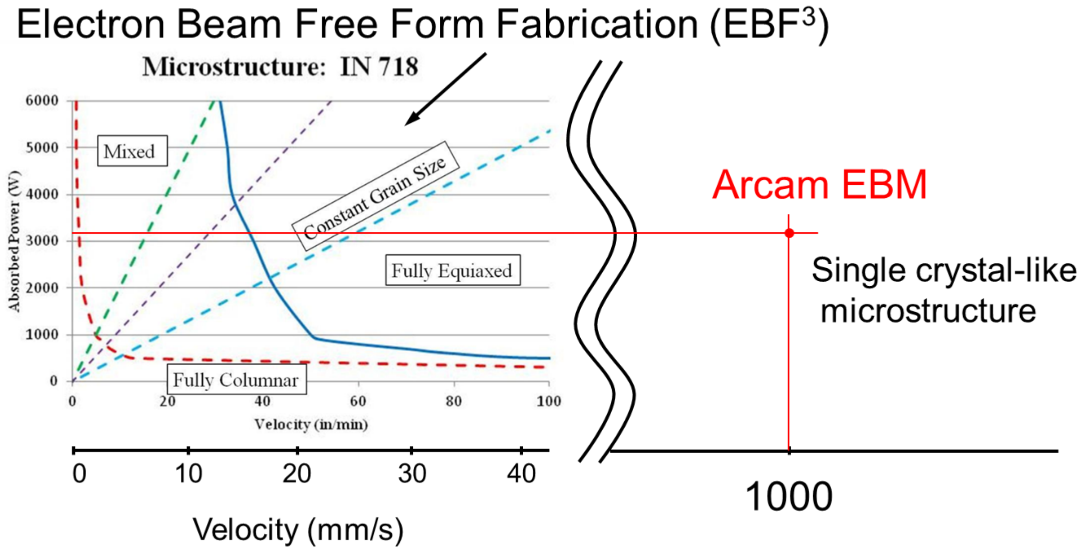

Fig.2-13 Comparison between Inconel 718 microstructure predicted by process map of EBF^3 process and actual microstructure in electron beam melting process (EBM) in the same absorbed power and scanning velocity condition [17]. The result suggests that the process map of Inconel 718 in the EBM process is different from that in the EBF3 process because of the additional preheating process in EBM process.

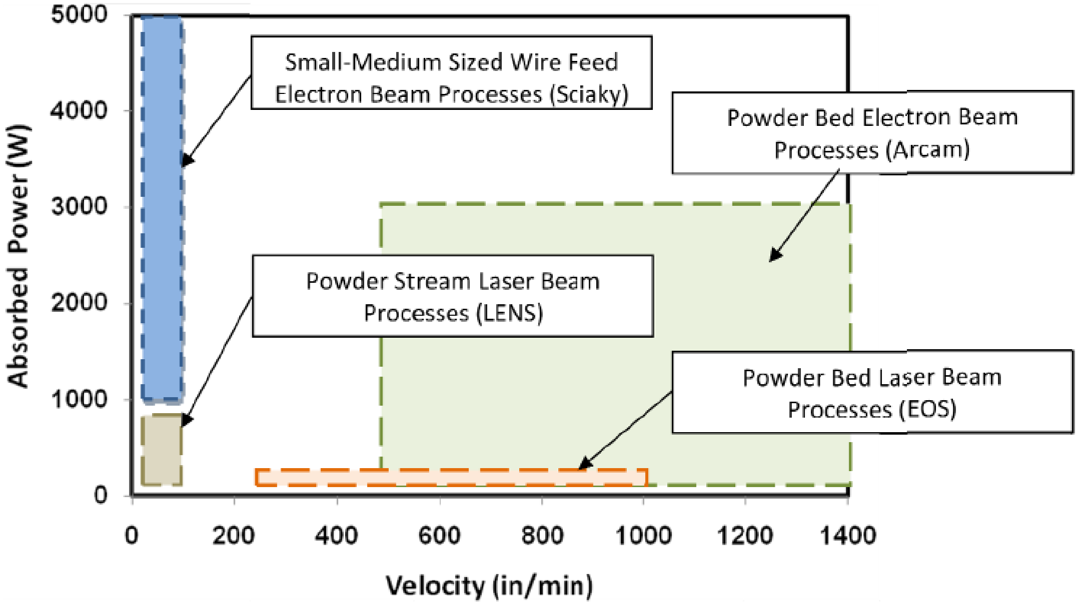

Fig.2-14 Comparison of the maximum absorbed power and scanning velocity parameter ranges used for object fabrication in four commercial additive manufacturing equipments for metals [3].

Table 2-1 Beam parameters for Rosenthal solution and thermophysical properties of Co–Cr–Mo alloy.

Beam power (W)	Absorption efficiency	Thermal conductivity (W/(m•K))	Density (g/cm^3)	Heat capacity (J/g•K)	Preheating temp. (K)	Melting temp. (K)
3500	0.9	29.1	8.42	0.655	1023	1670

References

[1] S. A. David and J. M. Vitek, “Correlation Between Solidification Parameters and Weld Microstructures,” *International Materials Reviews*, vol. 34, no. 1, pp. 213–245, Jan. 1989.

[2] W. Kurz and D. J. Fisher, *Fundamentals of solidification*, 4th ed. Hampshire, United Kingdom: Trans Tech Publications, 1998, pp. 65–89.

[3] J. Beuth, J. Fox, J. Gockel, C. Montgomery, R. Yang, H. Qiao, E. Soylemez, P. Reeseewatt, A. Anvari, S. Narra, and N. Klingbeil, “Process Mapping for Qualification Across Multiple Direct Metal Additive Manufacturing Processes,” *Solid Freeform Fabrication Symposium*, 2013, pp. 655–665.

[4] A. Vasinonta, J. L. Beuth, and M. L. Griffith, “Process Maps for Controlling Residual Stress and Melt Pool Size in Laser-Based SFF Processes,” *Solid Freeform Fabrication Proceedings*, 2000, pp. 200–208.

[5] A. Vasinonta, J. L. Beuth, and M. Griffith, “Process Maps for Predicting Residual Stress and Melt Pool Size in the Laser-Based Fabrication of Thin-Walled Structures,” *Journal of Manufacturing Science and Engineering*, vol. 129, no. 1, p. 101, Feb. 2007.

[6] J. Schwerdtfeger and C. Körner, “Selective Electron Beam Melting of Ti–48Al–2Nb–2Cr: Microstructure and Aluminium Loss,” *Intermetallics*, vol. 49, pp. 29–35, Jun. 2014.

[7] V. Juechter, T. Scharowsky, R. F. Singer, and C. Körner, “Processing Window and Evaporation Phenomena for Ti–6Al–4V Produced by Selective Electron Beam Melting,” *Acta Materialia*, vol. 76, pp. 252–258, Sep. 2014.

[8] J. Gockel and J. Beuth, “Understanding Ti–6Al–4V Microstructure Control in Additive Manufacturing via Process Maps,” *Solid Freeform Fabrication Proceedings,* 2013, pp. 666–674.

[9] S. Bontha, N. W. Klingbeil, P. A. Kobryn, and H. L. Fraser, “Effects of Process Variables and Size-Scale on Solidification Microstructure in Beam-Based Fabrication of Bulky 3D Structures,” *Materials Science and Engineering: A*, vol. 513–514, pp. 311–318, Jul. 2009.

[10] N. Christiansen, V. Davies, and K. Gjermundsen, “Distribution of Temperatures in Arc Welding,” *British Welding Journal*, vol. 12, pp. 54–75, 1965.

[11] A. Vasinonta, J. L. Beuth, and M. L. Griffith, “A Process Map for Consistent Build Conditions in the Solid Freeform Fabrication of Thin-Walled Structures,” *Journal of Manufacturing Science and Engineering*, vol. 123, no. 4, p. 615, Nov. 2001.

[12] N. Shen and K. Chou, “Thermal Modeling of Electron Beam Additive Manufacturing Process: Powder Sintering Effects,” *ASME 2012 International Manufacturing Science and Engineering*

Conference Collocated with the 40th North American Manufacturing Research Conference and in Participation with the International Conference on Tribology Materials and Processing., 2012, pp. 287–295.

[13] C. Körner, E. Attar, and P. Heinl, “Mesoscopic Simulation of Selective Beam Melting Processes,” *Journal of Materials Processing Technology*, vol. 211, no. 6, pp. 978–987, Jun. 2011.

[14] M. F. Zäh and S. Lutzmann, “Modelling and Simulation of Electron Beam Melting,” *Production Engineering*, vol. 4, no. 1, pp. 15–23, Dec. 2009.

[15] R. Rai, J. W. Elmer, T. a Palmer, and T. DebRoy, “Heat Transfer and Fluid Flow during Keyhole Mode Laser Welding of Tantalum, Ti–6Al–4V, 304L stainless steel and vanadium,” *Journal of Physics D: Applied Physics*, vol. 40, no. 18, pp. 5753–5766, Sep. 2007.

[16] M. Jamshidinia, F. Kong, and R. Kovacevic, “Numerical Modeling of Heat Distribution in the Electron Beam Melting V of Ti–6Al–4V,” vol. 135, no. December, pp. 1–14, 2013.

[17] J. R. Thompson, “Relating Microstructure to Process Variables in Beam-Based Additive Manufacturing of Inconel 718,” Wright State University, 2014.

Chapter 3

3. Microstructure of Inconel 718 with various build directions

3.1 Introduction

Inconel 718 is a kind of precipitate hardening nickel based superalloy, containing significant amounts of Fe, Cr and minor amounts of Nb, Mo Ti and Al, primarily strengthened by γ″ phase (Ni_3Nb, $D0_{22}$) and complementarily by γ′ phase (Ni_3(Al, Ti, Nb), $L1_2$) [1]. The volume fraction of γ″ and γ′ in the peak aged condition are about 15% and 4% [2], respectively. Inconel 718 combines good corrosion resistance and high temperature strength, as well as excellent weldability, therefore it is often used as turbine disk, compressor blade, airfoil, cryogenic storage tanks, pressure vessels and pipes [3-5]. The service temperature is usually below 650 ℃ at which yield strength reaches the maximum and decreases quickly with further increase of temperature because of the rapid coarsening, dissolution of γ″, and transformation to the stable δ phase (Ni_3Nb, $D0a$) [1,6,7].

The common precipitates in the γ-fcc matrix of Inconel 718 include γ′ phase [1,8-10], γ″ phase [1,8-10], δ phase[11-15], Laves phase ($(Ni,Cr,Fe)_2(Nb,Mo,Ti)$, $C14$) [4,16-19], and carbide ((Ni,Ti)C, $B1$) [6,16]. In addition, η phase (Ni_3Ti, $D0_{24}$) [20-22], σ phase (FeCr, $D8_b$) [6,20,21], and α-chromium ($A2$) may appear in the matrix depending on the stress and temperature condition. γ′ phase is spherical shape with the diameter about 15 nm [23] in the wrought material and is coherent with γ matrix as observed in many other nickel based superalloys [1,8]. γ″ phase is disk-like shape with the thickness about 5 nm and diameter about 15 nm [24] in the hot isostatic pressing (HIP) material, whose c axis is perpendicular to the disks. γ″ phase is also coherent with γ matrix, keeping the following orientation relationship with γ matrix [1,8]:

$< 100 >_{\gamma''} \| < 001 >_{\gamma}$; $\{001\}_{\gamma''} \parallel \{001\}_{\gamma}$.

In the $D0_{22}$ structure of γ'' phase, the Nb sublattice has body centered tetragonal structure, c axis of γ'' phase can be parallel to [100], [010], and [001] of γ matrix, forming three possible variants. These variants keeps the following orientation relationship with γ matrix [1]:

Variant 1, $[001]_{\gamma''} // [001]_{\gamma}$,

Variant 2, $[010]_{\gamma''} // [001]_{\gamma}$,

Variant 3, $[100]_{\gamma''} // [001]_{\gamma}$.

Furthermore, the correspondence of interplanar distance, can be written as follows,

$d(100)_{\gamma''} \simeq d(100)_{\gamma}$,

$d(010)_{\gamma''} \simeq d(010)_{\gamma}$,

$d(002)_{\gamma''} \simeq d(002)_{\gamma}$.

The solution temperatures of γ′ and γ″ are determined to be 948 ℃ and 950 ℃ by the calculation with Thermo-Calc software, respectively [25]. However, Strondl et al. [6] indicated that the solution temperatures of γ′ and γ″ are 920 ℃ and 900 ℃ by the differential thermal analysis (DTA) of as-EBM-built Inconel 718, respectively. δ phase has generally a plate-like shape keeping the following orientation relationship with the γ matrix [11]:

$(010)_{\delta} // \{111\}_{\gamma}$; $[100]_{\delta} // [1\bar{1}0]_{\gamma}$.

δ phase precipitates preferentially at grain and twin boundaries with the thin plates extending into the grains [11]. With increasing the aging temperature and prolonging the duration time, δ phase will precipitate in the interior of the grains [11], sometimes presents the granular shape [24]. Generally, δ phase is thought to transform from the metastable γ″ [1,9], however, Dehmas et al. [13] indicated that δ phase may grow directly from the supersaturated γ matrix. The maximum precipitation temperature is around 920 ℃ [9,18,26], and the solvus temperature is around 1025 ℃ [9,11,14,18,26]. δ phase can partly dissolve into matrix at the solution treatment of 980 ℃[14]. Laves phase ($(Ni,Cr,Fe)_2(Nb,Mo,Ti)$, *C*14) with the sheet shape is often found at the grain boundaries of the heat affected zone (HAZ) in the welding process [16,17,27,28]. It forms as a result of segregation of niobium [4], which depends strongly on the heat input and the cooling rate in the welding [17,29], laser engineered net shaping [4], and selective laser melting process [30]. In some references [17,19], it is said that Laves phase can be dissolved at a solution treatment over 1080 ℃. However, Strondl et al. [6] indicated that the solvus temperature of Laves phase is 1150 ℃ by the differential thermal analysis (DTA) of as-EBM-built Inconel 718. In some area with extensive Laves sheets, Laves phase can keep the following relationship with the γ matrix [8,16]:

$(0001)_{\mathrm{Laves}} \,//\, \{111\}_{\gamma}$; $(10\bar{1}0)_{\mathrm{Laves}} \,//\, \{110\}_{\gamma}$.

*M*C carbide (*M*=Ti,Nb) has spherical shape with size about 2 μm [6], which forms during the solidification. They are not easy to be solved into the matrix by heating unless the solution heat treatment is raised above 1250 ℃ [6,18,25]. α-chromium forms as globular particles at grain boundaries when nickel is depleted to form the intermetallic phases, such as γ' , γ'', δ and Laves phase, extensively [9].

Owing to macro-segregation, formation of freckles, laves phase and white spots in cast Inconel 718 alloy [24], which cannot be completely solved by the subsequent wrought process, powder metallurgy (PM) method is usually used to fabricate Inconel 718 product. As a kind of PM technology, HIP can fabricate intricate shaped component with near theoretical density and isotropic properties directly, saving the cost in machining and forging process [24]. However, HIP lacks the design flexibility and still needs the molds, which limits its application. The recently emerging 3D printing technology, additive manufacturing [31,32] can make up these shortcomings. It can fabricate the unusual and complex metal and alloy product by using laser or electron beam to selectively melt the precursor powder layer by layer along a series of two-dimensional (2D) slices of a 3D object repeatedly, under the direct of the computer aided design data.

Currently, major AM processes used to produce Inconel 718 are selective laser melting (SLM) [5], and electron beam melting (EBM) [6]. The primary strengthening phase γ'' could be observed in both of two processes. Because of directional solidification for the melt pool, there were <001> texture in the build direction in both the EBM-built [6,7] and laser-built [5,33] Inconel 718 samples. However, EBM-built sample exhibited cube texture with the grains oriented to <001> in the build direction [6], while laser-built [5] sample exhibited another orientation such as <111> and <311>, and the width of the columnar grains was only around 0.8 μm. The melt pool appearance and deposit layer can be observed in optical microstructure of vertical cross section of laser-built sample [5], while they were not observed in the EBM-built sample [6]. Moreover, extensive dendritic grains across a number of deposit layers can be observed occasionally in laser-built sample. The microstructure morphology difference in EBM and SLM process may be caused by the melt pool geometry difference. Deeper melt pool can be formed in EBM process because of strong penetration ability of electron beam, which is conductive to the formation of unidirectional temperature field.

Because <001> texture can form in the build direction of EBM-built Inconel 718 owing to the directional solidification, the crystal orientation within build parts is anticipated to depend on the orientation of the build part with reference to the build direction. The purpose in this chapter is to investigate the effect of the build direction on the microstructure of Inconel 718 fabricated EBM.

3.2 Experimental

Inconel 718 rods were fabricated on an Arcam A2 EBM system (Arcam AB, Mölndal, Sweden) with gas atomized powder. Fig.3-1 shows powder morphology in different magnification. The powders were spherical or irregular in shape with attached small particles, ranged from 45-150 μm with an average value of 74 μm. The surface of some larger powders were rough, and were attached with numerous small particles (Fig.3-1(c)), while the surface of some larger powder were smooth, attaching with a few small particles. The chemical composition of Inconel 718 alloy powder is shown in Table 3-1. Fig.3-2 shows the schematic of rod cylindrical orientations relative to the electron-scanning direction and the stacking direction (i.e. build direction) during the EBM process. The cylindrical axes of the rods were oriented to stacking direction (i.e. build direction, designated as *z* axis), face diagonal and space diagonal of the coordinate system consisting of stacking direction and two perpendicular scanning directions (designated as *x* and *y* axis, respectively), as well as the scanning direction, respectively, forming 0°, 45°, 55°, and 90° with the build direction (*z* axis). Hereafter, the Inconel 718 rods fabricated in the directions of 0°, 45°, 55°, and 90° from the *z* axis are designated as the 0°-sample, 45°-sample, and so on. The rods were 15 mm in the diameter, and 85 mm in the height. The rods for each orientation are fabricated separately, and the primary parameters to build each orientation rods during the EBM process were listed in Table 3-2. The scanning direction of the electron beam will rotated by 90° on each neighboring layer to homogenize the temperature in the build region, as shown Fig.1-10(b).

Fig.3-3 shows the schematic showing the way of cutting the rod into samples for microstructure observation. First, one of the as-EBM-built rods for each orientation was cut into two halves along the plane consisting of the cylindrical axis and *z* axes. In the case of 0°-sample, the cutting plane was set to consist of the cylindrical axis and *x* axes since the cylindrical axis was parallel to the *z* axes. This way of cutting allowed us to examine the crystal orientation relative to the build direction and beam-scanning direction. One half of the rod was then cut into13 blocks perpendicular to the cylindrical axis of the rod with a constant thickness of 6.6 mm. And the blocks cut from the portion at the height of 13 mm, 40 mm, and 67 mm from the bottom were selected for microstructure observation, and will be called “bottom part”, “center part” and “top part”, respectively. The longitudinal cross-section microstructures of the specimens were investigated by electron backscatter diffraction (EBSD), scanning electron microscopy (SEM), and electron probe microanalyzer (EPMA).

3.3 Results

3.3.1 Microstructures in different build direction samples

Fig. 3-4 shows SEM microstructures on the longitudinal cross-section of the top parts of the as-EBM-built samples. The morphologies of the precipitates were similar in all the samples, which suggest that precipitate type is the same in the different build direction samples. The precipitates were found to be aligned along the *z* axis in all the samples, which is thought to be caused by the element segregation due to the directional solidification. Some long pits indicated by the white arrows, can be observed to be parallel to the *z* axis in all the samples, which may be caused by the deciduous precipitates during the etching process.

Fig. 3-5 shows EBSD-inverse pole figure (IPF) maps on longitudinal cross-section of as-EBM-built samples. Low angle boundaries (LAB) ($2° \leq \theta < 15°$) and high angle boundaries (HAB) ($15° \leq \theta$), represented by black and light blue lines, respectively, were shown on the IPF maps. The orientations shown in the IPF maps were in the cylindrical axis, which indicate that the cylindrical axial directions were near [001], [110], [111], and [100] in the 0°-, 45°-, 55°-, and 90°-samples, respectively. Some regions consisting of fine grains with random crystal orientations were in the columnar grain matrix, which are thought to be caused by the unmelt particles. The grain size was measured by the interception method, and the ones perpendicular to the *z* axis were 21 μm, 27 μm, 50 μm, and 84 μm, in the 0°-, 45°-, 55°-, and 90°-samples, respectively, and the ones parallel to the *z* axis were 41 μm, 244 μm, 822 μm, and 106 μm, in the 0°-, 45°-, 55°-, and 90°-samples, respectively.

The fine grain regions in 0°-sample were considered to consist of unmelt particles caused by the inappropriate condition of the EBM process. Therefore, 0°-sample were rebuilt by increasing the preheating temperature and beam current, and decreasing the layer thickness, focus offset and line offset, as shown in Table 3-2, in order to ensure the full melt of the powders. Fig. 3-6 shows SEM microstructure on the longitudinal cross-section of the top part of 0˚-sample fabricated by the modified condition. Fig. 3-6(a) shows that larger plate-like precipitates were formed after modifying the build condition, and that the precipitates were still aligned along the build direction. Fig. 3-6(b) shows the single crystal-like microstructure with the <001> orienting to the build direction can be formed in the EBM process, which agrees with the result of Strondl et al. [6].

Fig. 3-7 shows EPMA element maps on the longitudinal cross-section of the top part of as-EBM-built 0˚-sample. The spherical precipitate indicated by the red arrow consisted of Nb,Ti, C, and B, which suggests that the precipitate is (Nb, Ti)(C,B). The plate-like precipitate indicated by the black arrow consisted of Ni, Nb and Ti, which suggests that the precipitate is δ-Ni_3(Nb, Ti). These are supported by the results of Strondl et al. [6,7].

Fig. 3-8 shows EPMA element maps on the longitudinal cross-section of the top part of as-EBM-built 0˚-sample fabricated by the modified condition. The precipitate indicated by arrow “a” is rich in the elements of Nb, Ti, Mo, C and B, which suggests the precipitate is $(Nb,Ti,Mo)_3(C,B)_2$ [16]. The precipitate indicated by arrow “b” is rich in the elements of Nb, Ti, C and B, which suggests the precipitate is (Nb,Ti)(C,B) [6]. The precipitate indicated by arrow “c” is rich in the elements of Ni, Nb and Ti, which suggests the precipitate is δ-Ni_3(Nb, Ti) [6,7]. The precipitate indicated by arrow “d” is rich in the elements of Ni, Fe, Cr, Mo and Ti, which suggested suggests the precipitate is Laves phase, $(Ni,Fe,Cr)_2(Mo,Ti)$ [16,17,27,28].

3.3.2 Microstructure variation along the build height

Fig. 3-9 shows microstructure on the longitudinal cross-section observed at different heights of 0 ˚-sample fabricated under the modified condition. The types of precipitates indicated on the images were estimated by comparing their morphology with that of precipitate whose compositions were analyzed by EPMA. The amounts of precipitates on the bottom were larger than that on the center and bottom, which suggests that the precipitate amount deceases with increasing the distance from the bottom of the EBM-built rod. Fig. 3-9(d,e) shows that numerous small plate-like and spherical-like precipitates were aligned along grain boundaries, which were different from that on the top part (last-built part). To confirm the type of precipitates, EPMA was carried out on the bottom part.

Fig. 3-10 shows EPMA element maps on the longitudinal cross-section of the bottom part of as-EBM-built 0°-sample fabricated under the modified condition. The plate-like precipitate indicated by arrow “a” are rich in concentration of Ni, Nb, and Ti, and suggested to be γ''-$Ni_3(Nb,Ti)$ [1,6,8] or δ-$Ni_3(Nb,Ti)$ [11-15], because they have the similar plate-like morphology (though δ-$Ni_3(Nb,Ti)$ is usually much larger than γ''-$Ni_3(Nb,Ti)$) and the same chemical composition. Because δ-$Ni_3(Nb,Ti)$ keeps the following orientation relationship with the γ matrix [11]:

$$(010)_{\delta} // \{111\}_{\gamma} \;;\; [100]_{\delta} // [1\bar{1}0]_{\gamma}$$

the elongated direction of the δ phase is usually parallel to the {111} plane of γ matrix. If the precipitate indicated by arrow “a” were δ-$Ni_3(Nb,Ti)$, the elongated direction of the precipitate would have an angle of 45 ° with the build direction on this observation plane, because the build direction and observation plane are near <001> direction and {001} plane according to the result of EBSD analysis (Fig.3-6). However, for the precipitate indicated by arrow “a”, the elongated direction is parallel to the build direction (*z* axis), which suggests the precipitate is not δ-$Ni_3(Nb,Ti)$. Because γ'' phase keeps the following orientation relationship with γ matrix [1,8]:

$$(001)_{\gamma''} // \{001\}_{\gamma} \;;\; [100]_{\gamma''} // [100]_{\gamma}$$

the elongated direction of the γ'' phase is parallel to the {001} plane of γ matrix. This just accords with result in Fig. 3-10. Therefore, the precipitate indicated by arrow “a” is identified to be γ'' - $Ni_3(Nb,Ti)$. The spherical precipitate indicated by arrow “b” also consisted of Ni, Nb, and Ti, which suggests that the precipitate is γ'-$Ni_3(Nb,Ti)$ [1,6,8].

Fig. 3-11 shows TEM dark field images (DFI) and corresponding selective area diffraction (SAD) patterns on the top and bottom of parts of as-EBM-built 0°-sample.

The diffraction spots selected to take the DFIs were designated with the green dashed circles. In the [001] incident direction of γ matrix, the diffraction patterns from the γ′ and γ″ could be observed on both the top and bottom parts (Fig. 3-11(b,d)), which suggests that γ′ and γ″ can exist throughout the build height during the EBM process. Fig. 3-11(a) shows that γ′ was about 12 nm in the diameter, and γ″ was 4 nm in the thickness and 16 nm in the length on the top part of the rod. Fig. 3-11(b) shows that γ′ was about 11 nm and γ″ was 7 nm in the thickness and 16 nm in the length on the bottom part of the rod. These results suggest that the sizes of γ′ and γ″ in the early-built part are similar to those in the latter-built part, do not grow significantly during the EBM process.

3.4 Discussion

3.4.1 Effect of unmelt powder on the crystal growth

The fine grain regions can be formed by solidification of the melt pool at low temperature gradient and high solidification rate [34], or by aggregation of the incompletely melt powders. In order to clarify the formation mechanism of the fine grain regions with random crystal orientations, the powder microstructure and fine grain region microstructure were compared by EBSD, as shown in Fig. 3-12. Fig. 3-12(a) shows that the powder consisted of the equiaxed grains with the average grain size of 4.9 ± 1.3 μm. On the horizontal cross-section of the as-EBM-built 0˚-sample (Fig. 3-12(b)), average grain size of the fine grain region (indicated by the dash circles) was determined to be 19.5 ± 7.0 μm. The fine grain region was observed to be about 500 μm in the horizontal direction, and about 100 μm in the build direction on the vertical cross-section (Fig. 3-12(c)), while the powder diameter was in the range of 45-150 μm. Based on the similarity of the grain size and geometry sizes between the powders and the fine grain region, the fine grain regions with random crystal orientations are thought to be formed by the aggregation of the incompletely melt powders. If the fine grain regions were formed by solidification of the melt pool under condition of the equiaxed grain formation in the solidification map (i.e. temperature gradient (G) - growth rate (R) space), the fine grain regions would not be localized to limited regions, and would be formed more uniformly.

Though the unmelt powder are often considered to be caused by the low energy density [35-37] and beam interruption during final melt scanning [38], the detail formation process have never been indicated. The low energy density will cause the uneven melt pool surface [36], which may be a possible reason for the formation of fine grain regions because of the layer by layer fabrication process of EBM. Fig. 3-13 shows the schematic of the effect of previous build layer surface morphology on the crystal growth. When the previous build layer surface is uneven, more powders will be filled into the hollow place during the powder raking process. In the subsequent melting process, the lower part of the powders in the hollow place will not be sufficiently heated by the electron beam because of the deviation from the focus point. Then the incompletely melt powders forms, and they will be embedded in the solidified microstructure. As a result, the single crystal growth will be break down because of the heterogeneous nucleation on the incompletely melt powders. If the previously build layer surface is flat, the powders can be fully melted by the electron beam in the next build layer, and the grains with crystal orientation near to <001> will grow faster because of directional solidification, forming the single crystal-like microstructure above the fine grain region.

3.4.2 Effect of build direction on crystal orientation

Fig. 3-14 shows EBSD-IPF map of top part (last built part) of 0°-sample fabricated under the modified condition. The observation plane was on the longitudinal cross-section. Low angle boundary (LAB) (2°≤θ<15°) and high angle boundary (HAB) (15°≤θ) were shown on the IPF maps. Figs. 3-14(a), (c), (e) are the IPF maps showing the crystal orientations in the directions parallel to z axis (cylinder axis), y axis, and x axis, respectively. Figs. 3-14(b), (d), and (f) are corresponding

IPFs for z axis, y axis and x axis, respectively. Figs. 3-14(a) and (b) revealed that there was strong <001> texture in the build direction. Figs. 3-14(c), (d), (e), and (f) revealed that although there were some crystal orientations deviating from <001> orientation in the two perpendicular scanning directions (i.e. *x*- and *y*-axis directions), there were still strong <001> texture. These results suggest that cube texture with <001> oriented to build direction, and two perpendicular scanning directions, respectively, could form in the EBM-built fcc based alloy. Therefore, the crystal orientation can be controlled by selecting the oriented direction relative to coordinate system consisting of the build direction (*z*-axis) and two perpendicular scanning directions (i.e. *x*-axis, *y*-axis directions), thus the mechanical properties can be controlled as a result.

The <001> texture in the build direction is formed because of the preferential crystal growth of fcc-based alloy in the directional solidification process [39]. The <001> textures in the two perpendicular scanning directions are related to the tear drop melt pool shape. The simulation results shows that the melt shape during the EBM could be tear drop shape with the elongation direction oriented to the scanning direction [40,41], which will result in the <001> crystal growth perpendicular to the scanning direction [42]. Therefore, <001> texture could also form in the two perpendicular scanning directions. The longer and narrower the melt pool is, the stronger the <001> texture intensities are in the two perpendicular scanning directions.

Fig. 3-15 shows the schematic of formation process of the single crystal-like microstructure from the consecutive solidified bead in the EBM process. The melt pool is supposed to be narrow and deep on the plane perpendicular to the scanning direction because of the deep penetration depth of electron beam. As a result, the isothermal line exhibits a concave shape. During the solidification of the melt pool, the grains will nucleate on the powder near the melt pool at first, and then grows along the maximum temperature gradient direction on the solid-liquid interface. The curved-columnar grains will form on the side of the melt pool, and straight columnar grains will form in the center of the melt pool. The crystal orientation of the straight columnar grain is near <001>, because <001> is known to be the preferential growth direction for fcc based alloy [39]. Because the electron beam travels with a zigzag shape, the melt pools on the neighboring scanning routes will overlap with each other. Then the grains in the overlap part (primarily being the curved-columnar grains) will be remelted. For the melt pool near the columnar grains, the grain will grows on the previous columnar grain, increasing the columnar grain size, especial for the <001> oriented grains. For the melt pool near the powders, the curved-columnar grains will form again. But this part will be remelted again in the next scanning route. Then, the melt pool near the columnar grains will also be preferred for the columnar grain formation. As a result, the single crystal-like microstructure can be formed in the center part of the build object fabricated by EBM.

3.4.3 Effect of build height on precipitates

In the EBM process, the early-built part will be heated repeatedly when a new layer is preheated and melted by the electron beam, therefore its temperature will be kept at the temperature near the preheating temperature until the completion of the building process. As a result, post-built heating process, which is similar to an aging process, will change the microstructure in the early-built part if the post-built time is long enough. Fig. 3-16 shows the comparison between cooling curves of 0˚-sample fabricated by the modified condition and TTT curves of the precipitates in Inconel 718 alloy. The cooling curve corresponds to the temperature variation from the initiation of the building to the end beneath the stainless substrate during the EBM process, which is measured by the thermocouple. Because of the high thermal conductivity of the metals, the temperature in the bottom of the build part will be similar to that beneath the stainless substrate. Therefore, the cool curve can be used to evaluate the temperature variation in the build part. The TTT curves of Inconel 718 alloy is from the research of Brooks et al. [9]. Fig. 3-16 shows the cooling curve went through the γ', γ'', and δ region, which can explain the existence of γ', γ'', and δ in the γ matrix of bottom part. If it is assumed that each position of the built rod goes through the similar thermal history, γ', γ'', and δ will exist throughout the build height. This assumption is proved by the actual experimental result. The post-built time decreases with increasing the height from the bottom, therefore the amount of precipitate, decreases with increasing the build height.

3.4.4 Effect of energy density on Laves phase

The formation of laves phase depends on segregation of niobium and molybdenum [4], which are related to the heat input and the cooling of the melt pool, as well as the post-built process. Because Laves phase only appears in the modified 0°-sample, although the post-built temperature is less than 1000 ℃ in both modified and unmodified 0°-sample, this suggests that the formation of Laves phase is related to the solidification of the melt pool, rather than the post-built heat process. Table 3-3 shows the line energy and energy density of 0°-sample with and without the modified condition. The higher energy density usually generates higher temperature of the melt pool, therefore, higher temperature gradient will form at solid/liquid interface of the liquid part. When the solidification rate is assumed to be proportional to the scanning rate (the scanning rate is usually much larger than solidification rate when forming tear drop shape melt pool [41]), the modified 0°-sample will exhibit smaller solidification rate because of its higher energy density and smaller scanning speed. Therefore, strong segregation of Nb and Mo will occur at the solid/liquid interface of the melt pool in the modified 0°-sample. On the other hand, because segregated Nb and Mo elements from the melt pool exist on the boundary of the dendritic or cellular grains, modified 0°-sample with single crystal-like microstructure will contain higher amount of Nb and Mo elements on the grain boundary than unmodified 0°-sample with cellular columnar grains. Laves phase ($(Ni,Fe,Cr)_2(Nb,Mo,Ti)$) contains much higher Nb and Mo than δ phase ($Ni_3(Nb,Ti)$), therefore, high amount of Nb and Mo elements contributes to the formation of Laves. As a result, long chain of Laves phase forms in modified 0 °-sample, which agrees with the simulation and experiment results reported by Nie et al. [30]. Laves phase is detrimental to the mechanical property because it consumes niobium, and decrease the amount of primary strengthening phase γ''. Therefore, it is expected that further strengthening is possible by further optimizing the build condition for 0 °-sample .

3.5 Conclusions

The effects of the build direction on the microstructure of Inconel 718 fabricated EBM have been investigated and the following conclusions have been obtained.

(1) Single crystal-like microstructure can be obtained by increasing energy density (via by increasing the beam current and/or by decreasing the line offset) and decreasing the scanning speed to ensure the completely melt of the powders.

(2) The remelt of curved-columnar grains in the overlap part of the melt pools in the two neighboring scanning route may be favorable for the formation of the single crystal-like microstructure.

(3) <001> texture was formed in the build direction and two perpendicular scanning directions. As a result, crystal orientation in EBM-built parts can be controlled by choosing an appropriate orientation relative to the build direction.

(4) The cylindrical axes were oriented near <100>, <110>, <111> and <100> directions in samples whose cylindrical axes were parallel to the build direction, the diagonal direction of x-z (or y-z) plane, space-diagonal of x-y-z space, and x-or y- scanning direction, which were deviated from z axis by 0 °, 45 °, 55 °, and 90 °, respectively.

(5) Precipitate amount was dependent on the build height because the early-built part was kept at high temperature for longer time when waiting for the fabrication of the latter-built part.

(6) Beside (Nb,Ti)(C,B) particle, δ-Ni_3(Nb, Ti) phase and/or Laves phase were

aligned along the build direction based on the build condition.

(7) γ'- and γ''-phases were formed in the as-EBM-built sample, and did not grow significantly with increasing the post-built time. On the top of the build rod, γ'-phase was about 12 nm in size, and γ'' was 4 nm in the thickness and 16 nm in the length.

(8) The formation of single crystal-like microstructure accompanied with appearance of Laves phase, which was related to the strong segregation of Nb and Mo at grain boundary in high energy density and lower scanning speed.

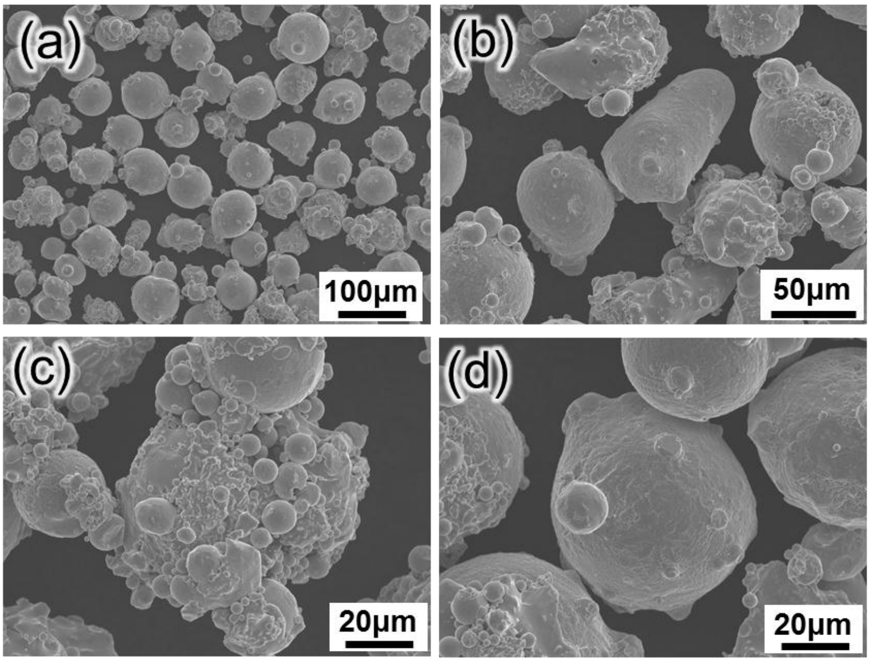

Fig.3-1. Powder morphology of Inconel 718 for electron beam melting in different magnifications. (a) 200 times, showing the spherical or irregular powders with attached small particle, (b) 500 times, hollow powder was not observed, (c) 1000 times, larger powder with rough surface attached with numerous small particles, and (d) larger powder with slippy surface attached with a few small particles.

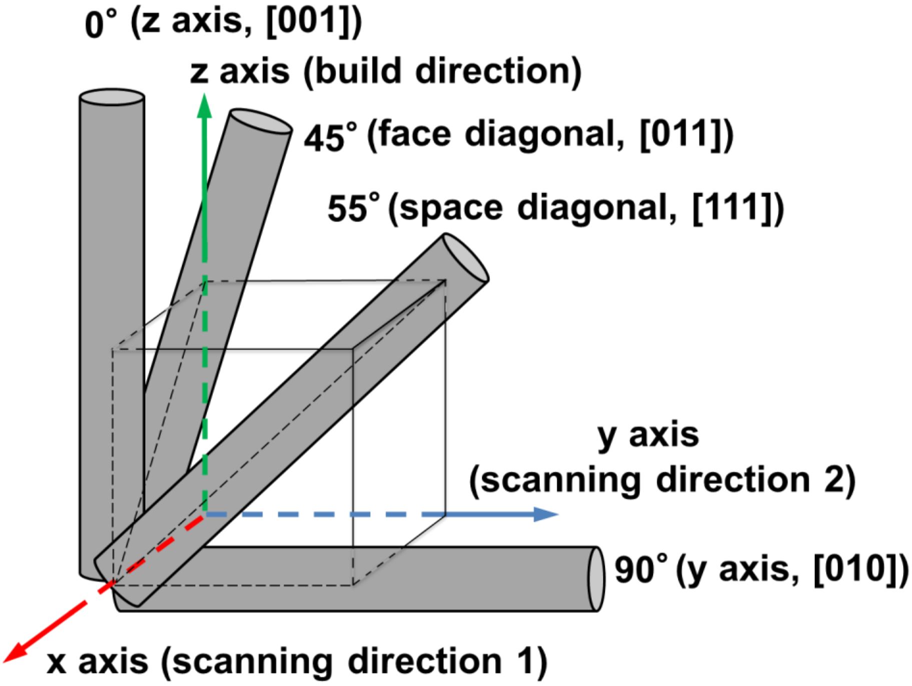

Fig. 3-2. Schematic of rod cylindrical orientations relative to the electron-scanning direction and the stacking direction (i.e. build direction) for Inconel 718 fabricated by electron-beam melting.

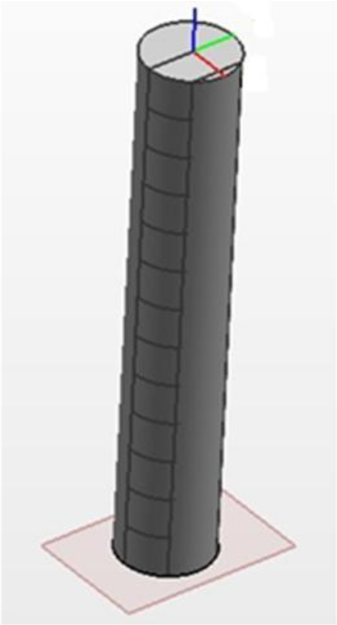

Fig. 3-3. Schematic of the rod cutting way for microstructure observation.

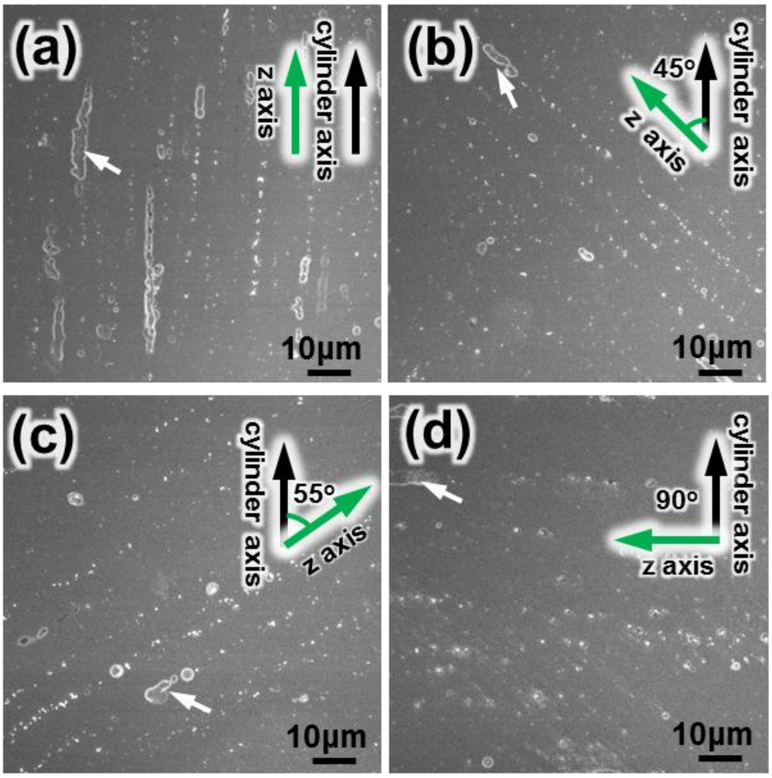

Fig. 3-4. SEM microstructures on the longitudinal cross-section of as-EBM-built samples (top part, about 75 mm from the bottom of the rods). (a) 0˚-sample, (b) 45˚-sample, (c) 55˚-sample, and (d) 90˚-sample.

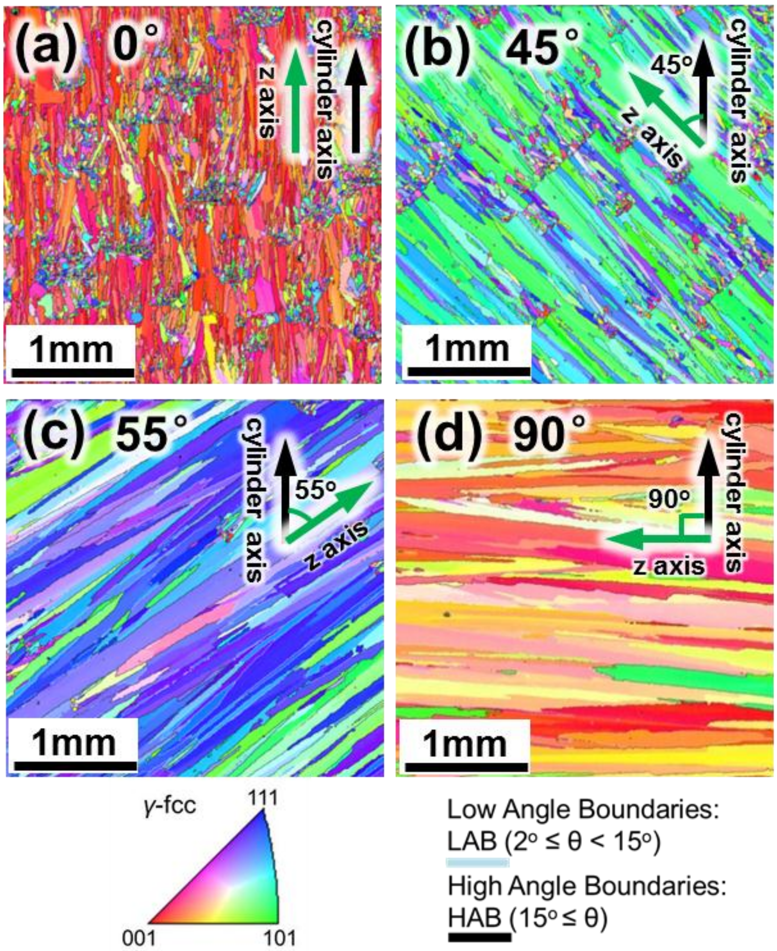

Fig. 3-5. EBSD-IPF maps on the longitudinal cross-section of the top part of as-EBM-built samples. The cylinder axes were near <100>, <110>, <111>, and <100>, respectively in (a) 0 °-, (b) 45 °-, (c) 55 °-, and (d) 90 °-sample.

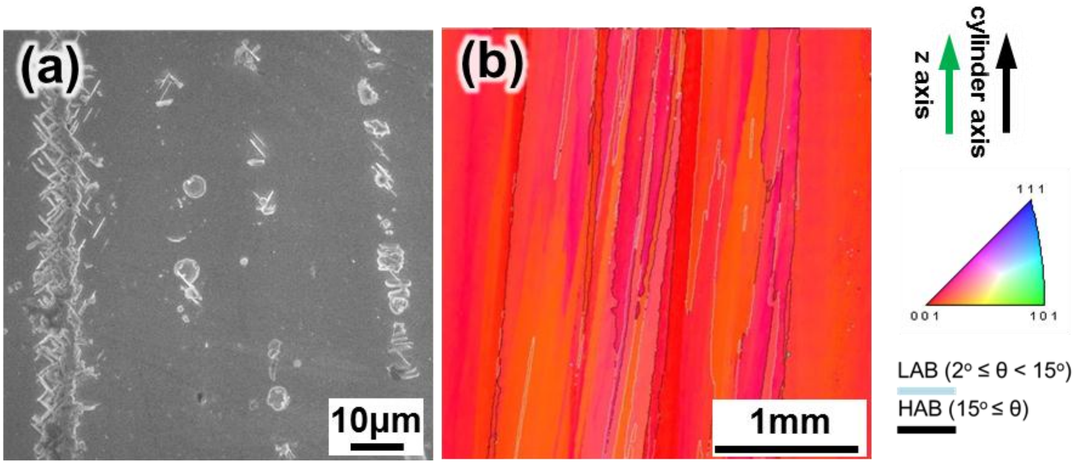

Fig. 3-6. Microstructure on the longitudinal cross-section of the top part of 0 °-sample fabricated by the modified condition. (a) SEM figure, showing the precipitate arrangement along the build direction, (b) EBSD-IPF map, showing the single crystal-like microstructure with the <001> orienting to the build direction.

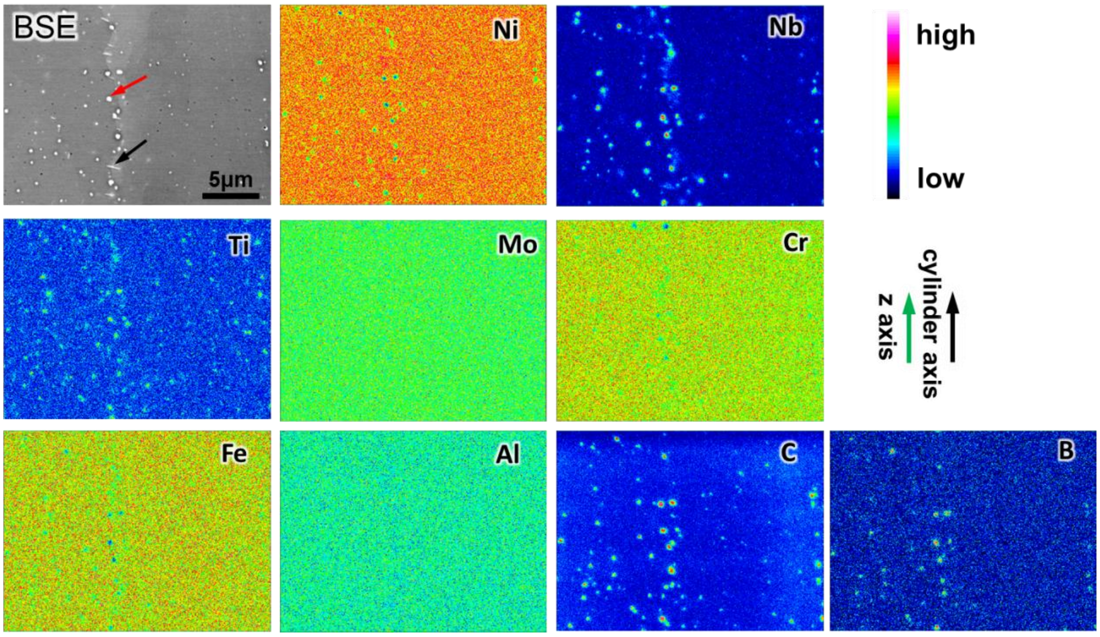

Fig. 3-7. EPMA element maps on the longitudinal cross-section of the top part of as-EBM-built 0˚-sample.

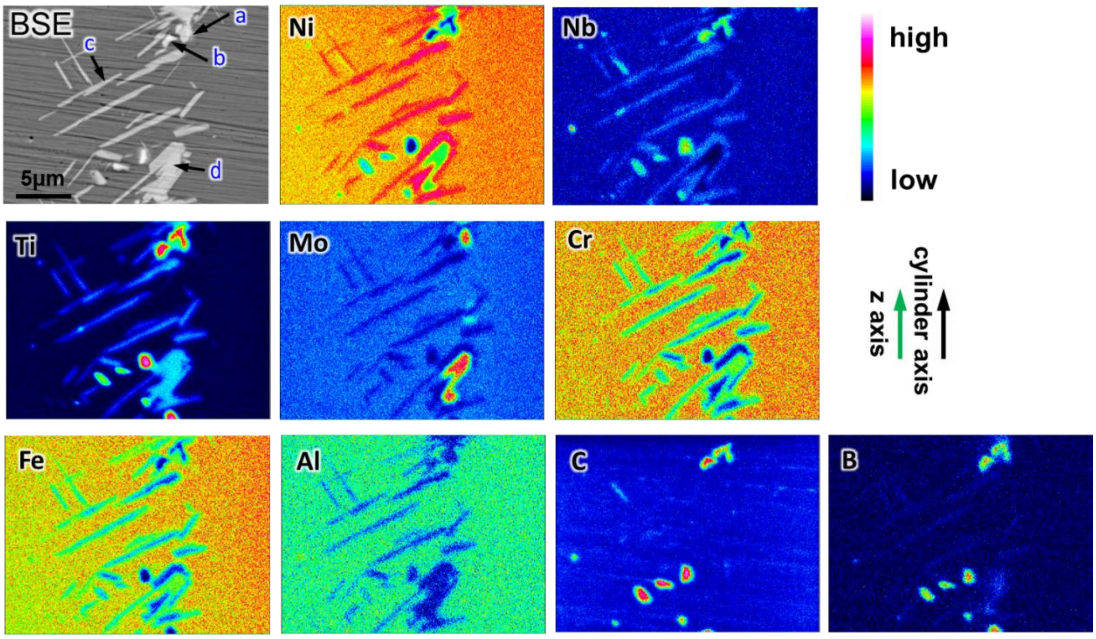

Fig. 3-8. EPMA element maps on the longitudinal cross-section of the top part of as-EBM-built 0˚-sample fabricated under the modified condition.

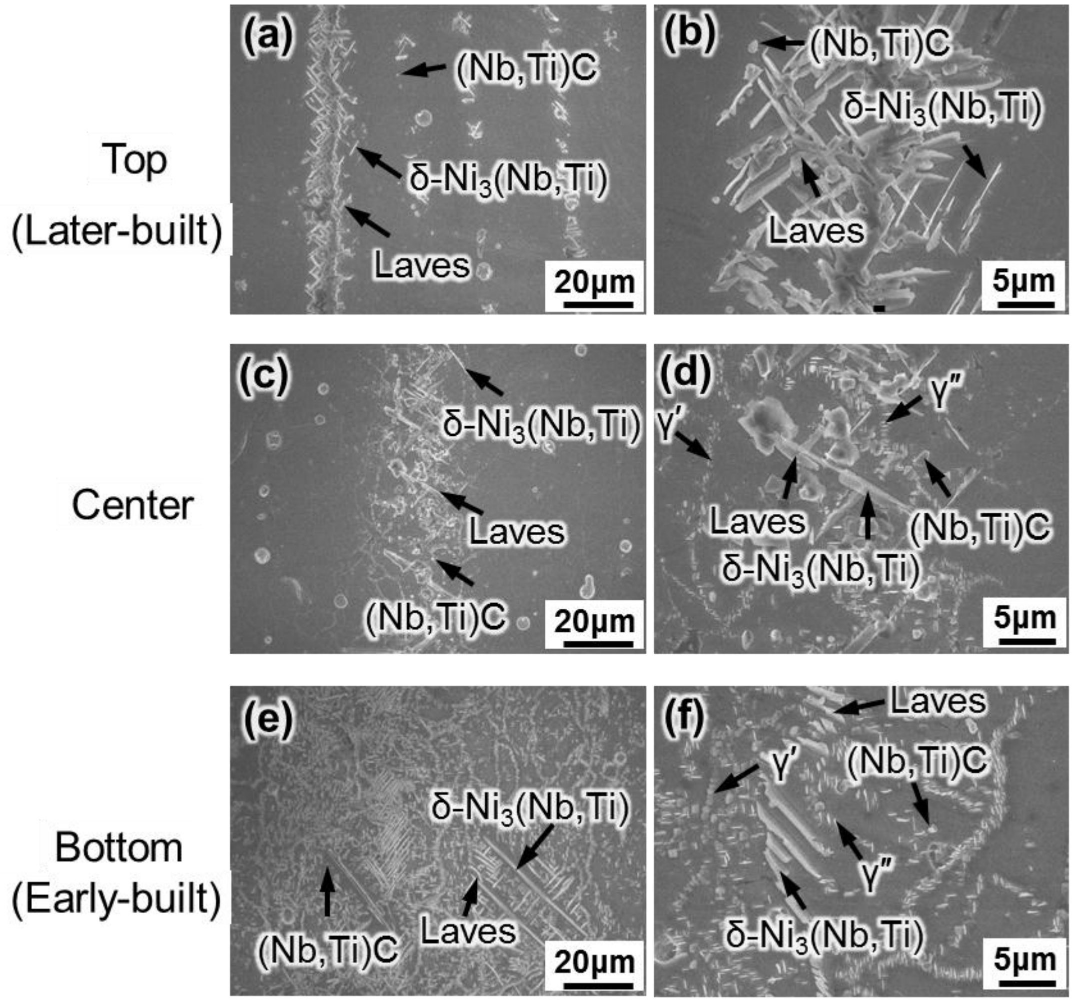

Fig. 3-9. SEM microstructure on the longitudinal cross-section of different height of 0°-sample fabricated under the modified condition. (a,b) Top part, (c,d) center part, and (e,f) bottom part.

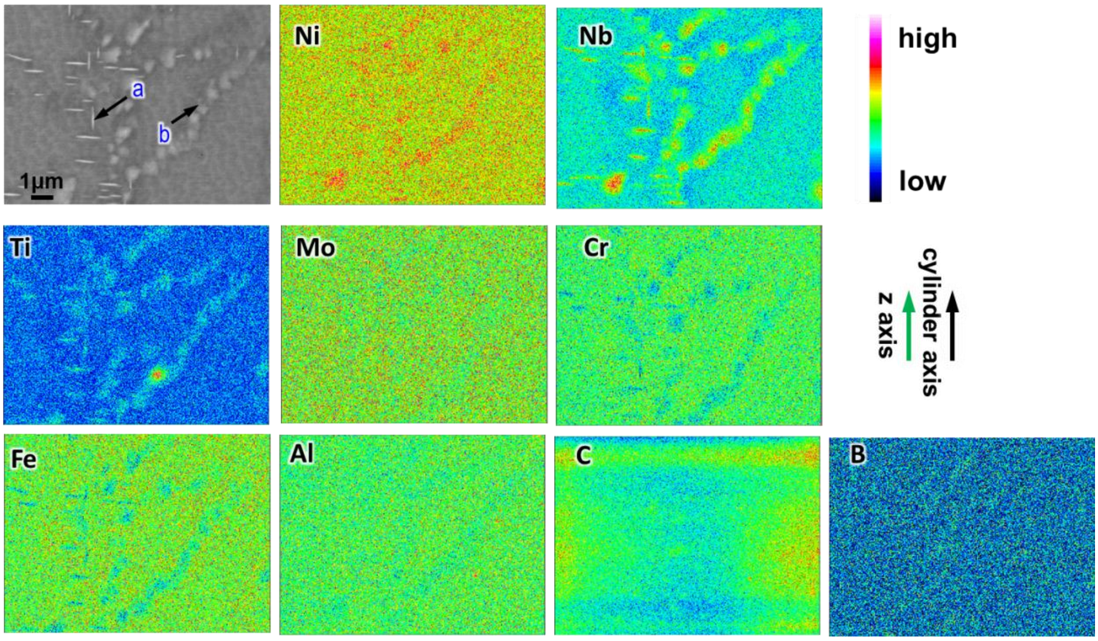

Fig. 3-10. EPMA element maps on the longitudinal cross-section of the bottom part of as-EBM-built 0˚-sample fabricated by the modified condition.

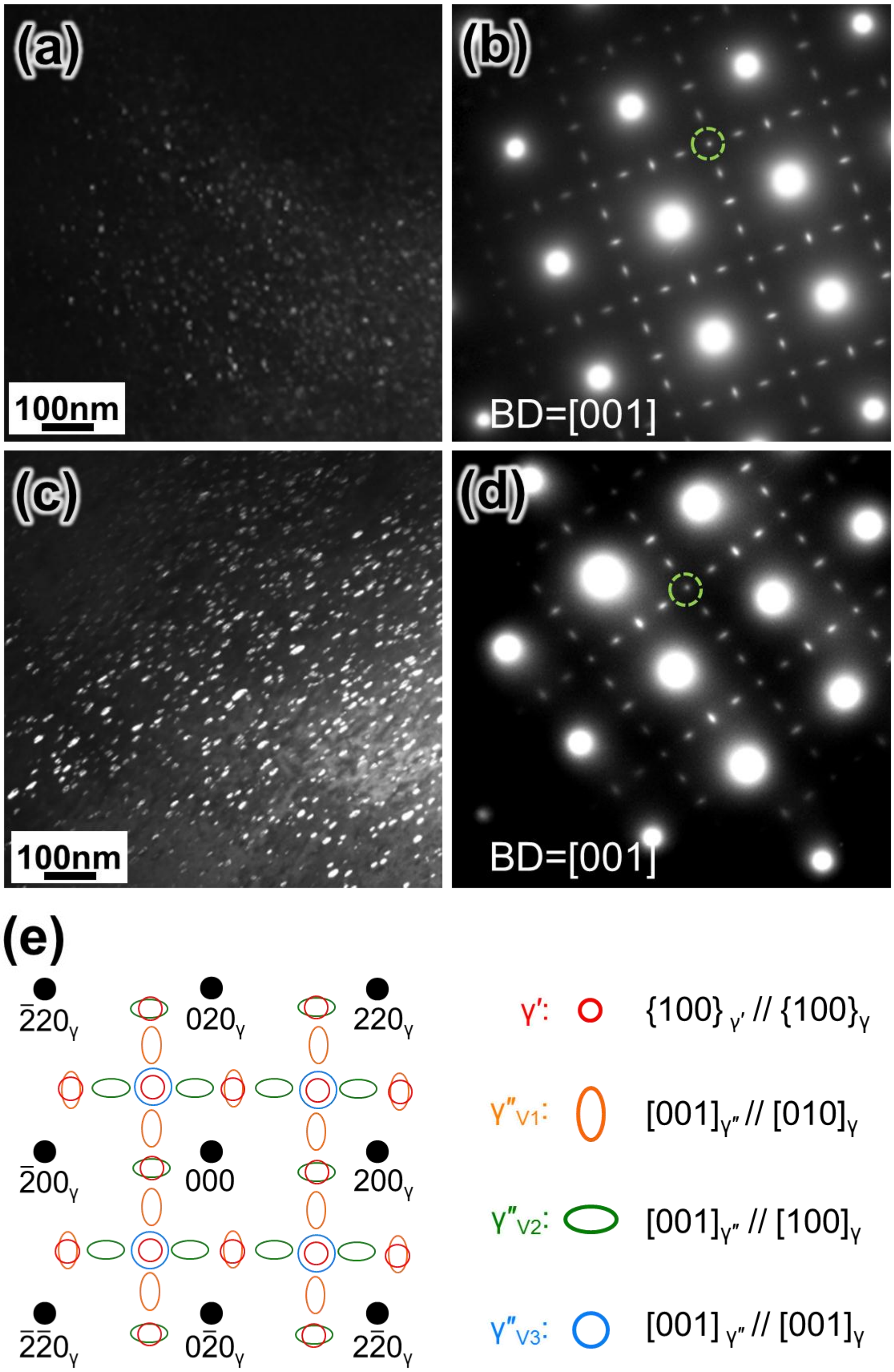

Fig. 3-11. TEM dark field images (DFI) and corresponding selective area diffraction (SAD) patterns on the top and bottom of parts of as-EBM-built 0˚-sample. (a) DFI on the top part, (b) corresponding SAD pattern for image (a), (c) DFI on the bottom part, (d) corresponding SAD pattern for image (c), and (e) key to the SAD patterns in (b) and d.

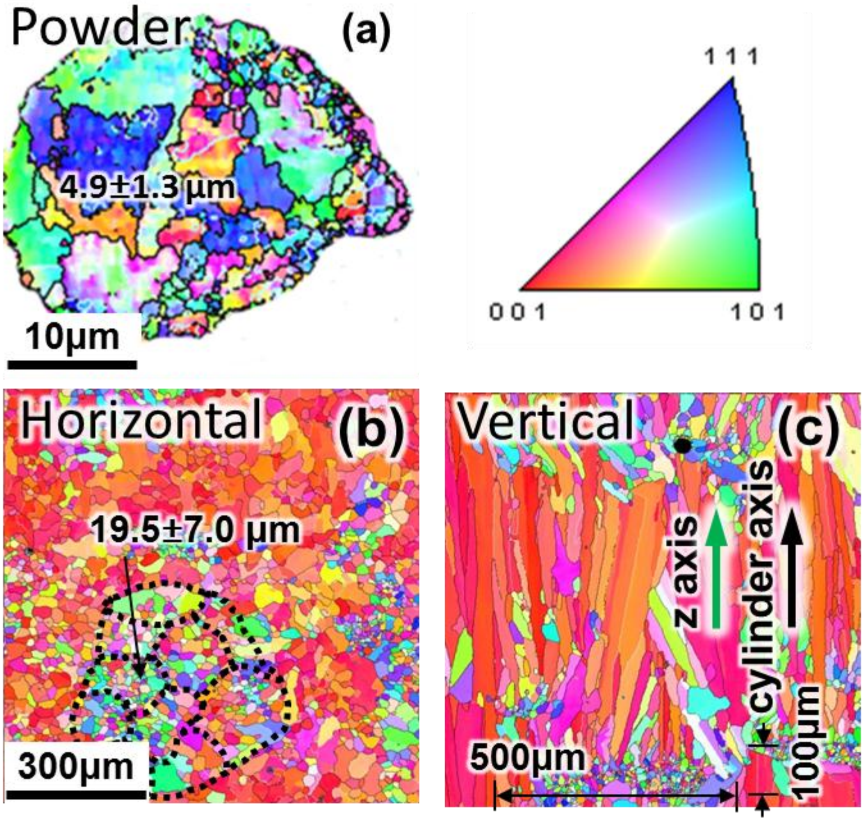

Fig. 3-12. EBSD-IPF maps of Inconel 718 powder and the build part of as-EBM-built 0˚-sample. (a) Powder, (b) horizontal cross-section of the build part, and (c) vertical cross-section of the build part.

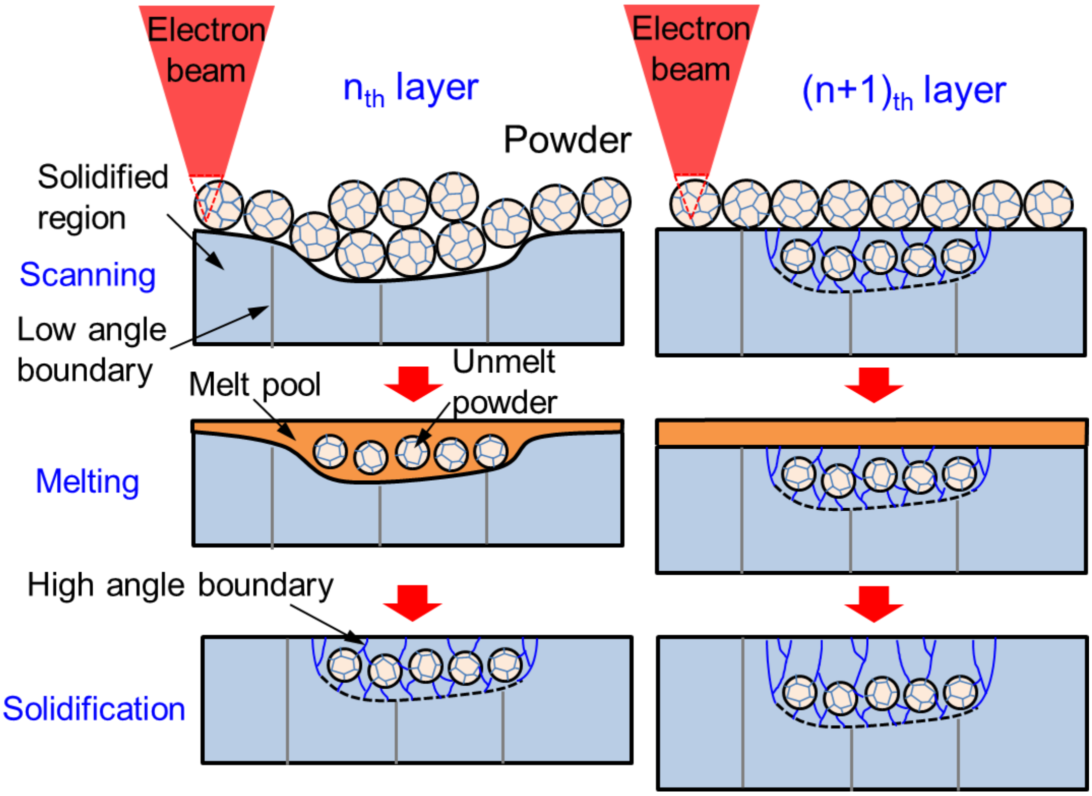

Fig. 3-13. Schematic of effect of previous build layer surface morphology on the crystal growth.

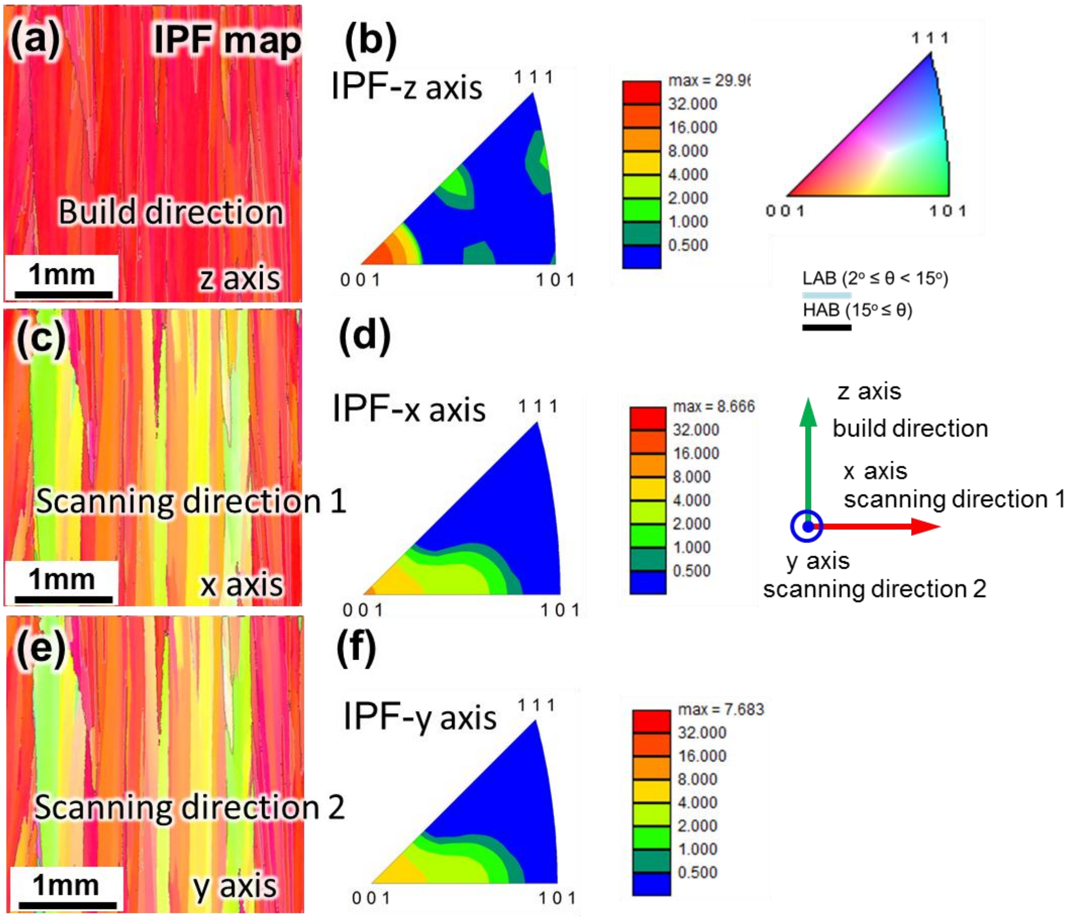

Fig. 3-14. EBSD-IPF map of top part (last built part) of 0°-sample fabricated by the modified condition. (a,c,e) IPF maps oriented to z axis, x axis, and y axis, (b,d,f) IPFs for z axis, x axis, and y axis.

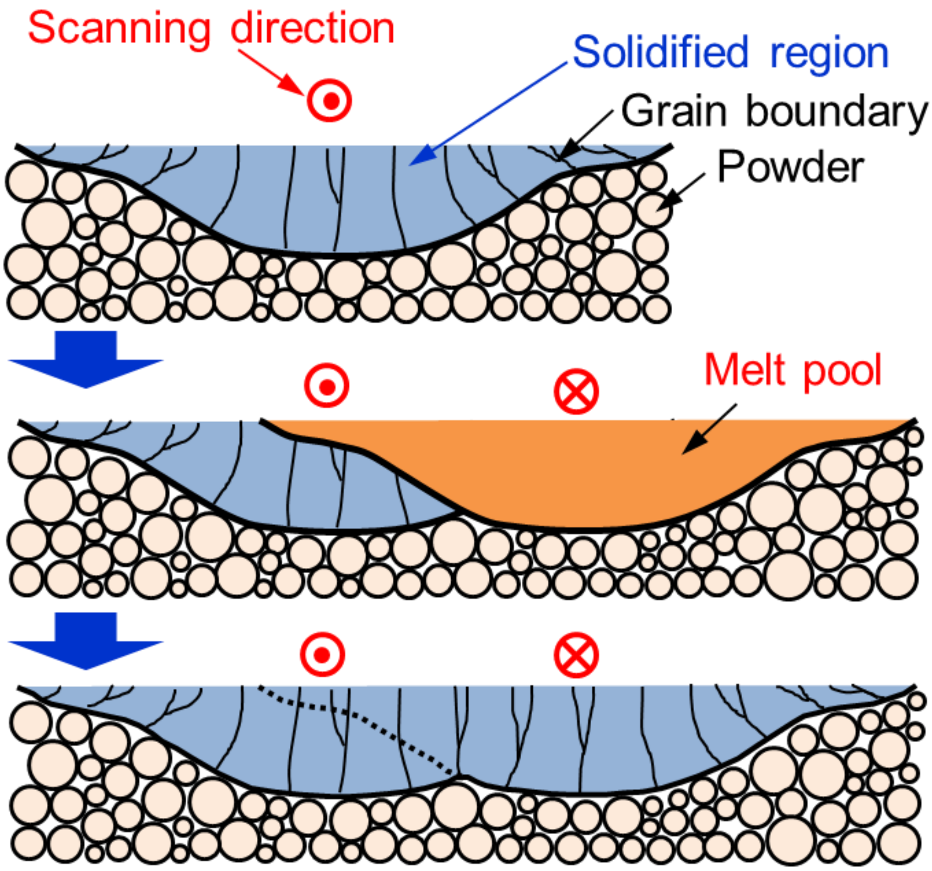

Fig. 3-15. Schematic of formation process of the single crystal-like microstructure from the consecutive solidified bead in the EBM process

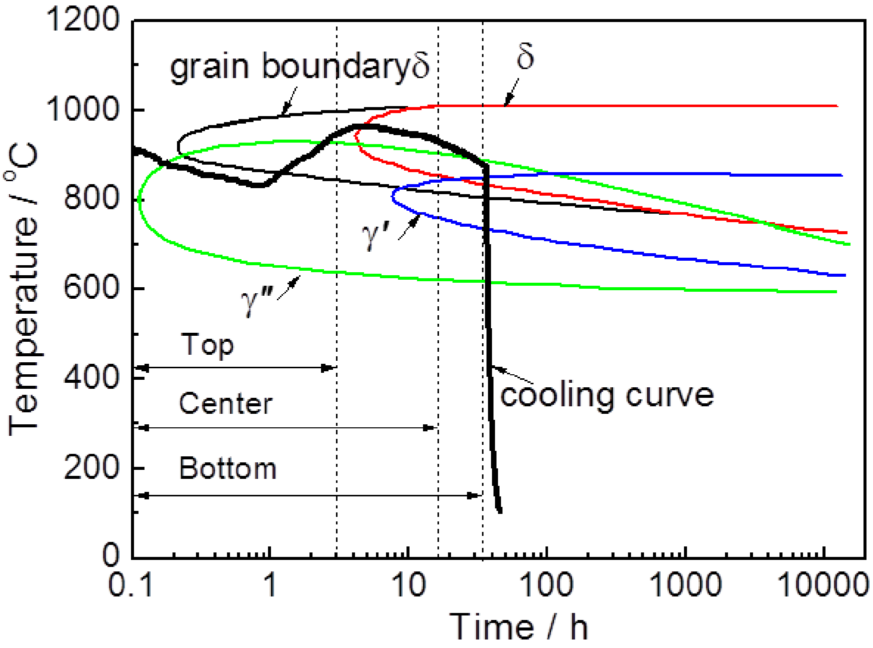

Fig. 3-16. Comparison between cooling curves of 0°-sample fabricated by the modified condition and TTT curves of the precipitates in Inconel 718 alloy.[9].

Table 3-1. Chemical composition of Inconel 718 powder used in the EBM (wt.%).

Ni	Cr	Mo	Nb	Ti	Co	Al	C	N	Fe
53.5	19.4	2.97	4.88	0.84	0.10	0.48	0.0355	0.0077	Bal.

Table 3-2. Primary parameters to build each orientation rods during the EBM process

Condition	**0 °**	**0 ° (modified)**	**45 °**	**55 °**	**90 °**
Preheating temp. / ℃	1000	1025	1000	1000	1000
Layer thickness / μm	90	50	90	90	90
Beam current / mA	8.6	6.5	7.3	14	8.2
Focus offset / mA	20	16	22	22	22
Line offset / μm	200	150	200	200	200
Scanning speed / mm/s	246~662	234~410	206~350	183~383	1014~2040

Table 3-3. Line energy and energy density of 0˚-sample with and without the modified build condition.

Condition	Voltage	Beam current / mA	Scanning speed / mm/s	Line offset / µm	Line Energy / $J{\cdot}m^{-1}$	Energy density /$J{\cdot}m^{-2}$
0 ° (Unmodified)	60	8.6	246~662	200	779~2098	0.4×10^{7}~ 1×10^{7}
0 ° (modified)	60	6.5	234~410	150	951~1667	0.6×10^{7}~ 1.1×10^{7}

References

[1] D. F. Paulonis, J. M. Oblak, and D. S. Duvall, “Precipitation in Nickel-Base Alloy 718,” *Trans. ASM (Amer. Soc. Metals)*, vol. 62, pp. 611-622, Jan. 1969.

[2] M. C. Chaturvedi and Y. Han, “Strengthening Mechanisms in Inconel 718 Superalloy,” *Metal Science*, vol. 17, no. 3, pp. 145–149, Mar. 1983.

[3] P. L. Blackwell, “The Mechanical and Microstructural Characteristics of Laser-Deposited IN718,” *Journal of Materials Processing Technology*, vol. 170, no. 1–2, pp. 240–246, Dec. 2005.

[4] H. Qi, M. Azer, and A. Ritter, “Studies of Standard Heat Treatment Effects on Microstructure and Mechanical Properties of Laser Net Shape Manufactured Inconel 718,” *Metallurgical and Materials Transactions A*, vol. 40, no. 10, pp. 2410–2422, Aug. 2009.

[5] K. N. Amato, S. M. Gaytan, L. E. Murr, E. Martinez, P. W. Shindo, J. Hernandez, S. Collins, and F. Medina, “Microstructures and Mechanical Behavior of Inconel 718 Fabricated by Selective Laser Melting,” *Acta Materialia*, vol. 60, no. 5, pp. 2229–2239, Mar. 2012.

[6] A. Strondl, R. Fischer, G. Frommeyer, and A. Schneider, “Investigations of MX and γ′/γ″ Precipitates in the Nickel-Based Superalloy 718 Produced by Electron Beam Melting,” *Materials Science and Engineering: A*, vol. 480, no. 1–2, pp. 138–147, May 2008.

[7] A. Strondl, M. Palm, J. Gnauk, and G. Frommeyer, “Microstructure and Mechanical Properties of Nickel Based Superalloy IN718 Produced by Rapid Prototyping with Electron Beam Melting (EBM),” *Materials Science and Technology*, vol. 27, no. 5, pp. 876–883, May 2011.

[8] R. Cozar and A. Pineau, “Morphology of γ′and γ″ Precipitates and Thermal Stability of Inconel 718 Type Alloys,” *Metallurgical Transactions*, vol. 4, no. January, pp. 47–59, 1973.

[9] J. W. Brooks and P. J. Bridges, “Metallurgical Stability of Inconel Alloy 718,” *Superalloys*, vol. 88, pp. 33–42, 1988.

[10] Y. Han, P. Deb, and M. C. Chaturvedi, “Coarsening Behaviour of γ″- and γ′-Particles in Inconel alloy 718,” *Metal Science*, vol. 16, no. 12, pp. 555–562, Dec. 1982.

[11] M. Sundararaman, P. Mukhopadhyay, and S. Banerjee, “Precipitation of the δ-Ni_3Nb Phase in Two Nickel Base Superalloys,” *Metallurgical Transactions A*, vol. 19, no. 3, pp. 453–465, Mar. 1988.

[12] S.H. Chang, “In situ TEM Observation of γ′, γ″ and δ Precipitations on Inconel 718 Superalloy through HIP Treatment,” *Journal of Alloys and Compounds*, vol. 486, no. 1–2, pp. 716–721, Nov. 2009.

[13] M. Dehmas, J. Lacaze, A. Niang, and B. Viguier, “TEM Study of High-Temperature Precipitation of Delta Phase in Inconel 718 Alloy,” *Advances in Materials Science and Engineering*, vol. 2011, pp. 1–9, 2011.

[14] D. Cai, W. Zhang, P. Nie, W. Liu, and M. Yao, “Dissolution Kinetics of δ Phase and Its Influence on the Notch Sensitivity of Inconel 718,” *Materials Characterization*, vol. 58, pp. 220–225, 2007.

[15] H. Lee and W. Hou, “Study of δ Phase on Static Recrystallization Behavior of Inconel 718 Alloy,” *Journal of nanoscience and nanotechnology*, vol. 12, no. 9, pp. 6987–6995, 2012.

[16] R. Vincent, “Precipitation around welds in the Nickel-base superalloy, Inconel 718,” *Acta Metall.*, vol. 33, no. 7, pp. 1205–1216, 1985.

[17] C. Radhakrishna and K. P. Rao, “The Formation and Control of Laves Phase in Superalloy 718 Welds,” *Journal of Materials Science*, vol. 32, no. 8, pp. 1977–1984, Apr. 1997.

[18] A. Oradei-Basile and J. F. Radavich, “A Current TTT Diagram for Wrought Alloy 718,” *Superalloys*, pp. 325–335, 1991.

[19] G. D. Janaki Ram, A. Venugopal Reddy, K. Prasad Rao, G. M. Reddy, and J. K. Sarin Sundar, “Microstructure and Tensile Properties of Inconel 718 Pulsed Nd-YAG Laser Welds,” *Journal of Materials Processing Technology*, vol. 167, no. 1, pp. 73–82, Aug. 2005.

[20] W. J. Sames, K. a. Unocic, R. R. Dehoff, T. Lolla, and S. S. Babu, “Thermal Effects on Microstructural Heterogeneity of Inconel 718 Materials Fabricated by Electron Beam Melting,” *Journal of Materials Research*, vol. 29, no. 17, pp. 1920–1930, Jul. 2014.

[21] D. Connétable, M. Mathon, and J. Lacaze, “First Principle Energies of Binary and Ternary Phases of the Fe–Nb–Ni–Cr system,” *Calphad*, vol. 35, no. 4, pp. 588–593, Dec. 2011.

[22] J. C. Zhao, V. Ravikumar, and A. M. Beltran, “Phase Precipitation and Phase Stability in Nimonic 263,” *Metallurgical and Materials Transactions A*, vol. 32, no. 6, pp. 1271–1282, Jun. 2001.

[23] M. C. Chaturvedi and Y. Han, “Effect of Particle Size on the Creep Rate of Superalloy Inconel 718,” *Materials Science and Engineering*, vol. 89, pp. 7–10, 1987.

[24] G. A. Rao, M. Kumar, M. Srinivas, and D. S. Sarma, “Effect of Standard Heat Treatment on the Microstructure and Mechanical Properties of Hot Isostatically Pressed Superalloy Inconel 718,” *Materials Science and Engineering: A*, vol. 355, no. 1–2, pp. 114–125, Aug. 2003.

[25] F. Liu, X. Lin, M. Song, W. Zhao, J. Chen, and W. Huang, “Effect of Intermediate Heat Treatment Temperature on Microstructure and Notch Sensitivity of Laser Solid Formed Inconel 718 Superalloy,” *Journal of Wuhan University of Technology-Mater. Sci. Ed.*, vol. 26, no. 5, pp. 908–913, Nov. 2011.

[26] X. Xie, C. Xu, G. Wang, J. Dong, W. Cao, and R. Kennedy, “TTT Diagram of a Newly Developed Nickel-Base Superalloy-Allvac®718Plus^{TM},” in *Superalloys 718,625,706 and Derivatives 2005*, 2005, pp. 193–202.

[27] G. D. J. Ram, A. V. Reddy, K. P. Rao, and G. M. Reddy, “Microstructure and Mechanical Properties of Inconel 718 Electron Beam Welds,” *Materials Science and Technology*, vol. 21, no. 10, pp. 1132–1138, Oct. 2005.

[28] P. Gao, K. F. Zhang, B. G. Zhang, S. S Jiang, and B. W. Zhang, “Microstructures and High Temperature Mechanical Properties of Electron Beam Welded Inconel 718 Superalloy Thick Plate,” *Transactions of Nonferrous Metals Society of China*, vol. 21, pp. s315–s322, 2011.

[29] W. J. Mills, “Effect of Heat Treatment on the Tensile and Fracture Toughness Behavior of Alloy 718 Weldments,” *Welding Journal*, vol. 63, pp. 237s–245s, 1984.

[30] P. Nie, O. A. Ojo, and Z. Li, “Numerical Modeling of Microstructure Evolution during Laser Additive Manufacturing of a Nickel-Based Superalloy,” *Acta Materialia*, vol. 77, pp. 85–95, Sep. 2014.

[31] L. E. Murr, E. Martinez, K. N. Amato, S. M. Gaytan, J. Hernandez, D. A. Ramirez, P. W. Shindo, F. Medina, and R. B. Wicker, “Fabrication of Metal and Alloy Components by Additive Manufacturing: Examples of 3D Materials Science,” *Journal of Materials Research and Technology*, vol. 1, no. 1, pp. 42–54, Apr. 2012.

[32] L. E. Murr, S. M. Gaytan, F. Medina, H. Lopez, E. Martinez, B. I. Machado, D. H. Hernandez, L. Martinez, M. I. Lopez, R. B. Wicker, and J. Bracke, “Next-Generation Biomedical Implants Using Additive Manufacturing of Complex, Cellular and Functional Mesh Arrays.,” *Philosophical Transactions. Series A, Mathematical, Physical, and Engineering Sciences*, vol. 368, no. 1917, pp. 1999–2032, Apr. 2010.

[33] X. Zhao, J. Chen, X. Lin, and W. Huang, “Study on Microstructure and Mechanical Properties of Laser Rapid Forming Inconel 718,” *Materials Science and Engineering: A*, vol. 478, no. 1–2, pp. 119–124, Apr. 2008.

[34] J. R. Thompson, “Relating Microstructure to Process Variables in Beam-Based Additive Manufacturing of Inconel 718,” Wright State University, 2014.

[35] V. Juechter, T. Scharowsky, R. F. Singer, and C. Körner, “Processing Window and Evaporation Phenomena for Ti–6Al–4V Produced by Selective Electron Beam Melting,” *Acta Materialia*, vol. 76, pp. 252–258, Sep. 2014.

[36] C. Körner, E. Attar, and P. Heinl, “Mesoscopic Simulation of Selective Beam Melting Processes,” *Journal of Materials Processing Technology*, vol. 211, no. 6, pp. 978–987, Jun. 2011.

[37] J. Schwerdtfeger and C. Körner, “Selective Electron Beam Melting of Ti–48Al–2Nb–2Cr: Microstructure and Aluminium Loss,” *Intermetallics*, vol. 49, pp. 29–35, Jun. 2014.

[38] S. M. Gaytan, L. E. Murr, F. Medina, E. Martinez, M. I. Lopez, and R. B. Wicker, “Advanced Metal Powder Based Manufacturing of Complex Components by Electron Beam Melting,” vol. 24, no. 3, 2009.

[39] W. Kurz and D. J. Fisher, *Fundamentals of solidification*, 4th ed. Hampshire, United Kingdom: Trans Tech Publications, 1998, pp. 65–89.

[40] M. Jamshidinia, F. Kong, and R. Kovacevic, “Numerical Modeling of Heat Distribution in the Electron Beam Melting V of Ti-6Al-4V,” vol. 135, no. December, pp. 1–14, 2013.

[41] N. Shen and K. Chou, “Thermal Modeling of Electron Beam Additive Manufacturing Process: Powder Sintering Effects,” in *ASME 2012 International Manufacturing Science and Engineering Conference collocated with the 40th North American Manufacturing Research Conference and in Participation with the International Conference on Tribology Materials and Processing*, 2012, pp. 287–295.

[42] S. A. David and J. M. Vitek, “Correlation between Solidification Parameters and Weld Microstructures,” *International Materials Reviews*, vol. 34, no. 1, pp. 213–245, Jan. 1989.

Chapter 4

4. High temperature mechanical properties of Inconel718 with various build directions

4.1 Introduction

At present, Inconel 718 is extensively used at the wrought state. Therefore, the main application in the aerospace field is limited to the gas turbine engine disk because of the equiaxed grains and machining difficulty for complex components. With the emerging of EBM，it is possible to use Inconel 718 to produce the more complex parts, such as gas turbine blade, from the perspective of shape forming ability. In the previous study about the microstructure of Inconel 718 fabricated by EBM [1], <001> texture was found to form in the build direction. This suggests the single crystal-like microstructure requirement for gas turbine blade can be also satisfied, and anisotropic mechanical will be formed in the build component. Because EBM is the layer-by-layer process, the strength in the build direction may be weaker than that in the direction being perpendicular to the build direction if defect exists in the layer and layer connection part. Therefore, the mechanical property will strongly depend on the build direction.

In this Chapter, the effect of the build direction on the high temperature mechanical properties of Inconel 718 rod fabricated by EBM with various build directions will be investigated.

4.2 Experimental

Inconel 718 rods were fabricated on an Arcam A2 EBM system (Arcam AB, Mölndal, Sweden) with gas atomized powder (Fig.3-1). The chemical composition of Inconel 718 alloy powder is shown in Table 3-1. The cylindrical axes of the rods were oriented to stacking direction (i.e. build direction, designated as *z* axis), face diagonal and space diagonal of the coordinate system consisting of stacking direction and two perpendicular scanning directions (designated as *x* and *y* axis, respectively), as well as the scanning direction, respectively, forming 0°, 45°, 55°, and 90° with the build direction (*z* axis) (Fig.3-2). Hereafter, the Inconel 718 rods fabricated in the directions of 0°, 45°, 55°, and 90° from the *z* axis are designated as the 0°-sample, 45°-sample, and so on. The rods were 15 mm in diameter, and 85 mm in height. The rods for each orientation are fabricated separately, and the primary parameters to build each orientation rods during the EBM process were listed in Table 3-2. The scanning direction of the electron beam will rotated by 90° on each neighboring layer to homogenize the temperature in the build region, as shown Fig.1-10(b).

The standard heat treatment used for the wrought counterpart was carried out on the as-EBM-built samples for tensile test. It consists of solution treatment (ST) and two step aging treatments (AT). ST was carried out at 980 ℃ for 1 h and then water quenched. The first AT was carried out at 720 ℃ for 8 h and then cooled to 620 ℃ in furnace at 50 ℃/h. Subsequently, the second AT was carried out at 620 ℃ for 8 h and then water quenched to room temperature. The specimens for heat treatments were sealed in quartz capsules partially filled with argon. Because the solvus temperature of δ phase was reported to be around 1025 °C [2-6], ST temperature at 980 ℃ may not be high enough to dissolve the δ phase fully. As a result, the amounts of γ′ and γ″ formed in the following two step ATs will decrease, and the corresponding strength may also decease by the influence of the decreased γ′ and γ″ amounts. Therefore, the ST temperature was increased to 1045 ℃ for the creep test samples. Another reason is that the δ phase on the grain boundary may shorten the creep rupture time, because it may be a possible resource for the crack generation at creep process [7].

One of the heat treated rods for each orientation was cut as shown in Fig.3-3, and the blocks cut from the portion at the height of 13 mm, 40 mm, and 67 mm from the bottom were selected for microstructure observation, and will be called “bottom part”, “center part” and “top part”, respectively. The longitudinal cross-section microstructures of the heat treated samples were investigated by scanning electron microscopy (SEM), electron backscatter diffraction (EBSD), and electron probe microanalyzer (EPMA) on the vertical cross section consisting of the cylindrical and z axes.

The tensile samples were taken from the top part of the rod with ST(980 ℃)+AT and cut so that the tensile direction was parallel to the cylindrical axis. The gauge part was rectangular, measuring 11 mm in length, 2 mm in width, and 1 mm in thickness. Tensile tests were conducted at 650 ℃ with a strain rate of 1.5×10^{-4} s^{-1} on an Instron 8562 testing machine. The fracture surfaces were observed by SEM to investigate the effect of carbide array on high temperature deformation.

The gauge part of the creep specimen was cylinder shape with 6 mm in diameter and 30 mm in length. Creep tests were conducted in temperature range from 625 ℃ to 700 ℃, and stress range from 675 MPa to 700 MPa. The microstructure near the fracture was observed by TEM to investigate the effect of γ'' stability on creep deformation.

4.3 Results

4.3.1 Microstructure after heat treatment

Fig. 4-1 shows microstructures on the horizontal cross sections of bottom and top parts of 0°-sample before and after heat treatment. In the as-EBM-built state, the microstructure was inhomogeneous, with δ-Ni_3(Nb,Ti) and (Nb,Ti)C on the bottom (Fig. 4-1(a)), but primarily (Nb,Ti)C on the top (Fig. 4-1(b)). However, after solution (980 ℃ for 1 h) and aging treatments, although small amount of δ-Ni_3(Nb,Ti) would appear on the grain boundary, as shown on the top part (Fig. 4-1(d)), the amount of δ phase would decreased significantly, especially on the bottom part (Fig. 4-1(c)). To examine the effect of heat treatment on precipitate distribution, the hardness variations throughout the build height of 0°-sample before and after heat treatment were investigated, as shown in Fig. 4-2. In the as-EBM-built sample, the hardness decreased along the build height, which suggests that more precipitates exist on the bottom part because of its longer post-built heating time for microstructure variation. After heat treatment, uniform and higher hardness can be obtained throughout the build height, which suggests that previously formed δ phase dissolves into the matrix during the solution treatment (980 ℃ for 1 h) and more γ′ and γ″ form in the matrix by the Nb element from dissolved δ phase in the subsequent aging treatment.

Fig. 4-3 shows EPMA element maps on the longitudinal cross-section of the top part of 0°-sample with solution (980 ℃ for 1 h) and aging treatments. The spherical precipitate indicated by the black arrow consisted of Nb,Ti, C, and B, which suggests that the precipitate is (Nb, Ti)(C,B) [1]. The plate-like precipitates indicated by the red arrows consisted of Ni, Nb and Ti, which suggests that the precipitates are δ-Ni$_3$(Nb, Ti) [8]. The solvus temperature of MC carbide (M=Ti,Nb) is 1250 ℃ [1,5,9], therefore it cannot be dissolved into the matrix at 980 ℃. It is reported that the solvus temperature of δ phase is around 1025 °C [2-6], and δ phase can only partly dissolve into matrix at the solution treatment of 980 ℃ [4]. This may be the reason why δ phase is not dissolved into the matrix at 980 ℃, instead it can precipitate out on the grain boundary. These results suggest that the standard solution treatment for wrought Inconel 718 is not proper for EBM-built sample in order to fully dissolve the previously formed δ phase on the early-built part, though the uniform hardness distribution shows the microstructure become homogeneous.

Fig. 4-4 shows EBSD-IPF maps on the longitudinal cross-sections of the top parts of samples with solution (980 ℃ for 1 h) and aging treatments. LAB and HAB, represented by black and light blue lines, respectively, were shown on the IPF maps. The orientations shown in the IPF maps were in the cylindrical axis, which reveals that the preferential crystal orientations in the cylindrical axes can be kept after heat treatment, were near [001], [110], [111], and [100] in the 0°-, 45°-, 55°-, and 90°-samples, respectively. This suggests that recrystallization does not occur during heat treatment process. The fine grain regions still existed in the matrix after heat treatment, which suggests that grain does not grow significantly during heat treatment process. The average grain sizes perpendicular to the *z*-axis (build direction) for 0°-, 45°-, 55°-, and 90°-samples were 135 μm, 41 μm, 49 μm, and 68 μm, respectively. And the average grain sizes parallel to the *z*-axis for 0°-, 45°-, 55°-, and 90°-samples were 646 μm, 380 μm, 650 μm, and 103 μm, respectively. The grain size was measured by the intercept length.

Fig. 4-5 shows SEM microstructures on the longitudinal cross-sections of the top parts of samples with solution (980 ℃ for 1 h) and aging treatments. The precipitates were still aligned along the *z* axis in all the samples. The 0°-sample shown here was fabricated by EBM with the modified condition, the previously formed Laves phase still existed in the matrix after heat treatment. Strondl et al. [1] indicated that the solvus temperature of Laves phase is 1150 ℃ by the differential thermal analysis (DTA) of as-EBM-built Inconel 718. Therefore, laves phase cannot dissolve into matrix at 980 ℃. The δ phase and Laves phase can also be confirmed by EPMA analysis, as shown in Fig. 4-6. The precipitate indicated by arrow “a” is rich in the elements of Ni, Fe, Cr and Mo, which suggests the precipitate is Laves phase, $(Ni,Fe,Cr)_2Mo$ [10-13]. The precipitate indicated by arrow “b” is rich in the elements of of Ni, Nb and Ti, which suggests the precipitate is δ-Ni_3(Nb, Ti) [1,8]. The precipitate indicated by arrow “c” has high concentration of Nb, Ti, C and B, which suggests the precipitate is (Nb,Ti)(C,B) [1]. The precipitate indicated by arrow “d” has high concentration of Nb, Mo, Cr, C and B, which suggests the precipitate is $(Nb,Mo,Cr)_3(C,B)_2$ [10]. The above results indicates that the standard solution treatment for wrought Inconel 718 is not proper for EBM-built sample in order to dissolve the previously formed δ and Laves phases on the early-built part.

Chen et al. [7] indicated that δ phase on the grain boundary will shorten the creep rupture time, because it may be a possible resource for the crack generation during the creep process. Therefore, the ST temperature of creep test samples was increased to 1045 ℃. Fig. 4-7 shows EBSD-IPF maps on the longitudinal cross-sections of the center parts of samples with solution (1045 ℃ for 1 h) and aging treatments. LAB and HAB, represented by black and light blue lines, respectively, were shown on the IPF maps. The orientations shown in the IPF maps were in the cylindrical axis, which reveals that the preferential crystal orientation in the cylindrical axis can be kept even after the heat treatment with increased ST temperature, and were near [001], [110], [111], and [100] in the 0°-, 45°-, 55°-, and 90°-samples, respectively. Amato et al. [14] indicated that recrystallization would occur extensively in the SLM-built Inconel 718 samples at 1160 ℃ for 4 h. One possible reason for the absence of static recrystallization is that the ST time (1 h) may be too short and the ST temperature is not high enough. Another possible reason is the dislocation density in the EBM-built sample is lower than that in the SLM-built sample, because additional preheating process exists in the EBM process, which can reduce the dislocation density. The fine grain regions still existed in the matrix after heat treatment, which suggests that grain does not grow significantly even though ST temperature is increased to 1045 ℃. The average grain sizes perpendicular to the *z*-axis for 0°-, 45°-, 55°-, and 90°-samples were 94 μm, 29 μm, 29 μm, and 94 μm, respectively. And the average grain sizes parallel to the *z*-axis for 0°-, 45°-, 55°-, and 90°-samples were 467 μm, 248 μm, 1583 μm, and 120 μm, respectively.

Fig. 4-8 shows SEM microstructures on the longitudinal cross-sections of the center parts of samples with solution (1045 ℃ for 1 h) and aging treatments. The precipitates were aligned along the *z* axis in all the samples. δ phase can be rarely found in the matrix, which suggest it has already been dissolved into matrix during solution treatment at 1045 ℃ for 1 h. Because the solvus temperature of Laves phase is 1150 ℃ [1], it will still exist in the matrix.

Fig. 4-9 shows TEM dark field images (DFI) and corresponding selective area diffraction (SAD) patterns on the middle parts of 0°- and 55°-samples after solution (1045 ℃ for 1 h) and aging treatments. The diffraction spots selected to take the DFIs were indicated by the green circles on Fig. 4-9(c,d). In the [001] incident direction of γ matrix, the diffraction patterns from all the γ″ variants could be observed on both the 0°- and 55°-samples (Fig. 4-11(c,d)), which suggests that all the γ'' variants, whose [001] orientations are parallel to [100], [010] and [001] of γ matrix, respectively, can exist in the matrix after heat treatment. Fig. 4-11(a) shows that elliptical γ'' had an average minor axis of 9 nm, and average major axis of 32 nm in the 0°-sample. Fig. 4-11(b) shows that elliptical γ'' had an average minor axis of 8 nm, and average major axis of 39 nm in the 55°-sample. Compared with the γ'' size in the bottom part (it has the longest post-built heating time) of as-EBM-built 0°-sample (Fig. 3-11(c)), the γ'' precipitate size in 0°-sample has nearly doubled after heat treatment.

4.3.2 High temperature tensile properties

Fig. 4-10 shows stress-strain curves of 0°-sample before and after solution treatment (980 ℃ for 1 h) followed by aging treatment tested at 650 ℃ with strain rate of 1.5×10^{-4} s^{-1}. It was found that the strength and elongation were improved greatly after solution treatment and subsequent aging treatment. Necking was observed obviously in the tensile test of the heat-treated sample, whereas, it did not occur significantly in that of as-EBM-built sample. This is probably because the precipitate distribution becomes uniform and there may be more γ' and γ'' precipitates and less δ-phase after heat treatment. Therefore, further investigations of the mechanical properties for the samples with other build directions were conducted only for the samples after solution treatment and subsequent aging treatment with particular focus on the mechanical properties caused by γ' and γ'' precipitates and not affected by the coarse precipitates.

Fig. 4-11 shows stress-strain curves of the samples with various build directions after solution treatment (980 ℃ for 1 h) followed by aging treatment tested at 650 ℃ with strain rate of 1.5×10^{-4} s^{-1}. Higher *UTS* of the samples was obtained in the order of 0°-, 55°-, 45°-, and 90°-samples. The 0.2% yield stresses of the 0°-, 45°-, 55°- and 90°-samples were 951 MPa, 757 ± 8 MPa, 843 ± 13 MPa, and 815 ± 27 MPa respectively. All the samples exhibited good ductility, and the elongations of the 0°-, 45°-, 55°- and 90°-samples were 17.3%, 16.2 ± 5.5%, 11.4 ± 2.7%, and 8.5 ± 3.1%, respectively. The mechanical property comparison between EBM-built samples and wrought [15] as well as HIP [16] counterparts at 650 ℃ are listed in Table 4-1. The elongations of EBM-built samples were comparable with those of wrought and HIP counterparts, but the strengths of EBM-built samples were lower than those of wrought and HIPed counterparts. The grain size of 0°-sample with modified condition, which exhibited the highest strength among the EBM-built samples, was 135 μm measured by the interception perpendicular to the *z*-axis, while those of wrought and HIPed counterparts were about 10 μm [16]. Therefore, larger grain size may decrease the strength of EBM-built samples. In Table 4-1, it is found that the strength and elongation of EBM-built 0°-sample can be improved significantly after modifying the build condition. This suggests the unmelt particle may decrease the strength and ductility. The mechanical properties of the other EBM-built samples are expected to be also improved by modifying the EBM build condition to form single crystal-like microstructures.

Fig. 4-12 shows the fracture surface of samples with various build directions after tensile test. All the samples exhibited dimple-type fracture surfaces, suggesting that intragranular facture occurred. 0°-sample built with modified condition exhibited larger and deeper dimples than the other samples, which suggests very large local deformation occurred in this sample. This is consistent with the result that 0°-sample built with modified condition (hereafter, designated as "modified 0°-sample") exhibited the largest elongation and the most obvious necking among the samples. Beside the dimples, some large hole (indicated by while arrows) and long grooves (indicated by white dashed lines) can be observed on the fracture surface. The large holes are thought to be caused by the detached unmelt particles which have relatively small size. The long grooves are thought to be formed along the arranged carbides and coarse δ phase because the grooves are parallel to the *z*-axis projection. These defects (i.e. holes and precipitates) are thought to decrease the ductility of samples because the modified 0°-sample, in which defects are not observed, exhibited the largest elongation and the most obvious necking among all the samples. In the 0°-sample built with the unmodified condition (hereafter designated as “unmodified 0°-sample”), an area consisting of numerous long grooves which were parallel to the *y*-axis can be observed as seen in the area surrounded by the while dash line in Fig. 4-12(a). However, the grooves should not be observed on the fracture surface (*x*-*y* plane), if the grooves were caused by the arranged carbides and coarse δ phase, because the carbides and coarse δ phase are aligned along the *z*-axis in 0°-sample. Therefore, the fracture morphology in this area is thought to be caused by the carbides and/or dendritic crystals in the fine grain region (Fig. 3-12(b)) consisting of unmelt particles. The grooves may be just coincidentally parallel to the *y*-axis. Because of the existence of numerous unmelt particles, the unmodified 0°-sample exhibited nearly no ductility. In 90°-sample, the grooves caused by the coarse precipitates were perpendicular to the loading direction, which will lead to fracture easily. As a result, 90°-sample exhibited lower *UTS* and elongation than the modified 0°-sample though both of them had the <001> orientation.

4.3.3 Creep properties

4.3.3.1 Stress dependence of creep behavior

Fig. 4-13 shows the creep curves of samples with various build directions at 650˚C with stress of 700 MPa. At the early creep deformation stage (Fig. 4-13(a)), it is found that primary creep was not recognized in 55°-sample. Although the other samples exhibited primary creep, the period was very short. Moreover, 45°-sample even exhibited short period of steady state creep. The creep stage can be easily identified by the relationship between creep rate and time, as shown in Fig. 4-14. 55°-sample exhibited the smallest minimum creep rate among the samples, and it might be expected that 55°-sample exhibits the longest creep rupture time among the samples. However, eventually, the modified 0°-sample exhibited the longest creep rupture time as seen in in the creep curves to rupture (Fig. 4-13(b)). For commercial single crystal nickel-based superalloys, the orientation with longest creep rupture time can be <001> or <111> depending on the composition [17-21].

Fig. 4-15 shows the creep curves of samples with various build directions at 650 ℃ with different stresses. All the samples did not exhibit the primary creep obviously in the tested stress region, which suggests that the work hardening reaches equilibrium with recovery in a very short time. This is thought to be the character of nickel based alloy strengthened by intermetallic phases [22]. Overall, the creep rupture time increased with decreasing the applied stresses for all the samples. Fig. 4-16 shows stress dependence of creep behavior of samples with various build directions at 650 ℃. Fig. 4-16(a) shows the smallest minimum creep rate was obtained for the 55°-sample, followed by 0°-, 45°-, and 90°-samples, whereas Fig. 4-16(b) shows creep rupture time was longer for 0°-, 55°-samples, and followed by 45°- or 90°-samples. Fig. 4-16(c) shows creep rupture strain was kept nearly constant against the increase in the stress for all the samples, and higher creep rupture strain was obtained in the order of 0°-, 45°-, and 55°- or 90°-samples. The minimum creep rate and creep rupture time can be expressed by the Monkman-Grant equation [23]:

$$(\dot{\varepsilon}_m)^n \cdot t_r = \mathrm{C} \tag{4.1}$$

where $\dot{\varepsilon}_\mathrm{m}$ is the minimum creep rate, n is the material constant, t_r is the creep rupture time, and C is a constant directly proportional to the log of creep rapture strain of the material. Smaller minimum creep rate do not necessarily mean longer creep fracture time, if creep rapture strain is not constant. Therefore, the much smaller creep strain in 55°-sample than that in 0°-sample is the reason for shorter creep ruptures time in 55°-sample, although the 55°-sample always exhibits smaller minimum creep rate than 0°-sample.

4.3.3.2 Temperature dependence of creep behavior

Fig. 4-17 shows the temperature dependence of creep behavior of samples with various build directions. For all the samples, the minimum creep rate increased with increasing temperature, while the creep rupture time decreased with increasing temperature. Creep rupture strain was kept nearly constant against the increase in temperature. When compared at a same temperature, the minimum creep rate and creep rupture time for 0°- and 55°-samples were similar, and those for 45°- and 90°-samples were similar.

4.3.3.3 Creep rupture time comparison with wrought counterpart

Fig. 4-18 shows the creep rupture time comparison between EBM-built and wrought Inconel 718 [24]. Compared with the wrought counterpart, the EBM-built 0°- and 55°-samples can exhibit comparable and even longer creep rupture time at the same stress, while 45°- and 90°-samples exhibited shorter creep rupture time. These suggest that the EBM-built 0°- and 55°-samples can exhibit comparable and even superior creep resistant, while 45°- and 90°-sample exhibited inferior creep resistant, when compared with wrought counterpart.

4.3.3.4 Creep mechanism analysis based on constitutive equation

Considering creep as thermally activated phenomenon, creep behavior is usually characterized by the following empirical equation,

$$\dot{\varepsilon}_{\mathrm{m}} = \mathrm{A}\sigma^{n} exp(-\frac{Q}{\mathrm{R}T}) \qquad (4.2)$$

where $\dot{\varepsilon}_{\mathrm{m}}$ is the minimum creep rate, A is a constant, σ is the applied stress, n is the stress exponent for creep, Q is the apparent activation energy for creep, R is the universal gas constant, and T is the absolute temperature.

Fig. 4-19 shows stress and temperature reciprocal dependence of minimum creep rate with various build directions. Fig. 4-19(a) shows that the logarithm of minimum creep rate exhibited a linear relationship with logarithm of stress. This suggests the samples exhibited the power law creep. The apparent stress exponent of the samples can be determined to be 31, 20, 28, and 18 for 0°-, 45°-, 55°-, and 90°-samples by the slope, respectively. The values are larger than 3, which suggest that the creep deformation is mainly controlled by dislocation motion. For the cold rolled Inconel 718, the apparent stress exponent was between 9 and 15 [25], while for the hot forged Inconel 718, the apparent stress exponent was 36.5 [26]. These suggest that the deformation mechanism for EBM-built and wrought Inconel 718 are the same, both of them are controlled by dislocation motion.

Fig. 4-19(b) shows that the logarithm of minimum creep rate also exhibited a linear relationship with temperature reciprocal. The apparent activation energy of the creep deformation can be determined to be 437 kJ/mol, 557 kJ/mol, 614 kJ/mol and 627 kJ/mol for 0°-, 45°-, 55°-, and 90°-samples by the slope, respectively. The apparent activation energy in EBM-built Inconel 718 is much larger than self-diffusion activation energy (285 kJ/mol [27]) of Ni, which may be because the influence of temperature on shear modulus and back stress are not considered. When shear modulus and back stress are considered in cold rolled Inconel 718 [25], the activation energy will change from 375±17 kJ/mol to 310±8 kJ/mol. For the hot forged Inconel 718, the apparent activation energy was 513 kJ/mol [26]. The larger apparent activation energy in EBM-built Inconel 718 than that in wrought Inconel 718 may be the reason for the superior creep resistance of EBM-built Inconel 718.

For the material with superplasticity, the relationship between applied stress and strain rate is usually express as [28]:

$$\sigma = \mathrm{K}\varepsilon^{l}\dot{\varepsilon}^{m} \tag{4.3}$$

and, $l = \frac{\partial(\ln\sigma)}{\partial(\ln\varepsilon)}$, $m = \frac{\partial(\ln\sigma)}{\partial(\ln\dot{\varepsilon})}$.

where, σ is the applied stress, ε is the strain, $\dot{\varepsilon}$ is the strain rate, l is the strain hardening exponent, and m is the strain rate sensitivity exponent. The condition for the occurrence of grain boundary slip in material with superplasticity is that strain rate sensitivity exponent m is larger than 0.5. Assuming creep strain and temperature are constant during creep deformation, and comparing Eq.(4.2) with Eq.(4.3), it is suggested that the apparent stress exponent, n, of creep should be smaller than 2 if grain boundary slip is the major mechanism of creep deformation. In fact, the *n*s of the samples are much larger than 2, which suggest that grain boundary slip is not the major mechanism of creep deformation.

4.4 Discussion

4.4.1 Dominant factors affecting high-temperature tensile properties

There are several possible factors which can give rise to the differences in the tensile properties of the EBM-built Inconel 718 with different build-directions, i.e. the anisotropy of grain boundary, γ′ and γ″ arrangement and crystal orientation. Here the roles of the factors are discussed.

4.4.1.1 Effect of grain boundary on deformation

Fig.4-20 shows the relationship between columnar grains and {111} slip planes in samples with various build directions. The columnar grain is assumed to have hexagonal shape with its longitudinal axis oriented to the [001], and the longitudinal axes of the rectangle (i.e. cylindrical axis of the rod) are oriented to [001], [011], [111], and [010] in 0 °-, 45 °-, 55 °-, and 90 °-samples, respectively. Then the {111} slip planes relative to the columnar grains can be obtained, as shown in Fig.4-20(a,b,c,d). Assuming the mean intercept length (d_s) of the grain boundaries is measured on the plane consisting of cylindrical axis and build direction (*z* axis), the effective slip distance (d_{eff}) for edge dislocation can be determined based on the above crystal model, the results are as listed in the Table 4-2. Then the effect of grain boundary on strength will be discussed based on the Hall-Petch relationship:

$$\sigma=\sigma_0+\mathrm{k}\, d_{\mathrm{eff}}^{-1/2} \tag{4.3}$$

where, σ is the yield strength, σ_0 is the friction stress, k is the constant, and d_{eff} is the effective slip distance for edge dislocation. Fig.4-21 shows the effect of grain boundary on the yield strength in the sample with various build directions. Higher yield strength was obtained in the order of 55 °-, 45 °-, 90 °-, and 0 °-samples.

4.4.1.2 Effect of precipitate on deformation

Because Inconel 718 is mainly strengthened by γ′ and γ″ [29-31], the precipitates in Inconel 718 considered on the {111} slip planes are γ′ and γ″, which are assumed to distribute in the γ matrix equably. The major axes of elliptical-shaped γ″ are parallel to [100], [010] and [001] of γ matrix, respectively, because the [001] orientations of γ″ are parallel to [100], [010] and [001] of γ matrix, respectively. Then the γ′ and γ″ arrangements on the four nonparallel {111} slip planes are shown in Fig. 4-22. The arrows indicate the slip directions of perfect dislocations with the two highest Schmid factors for <110>{111} slip systems in 0 °-, 45 °-, 55 °-, and 90 °-samples. Arrows and corresponding built-angles are shown with the same color. When the two slip directions are both same for different built-angles, one same color is used for the different built-angles. Because the angles between major axis (<001>) of γ″ and normals of the four {111} planes (i.e. α-, β-, γ-, and δ-planes) of γ matrix are equally 54.76 °, the cross sections of γ″ on {111} planes are the same. Because γ′ is spherical shape, the cross sections of γ′ on {111} planes are round. Owing to the assumption of regular arrangement of γ′ and γ″ in the matrix, their arrangement on the α-, β-, γ-, and δ-planes are very similar. The average size of γ′ and γ″ measured in the direction perpendicular to the slip direction is around 30 nm, and the distance between the precipitates is around 10 nm, therefore, shearing mechanism is dominant at such small particle size with high volume fraction [31]. Even though there is difference in the γ″ shapes in different slip directions in the local region, its effect on the strength can be neglected in the whole slip plane by considering the average effect. This suggests that there is no difference in the effect of γ′ and γ″ arrangement on dislocation slip on the different {111} planes.

4.4.1.3 Effect of crystal orientation on deformation

Table 4-3 lists the maximum Schmid factors (μ_{max}) for {111}<110> slip system in the samples with various build directions, which are calculated with the assumption that the loading axes are exactly parallel to [001], [011], [111], and [010] directions for 0°-, 45°-, 55°-, and 90°-samples, respectively. The maximum μ was 0.408 for 0°-, 45°-, and 90°-samples, while it was 0.272 for 55°-sample. The shear stress and the normal stress can be expressed by the following equation:

$$\tau = \sigma \cdot \mu \tag{4.4}$$

where τ is the shear stress, σ is the normal stress, and μ is Schmid factor. Therefore, The 55°-sample will exhibit the highest yield stress among the samples at the same critical shear stress.

4.4.1.4 Determination of the most dominant factor of the strength

The factors discussed above can give rise to different build direction dependences of strength. Here, the most dominant factor for the anisotropy of strength is discussed. Because the unmelt particles exist in the EBM-built samples except for the modified 0°-sample, the intrinsic strength of the samples might be hidden by the defects associated with the defects. Nevertheless, it is possible to examine which is dominating the anisotropy by comparing the anisotropy of strength of the Inconel 718 built in various directions with those expected from the orientations of grain boundaries, γ' and γ'' precipitate arrangement, and crystallographic orientation.

By considering the orientation dependence of Schmid factor for the operative slip systems, the strength of sample is expected to be highest for 55°-sample. Because γ' and γ'' arrangements on the different slip planes are similar, γ' and γ'' arrangement will not change the strength order of the samples by considering their arrangement on the different operative slip plane in different crystal orientation samples. The grain boundaries of 45°-sample are parallel to the maximum shear stress direction. Therefore, it is expected that 45°-sample would exhibit the lowest strength among the samples, if grain boundary sliding could occur in the high temperature tensile test process. The inclination angle of grain boundaries in 55°-sample is deviated from that of the maximum shear stress plane by only 10°, and therefore the strength of 55°-sample would be relatively low if grain boundary sliding is the dominant deformation mechanism. However, in fact, 55°-sample exhibited the highest strength among the samples. This strongly suggests that the deformation is mainly governed by the dislocation slip.

The columnar grains in 90°-sample are elongated to the direction perpendicular to the loading axis, and significant amount of grain boundaries in 90°-samples are perpendicular to the loading axis. Therefore, it is very easy for cracks to initiate on and propagate along grain boundaries. This is probably responsible for the result that, 90°-sample exhibited lower strength than 0°-sample. Finally, the higher strength of sample is expected to be obtained in the order of 55°-sample, 0°- sample, 90°- sample, and 45°-samples.

4.4.2 Effect of γ'' stability on creep deformation

Fig. 4-23 shows TEM DFIs and corresponding SAD patterns of samples after creep test. 0°- and 55°-samples were crept at 650 ℃ under stress of 775 MPa, while 45°- and 90°-samples were crept at at 650 ℃ under stress of 725 MPa. The thin foils were taken along the tensile axis (i.e. the cylindrical axis). The diffraction spots selected to take the DFIs were indicated by the green circles on Fig. 4-23(b,d,f,h). Fig. 4-23(a,c,e,g) shows that metastable γ'' phase can still exist even after creep test. However, Fig. 4-23(b,h) shows that the diffraction patterns from [100] or [010] variant of γ'' (indicated by the brown or green ellipses in Fig. 4-23(i)) can not be observed after creep test in the 0°- and 90°-samples, which suggests that [100] or [010] variant of γ'' phase dissolves into the matrix during creep deformation. The diffraction patterns from all the γ'' variants could be observed in 45°- and 55°-samples (Fig. 4-23(d,f)), which suggests that all the γ'' variants can exist in the matrix after creep test in 45 °-and 55 °-samples.

At the same stress, 0 °-sample exhibited longer creep rupture time than 55 °-sample, which seems to suggest that the instability of γ'' may be caused by the longer creep rupture time. However, one of the γ'' variants in 90 °-sample can dissolve into matrix, even though 90 °-sample exhibited short creep rupture time than 45 °-sample. Therefore, the instability of γ'' is not governed by the creep rupture time here.

When the c axis of the γ'' variant is parallel to the loading axis, it can dissolve into the matrix [31]. Therefore, the stability of γ'' in tensile creep can be understood from the aspect of stress state of the lattice of γ'' variants. The lattice constants of γ'' are as follows [32]: a=0.3624 nm, c=0.7046 nm. The lattice constant of γ is 0.3616 nm [32]. The lattice of γ'' is coherent with that of γ matrix, and the interatomic distance in γ'' phase in its c-axis corresponding to the lattice constant of γ matrix is $c/2 = 0.3523$ nm, which is smaller than the lattice constant of γ-matrix. Therefore, the lattice of γ'' phase is expanded in c-axis direction by the γ matrix, while the lattice of γ'' is compressed in a-axis direction by the γ matrix. In the tensile creep for 0 °-and 90 °-samples, the [001] variant of γ'' in 0 °-sample and [010] variant of γ'' in 90 °-sample are highly stressed by the superposition of the applied external stress in the loading direction and the internal coherency stress from the γ-matrix, which is also parallel to the c-axis direction of the γ'' variants. Therefore, the [001] variant of γ'' in 0 °-sample and [010] variant of γ'' in 90 °-sample will be unstable and dissolve in matrix during the tensile creep. As a result, the number of strengthening γ''-precipitates decreases, causing the decrease of the flow stress. Hence, the creep rate of 0 °-and 90 °-samples will increase in the course of creep. In the 55 °-sample, all the γ'' variants are stable because they are equally stressed by the tensile load. Therefore, all the γ'' variants of 55 °-sample are stable in the course of creep. As a result, the creep rate of 55 °-sample will be lower than that of 0 °-sample under the same stress. In 45 °-sample, assuming the loading axis is parallel to 011 direction, then the compressive internal coherency stress from the γ-matrix in a axis of [100] γ'' is partly cancelled by the applied external stress in the loading direction, which contributes to the stability of the γ'' variant. For the [010] and [011] variants of γ″, the applied tensile stress can cause positive effect on the stability of γ″ variant in a axes, but negative effect on the stability of γ″ variant in c axes. Then these two γ″ variant can be stable because of the offset of the two effects. Therefore, all the γ″ variants of 45 °-sample are stable in the course of creep. As a result, the creep rate of 45 °-sample will be lower than that of 90 °-sample under the same stress.

4.5 Conclusions

High temperature mechanical properties of Inconel 718 alloy fabricated by EBM with various build directions have been investigated and the following conclusions have been obtained.

(1) Uniform precipitate distribution and higher hardness of the matrix can be obtained by solution treatment at 1045 ℃ for 1 h, and first aging treatment at 720 ℃ for 8 h as well as second aging treatment at 620 ℃ for 8 h. After this heat treatment, the preferential crystal orientation was found not to change significantly.

(2) Strength and ductility of EBM-built Inconel 718 alloy can be improved by heat treatment, probably due to the increase of γ″ and γ′ and decrease of δ phase.

(3) The unmelt particle may decrease the strength and ductility, the mechanical property are expected to be improved by improving the EBM fabrication condition to obtain the single crystal-like grains.

(4) The creep properties exhibited build direction dependence, which can be mostly attributed to the difference in the Schmid factors in the grain with different crystal orientations.

(5) Primary creep stage was not recognized for 55 °-sample, while it was found for the other samples, although the period was very short. 45 °-sample even exhibited short period of steady state creep, which may be because its grain boundary is parallel to the maximum stress direction, causing the easier occurrence of crack due to the grain boundary relative slip.

(6) 55 °-sample (near <111> orientation) exhibited the smallest creep rate among the

samples.

(7) The creep rupture time of EBM-built 0°-, 55°-sample were longer than that of the wrought counterpart in the same creep condition.

(8) The γ'' variant with c axis parallel to loading axis in 0°-and 90°-sample was found to dissolve into matrix during creep test, which will increase their minimum creep rate significantly.

(9) The relation between minimum creep rate and applied stress could be described by the constitutive equation: $\dot{\varepsilon}_m = \mathrm{A}\sigma^n exp(-\frac{Q}{\mathrm{R}T})$. The stress exponent n were determined to be 31, 20, 28, and 18 for 0°-, 45°-, 55°-, and 90°-samples, respectively. And apparent activation energy Q were determined to be 437 kJ/mol, 557 kJ/mol, 614 kJ/mol and 627 kJ/mol for 0°-, 45°-, 55°-, and 90°-samples, respectively.

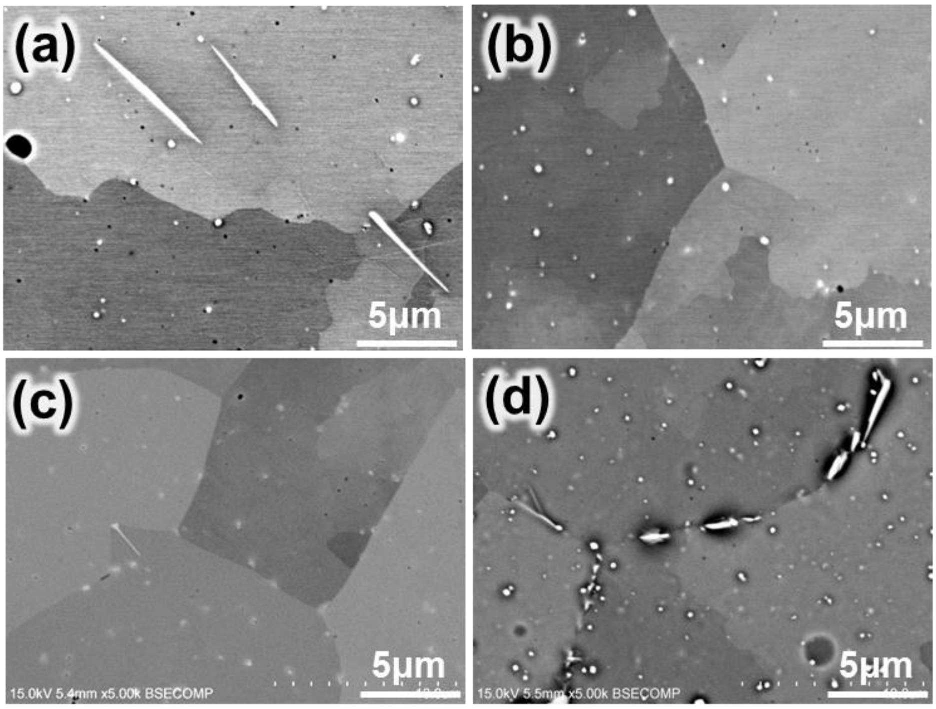

Fig. 4-1. Microstructures on the horizontal cross sections of bottom and top parts of 0˚-sample before and after heat treatment. (a) Bottom and (b) top parts of as-EBM-built 0°-sample, (c) bottom and (d) top parts of 0°-sample with solution treatment at 980 ℃ for 1 h and aging treatments at 720 ℃ for 8 h firstly and 620 ℃ for 8 h secondly.

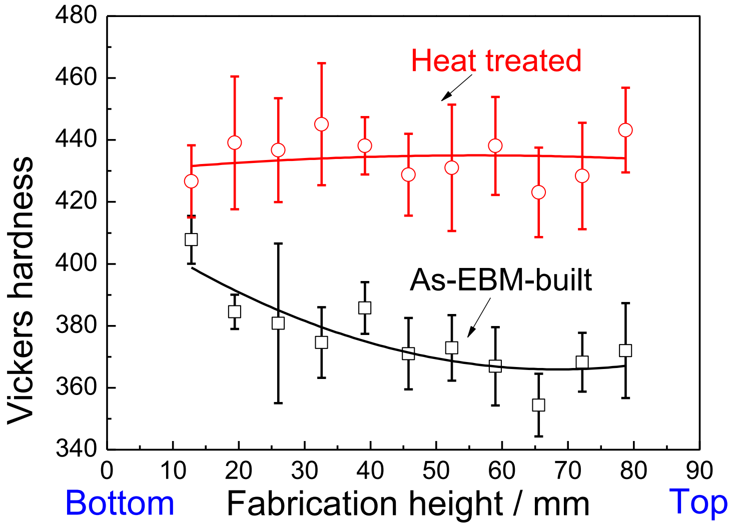

Fig. 4-2. Hardness variations along the build height in the as-EBM-built and heat treated 0°-sample rods.

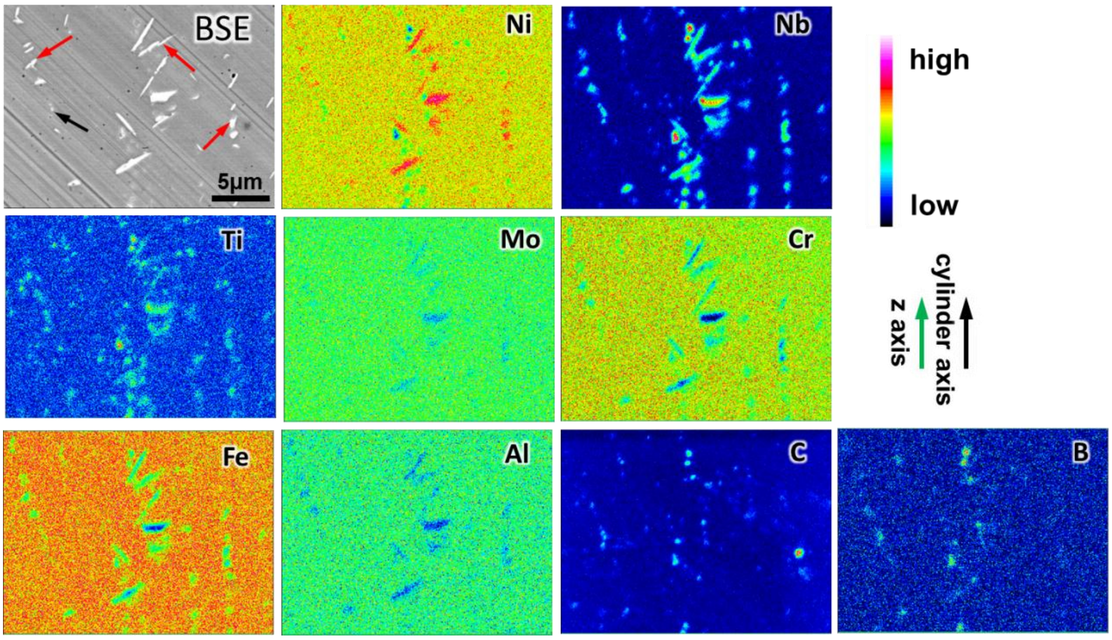

Fig. 4-3. EPMA element maps on the longitudinal cross-section of the top part of 0˚-sample with solution treatment at 980 ℃ for 1 h and aging treatments at 720 ℃ for 8 h firstly and 620 ℃ for 8 h secondly.

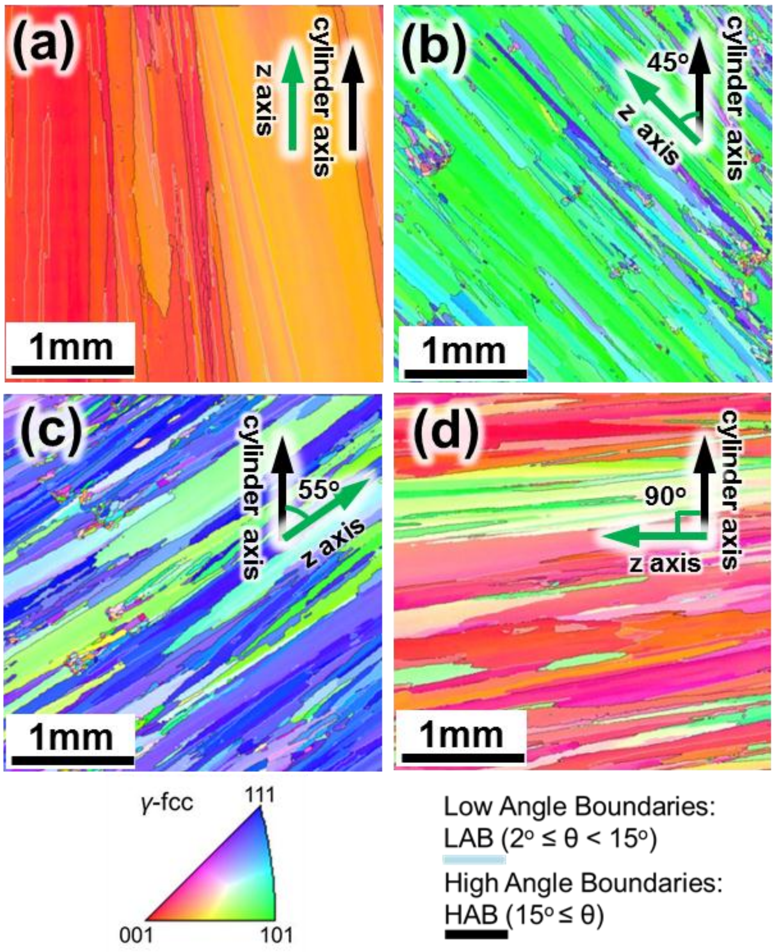

Fig. 4-4. EBSD-IPF maps on the longitudinal cross-sections of the top parts of samples with solution (980 ℃ for 1 h) and aging treatments. (a) 0˚-sample, (b) 45˚-sample, (c) 55˚-sample, and (d) 90˚-sample.

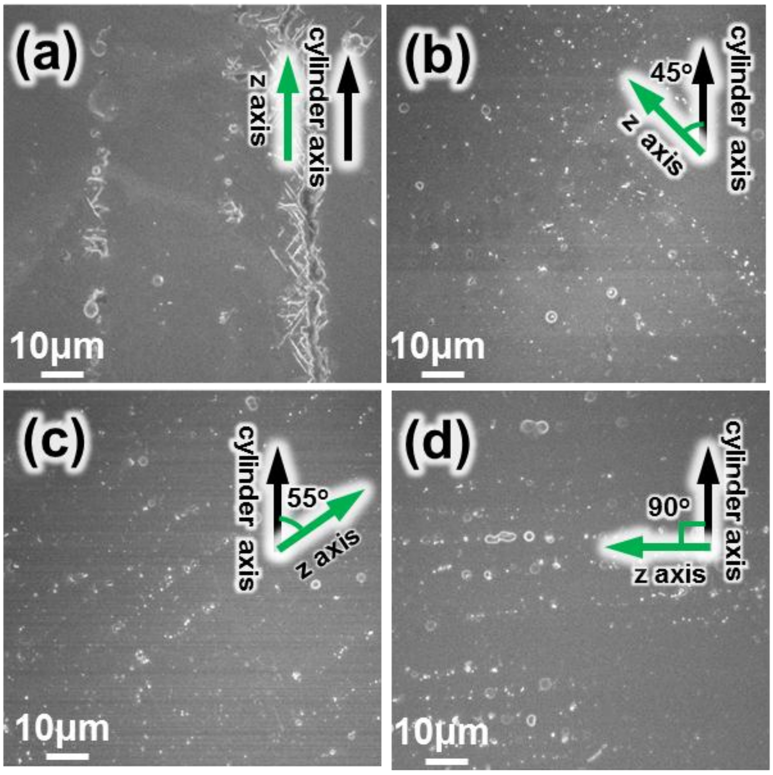

Fig. 4-5. Microstructures on the longitudinal cross-sections of the top parts of samples with solution (980 ℃ for 1 h) and aging treatments. (a) 0˚-sample, (b) 45˚-sample, (c) 55˚-sample, and (d) 90˚-sample.

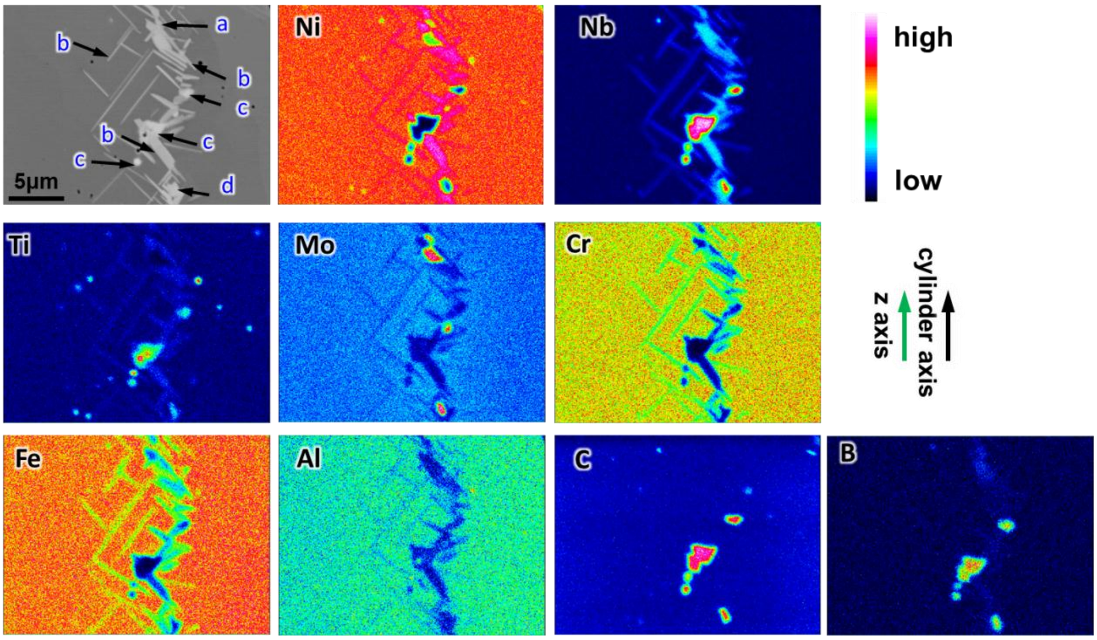

Fig. 4-6. EPMA element maps on the longitudinal cross-section of the top part of 0˚-sample (fabricated by modified condition) with solution treatment at 980 ℃ for 1 h and aging treatments at 720 ℃ for 8 h firstly and 620 ℃ for 8 h secondly.

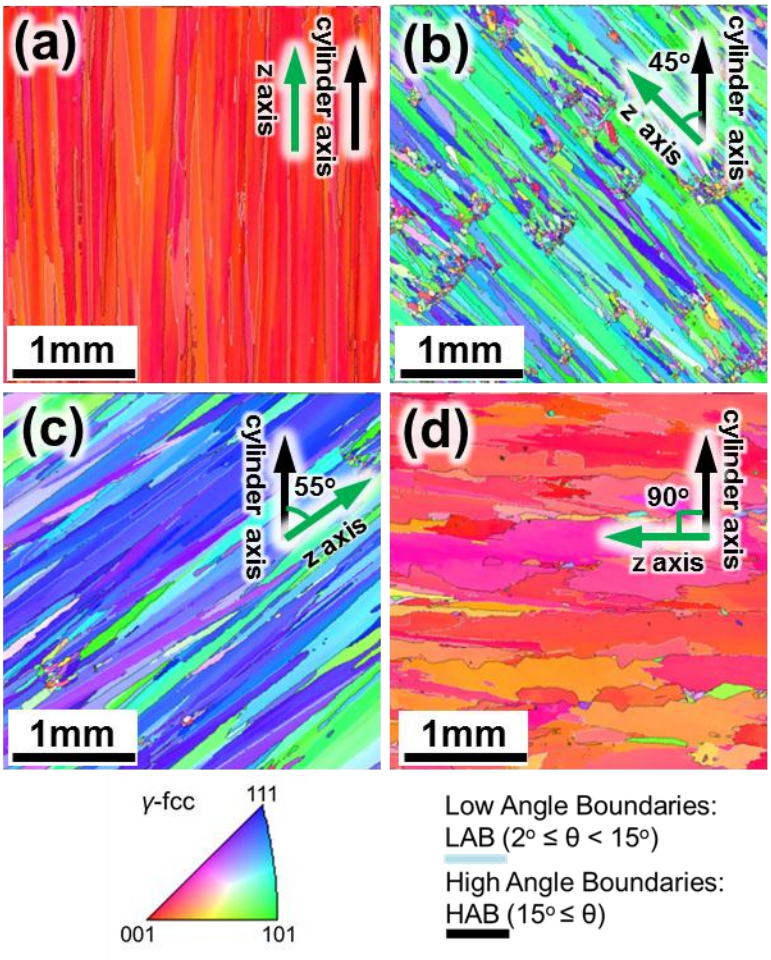

Fig. 4-7. EBSD-IPF maps on the longitudinal cross-sections of the center parts of samples with solution (1045 ℃ for 1 h) and aging treatments. (a) 0˚-sample, (b) 45˚-sample, (c) 55˚-sample, and (d) 90˚-sample.

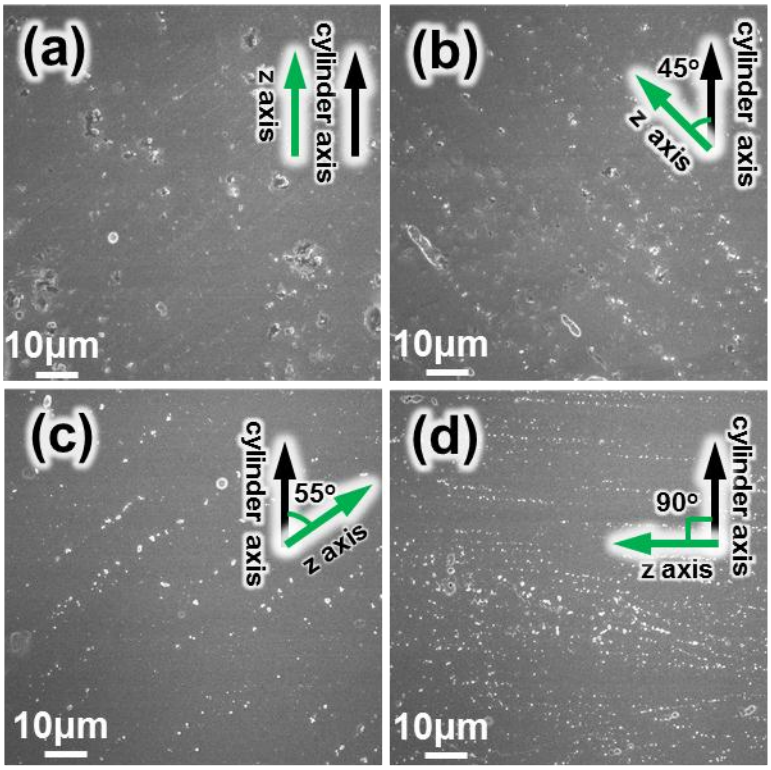

Fig. 4-8. SEM microstructure on the longitudinal cross-sections of the center parts of samples with solution (1045 ℃ for 1 h) and aging treatments. (a) 0˚-sample, (b) 45˚-sample, (c) 55˚-sample, and (d) 90˚-sample.

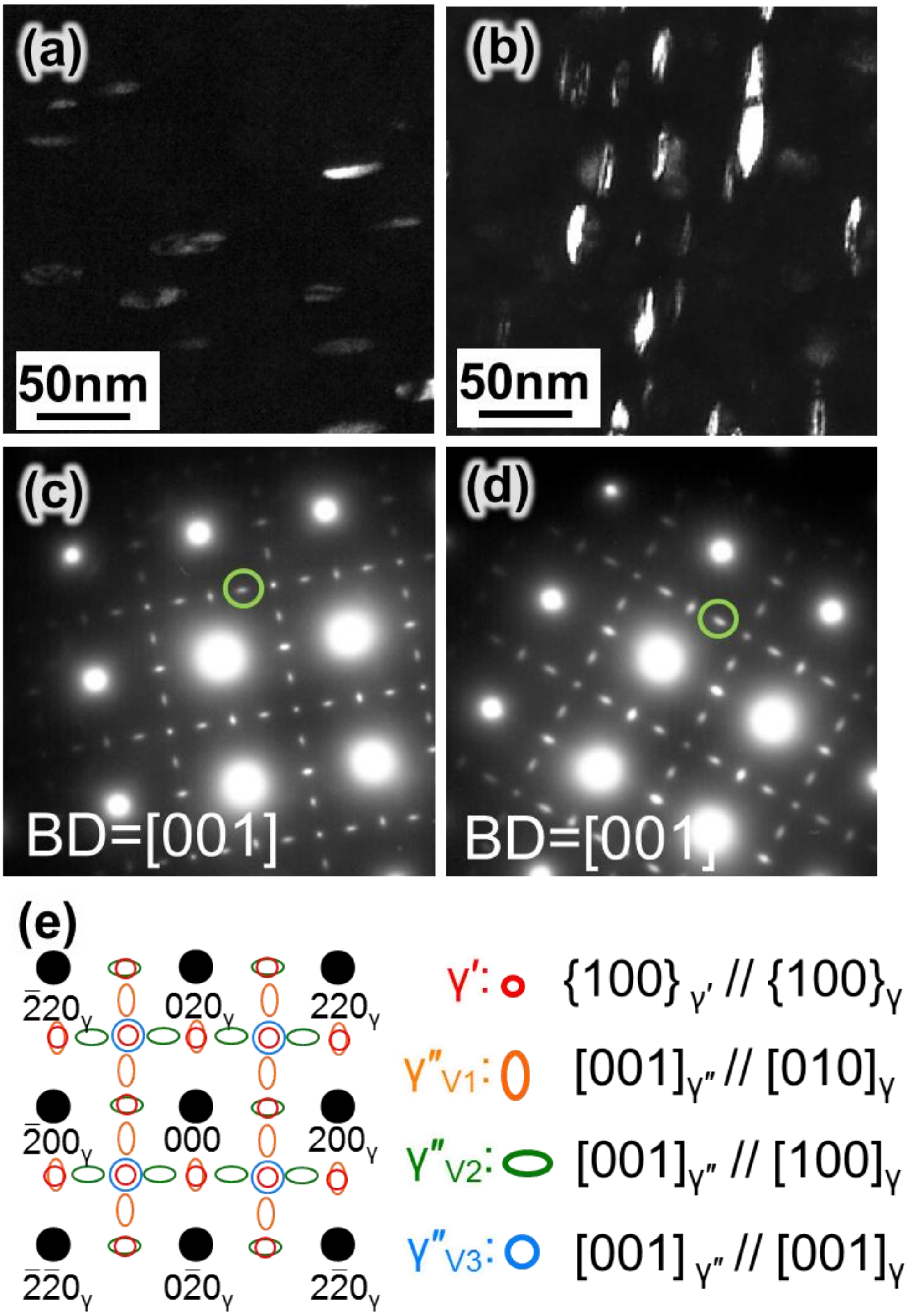

Fig. 4-9. TEM dark field images (DFI) and corresponding selective area diffraction (SAD) patterns on the middle parts of 0˚- and 55˚-samples after solution (1045 ℃ for 1 h) and aging treatments. DFI of (a) 0˚-sample and (b) 55˚-sample, (c,d) corresponding SAD patterns for image (a) and (b), the diffraction spots used to take the DFI are indicated by the green circle. (e) Key to the SAD patterns in (c) and (d).

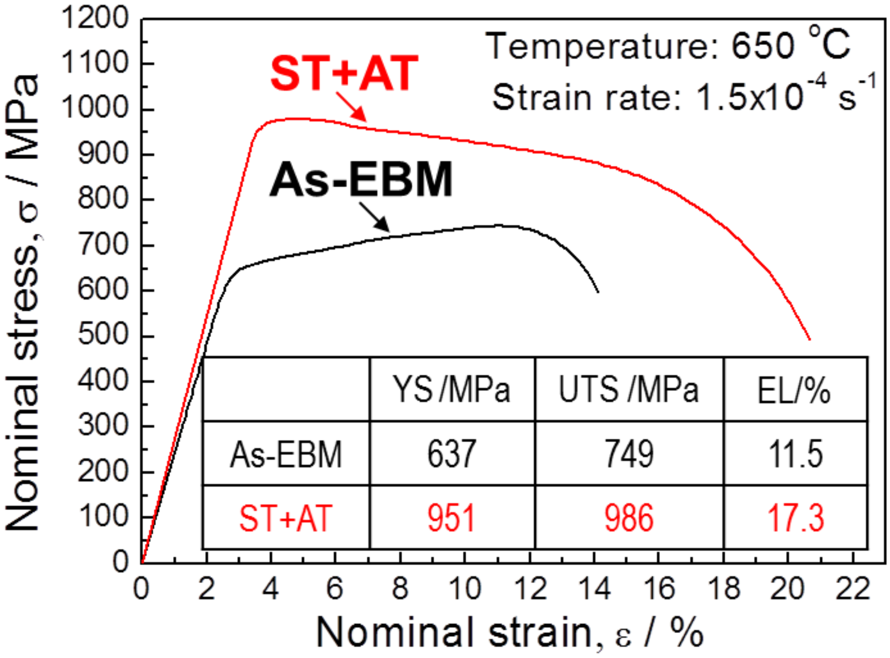

	YS /MPa	UTS /MPa	EL/%
As-EBM	637	749	11.5
ST+AT	951	986	17.3

Fig. 4-10. Stress-strain curves of 0°-sample before and after solution treatment followed by aging treatment tested at 650 ℃ with strain rate of 1.5×10^{-4} s^{-1}.

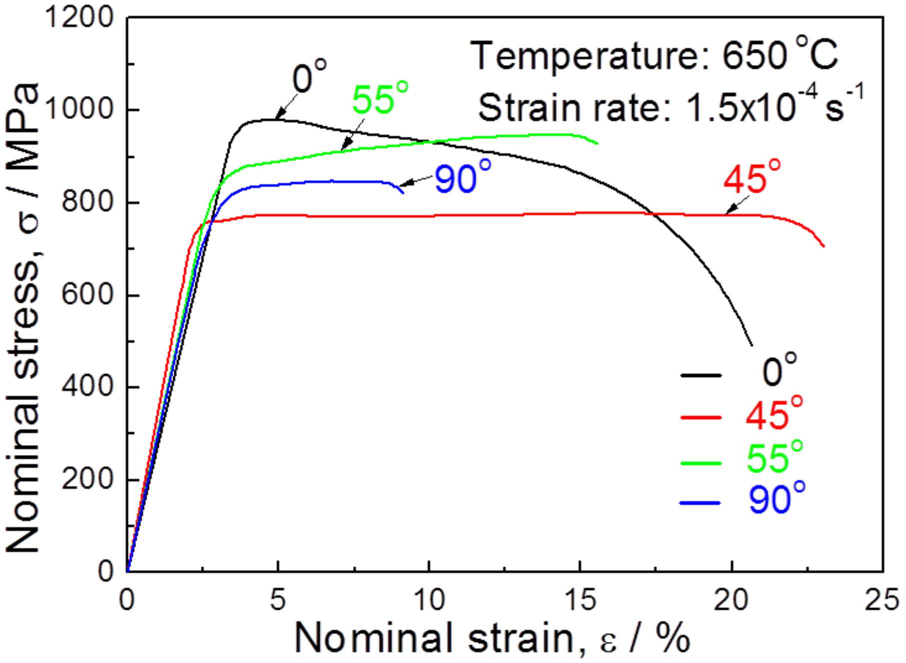

Fig. 4-11. Stress-strain curves of the samples after solution treatment (980 ℃ for 1 h) followed by aging treatment tested at 650 ℃ with strain rate of 1.5×10^{-4} s^{-1}.

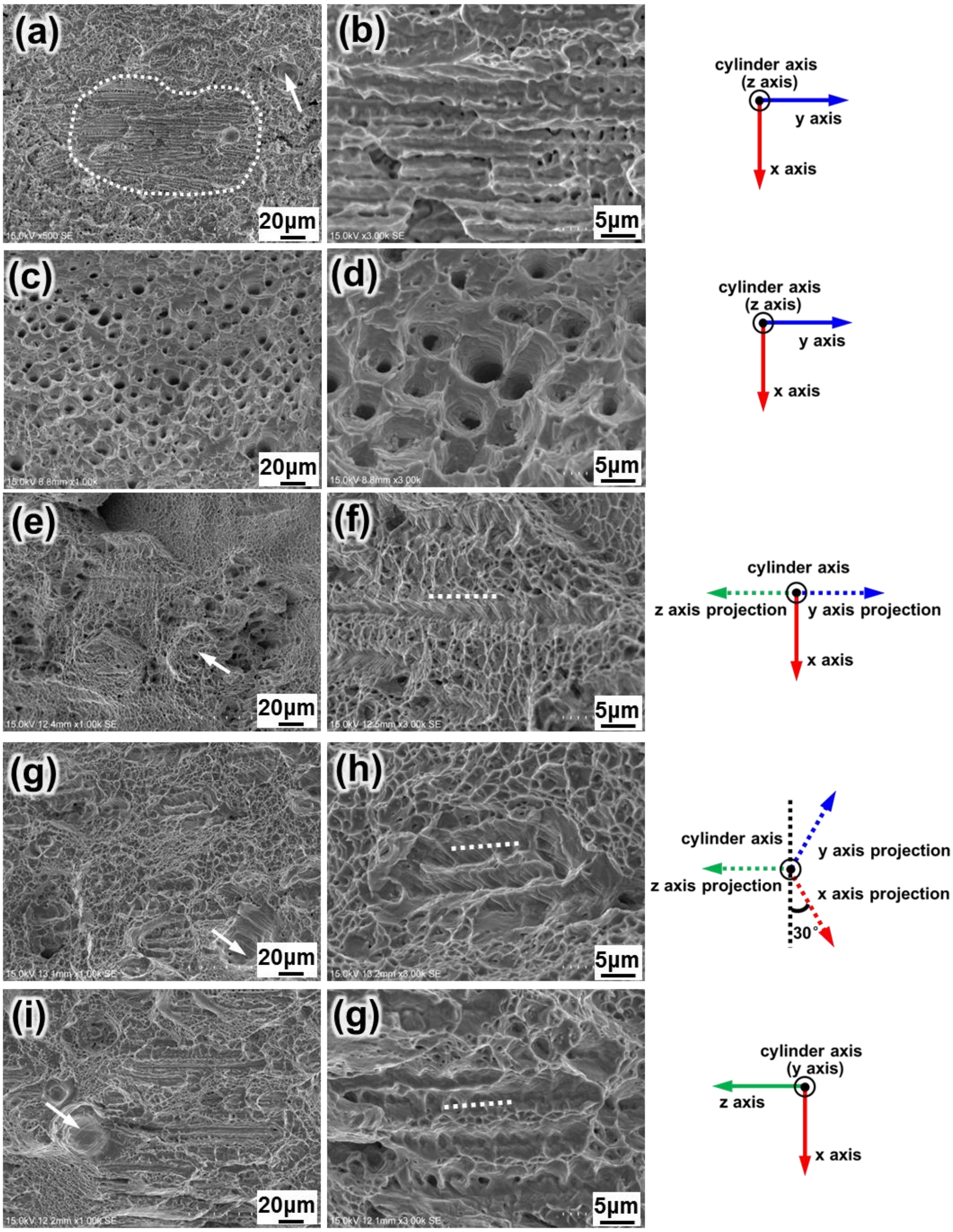

Fig. 4-12. Fracture surface morphology of samples after tensile test: (a, b) 0 °-sample built without modified condition; (c, d) 0 °-sample built with modified condition; (e, f) 45 °-sample; (g, h) 55 °-sample; (i, g) 90 °-sample.

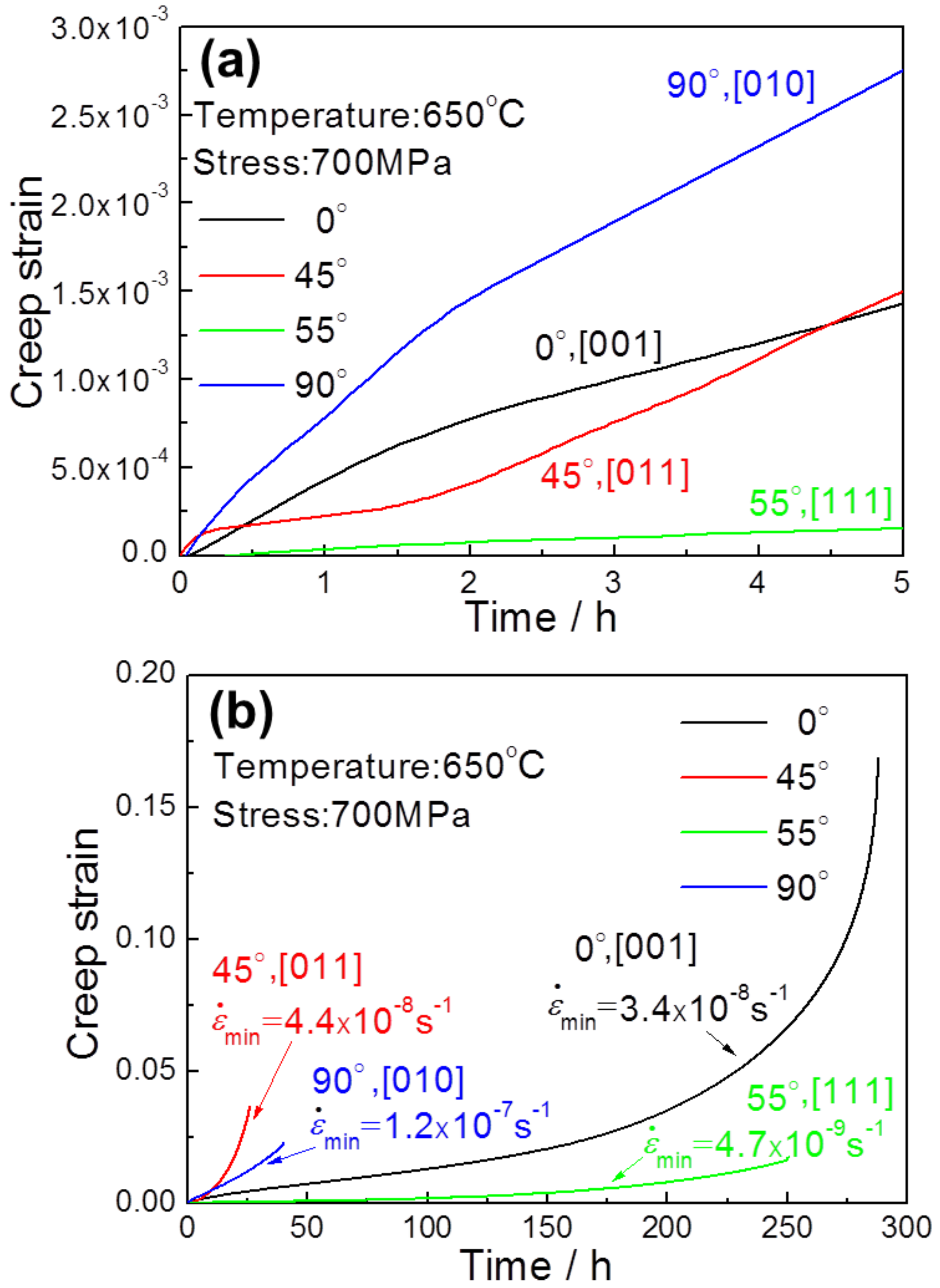

Fig. 4-13. Creep curves of samples with various build directions at 650 ℃ with stress of 700 MPa. (a) Early creep deformation stage, (b) the whole creep deformation stage.

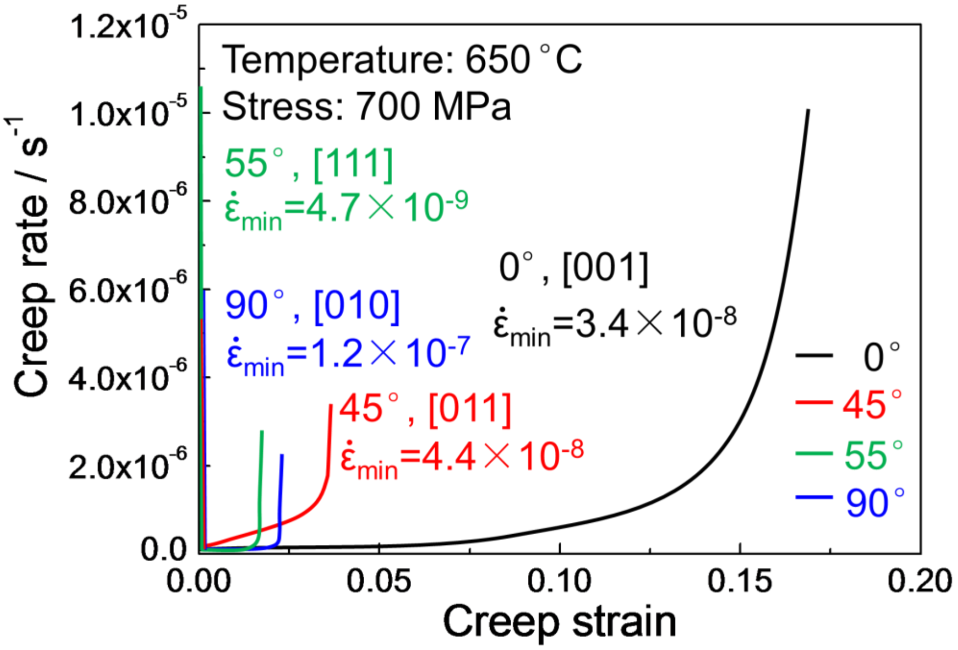

Fig. 4-14. Creep rate variation with creep strain in the samples with various build directions.

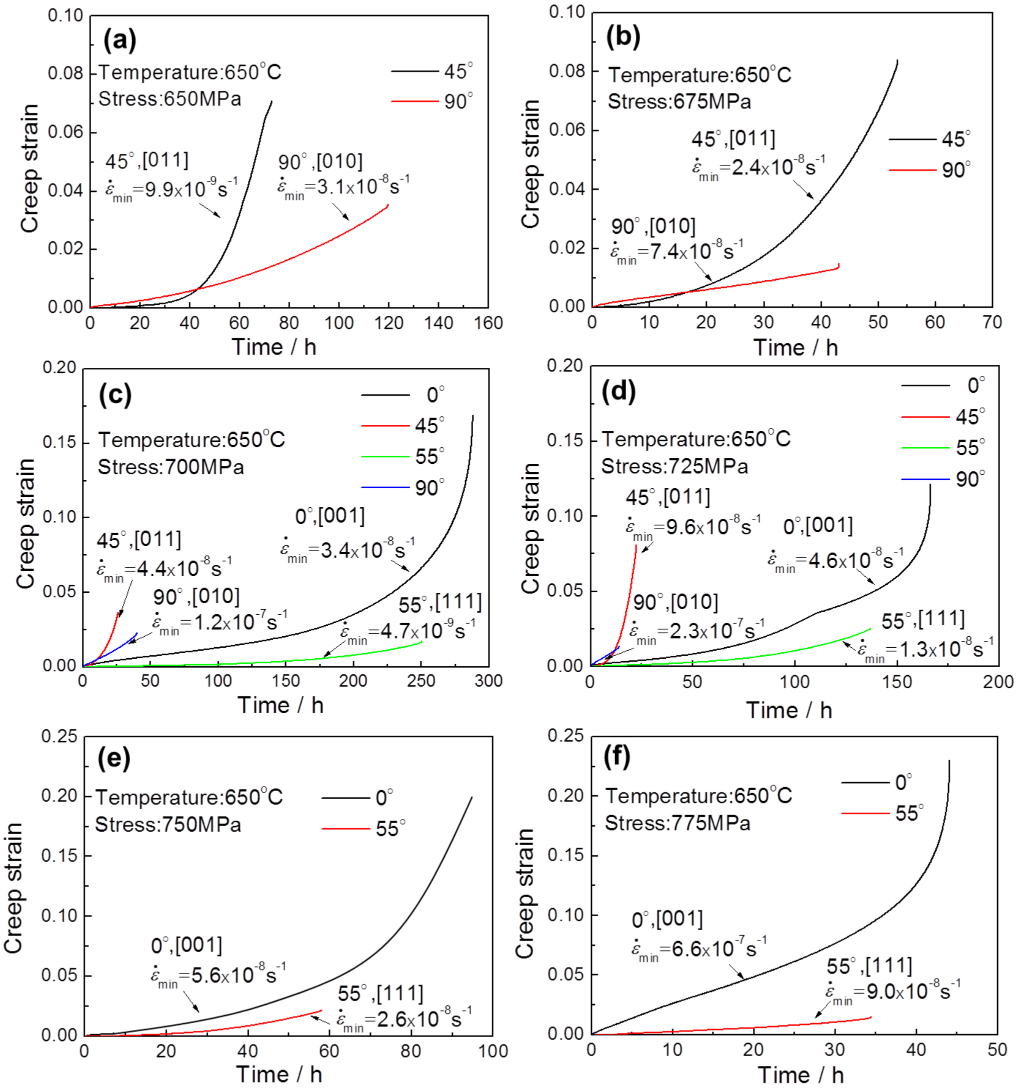

Fig. 4-15. Creep curves of samples with various build directions at 650˚C with different stresses.

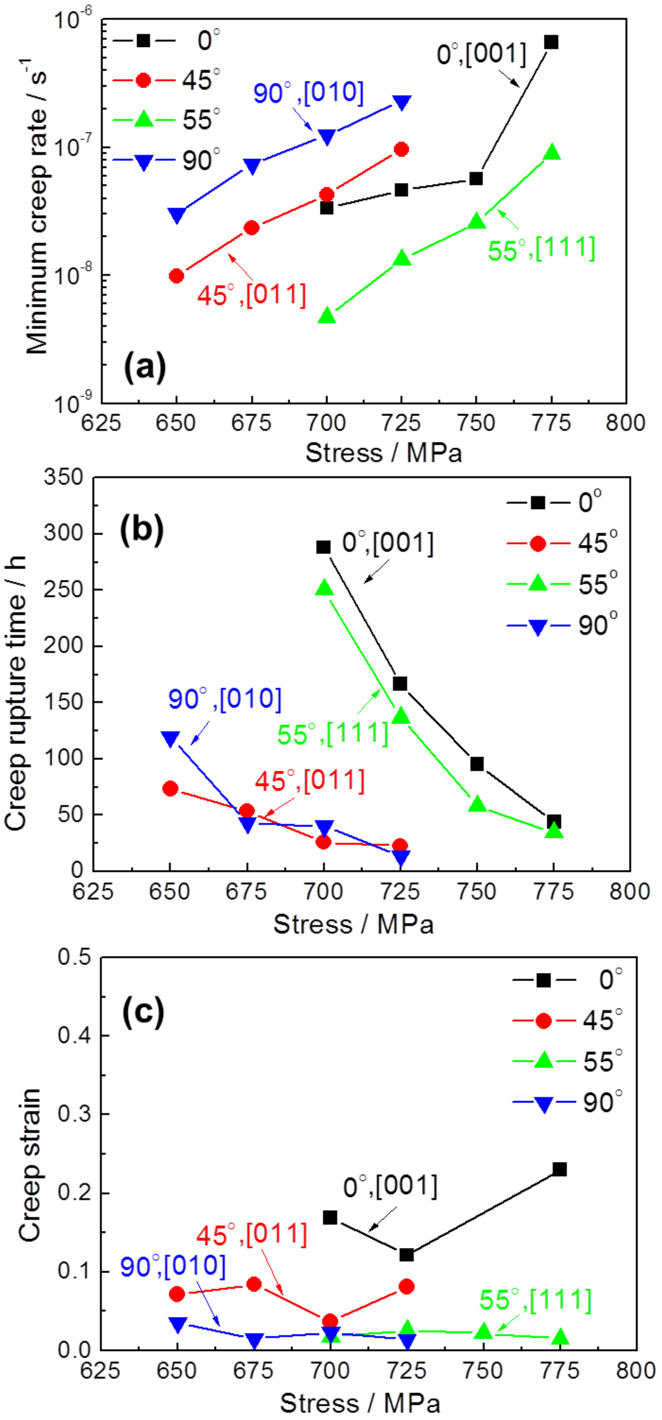

Fig. 4-16. Stress dependence of creep behavior of samples with various build directions at 650˚C.

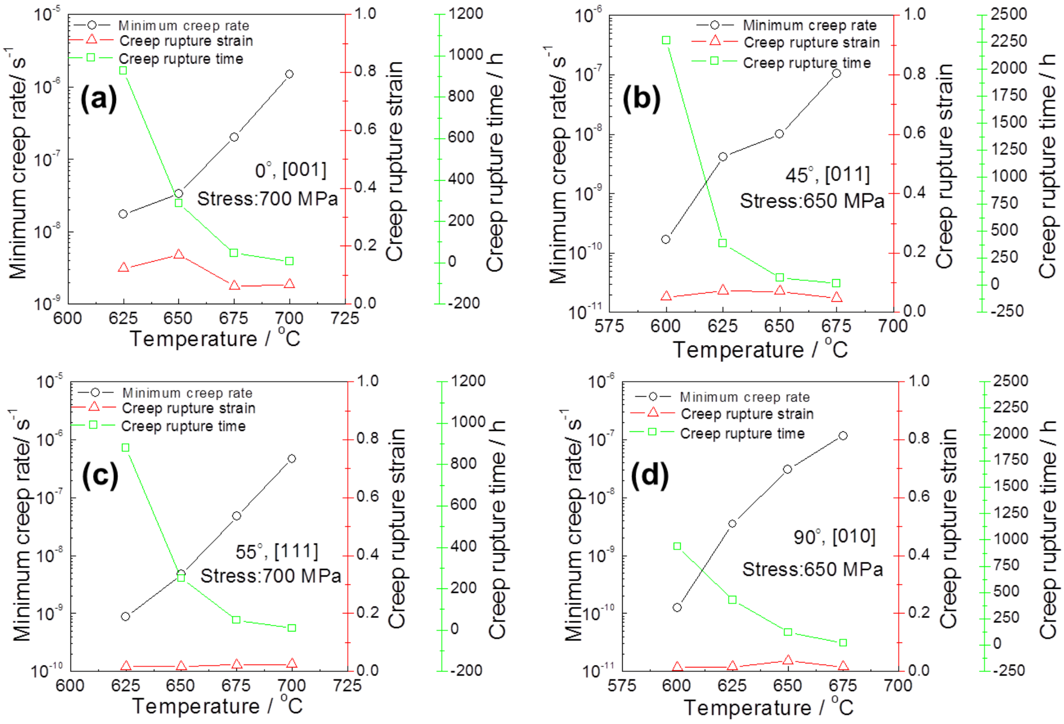

Fig. 4-17. Temperature dependence of creep behavior of samples with various build directions. (a) 0˚-sample, (b) 45˚-sample, (c) 55˚-sample, and (d) 90˚-sample.

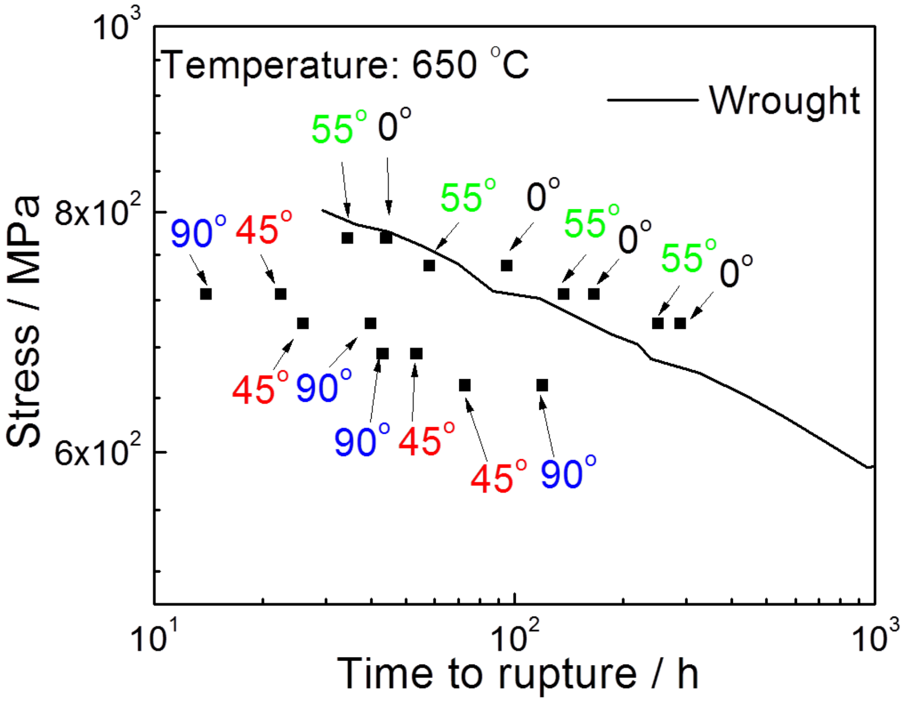

Fig. 4-18. Creep rupture time comparison between EBM-built and wrought Inconel 718 [24].

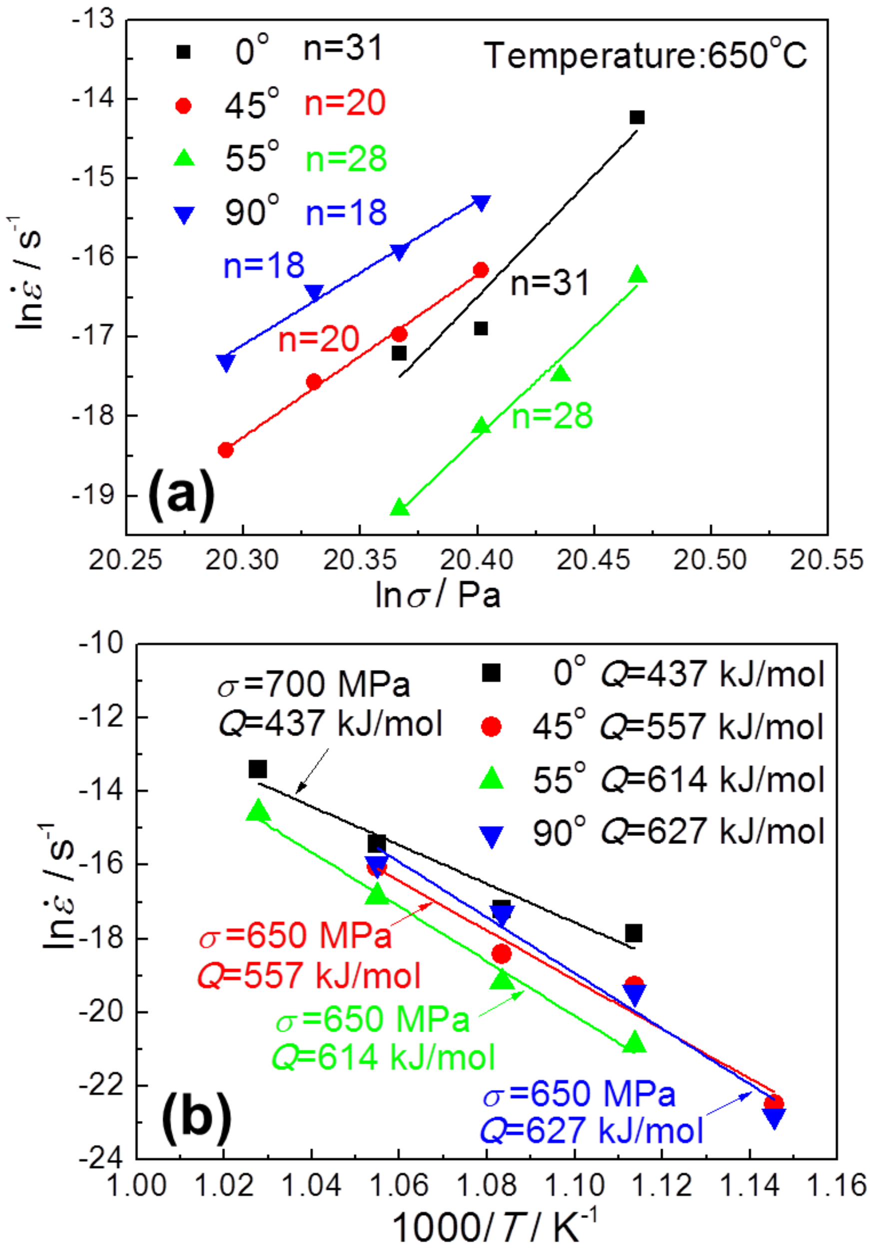

Fig. 4-19. (a) Applied stress and (b) temperature reciprocal dependence of minimum creep rate for the samples with various build directions.

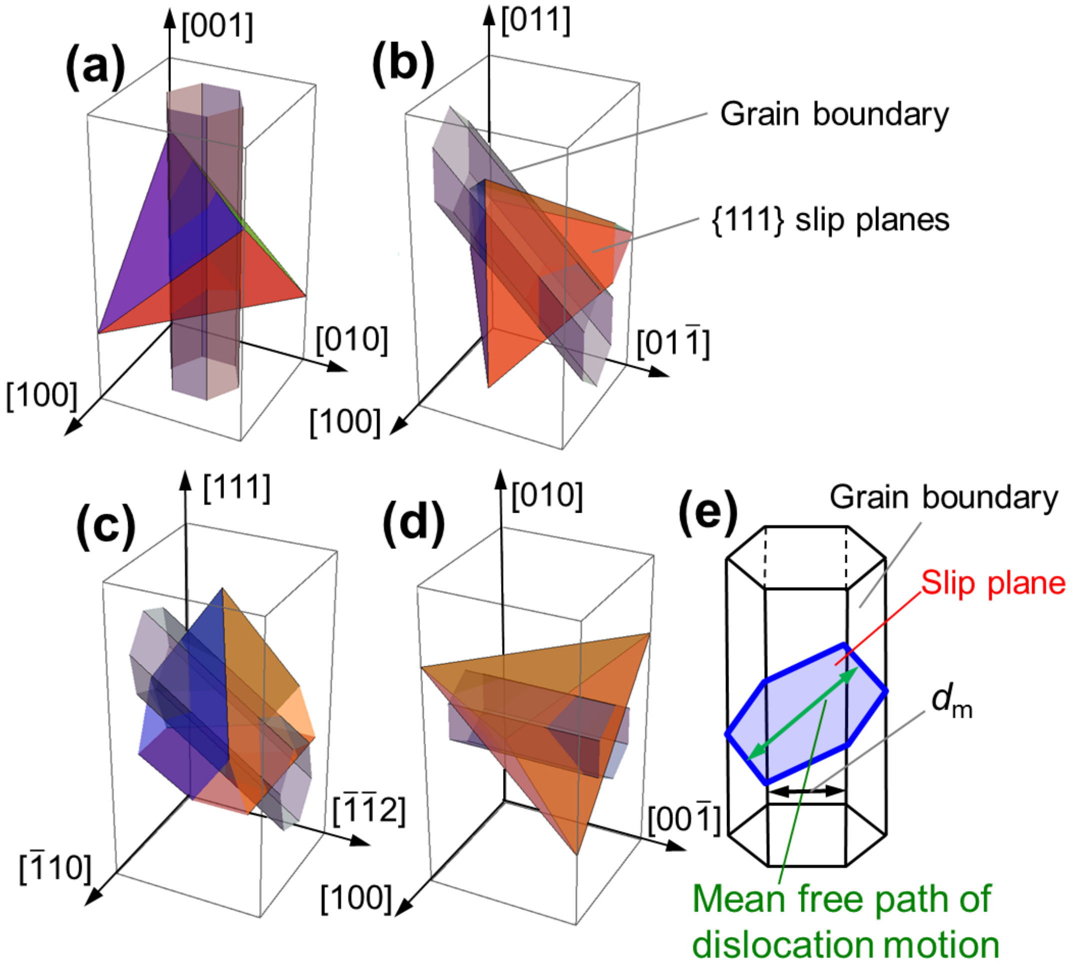

Fig. 4-20. Relationship between columnar grains and {111} slip planes in samples with various build directions. (a) 0˚-sample, (b) 45˚-sample, (c) 55˚-sample, (d) 90˚-sample, and (e) mean free path of dislocation motion on the slip plane.

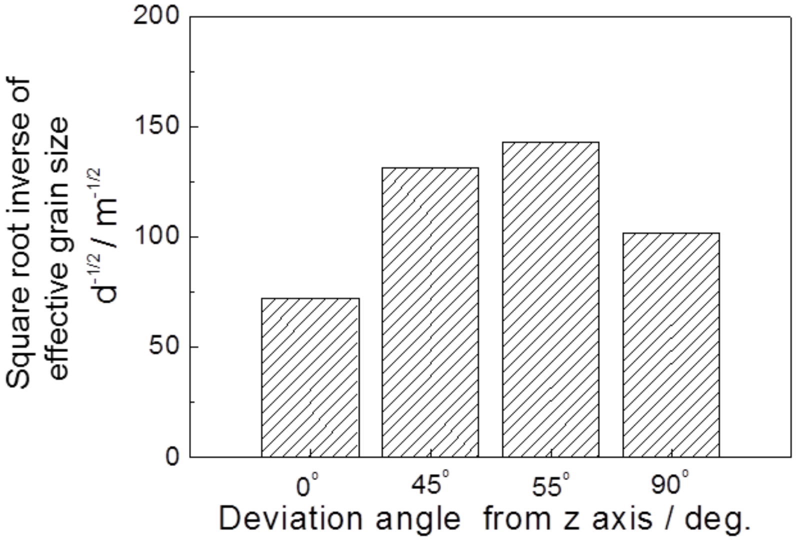

Fig. 4-21. Effect of grain boundary on yield strength in the samples with various build directions.

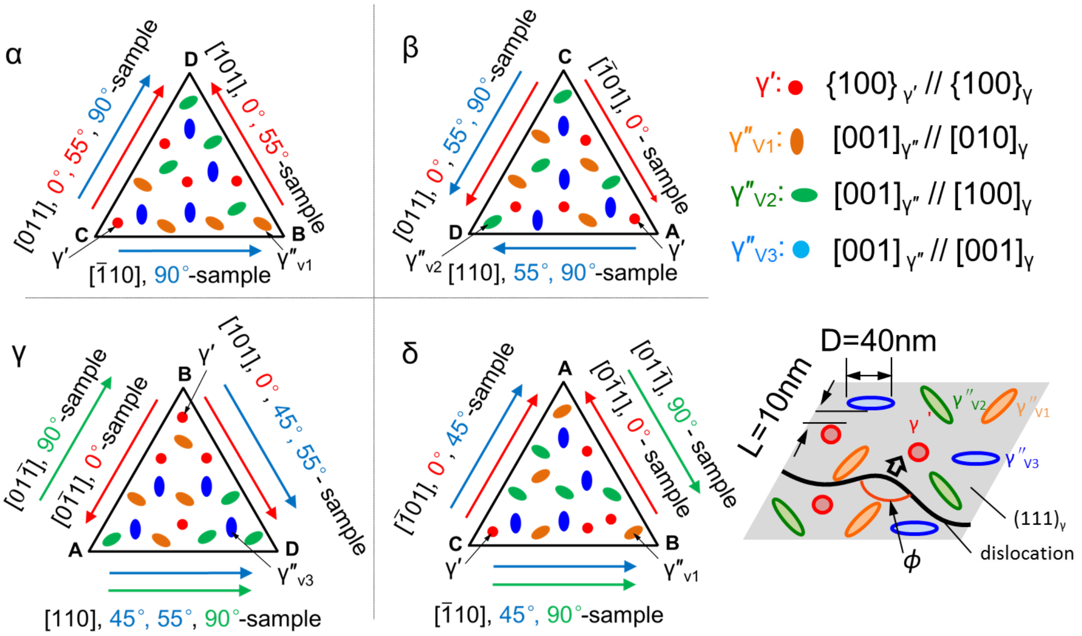

Fig. 4-22. γ' and γ'' arrangement on the four nonparallel {111} slip planes, α-, β-, γ-, and δ-planes of γ matrix. The color arrows correspond to the slip directions of perfect dislocations in 0°-, 45°-, 55°-, and 90°-samples with the same color in built angle.

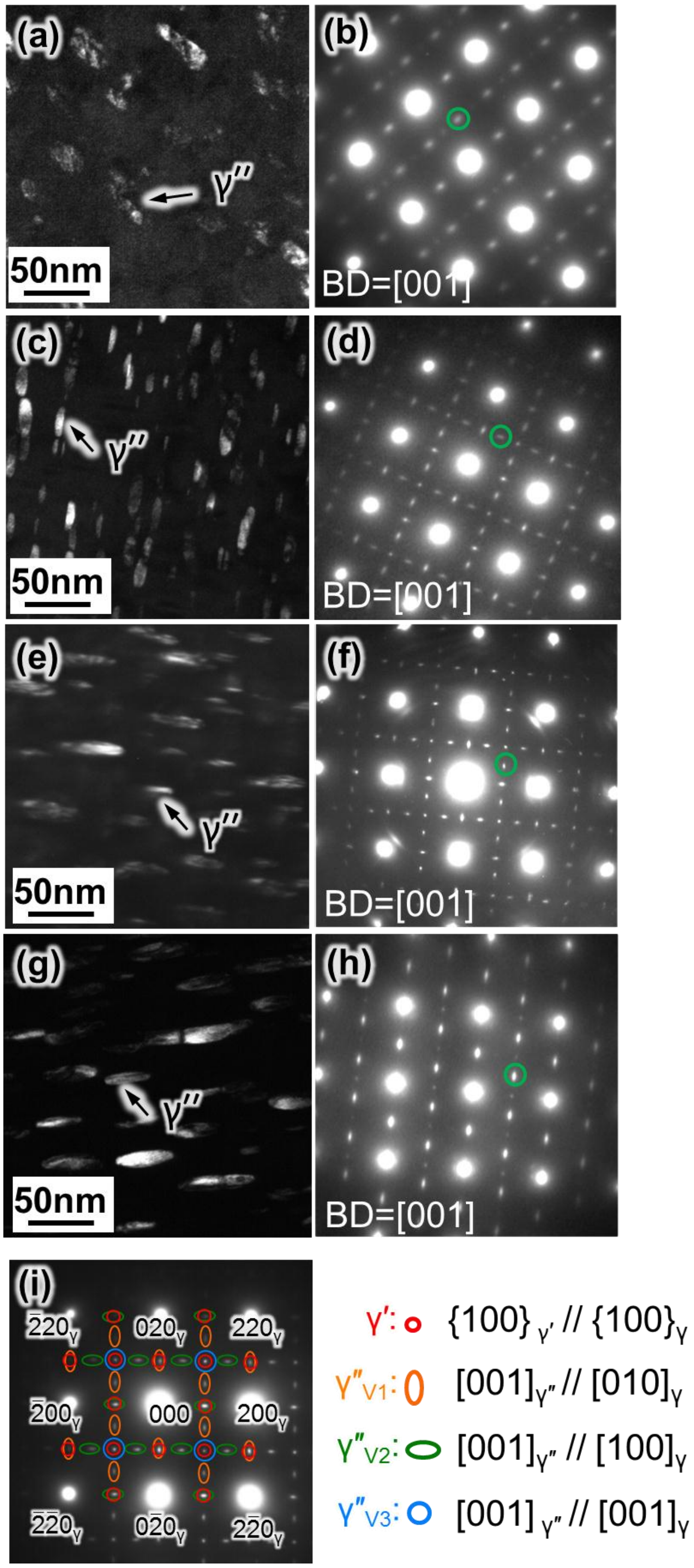

Fig. 4-23.TEM dark field images (DFI) (a,c,e,g) and corresponding selective area diffraction (SAD) patterns (b,d,f,h) of samples after creep test. (a,b) 0˚-sample, (c,d) 45˚-sample, (e,f) 55˚-sample, and (g,h) 90˚-s amle. (i) Key to the SAD patterns. The diffraction spots used to take the DFI are indicated by the green circle. 0˚- and 55˚-samples were crept at 650 ℃ under stress of 775 MPa, while 45˚- and 90˚-samples were crept at 650 ℃ under stress of 725 MPa.

Table 4-1. Mechanical property comparison between EBM-built samples and wrought [15] as well as HIP [16] counterparts at 650˚C.

Sample	0.2%YS (MPa)	UTS (MPa)	Elongation (%)
0 °	793 ±4	809 ±14	1 ± 0.5
0 °-modified	951	986	17.3
45 °	757 ±8	776 ±12	16.2 ±5.5
55 °	843 ±13	951 ±10	11.4 ±2.7
90 °	815 ±27	879 ±27	8.5 ±3.1
Wrought [15]	860-1000	1000-1200	12-19
HIP [16]	1018	1140	3

Table 4-2. Effective slip distance for edge dislocation on the slip plane in the samples with various build directions during tensile test.

Sample	0 °-sample	45 °-sample	55 °-sample	90 °-sample
d_s (μm)	135	41	49	68
d_eff	$\sqrt{2}d_\mathrm{s}$	$\sqrt{2}d_\mathrm{s}$	d_s	$\sqrt{2}d_\mathrm{s}$
d_eff (μm)	191	58	49	96

Table 4-3. Maximum Schmid factors (μ_{max}) for {111}<110> slip system in the samples with various build directions.

Slip planes	Samples			
	0 °	45 °	55 °	90 °
α	0.408	0	0.272	0.408
β	0.408	0	0.272	0.408
γ	0.408	0.408	0.272	0.408
δ	0.408	0.408	0	0.408
All the slip planes	0.408	0.408	0.272	0.408

References

[1] A. Strondl, R. Fischer, G. Frommeyer, and A. Schneider, “Investigations of MX and γ′/γ″ Precipitates in the Nickel-Based Superalloy 718 Produced by Electron Beam Melting,” *Materials Science and Engineering: A*, vol. 480, no. 1–2, pp. 138–147, May 2008.

[2] J. W. Brooks and P. J. Bridges, “Metallurgical Stability of Inconel Alloy 718,” *Superalloys*, vol. 88, pp. 33–42, 1988.

[3] M. Sundararaman, P. Mukhopadhyay, and S. Banerjee, “Precipitation of the δ-Ni3Nb Phase in Two Nickel Base Superalloys,” *Metallurgical Transactions A*, vol. 19, no. 3, pp. 453–465, Mar. 1988.

[4] D. Cai, W. Zhang, P. Nie, W. Liu, and M. Yao, “Dissolution Kinetics of δ phase and Its Influence on the Notch Sensitivity of Inconel 718,” *Materials Characterization*, vol. 58, pp. 220–225, 2007.

[5] A. Oradei-Basile and J. F. Radavich, “A Current TTT Diagram for Wrought alloy 718,” *Superalloys*, pp. 325–335, 1991.

[6] X. Xie, C. Xu, G. Wang, J. Dong, W. Cao, and R. Kennedy, “TTT Diagram of a Newly Developed Nickel-Base Superalloy-Allvac®718Plus^{TM},” in *Superalloys 718,625,706 and Derivatives 2005*, 2005, pp. 193–202.

[7] W. Chen and M. C. Chaturvedi, “The Effect of Grain Boundary Precipitates on the Creep Behavior of Inconel 718,” *Materials Science and Engineering: A*, vol. 183, pp. 81–89, 1994.

[8] A. Strondl, M. Palm, J. Gnauk, and G. Frommeyer, “Microstructure and Mechanical Properties of Nickel Based Superalloy IN718 Produced by Rapid Prototyping with Electron Beam Melting (EBM),” *Materials Science and Technology*, vol. 27, no. 5, pp. 876–883, May 2011.

[9] F. Liu, X. Lin, M. Song, W. Zhao, J. Chen, and W. Huang, “Effect of Intermediate Heat Treatment Temperature on Microstructure and Notch Sensitivity of Laser Solid Formed Inconel 718 Superalloy,” *Journal of Wuhan University of Technology-Mater. Sci. Ed.*, vol. 26, no. 5, pp. 908–913, Nov. 2011.

[10] R. Vincent, “Precipitation around Welds in the Nickel-Base Superalloy, Inconel 718,” *Acta Metall.*, vol. 33, no. 7, pp. 1205–1216, 1985.

[11] C. Radhakrishna and K. P. RAO, “The Formation and Control of Laves Phase in Superalloy 718 welds,” *Journal of Materials Science*, vol. 32, no. 8, pp. 1977–1984, Apr. 1997.

[12] G. D. J. Ram, a. V. Reddy, K. P. Rao, and G. M. Reddy, “Microstructure and Mechanical Properties of Inconel 718 Electron Beam Welds,” *Materials Science and Technology*, vol. 21, no. 10, pp. 1132–1138, Oct. 2005.

[13] P. Gao, K. F. Zhang, B. G. Zhang, S. S Jiang, and B. W. Zhang, “Microstructures and High Temperature Mechanical Properties of Electron Beam Welded Inconel 718 Superalloy Thick Plate,” *Transactions of Nonferrous Metals Society of China*, vol. 21, pp. s315–s322, 2011.

[14] K. N. Amato, S. M. Gaytan, L. E. Murr, E. Martinez, P. W. Shindo, J. Hernandez, S. Collins, and F. Medina, “Microstructures and Mechanical Behavior of Inconel 718 Fabricated by Selective Laser Melting,” *Acta Materialia*, vol. 60, no. 5, pp. 2229–2239, Mar. 2012.

[15] “SAE International, Aerospace Material Specification,AMS5662G.” 1993.

[16] G. A. Rao, M. Kumar, M. Srinivas, and D. S. Sarma, “Effect of Standard Heat Treatment on the Microstructure and Mechanical Properties of Hot Isostatically Pressed Superalloy Inconel 718,” *Materials Science and Engineering: A*, vol. 355, no. 1–2, pp. 114–125, Aug. 2003.

[17] S. Zhang, D. Wang, J. Zhang, and L. Lou, “Orientation Dependence of Stress Rupture Properties of a Ni-based Single Crystal Superalloy at 760 °C,” *Journal of Materials Science & Technology*, vol. 28, no. 3, pp. 229–233, Mar. 2012.

[18] T. Sugui, Z. Shu, L. Fushun, L. Anan, and L. Jingjing, “Microstructure Evolution and Analysis of a Single Crystal Nickel-Based Superalloy during Compressive Creep,” *Materials Science and Engineering: A*, vol. 528, no. 15, pp. 4988–4993, Jun. 2011.

[19] S. Zhang, J. Zhang, and L. Lou, “Anisotropie Creep Rupture Properties of a Nickel-base Single Crystal Superalloy at High Temperature,” *Journal of Materials Science & Technology*, vol. 27, no. 2, pp. 107–112, Feb. 2011.

[20] V. Sass, U. Glatzel, and M. Feller-Kniepmeier, “Anisotropic Creep Properties of the Nickel-Base Superalloy CMSX-4,” *Acta Materialia*, vol. 44, no. 5, pp. 1967–1977, May 1996.

[21] V. Sass and M. Feller-Kniepmeier, “Orientation Dependence of Dislocation Structures and Deformation Mechanisms in Creep Deformed CMSX-4 Single Crystals,” *Materials Science and Engineering: A*, vol. 245, no. 1, pp. 19–28, Apr. 1998.

[22] R. W. Swindeman and M. J. Swindeman, “A Comparison of Creep Models for Nickel Base Alloys for Advanced Energy Systems,” *International Journal of Pressure Vessels and Piping*, vol. 85, pp. 72–79, 2008.

[23] D. C. Dunand, B. Q. Han, and A. M. Jansen, “Monkman-Grant Analysis of Creep Fracture in Dispersion-Strengthened and Particulate-Reinforced Aluminum,” *Metallurgical and Materials Transactions A*, vol. 30, no. 13, pp. 829–838, Mar. 1999.

[24] C. R. Brinkman, M. K. Booker, and J. L. Ding, “Creep and Creep-Rupture Behavior of Alloy 718,” Jan. 1991.

[25] Y. Han and M. C. Chaturvedi, “Steady State Creep Deformation of Superalloy Inconel 718,” *Materials Science and Engineering*, vol. 89, pp. 25–33, 1987.

[26] T. Sugahara, K. Martinolli, D. A. P. Reis, C. Moura Neto, A. A. Couto, F. Piorino Neto, and M. J. R. Barboza, “Creep Behavior of the Inconel 718 Superalloy,” *Defect and diffusion forum*, vol. 326–328, pp. 509–514, 2012.

[27] K. Hirano, R. P. Agarwala, B. L. Averbach, and M. Cohen, “Diffusion in Cobalt-Nickel Alloys,” *Journal of Applied Physics*, vol. 33, no. 10, p. 3049, Jun. 1962.

[28] N. Chandra, “Constitutive Behavior of Superplastic Materials,” *International Journal of Non-Linear Mechanics*, vol. 37, no. 3, pp. 461–484, Apr. 2002.

[29] M. C. Chaturvedi and Y. Han, “Strengthening Mechanisms in Inconel 718 Superalloy,” *Metal Science*, vol. 17, no. 3, pp. 145–149, Mar. 1983.

[30] M.Sundararaman, P.Mukhopadhyay, and S.Banerjee, “Deformation Behavior of γ'' Strengthened Inconel 718,” *Acta Metall.*, vol. 36, no. 4, pp. 847–864, 1988.

[31] J. M. Oblak, D. F. Paulonis, and D. S. Duvall, “Coherency Strengthening in Ni Base Alloys Hardened by $D0_{22}$ Precipitates,” *Metallurgical transactions* , vol. 5, no. January, 1974.

[32] R. Cozar and A. Pineau, “Morphology of $\gamma'$and γ'' Precipitates and Thermal Stability of Inconel 718 Type Alloys,” *Metallurgical transactions*, vol. 4, no. January, pp. 47–59, 1973.

Chapter 5

5. Microstructure of Co–Cr–Mo alloy with various build directions

5.1 Introduction

Cobalt-based alloys have been extensively used as materials for valve seats in nuclear power plants, aerospace fuel nozzles and engine vanes, as well as orthopedic and dental implant materials because of their high strength at high temperature, good corrosion resistance, excellent wear resistance, and biocompatibility [1-5]. Casting and hot forging process are usually used to produce cobalt-based alloy component. However, components fabricated by casting process cannot satisfy strength requirement and complex shapes are difficult to be obtained by forging. Therefore, it is difficult to fabricate cobalt-based alloy components with both high strength and complex shape by conventional process.

Recently, electron beam melting (EBM) has become an established additive manufacturing technology to produce any three-dimensional (3D) complex structures from precursor powders of advanced metal alloys. When EBM was applied to Co–26Cr–6Mo–0.2C (CCM) alloys [6,7], $M_{23}C_6$ carbides were found to align along the build-direction (z axis) within grains owing to unidirectional heat flow. The ultimate tensile strength (*UTS*) of as-EBM-built sample was higher than that of as-cast or wrought ASTM F75 CCM alloys [15]. However, the microstructures of the CCM alloys fabricated by EBM have been observed only by optical microscopy to examine the carbide array and by transmission electron microscopy (TEM) for relatively local, lattice-defect structures. The phase constitution and grain structures, including the crystal orientation distribution (i.e., texture), should also be examined in order to understand the relationship between the microstructural and mechanical properties.

γ-fcc is a metastable phase at high temperature, which can even exist at low temperatures by adding nitrogen [8-10] or carbon [11], while *ε*-hcp is the stable phase in equilibrium. Therefore a variety of microstructure can be formed depending on the thermal history. Since <001> is known to be the preferential growth direction for fcc based alloy [12], and unidirectional heat extraction exists in EBM, the single crystal-like microstructure with metastable *γ*-fcc is anticipated to form in the EBM-built samples. Therefore, build direction has an effect on the microstructure of CCM alloy fabricated by EBM.

The purpose in this chapter is to investigate the effect of the build direction on the microstructure of CCM alloy fabricated EBM. In addition, the constituent phase variation along the build height will be investigated because the post-built heating process may change the constituent phase.

5.2 Experimental

The samples were fabricated on an Arcam A2 EBM system (Arcam AB, Mölndal, Sweden). The powder used in the experiment consisted of spherical particles and attached small satellite particles, with an average particle size of 64 μm, as show in Fig. 5-1. The chemical composition of the Co–28Cr–6Mo–0.23C–0.17N alloy powder is shown in Table 5-1, which was within the range of ASTM F75 standards. The carbon and nitrogen contents are relatively high within the range of the standard. Higher carbon and nitrogen contents are known to provide a large amount of precipitates and stabilize γ-phase. Carbon can stabilize the γ-fcc phase by decreasing the Gibbs energy of *γ*-fcc with respect to that of *ε*-hcp [11], and nitrogen increases the energy barrier for the tranformation from *γ*-fcc to *ε*-hcp via Cr-N cluster formation, respectively [8]. The cylindrical axes deviating from the build-direction (*z*- axis) by 0°, 45°, 55°, and 90°, as shown in Fig. 3-2, were chosen to orient the cylindrical axes to the [001], [110], [111], and [100] directions, respectively. Hereafter, the Co–28Cr–6Mo–0.23C–0.17N alloy rods fabricated in the directions of 0°, 45°, 55°, and 90° from the *z* axis are designated as the 0°-sample, 45°-sample, and so on. The rods were

15 mm in the diameter, and 85 mm in the height. The primary parameters to build each orientation rods during the EBM process were listed in Table 5-2. The scanning direction of the electron beam will rotated by 90 ° on each neighboring layer to homogenize the temperature in the build region, as shown Fig.1-10(b).

A series of isothermal heat treatment from 650 ˚C to 850 ˚C were carried out on the γ-fcc single phase specimens taken from the last built part of the as-EBM-built rod, to investigate the phase transformation from γ-fcc single phase to ε-hcp phase. One of the as-EBM-built rods 0 °-sample was cut into 13 portions along the build height with 6.6 mm intervals as show in Fig. 3-3, the transverse and longitudinal cross-section microstructures of each portion were investigated by electron backscatter diffraction (EBSD). The microstructure on the top part (67 mm from the bottom) of rod for each orientation was investigated by scanning electron microscopy (SEM), EBSD, and X-ray diffraction (XRD) on the longitudinal cross section consisting of the cylinder and z axes.

5.3 Results

5.3.1 Microstructures in different build direction samples

Fig. 5-2 shows SEM microstructures on the longitudinal cross-section of the top parts of the as-EBM-built samples. It can be observed that precipitates aligned along the build-direction were observed in all as-EBM-built samples. The average interval between the arrays of precipitates was approximately 3 μm. The XRD profiles (Fig. 5-3) and the phase diagram calculated by Thermocalc software (Fig. 5-4) suggested that the aligned precipitate mainly consisted of $M_{23}C_6$, Through further elemental surface scan analysis with EPMA, as shown in Fig. 5-5, M was identified as Cr, Mo, or Si in $M_{23}C_6$. The array of $M_{23}C_6$ along the build-direction was attributed to the unidirectional heat extraction in the build-direction. The lamellar structure of the M_2N precipitates and the ε-hcp phase originated from the eutectoid transformation ($\gamma \longrightarrow \varepsilon + M_2N$) [13].

Fig. 5-6 shows the EBSD analysis results of top part of as-EBM-built samples. The high-angle and low-angle grain boundaries are indicated by black and light blue lines, respectively, on the inverse pole figure (IPF) maps and phase maps. From Fig. 5-6 it can be seen that the boundaries basically aligned along *z* axis. The IPF maps showed the orientations in the direction of the cylindrical axis, it indicates that that the preferential orientations of the *γ* phase in the as-EBM-built samples along the cylindrical axial directions were near [001], [110], [111], and [100] in the 0°-, 45°-, 55°-, and 90°-samples, respectively, which are believed to be a result of oriented crystal growth of the *γ*-fcc phase along the <001> direction.

5.3.2 Constituent phase variation along the build height

Fig. 5-7 shows the EBSD results of longitudinal cross-section microstructures at different build heights of as-EBM-built 0°-sample rod. The heights (*h*s) of the center positions of the observed areas were about 79 mm (Fig. 5-7(a,b)), 32 mm (Fig. 5-7(c,d)) and 5 mm (Fig. 5-7(e,f)) from the bottom, and hereafter the positions are referred to as "top", "center-bottom", and "bottom", respectively. Low angle boundaries (LAB) ($2° \leq \theta < 15°$) and high angle boundaries (HAB) ($15° \leq \theta$) are shown on the phase maps and inverse pole figure (IPF) maps. The orientation shown in the IPF map is in the build direction (cylindrical axis). In the top part of the rod (h = 79 mm), as shown in Fig. 5-7(a), there were only *γ*-fcc columnar grains, and most of the grain boundaries were LAB. The grain orientations of center-bottom part were near <001> (Fig. 5-7(b)), which is regarded as a result of oriented crystal growth of *γ*-fcc along the <001> direction [12]. In the center-bottom (h = 32 mm), the *ε*-hcp equiaxed grains appeared and embedded in the *γ*-fcc columnar grains as shown in Fig. 5-7(c). Fig. 5-7(d) shows the orientations of the equiaxed grains tended to be random, while those of the columnar grains were still oriented to <001>. In the bottom (h = 5 mm), *γ*-fcc columnar grains nearly have already transformed into single *ε*-hcp equiaxed grains during post-melting process, as shown in Fig. 5-7(e). The color of most of the grains shown in IPF map (Fig. 5-7(f)) were close to purple, indicating there was a weak texture near $(20\bar{2}3)$ plane normal in the build direction.

Fig. 5-8 shows the phase map and pole figure on the transverse cross section of bottom and top part of the as-EBM-built 0°-sample. Normal direction (ND) corresponded to cylindrical axis, and reference direction (RD) and transverse direction (TD) corresponded to x- and y-direction of electron beam scanning in the EBM process, respectively. By comparing the position of (0001) plane (Fig. 5-8(b)) of ε-hcp phase in the bottom part (early-built part) (Fig. 5-8(a)) and that of {111} plane (Fig. 5-8(d)) of γ-fcc phase in the top part (late stage of EBM process) (Fig. 5-8(c)), the crystal orientation relationship between ε-hcp and γ-fcc during the phase transformation in the EBM process can be known. The peak position of (0001) pole figure (Fig. 5-8(b)) of ε-hcp phase in the bottom part presented as a ring-shaped band, which shows that (0001) plane normal (i.e. [0001] direction) was deviated from ND (i.e. the cylindrical axis which used to be oriented to [001] of γ phase before phase transformation) by proximately 55°. However, the (111) pole figure (Fig. 5-8(d)) of γ-fcc exhibited four distinct peaks. The peak positions of the (111) pole figure of γ-fcc in the top (Fig. 5-8 (d)) are mostly included in the ring-shaped band of (0001) pole figure of ε-phase in the bottom (Fig. 5-8(b)). This suggests that Shoji–Nishiyama (S-N) relationship was held with a considerably high probability in the phase transformation during the EBM process. This is probably because the isothermal martensitic transformation took place to hold the S-N relationship [11,14].

Fig. 5-9 shows γ phase fraction variation along build height of as-EBM-built 0°-sample rod. The γ phase fraction increased sharply from 0 in the bottom part (early-built part) and kept constant (near 100%) in the top part (last-built part). The single γ-fcc phase was approximately 40 mm from the top surface. This result suggests that even though metastable γ-fcc phase can be kept in a wide range of build height by large addition of carbon and nitrogen, which are thought to be γ-fcc stable element [8-11], the phase transformation to ε-hcp phase is inevitable in objects with high build height because of the long post-melt process, which is similar to an aging heat treatment.

5.4 Discussion

5.4.1 Effect of phase transformation during EBM on microstructure

There are two kinds of phase transformation from metastable γ-fcc phase to stable ε-hcp phase, i.e. isothermal martensitic transformation and diffusive transformation. The former one holds S-N orientation relationship ($(111)_\gamma$ // $(0001)_\varepsilon$; $[10\bar{1}]_\gamma$ // $[11\bar{2}0]_\varepsilon$) during phase transformation, while the latter one has no orientation relationship. In the research of isothermal transformation of Co–29Cr–6Mo alloy without addition of carbon or nitrogen by Kurosu et al. [11], isothermal martensitic transformation occurred at 700 ˚C or below, while massive transformation would occur at 900 ˚C, in which ε-hcp was randomly oriented. The two kinds of phase transformation are thought to compete with each other at temperatures between 700 ˚C and 900 ˚C. During EBM process, the local thermal history after local solidification varies depending on various factors including preheating temperature, electron beam power, electron beam size, selective melting area, size and shape of built object, and the position within the object, which determines the local cooling rate. Therefore, both isothermal martensitic transformation and diffusive transformation can occur during post-melting process depending on the position. Fig. 5-10 shows the temperature variation beneath the starting plate during the EBM process in the present study. The temperature variation corresponds to the building process consisting of (i) building bottom support part (80 mm), (ii) building object part (85 mm), (iii) and cooling after completion of the total build object. The building process started when the temperature of the starting plate reached to 750 ˚C (i.e. pre-set preheating temperature for the new raked powder), which is indicated by (A). The temperature decreased rapidly soon after the initiation of the selective melting for the support part (B), then it increased gradually at the following repeating preheating and melting for the newly raked layer (C). As the building layer became far from the starting plate (D), the temperature decreased again until the completion of the build part because of the increased heat loss from heat source to the early-built part. Supposed that each position of lower part of the built rod went through similar thermal history, the temperature of the bottom part of the rod could be estimated to be in the range of 600–700˚C during the building process for about 33 h. Such temperatures allow the isothermal martensitic transformation to occur in the bottom part during the post-melting period of the EBM process. Therefore, the weak texture of the ε-hcp phase in the bottom part of as-EBM-built rod is regarded as a result of the isothermal martensitic transformation. With increasing the build height, heat current toward the bottom plate is retarded and the latter-built part (far from bottom of the rod) will be held higher temperature than the earlier-built part (near bottom of the rod) because of the longer distance for the heat conduction through the earlier-built part. Hence, the post-build heating temperature at the latter-built part tends to become more preferable for the diffusive transformation. As a result, the orientation of transformed ε-hcp phase in the latter-built part (far from bottom) tends to become random. In the highest part of the rod, the post-melting period is too short for the transformation to take place, and the γ-phases are maintained. The above discussion can explain the reason for the formation of different orientation distribution of ε-hcp grains along the build height in the as-EBM-build rod.

To examine the assumption about the phase transformation temperature during the EBM process, isothermal phase transformation for the γ-single phase taken near the last-built part was investigated. Fig. 5-11 shows Temperature-Time-Transformation curves of ε-hcp phase transformed from γ-single during isothermal heat treatment. Isothermal phase transformation initiates after 48 h at 650 ˚C, but initiates after 7 h at 700 ˚C. Compared with the initial time of phase transformation during isothermal phase transformation, the initial time of phase transformation during EBM process is 16.4 h, which was estimated from the post-build heating time at the lowest position within the region where γ-single phase was maintained in the as-EBM-built sample. This means the initial temperature for phase transformation during post-build heating process can be estimated to be between 650 ˚C and 700 ˚C, which agrees with the previous assumed temperature range of 600–700˚C estimated from the temperature variation measures at the bottom of the starting plate. In addition, the *ε*-hcp phase obtained by isothermal heat treatment at 700˚C exhibits the S-N orientation relationship with parent *γ*-fcc phase, which also agrees with the weak texture in the bottom part of EBM-built rod.

5.4.2 Effect of temperature condition on microstructure

It should be noted that the average grain size of *ε*-hcp grains formed from single *γ*-fcc phase by isothermal heat treatment increased with increasing heat treatment temperature, as shown in Fig. 5-12. However, the grain size of *ε*-hcp grains formed at 700 ˚C is smaller than that of *ε*-hcp grains formed in the bottom (h = 5 mm) and center-bottom (h = 32 mm) part of the rod during post-build heating process (Fig. 5-7(c,e)), whose temperature is estimated to be between 650 ˚C and 700 ˚C. The possible reason is that temperature gradient exists during the EBM process, which limits the nucleus of *ε*-hcp grains. In addition, the growth of *ε*-grains can be accelerated by the coalescence of *ε*-hcp grains with other similarly orientated *ε*-hcp grains when isothermal martensitic transformation takes place. As a result, *ε*-hcp grains formed in the bottom and center-bottom part of the as-EBM-built rod were larger than those in the top part, though the post-build heating temperature is lower than the aging heat treatment temperature.

5.5 Conclusions

The effects of the build direction on the microstructure of Co-Cr-Mo alloy fabricated by EBM have been investigated and the following conclusions have been obtained.

(1) Single crystal-like microstructure of Co-Cr-Mo alloy with metastable γ-fcc can be obtained by EBM process.

(2) The preferential crystal orientations of the γ phase in the as-EBM-built 0°-, 45°-, 55°- and 90°-samples along the cylindrical axial directions were near <100>, <110>, <111>, and <100>, respectively.

(3) $M_{23}C_6$ precipitates were observed to align along the build-direction with intervals of around 3 μm in all the samples. M was determined to be Cr, Mo, or Si in $M_{23}C_6$.

(4) Although constituent phase varied along the build direction in the as-EBM-built rod, from single ε-hcp phase in the bottom to single γ-fcc phase in the top, γ-fcc phase can be obtained in a wide range of build height, i.e. approximately 40 mm from the top finishing plane.

(5) In the as-EBM-built rod, ε-hcp phase in the bottom (i.e. early-built part) exhibited weak texture, while that in the latter-built part (far from bottom of the rod) tend to exhibit random orientation. This can be attributed to the increase of post-build heating temperature along the build height.

(6) Displacive (i.e. martensitic) transformation, which holds Shoji–Nishiyama (S-N) orientation relationship ($(111)_\gamma$ // $(0001)_\varepsilon$; $[10\bar{1}]_\gamma$ // $[11\bar{2}0]_\varepsilon$), could occur in the phase transformation during the EBM process and resulted in a textured ε phase grains in the EBM-built sample

(7) Compared with aging heat treatment, larger ε-hcp grains were obtained in the EBM process in the similar temperature condition.

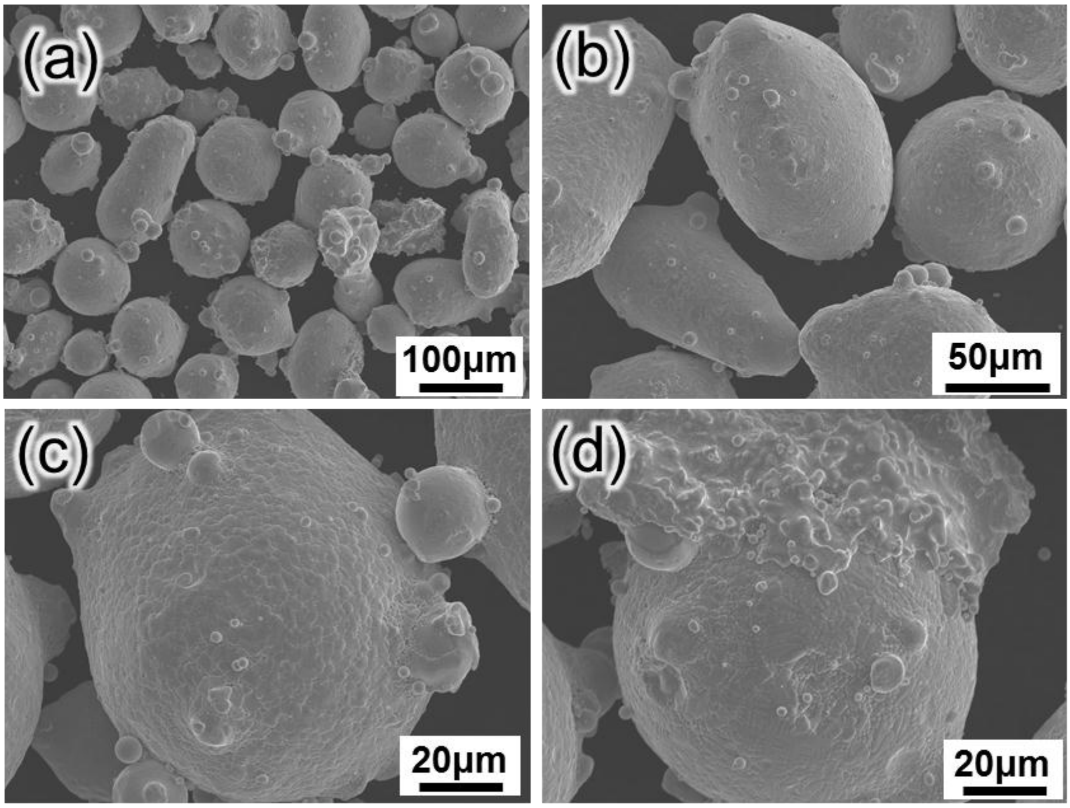

Fig.5-1.Powder morphology of Co–Cr–Mo alloy for electron beam melting in different magnifications. (a) 200 times, showing the spherical or irregular powder with attached small particle, (b) 500 times, hollow powder was not observed, (c) larger powder with slippy surface was attached with a few small particles, and (d) 1000 times, surface of larger powder was partly rough because of being attached with the large amount redundant liquid drop.

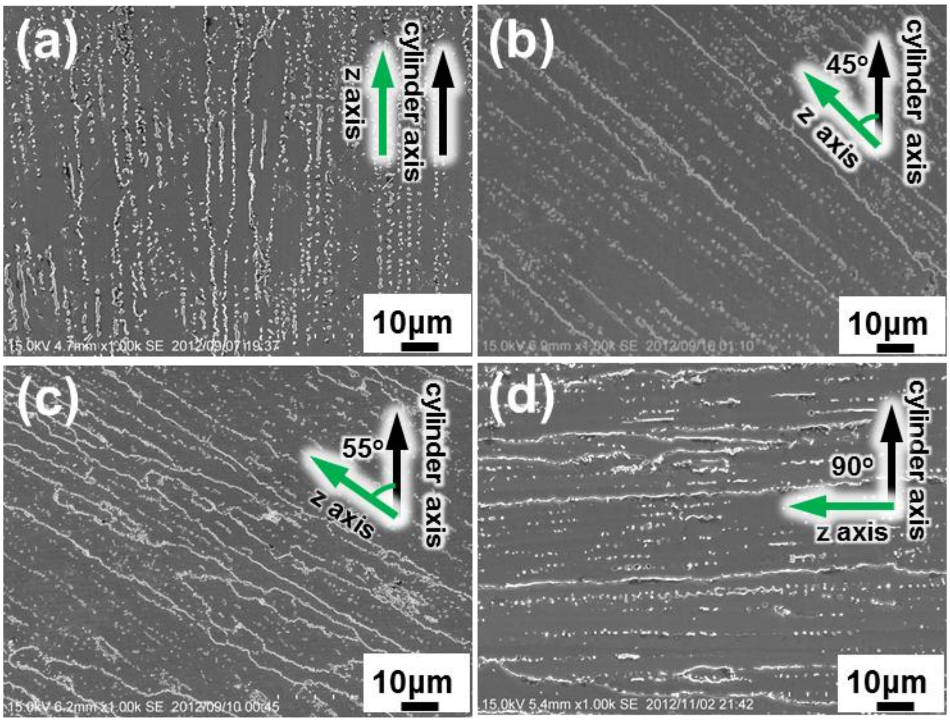

Fig. 5-2. SEM microstructures on the longitudinal cross-section of as-EBM-built samples (top part, about 75 mm from the bottom of the rods). (a) 0˚-sample, (b) 45˚-sample, (c) 55˚-sample, and (d) 90˚-sample.

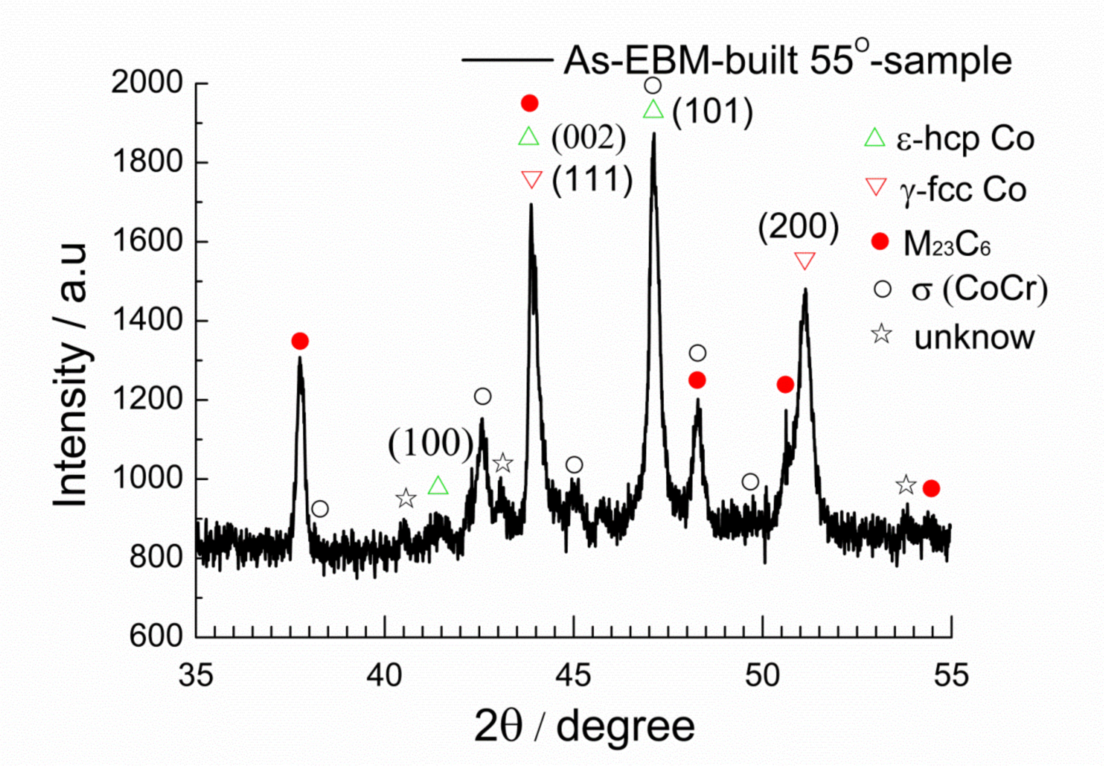

Fig. 5-3. XRD profiles of the vertical cross-section of as-EBM-built 55°-sample.

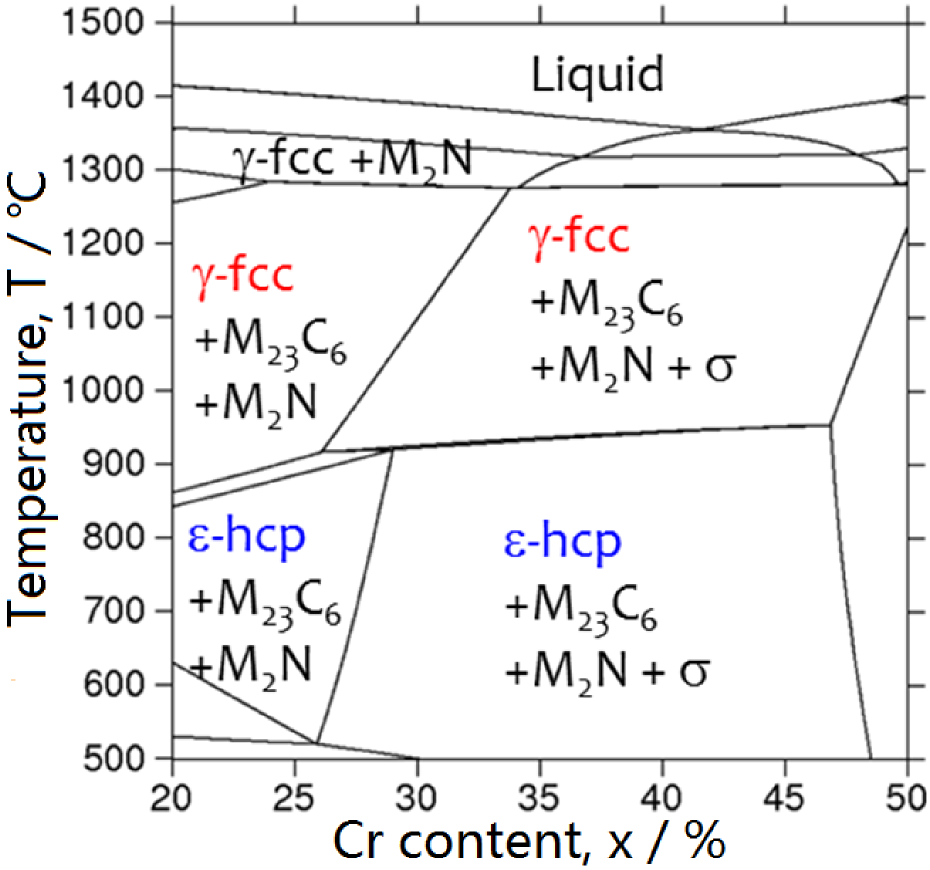

Fig. 5-4.Vertical section of the Co-rich portion of the phase diagram of the Co-xCr-6Mo-0.23C-0.17N calculated using Thermo-Calc software.

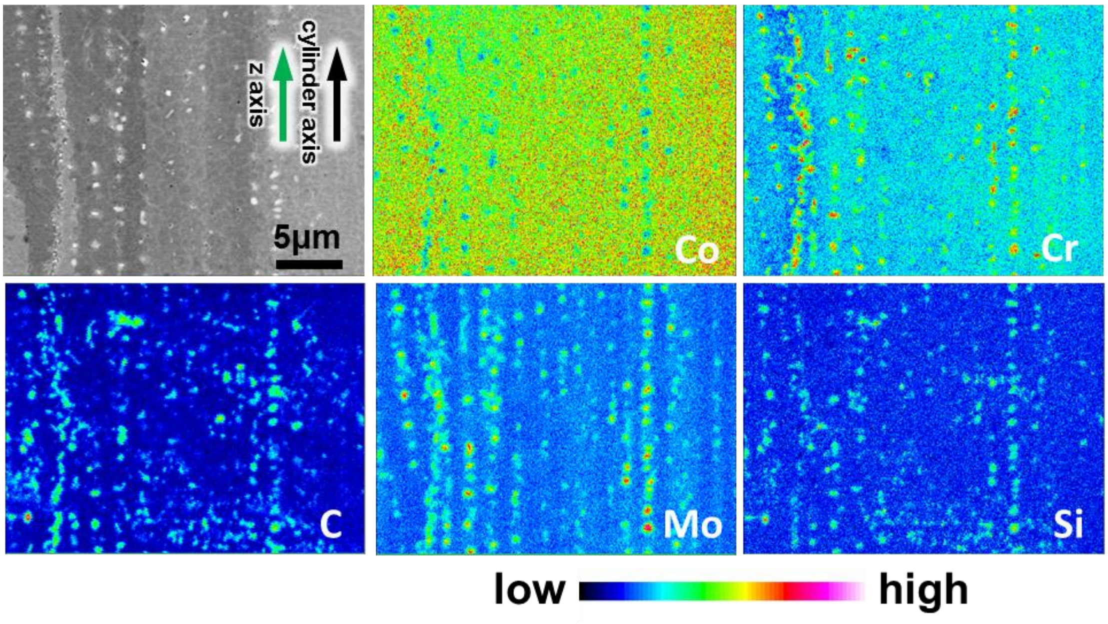

Fig.5-5. EPMA element maps on the vertical cross section of the top part of as-EBM-built 0˚-samples.

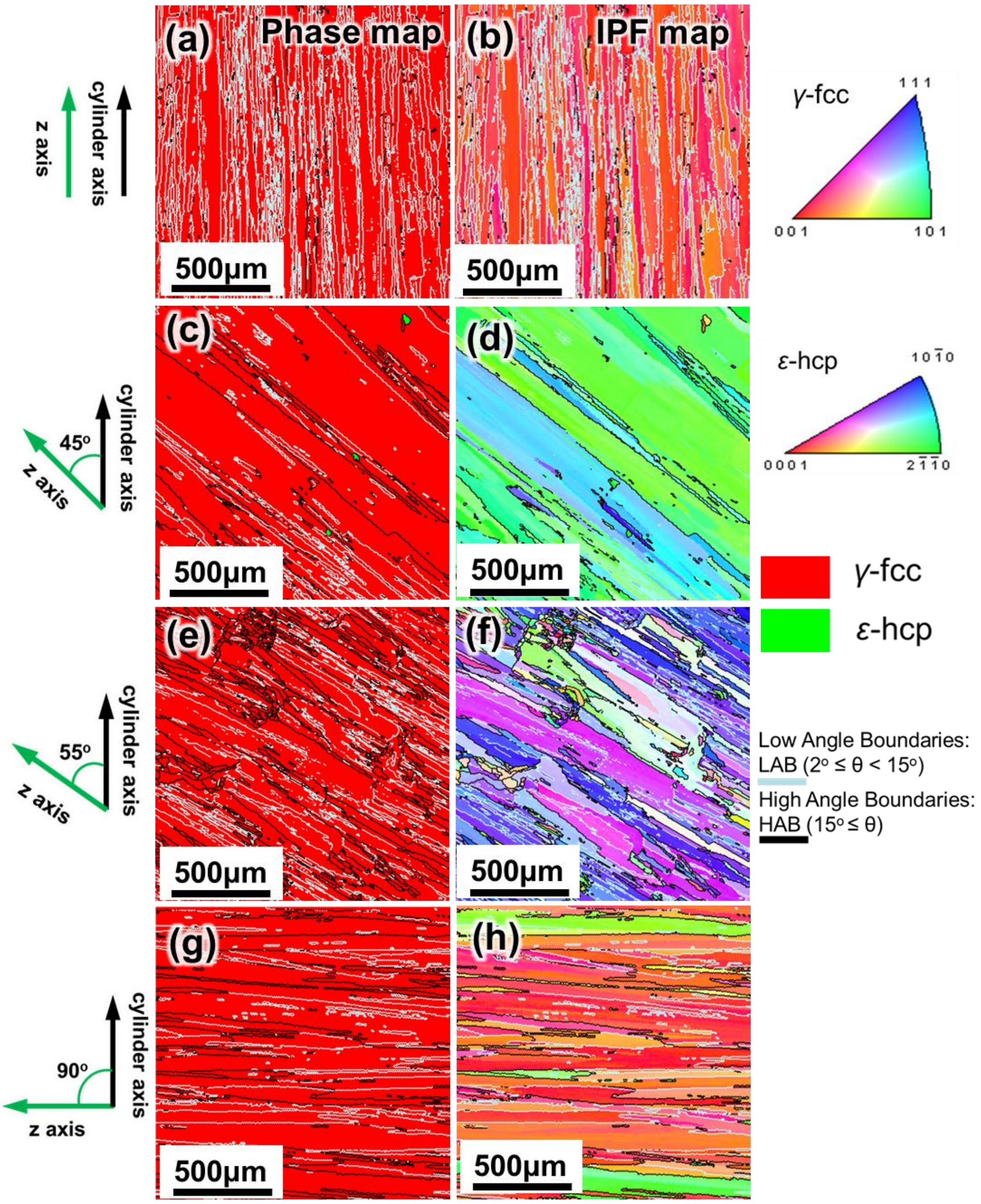

Fig. 5-6. EBSD phase maps (a, c , e, g) and IPF maps (b, d, f, h) on vertical cross section of top part of as-EBM-built samples, (a, b) 0 °-sample, (c, d) 45 °-sample, (e, f) 55 °-sample and (g, h) 90 °-sample. Single *γ*-fcc can form on the top part of the rod. The cylindrical axes were near [001], [011], [111], and [010], respectively in (a) 0 °-, (b) 45 °-, (c) 55 °-, and (d) 90 °-sample.

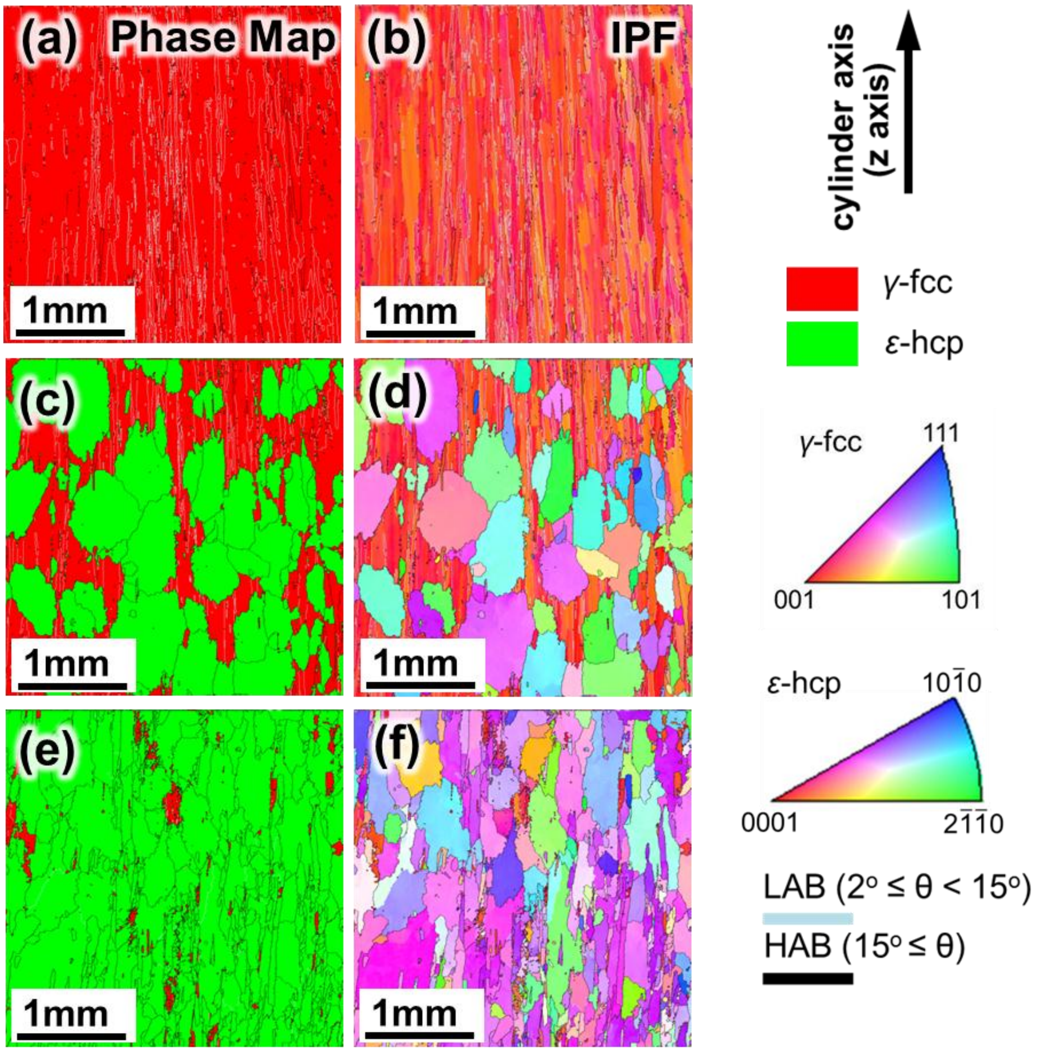

Fig. 5-7. EBSD Phase maps (a,c,e) and IPF maps (b,d,f) on longitudinal cross-section of different height of as-EBM-built 0 °-sample rod, (a,b) top part, (h=79 mm) (c,d) center-bottom part (h= 32mm), and (e,f) bottom part (h=5 mm).

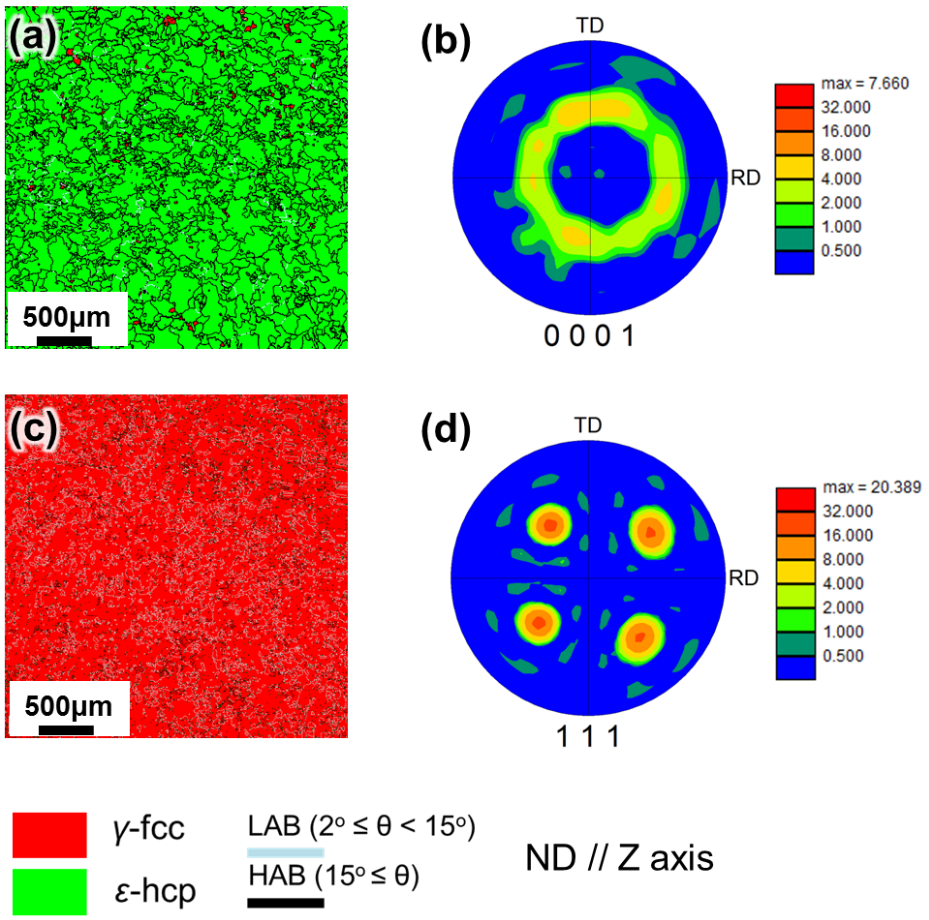

Fig. 5-8. (a, c) Phase map and (b, d) pole figure of the transverse cross section of bottom and top part of as-EBM-built 0 °-sample.

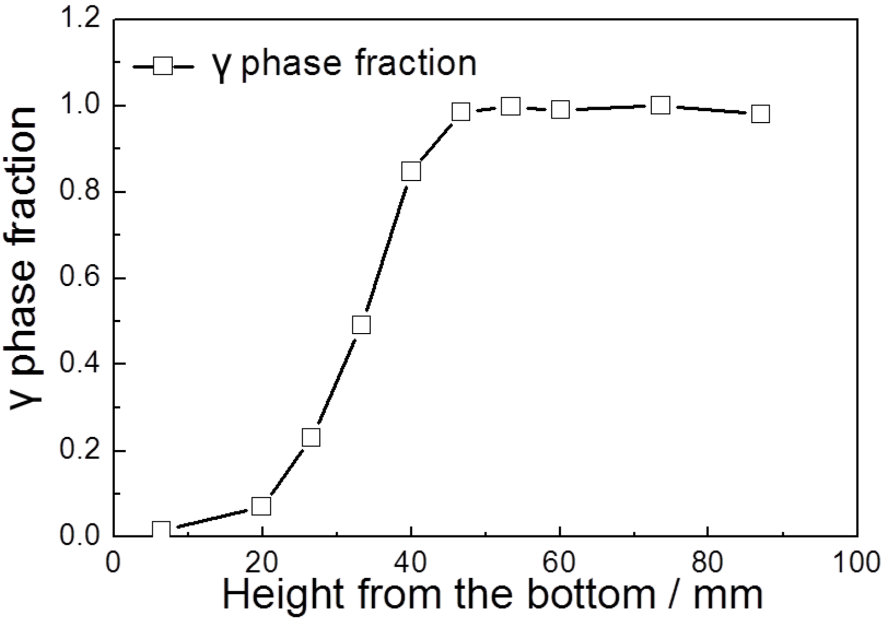

Fig. 5-9. γ phase fraction variation along built height of as-EBM-built 0 °-sample rod.

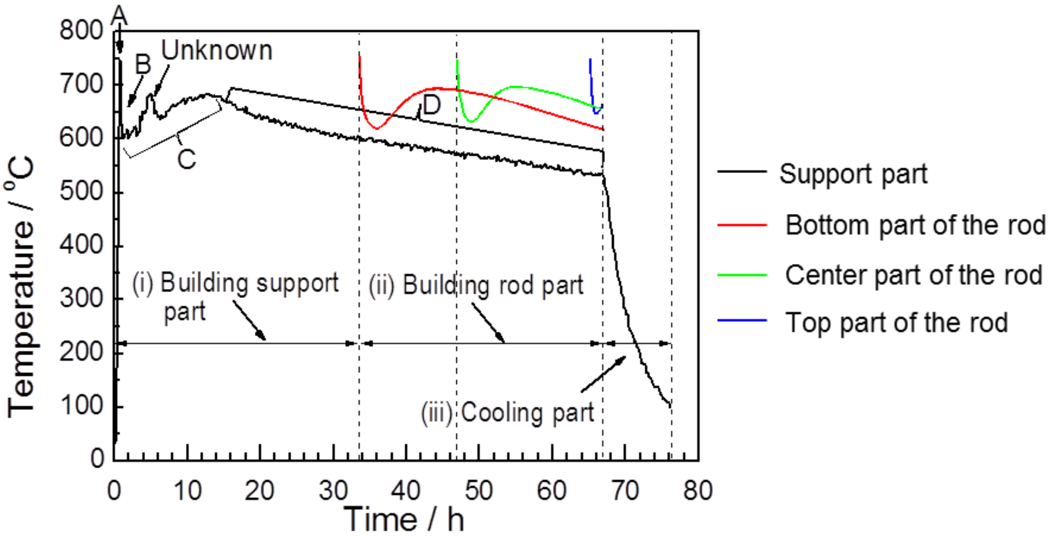

Fig. 5-10. Temperature variation beneath the starting plate during the electron beam melting process.

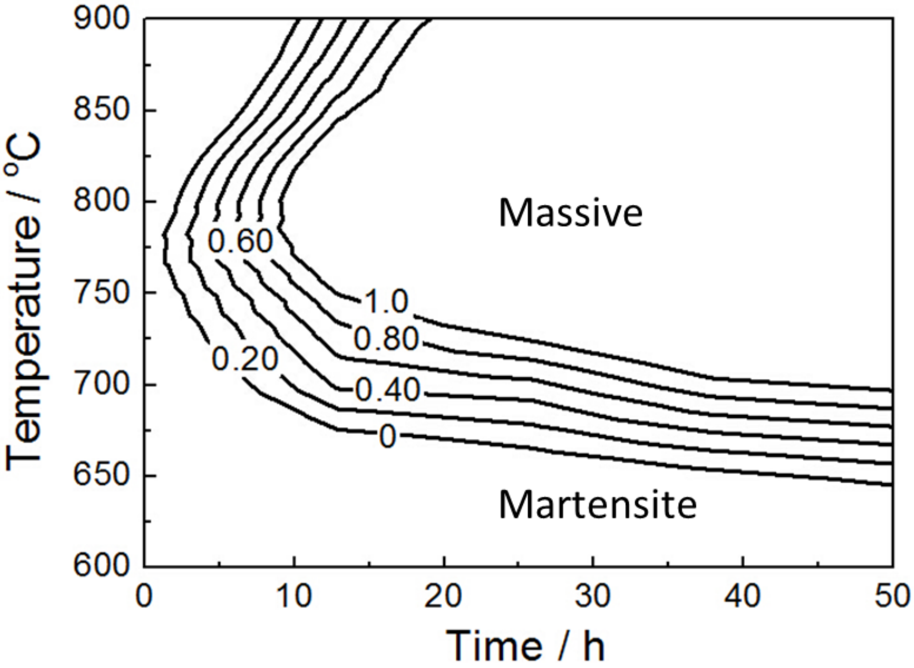

Fig. 5-11. Temperature-Time-Transition curves of ε-hcp phase transformed from γ-single phase during isothermal heat treatment.

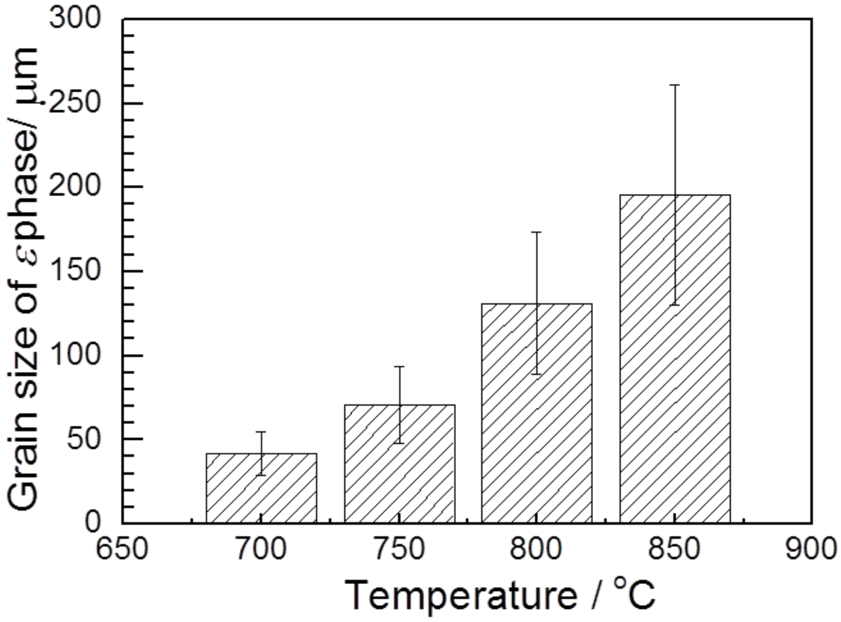

Fig. 5-12. Grain size variation of ε phase with isothermal heat treatment temperature.

Table 5-1 Chemical composition (wt.%) of the alloy used in the EBM process.

Co	Cr	Mo	Ni	Si	Mn	C	N	O
Bal.	28.4	6.66	0.18	0.45	0.69	0.23	0.2	0.023

Table 5-2. Primary parameters to build each orientation rods during the EBM process

Condition	**0 °**	**45 °**	**55 °**	**90 °**
Preheating temp. / ℃	750	750	750	750
Layer thickness / μm	70	70	70	70
Beam current / mA	3.2~6.6	3.1~8.5	3.8~10.7	3.6~17.8
Focus offset / mA	17	17	17	17
Line offset / μm	260	260	260	260
Scanning speed / mm/s	124~260	206~350	124~397	1086~1924

References

[1] W. Betteridge, *Cobalt and its alloys*. Chichester, West Sussex: E. Horwood, 1982.

[2] F. G. Hodge and L. Dominey, *Cobalt and cobalt alloys.Kirk-Othmer Encyclopedia of Chemical Technology*. Hoboken, NJ, USA: John Wiley & Sons, Inc., 2000, pp. 1–22.

[3] D. Coutsouradis, A. Davin, and M. Lamberigts, “Cobalt-Based Superalloys for Applications in Gas Turbines,” *Materials Science and Engineering*, vol. 88, pp. 11–19, Apr. 1987.

[4] A. Chiba, K. Kumagai, N. Nomura, and S. Miyakawa, “Pin-on-Disk Wear Behavior in a like-on-like Configuration in a Biological Environment of High Carbon Cast and Low Carbon Forged Co–29Cr–6Mo Alloys,” *Acta Materialia*, vol. 55, no. 4, pp. 1309–1318, Feb. 2007.

[5] A. Chiba, N. Nomura, and Y. Ono, “Microstructure and Mechanical Properties of Biomedical Co–29Cr–8Mo Alloy Wire Fabricated by a Modified Melt-Spinning Process,” *Acta Materialia*, vol. 55, no. 6, pp. 2119–2128, Apr. 2007.

[6] S. M. Gaytan, L. E. Murr, E. Martinez, J. L. Martinez, B. I. Machado, D. A. Ramirez, F. Medina, S. Collins, and R. B. Wicker, “Comparison of Microstructures and Mechanical Properties for Solid and Mesh Cobalt-Base Alloy Prototypes Fabricated by Electron Beam Melting,” *Metallurgical and Materials Transactions A*, vol. 41, no. 12, pp. 3216–3227, Aug. 2010.

[7] S. M. Gaytan, L. E. Murr, D. A. Ramirez, B. I. Machado, E. Martinez, D. H. Hernandez, J. L. Martinez, F. Medina, and R. B. Wicker, “A TEM Study of Cobalt-Base Alloy Prototypes Fabricated by EBM,” *Materials Sciences and Applications*, vol. 02, no. 05, pp. 355–363, May 2011.

[8] Y. P. Li, J. S. Yu, S. Kurosu, Y. Koizumi, H. Matsumoto, and A. Chiba, “Role of Nitrogen Addition in Stabilizing the γ Phase of Biomedical Co–29Cr–6Mo alloy,” *Materials Chemistry and Physics*, vol. 133, no. 1, pp. 29–32, Mar. 2012.

[9] K. Yamanaka, M. Mori, and A. Chiba, “Nanoarchitectured Co-Cr-Mo Orthopedic Implant Alloys: Nitrogen-Enhanced Nanostructural Evolution and Its Effect on Phase Stability.,” *Acta Biomaterialia*, vol. 9, no. 4, pp. 6259–67, Apr. 2013.

[10] Y. Li, Y. Yamashita, N. Tang, B. Liu, S. Kurosu, H. Matsumoto, Y. Koizumi, and A. Chiba, “Influence of Carbon and Nitrogen Addition on Microstructure and Hot Deformation Behavior of Biomedical Co–Cr–Mo alloy,” *Materials Chemistry and Physics*, vol. 135, no. 2–3, pp. 849–854, Aug. 2012.

[11] S. Kurosu, H. Matsumoto, and A. Chiba, “Isothermal Phase Transformation in Biomedical Co-29Cr-6Mo Alloy without Addition of Carbon or Nitrogen,” *Metallurgical and Materials Transactions A*, vol. 41, no. 10, pp. 2613–2625, Jun. 2010.

[12] W. Kurz and D. J. Fisher, *Fundamentals of solidification*, 4th ed. Hampshire, United Kingdom: Trans Tech Publications, 1998, pp. 65–89.

[13] S. Kurosu, H. Matsumoto, and A. Chiba, “Grain Refinement of Biomedical Co–27Cr–5Mo–0.16N Alloy by Reverse Transformation,” *Materials Letters*, vol. 64, no. 1, pp. 49–52, 2010.

[14] Y. Koizumi, S. Suzuki, K. Yamanaka, B.-S. Lee, K. Sato, Y. Li, S. Kurosu, H. Matsumoto, and A. Chiba, “Strain-Induced Martensitic Transformation near Twin Boundaries in a Biomedical Co–Cr–Mo Alloy with Negative Stacking Fault Energy,” *Acta Materialia*, vol. 61, no. 5, pp. 1648–1661, Mar. 2013.

Chapter 6

6. High temperature mechanical properties of Co–Cr–Mo alloy with various build directions

6.1 Introduction

The strengthening mechanisms of cobalt-based alloys include solid-solution strengthening, secondary-phase strengthening, and grain-refinement strengthening [1]. Solid-solution strengthening is generally attributed to the increase of frictional stress for dislocation motion resulting from the solute-dislocation interaction. Secondary-phase strengthening in cobalt-base alloys is mostly due to carbides. The carbides usually consist of carbon and one or more metal elements (*M)* of chromium, molybdenum, tungsten, niobium, tantalum, zirconium, vanadium, and titanium. Their reported forms include MC, M_6C, M_7C_3, $M_{23}C_6$, and occasionally M_2C_3 [1-6]. Nitrides such as TiN, HfN, and NbN may have a positive effect in superalloys [4], although they are thought to be less effective for strengthening owing to their lower thermodynamical stability than that of carbides, which causes degeneration reactions during service [3]. It has been also reported that CrN or Cr_2N is formed depending on the temperature and N content in the research of cast and forged Co–Cr–Mo alloys [7].

In addition, the strength of a Co–Cr–Mo alloy is known to depend significantly on its microstructure, which consists of the γ-fcc phase that is stable at high temperatures, the ε-hcp phase that is stable at lower temperatures, or both phases[8-10]. Since the γ-fcc phase can exist as a metastable phase even at low temperatures, where the ε-hcp phase is stable in equilibrium, a variety of microstructures can be formed depending on the thermal history. For example, the γ-fcc phase can be a secondary phase for the ε-hcp phase matrix and vice versa. Even in a single phase, various grain structures can be formed as a result of γ-to-ε or γ-to-ε phase transformation. The formation of ε-hcp phase will significantly affect the alloy mechanical property. It can not only enhance the wear resistance [11] and yield strength [12,13], but will also reduce the cold workability [14,15]. Matsumoto et al. [16] indicated that a polycrystalline Co–27Cr–5Mo alloy consisting of a single ε-hcp phase could have higher proof stress (0.2% proof stress: 630MPa) and elongation (38.3%) at room-temperature. By stabilizing the γ-fcc phase with nitrogen addition, the ductility of sample with γ-fcc can be improved without loss of strength [17].

Moreover, Cr_2N has been reported to contribute to grain-refinement strengthening of the biomedical Co–27Cr–5Mo–0.16N alloy by reverse transformation [9]. Ultrafine grain of biomedical Co–29Cr–6Mo alloy can be obtained by the conventional hot-compression deformation [18,19], and the strength of Co–29Cr–6Mo alloy was improved significantly [10,17].

At present, the product of CCM alloy fabricated by EBM is concentrating on hip and knee prostheses [20,21], because of their large manufacturing difficulty and high additional value. Based on the application condition, the mechanical property researches were mainly carried out at room temperature. Recently, CCM alloy has been developed to be used as Al die casting tool because of its relatively high resistance to thermo-mechanical fatigue cracking [22-24] and molten Al corrosion [25-27]. There is no composition development for CCM alloy as Al die casting tool, but Al corrosion resistance will be improved when uniform $(Cr,M)_2O_3$ (M= Co, Mo, Si) oxide layer was formed on the surface of CCM alloy by oxidation treatment at 750 ℃ for 24 h [25]. For the high temperature application, not only thermo-mechanical fatigue behavior but also the tensile and creep behaviors should be considered.

Because crystal orientation and carbide arrangement are dependent on build direction, the corresponding mechanical property is expected to depend on the build direction. Therefore, the purpose in this chapter is to investigate the effect of build direction on the high temperature mechanical properties of Co–28Cr–6Mo–0.23C–

0.17N alloy rods with various build directions.

6.2 Experimental

The samples were fabricated on an Arcam A2 EBM system (Arcam AB, Mölndal, Sweden). The powder used in the experiment consisted of spherical particles and attached small satellite particles with an average particle size of 64 μm, as shown in Fig. 5-1. The chemical composition of the Co–28Cr–6Mo–0.23C–0.17N alloy powder is shown in Table 5-1, which was within the range of ASTM F75 standards. Relatively higher carbon and nitrogen contents were selected in order to obtain a high amount of precipitates and to stabilize the γ-fcc phase, which allowed the γ-fcc crystal growth with <001> orientation. The cylindrical axes deviating from the build-direction (z- axis) by 0°, 45°, 55°, and 90°, as shown in Fig. 3-2, were chosen to orient the cylindrical axes to the [001], [110], [111], and [100] directions, respectively. Hereafter, the Co–28Cr–6Mo–0.23C–0.17N alloy rods fabricated in the directions of 0°, 45°, 55°, and 90° from the z axis are designated as the 0°-sample, 45°-sample, and so on. The rods were 15 mm in the diameter, and 85 mm in the height. The samples were held at 800 ℃ for 24 h to transform them into the single ε-hcp phase, since ε-hcp phase is stable at high temperature and may increase the strength owing its limited slip system. The Young's modulus of aging treated specimen with 50 mm in length, 10 mm in width and 2 mm in thickness, was measured by EG-HT high temperature Young's modulus equipment from room temperature to 800 ˚C with 10 ˚C interval.

The tensile samples were taken from the top part of the as-EBM-built samples and cut so that the tensile direction was parallel to the cylinder axis. The gauge part was rectangular, measuring 11 mm in length, 2 mm in width, and 1 mm in thickness. Tensile tests were conducted at 700 ℃ with a strain rate of $1.5 \times 10^{-4}\ \mathrm{s}^{-1}$ on an Instron 8562 testing machine. In order to examine the effect of the matrix phase on the high-temperature tensile properties, the tensile test was also conducted on the single-*γ*-phased 90°-sample. The single-*γ*-phased 90°-sample was formed by just skipping the post-EBM, aging heat treatment, because it requires a relatively low build height of 15 mm, which will avoid the *γ*-to-*ε* transition during the EBM process. The microstructures were investigated by scanning electron microscopy (SEM), electron backscatter diffraction (EBSD), and X-ray diffraction (XRD) on the vertical cross section consisting of the cylindrical and *z* axes. The fracture surfaces and neighboring microstructures were observed by SEM and EBSD, respectively, to determine the fracture mode and the effect of high-temperature tensile deformation on the microstructure.

The gauge part of the creep specimen was cylindrical shape with 6 mm in diameter and 30 mm in length. Constant load creep tests were conducted at temperature range of 650-800 ˚C, and stress range of 240-330 MPa. Creep test was also conducted on the single-*γ*-phased 90°-sample to investigate the effect of initial phase on creep properties. The longitudinal cross-section microstructures in both sides of the fracture surface were observed by EBSD and transmission electron microscopy (TEM), respectively, to investigate the microstructure evolution during creep test.

6.3 Results

6.3.1 Microstructure after aged at 800 ℃ for 24 h

Fig. 6-1 shows EBSD results of microstructures observed on longitudinal cross-section at different build heights. Phase maps (Fig. 6-1(a,c,e)) show *γ*-fcc phase has transformed into single *ε*-hcp phase after aging treatment at 800 ˚C for 24 h. Fig. 6-1(b) indicates that the orientations of *ε*-hcp grains obtained from single *γ*-fcc grains in the top (h = 79 mm) of the rod by aging treatment at 800 ˚C for 24 h was random. The random orientation of ε-phase indicates that the γ→ε transformation occurred via diffusive transformation not via a displacive (i.e. martensitic) transformation which would have resulted in a textured ε phase grains in which specific orientation were preferred. Fig. 6-1(d) indicates that grains were also random oriented when translated from the center-bottom (*h* = 32 mm) mix phase part, but the grain size was larger than that of the top part (Fig. 6-1(b)). Fig. 6-1 (f) indicates that the grain size did not change apparently from those before aging heat treatment in the bottom (Fig. 5-7 (f)) (*h* = 5 mm), where the microstructure had already become single *ε*-hcp phase in the as-EBM-built rod, and weak texture near $(20\bar{2}3)$ plane normal still existed in the build direction.

According to the EBSD results of transverse cross-section microstructure, *γ* phase volume fraction variation in the as-EBM-built rod and *ε* phase grain size variation in the rod after aging treatment at 800˚C for 24 h were evaluated and summarized in Fig. 6-2. This is to clarify the effect of *γ* phase volume fraction variation in the as-EBM-built rod on *ε* phase grain size variation in the aging treated rod. *γ*-fcc phase increased sharply from 0 in the bottom (early-built part) and kept constant (near 100 %) in the top part (last-built part) in as-EBM-built rod. The phase transformation to *ε*-hcp is difficult to avoid in the fabrication of large objects with large height since the early-built part are held at temperatures high enough for diffusive transformation to take place for long periods of post-melting process. Nevertheless, single *γ*-fcc phase was obtained in a wide range of build height in the as-EBM-built rod, i.e. approximately 40 mm from the top surface. However, the gauge part for creep test was still in the two phase region. For the tensile test, the gauge part of the sample (11 mm) can be in the single *γ* phase region. After aging treatment at 800 ˚C for 24 h, all the *γ*-fcc grains transformed to *ε*-hcp phase. When transformed from the mix phase region of the bottom part, *ε*-hcp grain size increased noticeably with increasing the initial *γ*-fcc phase fraction at first, and reached the maximum at the position where the volume fraction of initial *γ*-fcc phase was approximately 23%, then decreased rapidly with increasing initial *γ*-fcc phase fraction further until *γ*-fcc phase is 100%. *ε*-hcp grain size was relatively uniform when translated from the single *γ*-fcc phase region. It should be noted that the grain size decreased along the build height in the gauge region of the creep test samples, but was homogeneous for the tensile test samples. This will be important for understanding the tensile and creep fracture behavior at 700

°C.

Fig. 6-3 shows the EBSD results of samples with various build directions after aging treatment at 800°C for 24 h. Phase maps (Fig. 6-3(a,c,e,g)) show that all of the samples were transformed into the single ε phase by the aging treatment. And the as-EBM-built columnar grains with γ-fcc phase were tended to be replaced by equiaxed grains with ε-hcp grains, especially in the 0°-sample. The IPF maps (Fig. 6-3(b,d,f,h)) shows the orientations in the direction of the cylindrical axis. No significant preferential orientation was recognized in the ε grains, indicating that the Shoji–Nishiyama (S-N) orientation relationship ($(111)_\gamma$ // $(0001)_\varepsilon$; $[10\bar{1}]_\gamma$ // $[11\bar{2}0]_\varepsilon$) was not fully established during phase transformation. This suggests that diffusive phase transformation occurred during the aging treatment at 800 ℃. The average grain sizes of the 0°-, 45°-, 55°-, and 90°-samples in the gauge area after aging treatment were 45 μm, 32 μm, 25 μm, and 47 μm, respectively, which are calculated by the intercept length perpendicular to grain boundaries elongated direction (cylindrical axis).

Fig. 6-4 shows that the lamellar precipitate colonies indicated by a black ellipse arrows precipitated out the matrix after aging treatment. The thickness of the plate-like precipitate in the colonies was about 200 nm. The XRD profiles (Fig. 6-5) and the phase diagram calculated by Thermocalc software (Fig. 5-4) suggested that the plate-like precipitates in the lamellar colonies formed after aging treatment were predominately M_2N in equilibrium with the ε-hcp phase [9], and partly the $M_{23}C_6$ carbide in equilibrium with the ε-hcp phase [28,29], which did not fully precipitate out from the matrix. Further elemental surface scan analysis with EPMA (Fig. 6-6) clearly indicates there was nearly no carbon in the plate-like precipitate, which suggests that the plate-like precipitate is mainly M_2N. Because the wavelength of the X-ray reflected from N was very similar to that from Co, its distribution could not be distinguished. Therefore, the nitrogen distribution is not included in Fig. 6-6. M was identified as Cr, Mo, or Si in M_2N. The lamellar structure of the M_2N precipitates and the ε-hcp phase originated from the eutectoid transformation ($\gamma \rightarrow \varepsilon + M_2$N) [9].

6.3.2 High temperature tensile property

The stress–strain curves of samples after aging treatment are shown in Fig. 6-7. In order to examine the effect of phase constitution on the tensile properties, the tensile result of the 90°-sample with the γ phase is also shown in Fig. 6-7. Higher *UTS* of the aged specimens was obtained in the order of 55°-, 45°-, 0°-, and 90°-samples. The 0.2% yield stress of the 0°-, 45°-, and 55°-samples were 635 ± 13 MPa, 659 ± 30 MPa, and 684 ± 14 MPa, respectively, while that of the 90° sample was as low as 459 ± 4 MPa. The elongation of the 90°-sample was 2.5 ± 0.7%, which was comparable to those of the 0°-, 45°-, and 55°-samples: 3.1 ± 0.7%, 1.7 ± 0.1%, and 2.0 ± 0.5%, respectively. The mechanical properties are listed in Table 6-1. The differences in *UTS*, 0.2% yield stresses, and elongations of the samples indicated that the tensile properties strongly depended on the microstructure, including crystal orientation, grain shape, and array of precipitates. The strength of the 90°-sample with a single ε phase, represented by 0.2% yield stress and *UTS*, was higher than that with a single γ phase, but the elongation was as small as 2.5%, which was only about one fifth of that with the single γ phase. It indicates that although both of the matrices were strengthened by the carbide precipitates, the ε phase with a small number of slip systems and higher frictional stress [9,16] exhibited higher strength but lower ductility even at 700 ℃. Also, the smaller grain size in the aged, single-ε-phased samples was expected to be responsible for the higher strength to some extent.

Fig. 6-8 shows EBSD results of samples after the tensile tests. Because the gauge surface is very uneven after deformation, the confidence index is very low. Therefore, the gauge surface was polished, and the slip band was removed. No deformation twins were found in the samples. The average grain sizes of the 0°-, 45°-, 55°-, and 90°-samples were 37 μm, 25 μm, 24 μm, and 33 μm, respectively, after the tensile tests. Compared with samples before the tensile tests, the grain sizes were almost unchanged. The kernel average misorientation (KAM), which is the average misorientation angle of all adjacent measurement points in the grain, is widely acknowledged to indicate the density of geometrically necessary dislocations (GNDs)[30], and the value is usually high near grain boundaries owing to the constraint effect of grain boundaries. The KAM maps of the samples (Figs. 6-8 (b, d, f, h, j)) indicated that the GND densities were high not only near grain boundaries, but also inside some grains. The high KAM inside some grains suggests that some grains were in easily deformed orientations, and there were many dislocation pile-ups caused by the dispersion of carbide and nitride precipitates in the grains. The misorientation in the 90 °-sample with the γ phase was high in the entire observation area, which might be the result of dislocations piling up, caused by the precipitates and simultaneous operation of multiple slip systems in the γ-fcc phase. The ε-hcp phase was not observed in Fig. 6-8(k), suggesting that strain-induced martensitic transformation (SIMT) might not occur in the Co–28Cr–6Mo–0.23C–0.17N alloy.

Fig. 6-9 shows the fracture surface morphologies of the tensile samples. The whole area view of the fracture surface (Fig. 6-9(a,c,e,g,i)) shows facet character, which suggests the intergranular fracture occurred in all the samples during the tensile test. However, in the local area view (Fig. 6-9(b,d,f,h,j)), the dimple-type fracture surfaces can be observed, and carbide precipitates could be seen inside the dimples, as indicated by white arrows. Necking was not observed in any of the samples. The dimple features suggested that the voids were initiated around the precipitates, and their growth and coalescence led to fracture. A large amount of long continuous precipitates or long grooves could be seen on the fracture surface of the 90 °-samples (Figs. 6-9 g–j).

6.3.3 High temperature creep property

6.3.3.1 Creep property with different initial phases

Fig. 6-10 shows creep properties of 90 °-samples with different initial phases. Fig. 6-10(a) shows ε-hcp exhibited typical three creep stages under all the applied stress. That is the curve slope (i.e. creep rate, as shown in Fig. 6-10(b)) decreased slowly in the primary creep period, then it kept nearly constant in the secondary creep period, and accelerated until failure in the tertiary creep period. However, the creep curve of γ-fcc phase was very different from that in ε-hcp, especially at the initial part. Fig. 6-10(b) shows the creep rate of γ-fcc decreased rapidly in the initial period (A stage), then it increased after about 10 h (B stage). After about 10 more hours, the creep rate decreased again (C stage), and reached a minimum value with increase the time further (D stage). At the last stage (E stage), the creep rate increased significantly with increase of time until the final fracture. The additional variation for the creep rate of γ-fcc phase at the initial period suggests there is additional deformation process in the creep process.

Though the creep rupture times for γ-fcc phase and ε-hcp were similar, the minimum creep rate of ε-hcp phase was much smaller than that with γ-fcc phase in the same creep condition, which suggests ε-hcp exhibits higher creep resistance than γ-fcc phase. As shown in the calculated phase diagram in Fig. 5-4, metastable γ-fcc will transform into ε-hcp phase gradually during the creep test at 700 ℃, which will accelerate the dislocation slip and increase the creep rate. Hence, the additional deformation process of γ-fcc is thought to be related to the phase transformation from γ-fcc to ε-hcp during the creep process. The possible reasons causing the creep curve variation of γ-fcc are supposed as follows. In A stage, the creep rate decreases because of dislocation density propagation due to work hardening. The phase transformation begins in B stage, which will accelerate the dislocation slip. As a result, the creep rate increases. In C stage, the transformed ε-hcp can be the obstacle preventing the dislocation slip in γ-fcc, moreover the dislocation density can also increase in the transformed ε-hcp. Therefore, the creep rate decreases in the C stage. In the D stage, the work hardening and recovery softening will reach to the equilibrium, and the creep rate will also reach the minimum value, being similar to the steady state creep stage of the typical creep deformation. In the E stage, the crack will appear and propagate, therefore deformation will be accelerate again because of the increased applied stress due to the decrease of cross section.

6.3.3.2 Effect of inhomogeneous microstructure on creep property

6.3.3.2.1 Stress dependence of creep behavior

Fig. 6-11 shows the creep curves of 0°-sample at 700 °C under different stresses, and creep rate variation with creep strain. Fig. 6-11(a) shows that the creep curves exhibited typical three creep stages under all the applied stresses. The curve slope (i.e. creep rate) decreased slowly in the primary creep period, then it kept nearly constant in the secondary creep period, and accelerated until failure in the tertiary creep period. Overall, the creep rate increased with increasing applied stresses. Although the initial creep rate under the highest applied stress of 330 MPa was lower than those under lower stress, the minimum creep rate increased with increasing load and was the highest under the highest load of 330 MPa as shown in Fig.6-11 (b), Fig.6-11 (b) also indicates that creep deformation is nearly in the same stage when creep strain is the same under all the applied stresses.

Fig.6-12 shows the stress dependence of other creep properties of 0°-sample at 700°C as well. The minimum creep rate increased from 1.45×10^{-8} s^{-1} to 7.35×10^{-8} s^{-1} with increasing the applied stress from 240 MPa to 330 MPa, while the creep rupture time decreased from 188.2 h to 30.2 h with increasing the stress. Creep rupture strain was kept nearly constant between 0.01-0.02 against the increase in the stress.

6.3.3.2.2 Temperature dependence of creep behavior

Fig. 6-13 shows the creep curves of 0°-sample at 240MPa with different temperatures and creep rate variation with creep strain. Although the creep curves also exhibited typical three creep stages at all the temperatures examined as shown in Fig. 6-13(a,b,c,d), the creep rate dramatically increased with increasing temperature as shown in Fig.6-13(e). Note that the ranges of horizontal axes in Fig. 6-13(a,b,c,d), i.e. time, for different temperatures are quite different. The range was decreased by roughly one order of magnitude for the increase in temperature of 50 °C.

Fig. 6-14 shows temperature dependence of other creep properties of 0 °-sample at 240 MPa. The minimum creep rate increased from 1.85×10^{-9} s^{-1} to 1.17×10^{-6} s^{-1} with increasing the temperature from 650 ˚C to 800 ˚C, while the creep rupture time decreased from 1536.1 h to 2.0 h with increasing the temperature. Creep rupture strain was also nearly kept constant around 0.015 against the increase in the temperature.

6.3.3.2.3 *Creep mechanism analysis based on constitutive equation*

Considering creep as thermally activated phenomenon, creep behavior is usually characterized by the following equation,

$$\dot{\varepsilon}_{\mathrm{m}} = \mathrm{A}\frac{G\Omega}{\mathrm{b}^2\mathrm{k}T}\left(\frac{\sigma}{G}\right)^n exp\left(-\frac{Q}{\mathrm{R}T}\right) \qquad (6.1)$$

where $\dot{\varepsilon}_{\mathrm{m}}$ is the minimum creep rate, A is a constant, G is shear modulus, Ω is atomic volume, b is the magnitude of Burgers vector, k is Boltzmann's constant, σ is the applied stress, n is the stress exponent for creep, Q is the apparent activation energy for creep, R is the universal gas constant, and T is the absolute temperature.

Fig. 6-15 shows stress and temperature reciprocal dependence of minimum creep rate. The young's modulus and shear modulus of CCM alloy at different temperatures are listed in Table 6-2. Fig. 6-15(a) shows that the logarithm of minimum creep rate exhibited a linear relationship with logarithm of stress. This suggests the specimens exhibited the power law creep. The stress exponent of the specimens can be determined to be 5.0 by the slope. The value was larger than 1, which suggests that the deformation is mainly controlled by dislocation motion. Fig. 6-15(b) shows the logarithm of minimum creep rate also exhibited a linear relationship with temperature reciprocal. The apparent activation energy of the creep deformation can be determined to be 365 kJ mol^{-1} by the slope.

6.3.3.2.4 *Creep rupture life prediction by Lason-Miller parameter*

Creep data under different stresses and temperatures are usually analyzed by Lason-miller parameter to describe the creep behavior, which can be expressed as

$$P(\sigma)=T(\log t_r+\mathrm{C}) \tag{6.2}$$

where $P(\sigma)$ is the Lason-miller parameter, T is temperature, t_r is the creep rupture time, and C is a constant, which can be determined by temperature dependence of creep rupture time as shown in Fig. 6-16(a). Here C was determined to be 18.1 at the stress of 240 MPa, which is very close to the common value of 20. Fig. 6-16(b) shows Larson-Miller parameter plot of stress-rupture life. The stress is roughly proportional to the Lason-Miller parameter in the range examined in the experiment. It is noted that the Lason-Miller parameters at the stress of 240 MPa for different temperatures are scattering but they are reasonably close to the line of linear fitting.

6.3.3.2.5 Microstructure after creep test

Fig. 6-17 shows EBSD IPF maps of longitudinal cross-section microstructure on both sides of the main crack (i.e. the crack which led to the fracture of the specimen) of 0 °-sample at 700˚C under different stresses. Fig. 6-17(a,c,e,g) refer to IPF maps on the upper side of the main crack, while Fig. 6-17(b,d,f,h) refer to those on the lower side. The orientation was random in all the specimens. In the specimens crept under the stresses of 240 MPa (Fig. 6-17(a,b)) and 270 MPa (Fig. 6-17(c,d)), the grain sizes in the upper side were smaller than those in the lower side, and the microstructures were homogeneous in the upper side but inhomogeneous in the lower side. This result suggests that the fractures occurred near the region where the transition of microstructure from the $\gamma+\varepsilon$ duplex structure to γ single phase structure was observed in the as-EBM-built samples. For the microstructures of specimens at 300 MPa and 330 MPa, they were homogeneous on each side of the fracture, and there was little difference in grain sizes on the two sides of the fracture, as shown in Fig. 6-17(e,f,g,h). This result suggests that fracture occurred in the homogeneous fine grain region.

Fig.6-18 shows the EBSD IPF maps of longitudinal cross-section on both sides of the main crack of 0 °-sample crept under the load of 240 MPa at different temperatures. Fig. 6-18(a,c,e,g) refer to IPF maps on the upper side of the main cracks, while Fig.

6-18(b,d,f,h) refer to IPF maps on the lower side. The microstructure of specimens at 700 ˚C (i.e. the specimen at 240 MPa) was shown in Fig. 6-18(c,d) again for comparing temperature effect. By comparing these grain structures with those observed at various position of the rod before creep tests, it is suggested that fractures was in the homogeneously fine grained region.

The grain orientations were random in all the specimens. In the specimens crept at 650 ˚C (Fig. 6-18 (a,b)), 750 ˚C (Fig. 6-18 (e,f)), and 800 ˚C (Fig. 6-18 (g,h)), the grain structures were homogeneous on both sides of the fracture, and there was little difference in grain size on the two side of the fracture. In the specimen crept at 700 ˚C, the grain structure in the upper side is inhomogeneous but it is homogeneous in the lower side. These observations suggest that the fracture occurred in the fine grained area and/or the transition area between fine grained region and coarse grained region. This is consistent with the generally accept knowledge that high temperature strength of fine grained metals is lower than that of coarse grained counterparts because of the operation of deformation mechanisms enhanced by grain boundaries such as Coble creep and grain boundary sliding.

6.3.3.3 Effect of build direction on creep property

Fig. 6-19 shows creep curves of the samples with different build directions at 700˚C with different stresses and the effect of build direction on creep rupture time and steady state creep. All the samples exhibited typical three creep stages under all the applied stresses. And the creep rupture time and steady state creep rate was found to be independent of the build direction. The possible reasons are as follows. Firstly, the crystal orientation of ε-hcp was random after heat treatment (Fig.6-3), even though the previous γ-fcc exhibit strong texture. Secondly, the primary strengthen phase, carbides was similarly distributed on the slip plane in different samples if Shoji–Nishiyama (S-N) orientation relationship ($(111)_{\gamma}$ // $(0001)_{\varepsilon}$; $[10\bar{1}]_{\gamma}$ // $[11\bar{2}0]_{\varepsilon}$) is established during phase transformation. This will be discussed in detail in 6.4.1.3.

6.4 Discussion

6.4.1 Dominant factors affecting high-temperature tensile properties

There are several possible factors which can give rise to the differences in the tensile properties of the EBM-built CCM alloys with different build-directions, i.e. the anisotropy of grain boundary shape, carbide arrangement and crystal orientation. Also, the operating slip system should be taken into account for understanding the roles of these factors. Here the roles of the factors are discussed.

6.4.1.1 Grain shape anisotropy

If the anisotropy of grain boundary shape was the dominant factor, the 45 °-sample would exhibit the lowest strength among the samples with different build-directions since the largest shear stress, which is applied on planes inclined to the loading axis by 45 °, could be applied parallel to most of the grain boundaries which were mostly inclined to the loading axis by 45 °. Also, the probability of dislocations to be blocked by grain boundaries is lower in the shear parallel to the elongated grain than that in the shear perpendicular to the elongated grain. However, the 45 °-sample exhibited even higher *UTS* than the 0 °-sample. This suggests that the effect of grain-shape anisotropy is very weak. It appeared that the carbide dispersion hid the effect of grain-shape anisotropy. The grain boundary sliding was also very difficult probably because of the relatively large grain size and the $M_{23}\mathrm{C}_6$ precipitates aligned along the grain boundary. Thus, the effect of grain shape on deformation could be neglected.

6.4.1.2 Slip systems

Here, the operating slip system is discussed. TEM bright-field images of 55 °-sample after tensile tests are shown in Fig. 6-20. Straight line contrasts parallel to the trace of basal planes can be seen in Fig. 20(a) with the incident direction and operation vector being $[2\bar{1}\bar{1}0]$ and $(0\bar{1}12)$ plane normal, respectively. When the operation vector was (0002) plane normal, the straight line contrasts would disappeared. This indicates that most of the dislocations were on the basal plane, suggesting that the basal slip were operated during tensile deformation. Matsumoto et al. [16] showed that the room-temperature deformation mode of a polycrystalline Co–27Cr–5Mo alloy consisting of a single ε-hcp phase was the basal <**a**> or prismatic <**a**> slip, depending on the crystal orientation in accordance with the Schmid’s law. In spite of the relatively limited number of slip systems, the plastic elongation of Co–27Cr–5Mo alloy consisting of ε-hcp single phase was as large as 38.3% at room temperature in that study. In contrast, the maximum elongation of Co–28Cr–6Mo–0.23C–0.17N alloy, which also consists of ε-hcp phase, was only about 3% even at a high temperature of 700 ℃. One possible reason for the low plastic deformability measured in this study was the difference in the deformation mode owing to the temperature dependence of the stacking fault energy (*SFE*).

Generally, for calculating *SFE* of γ-fcc alloys[19,31,32], a SF in the γ-fcc crystal is regarded as a plate of the ε-hcp phase with a thickness of only two atomic layers, which has coherent interfaces with the S-N relationship on each side facing the γ-fcc matrix. *SFE* of a fcc structure can then be expressed by

$$\Gamma^{\gamma}_{SFE} = 2\rho\Delta G^{\gamma\to\varepsilon} + 2\sigma_{\gamma/\varepsilon} \qquad (6.3)$$

where $\Delta G^{\gamma\to\varepsilon}$ is the molar Gibbs energy change of the $\gamma\to\varepsilon$ phase transformation and $\sigma_{\gamma/\varepsilon}$ is the interfacial energy between the ε and γ phases, which is generally between 5 and 10 mJ m^{-2} for Co-Ni alloy [32]. In this research, it is set as 7.5 mJ m^{-2}. ρ is the molar surface density along {111} planes in the fcc structure[32], which is given by

$$\rho = \frac{4}{\sqrt{3}}\frac{1}{a^2 N} \qquad (6.4)$$

where N is the Avogadro’s number, and a is the lattice constant of the fcc phase, which is determined to be 0.3714 nm by XRD measurement. The calculated *SFE* for the Co–28Cr–6Mo–0.23C–0.17N alloy is negative (-90.0 mJ m^{-2}) at room temperature (25 ℃). It increases with increasing temperature, and becomes approximately 0 mJ m^{-2} at 709 ℃. On the other hand, to calculate *SFE* of the ε-hcp phase, a SF in the hcp crystal is regarded as a thin layer of the fcc phase, and *SFE* of the hcp structure can be expressed by

$$\Gamma^{\varepsilon}_{SFE} = 2\rho\Delta G^{\varepsilon\rightarrow\gamma} + 2\sigma_{\gamma/\varepsilon} \tag{6.5}$$

where $\Delta G^{\varepsilon\rightarrow\gamma}$ is the molar Gibbs energy change of the $\varepsilon\rightarrow\gamma$ phase transformation. This value of *SFE* at room temperature is positive (120.1 mJ m^{-2}) in contrast to the case of *SFE* in the γ-fcc phase. The value of *SFE* of the Co–28Cr–6Mo–0.23C–0.17N alloy with an ε-hcp phase decreases with increasing temperature, and it becomes approximately 0 mJ m^{-2} at 937 ℃. The difference between the values of *SFE* of the Co–28Cr–6Mo–0.23C–0.17N alloy with an ε-hcp phase and that of the Co–27Cr–5Mo alloy with an ε-hcp phase at a given temperature is negligibly small. The value of *SFE* of ε-hcp Co–28Cr–6Mo–0.23C–0.17N alloys at the deformation temperature of 700 ℃ is 31.2 mJ m^{-2} and is much lower than the value at room temperature. The extremely low *SFE* results in a very widely dissociated Shockley partial dislocation pair, which leads to low probability of cross slip of dislocations on the basal plane to the prism plane. The difficulty of the cross slip was probably responsible for the low ductility of the ε-hcp Co–Cr–Mo alloys at 700 ℃.

6.4.1.3 Carbide arrangement

Here, the role of carbide arrangement is discussed on the basis of fracture behavior. For the 90°-sample, regardless of whether the matrix phase was in the ε or γ phase, the loading axes were perpendicular to the direction of carbide array and longitudinal axes of elongated precipitates. Under such loading condition, voids were easily formed around the precipitates. Once the voids coalesced around the precipitates, long cracks could form in the transverse direction, which could easily lead to the final fracture. Therefore, it was natural that the 90°-sample had the lowest *UTS* value among the samples.

Although the appearances of the fracture surfaces were similar to those of Co–Cr–

Mo alloys deformed at room temperature with large elongations of more than 30% [9,16,33], the elongations obtained at 700 ℃ in the present study were as small as 3% at the maximum. The reason for the poor ductility should be clarified.

Since carbide can be found to exist in the dimples, it is suggested that large plastic deformation occurred locally around the precipitates. Though the fracture surface shows dimple character in the local area (Fig. 6-9(b,d,f,h,j)), the intragranular fracture characteristic (Fig. 6-9(a,c,e,g,i)) with the scraggy morphology in the whole fracture surface is observed. These observations suggest that the cracks tend to initiate at/near the grain boundaries, and propagated along grain boundaries decorated with precipitates in relatively macroscopic length scale, while the fracture occurred intragranularly in microscopic scale, associated with dimple appearances because of the large plastic deformation localized around the precipitates.

Kurosu et al. [34] showed that cracks in a Co–29Cr–6Mo–0.14N alloy initiated at grain boundaries and annealing twin boundaries, and then propagated along the interface between the γ-fcc matrix and the SIMT ε-hcp phase on {111} and annealing twin boundaries, resulting in an occurrence of a quasi-cleavage fracture. Lee et al. [35] made a similar conclusion for the cracks formed in Co–Cr–Mo–N alloys. In their studies, the matrix was the γ-fcc phase, and SIMT always occurred on the {111} plane of the matrix owing to low *SFE* in the Co–Cr–Mo alloy, which was the main reason for the quasi-cleavage fracture. However, in the EBM-built Co–Cr–Mo alloys used in our study, even though the matrix was in the single γ-fcc phase in the 90°-sample, the quasi-cleavage fracture character was not found. In the EBM-built Co–Cr–Mo alloys, carbide, and nitride precipitates are dispersed in the matrix, and grain boundaries are decorated with carbide particles and rods. For the 90°-sample of γ-single phase, as the precipitates on the {111} plane of the γ-fcc matrix would impede the shear deformation on the {111} slip plane, SIMT could not occur (Fig. 6-8k) and certainly would not propagate along the interface between the γ-fcc matrix and SIMT ε-hcp phase on {111} to form a quasi-cleavage fracture. For the age-treated samples, the matrix phase had already transformed to a single ε-hcp phase, and thus no SIMT was possible. The grain interior did not deform much because of the restriction of a limited slip system in the hcp-structure and the low value of *SFE* at 700 ℃, as mentioned above. The limited slip system resulted in the incompatibility of plastic deformation across grain boundaries and thus high stress concentrated. Also, the carbides decorating the grain boundaries increased the incompatibility of the plastic deformation across the grain boundaries. Therefore, the cracks were inclined to initiate along the grain boundaries. However, large plastic deformation could take place in the vicinity of a crack because a dislocation slip was not difficult under high stress owing to the stress concentration near crack tips. Voids could initiate around the precipitates as a result of large plastic deformation near the crack tip, and their growth and coalescence along the grain boundaries would lead to final fracture. The above should explain the apparent discrepancy between the low ductility and the ductile fracture surface of the EBM-built Co–28Cr–6Mo–0.23C–0.17N alloy with an ε-hcp phase deformed at 700 ℃.

6.4.1.4 Crystal orientation

The phase transformation from γ-fcc to ε-hcp with S–N orientation relationship is modeled in Fig. 6-21. This is in order to examine the possible orientation dependence of tensile properties for the case the phase transformation occurred by isothermal martensitic transformation with holding S-N relationship, which was actually observed at the bottom part of the as-EBM-built sample (Fig. 5-8). The basal plane of ε-hcp corresponds to four nonparallel {111} planes, α, β, γ, and δ of parent γ-fcc. Hereafter, the four ε-hcp variants corresponding to α, β, γ, and δ of parent γ-fcc were designated as ε_α, ε_β, ε_γ, and ε_δ, respectively. $M_{23}C_6$ carbides were supposed to align along [001] direction of parent γ-fcc discontinuously, and distribute in the parent γ-fcc with the equal intervals of 3 μm, as shown in Fig. 6-21(a,b).

Fig. 6-22 shows the carbide array on the basal plane of ε_α, ε_β, ε_γ, and ε_δ. The arrows indicate the slip directions of perfect dislocations with the two highest Schmid factors for basal slip in 0°-, 45°-, 55°-, and 90°-samples. Arrows and corresponding built-angles are shown with same color. When the two slip directions are both same for different built-angles, one same color is used for the different built-angles. Because the angles between [001] direction of carbide array and normal of the four {111} planes (i.e. α-, β-, γ-, and δ-planes) on parent γ-fcc phase are equally 54.76 °, the cross section of carbides on basal planes were the same. In the meantime, owing to the assumption of regular arrangement of carbides, the carbide array on the basal plane of ε_α, ε_β, ε_γ, and ε_δ are exactly the same. This suggests that there is no difference in the effect of carbide arrangment on dislocation slip in the different ε-variants. There are slight differences in the carbide intervals along the slip direction in the different variants because of the elongated cross section shape of the carbide on the slip plane. But they can be neglected because of the small size of carbide compared to the carbide-carbide intervals and its fluctuation. Therefore, only the effect of Schmid factor on the dislocation slip should be considered.

Schmid factor μ for basal <**a**> system of ε_α, ε_β, ε_γ, and ε_δ are shown in Table 6-3. The loading axes in 0 °-, 45 °-, 55 °-, and 90 °-samples are supposed to be [001], [011], [111], and [010] of parent γ-fcc, respectively. The maximum μ was 0.408 for 0 °-, 45 °-, and 90 °-samples, while it was 0.272 for 55 °-sample. This suggests that the dislocation in 55 °-sample was the most difficult to slip. Supposing the probabilities for ε_α, ε_β, ε_γ, and ε_δ are the same, only 50% grains in 45 °-samples will deform according to the Schmid factor, while 33.3% grains for 55 °-sample, 100% grains for 0 °- and 90 °-samples. Therefore 45 °-samples would be much difficult to deform than 0 °- and 90 °-samples, though their maximum Schmid factors are the same. Based on the discussion above, the strength is expected to be high in the order of 55 °-, 45 °-, and 0 °- or 90 °-samples.

When the grain orientation of ε-hcp was random as a result of the diffusive transformation, such an orientation dependence of strength would diminish. However, the order of the strength of samples was similar to those expected for the case of S-N relationship. This suggests that some portions of the ε-phase grains formed by the aging-treatment are formed by isothermal martensitic transformation holding the S-N relationship.

Also, it is suggested that the conditions of heat treatment to homogenize the microstructure throughout the height of EBM-built object should be determined by taking into account the thermal history during the post-melt period of the EBM process especially when the solid-solid transformation is sluggish.

6.4.2 Effect of inhomogeneous microstructure on creep behavior

Here, the effect of inhomogeneous grain size on creep rupture is discussed based on the grain structures on both sides of fracture. Fig. 6-23(a) shows the schematic of the positions for grain structure observation in the fracture specimens. The center of the observation area was 1.55 mm away from the fracture position. Fig. 6-23(b) shows the grain sizes on both sides of the fracture in different crept specimens. The distribution of grain size throughout the whole height before creep test is also shown together in Fig. 6-23(b) for comparison. The fracture position is between the two observation positions of each sample. The grain size of each point in Fig. 6-23(b) is taken the average grain size of the observation area with 3.1 mm×3.1 mm on the longitudinal cross section. Fig. 6-23(a) indicates that the fracture was within the homogeneous fine grain region which used to be single γ-fcc phase before aging treatment in all the samples except for the one crept at 700˚C with the 270 MPa load. The grain sizes after creep are very close to the initial grain size, which suggests that the grain growth is not so significant. The probable reason is that the carbides on the grain boundaries inhibit the grain boundary migration and dislocation motion.

On the other hand, grain refinement by recrystallization which usually occurs after large deformation, does not occur either. This is because the creep strains of the specimens were very low, ranging from 1.11% to 1.68% for all the temperature and applied stress examined. Local large straining, such as shrinking of cross section (i.e. necking) near the fracture was not observed either. As a result, the grain size did not change during creep test. It should be mentioned that the grain sizes on the lower side of the sample crept at 700˚C under the stress of 240 MP and those in the sample crept at 700˚C under the stress of 270 MP are larger than the grain sizes before creep. These may be caused by the fluctuation of the grain size in different samples before creep test.

Because of oxidization, it is difficult to observe the fresh fracture surface. Instead, the cross sectional microstructure in the adjacent area of fracture surface was investigated by EBSD to examine the crack path. Fig. 6-24 shows EBSD analysis result of the longitudinal cross-section microstructure near the fracture position of specimens at 650 ˚C under stress of 240 MPa as an example. The IPF map (Fig. 6-24 (a)) clearly indicates that crack propagated along grain boundary. In the kernel average misorientation (KAM) map (Fig. 6-24 (b)), it appears that the KAM values are high in the vicinity of grain boundaries as generally observed in deformed polycrystal metals. When the KAM distributions is examined carefully, it is noticed that KAM values are not always high on both side of grain boundaries, i.e. KAM on one size of grain boundaries are much lower than on the opposite side of many grain boundaries. This suggests that the plastic deformation of a grain did not propagate across such grain boundaries, which leads to the incompatibility of strain at grain boundaries and the intergranular fracture. The possible reasons for this incompatible straining across grain boundaries and resultant grain boundary fracture include of limited slip systems in ε-hcp phase, dispersed $M_{23}C_6$ and M_2N precipitates and lower stacking fault energy. The intergranular fracture in creep test is consistent with that in tensile test at 700 ˚C (Fig. 6-9).

The preferential occurrence of fracture within the fine grain region is understood as in the following. During creep deformation under high temperature and low stress, the relative sliding of grains i.e. grain boundary sliding can proceed sufficiently with the assist of grain boundary diffusion. This promotes the initiation and propagation of void at triple junction of grain boundaries, which can develop into cracks and initiate the intergranular fractures which were observed in the specimens examined. This mechanism can take place more easily in fine grains than in the coarse grains. In the meantime, the fine grains have more grain boundaries than coarse grains in a unit volume, which can increase the crack occurrence site. In addition, grain boundaries are more flat in fine grain region than in coarse grain region, which leads the crack propagation to be easier. These factors may be the reason for the high occurrence probability of fracture in fine grain region.

Based on the above discussion, the effect of microstructure inhomogeneity on creep behavior is essentially the effect of grain size on creep behavior. This implies that the creep rupture life can be improved by increasing the grain size. The process to obtain coarse grains in the bottom part of EBM-built rod gives enlightenment how to obtain coarse grains by heat treatment. That is two-step aging heat treatment (Fig. 5-7 (e,f)). ε-hcp nucleus keeping S-N relationship with parent γ-fcc phase can be formed by directional annealing at lower temperature (for example, 700 ˚C), then the ε-hcp grains can grows coarser by isothermal aging heat treatment at higher temperature (for example, 800 ˚C), until the completion of phase transformation from γ-fcc to ε-hcp.

6.4.3 Effect of stacking fault on creep deformation

Fig. 6-25 shows TEM bright-field images of 0°-sample crept at different conditions. The TEM samples were taken near the fracture position. Straight line contrast was always parallel to (0001) plane trace when the incident beam direction **B** was near $[2\bar{1}\bar{1}0]$, which indicates that basal slip was operated during creep deformation. This may be related to very low stacking fault energy (*SFE*) of ε-hcp phase at creep test temperature range.

The *SFE* of ε-hcp in different temperatures is shown in Table 3. *SFE* of ε-hcp was only 37.8 mJm^{-2} at 650 ˚C, and decreased with increasing temperature, which means Shockley partial dislocation pair will expand wider with increasing temperature.

Based on isotropic elasticity theory [36], the width of stacking fault can be express by

$$d=\frac{G_{\mathrm{eff}}b_{\mathrm{p}}^{2}}{8\pi\gamma}\frac{2-\upsilon_{\mathrm{eff}}}{1-\upsilon_{\mathrm{eff}}}\left(1-\frac{2\upsilon_{\mathrm{eff}}\cos 2\beta}{2-\upsilon_{\mathrm{eff}}}\right) \tag{6.6}$$

where γ is the *SFE*, b_p is the $a/3\langle 10\bar{1}0\rangle$ partial dislocation Burgers vector, and β is the angle between Burgers vector and dislocation direction. υ_{eff} is the effective Poisson ratio and G_{eff} is the effective shear modulus, which can be obtained by Young's modulus measurement, as shown in Table 6-2. For the cases of edge and screw dislocation, the width of stacking fault at different temperatures is shown in Table 6-5.

The stacking fault can exist only when its width is twice larger than the atom diameter (i.e. 0.5252 nm), therefore, the screw dislocation actually do not dissociate at temperature lower than 720 ˚C, which make it possible for cross slip of dislocations on the basal plane to the prism plane. However, during the course of creep, deformation is controlled by climb of edge dislocation, which can dissociate into Shockley partial dislocation pair and expand widely in the temperature range of 650–800 ˚C. As a result, basal slip becomes the dominant.

The effective activation energy of creep is usually closed to self-diffusion activation energy [37]. However, the apparent activation energy of creep for CCM alloy (365 $kJmol^{-1}$) in this research is much larger than the self-diffusion activation energy of pure cobalt (274$kJmol^{-1}$ [38]). The increased part is thought to be partly caused by *SFE,* which can also affect minimum creep rate. When the edge dislocation dissociate to Shockley partial dislocation pair, the climb of extended edge dislocation needs the nucleation of prismatic vacancy loops at one of the Shockley partial dislocation and its propagation across the stacking fault toward the other partial [39]. The spontaneous emission of supersaturated vacancies is necessary to complete the propagation of prismatic vacancy loops. Therefore, emission of vacancies is restricted by stacking fault. As a result, apparent activation energy is much higher than that of self-diffusion activation energy.

Though atom vibration increases significantly with increasing temperature, which may shrink the width of stacking fault, Shockley partial dislocation pair can still expand widely at higher temperature because the *SFE* of ε phase decreases with increasing temperature. Hence, the stacking fault still has strong effect on the dislocation recovery at higher temperature and the minimum creep rate at higher temperature will not increase significantly.

The effect of stacking fault energy on minimum creep rate can be described as[40]

$$\frac{\dot{\varepsilon}_{\mathrm{m}}\mathrm{k}T}{D_L Gb}=\mathrm{A}\phi\left(\frac{\gamma}{Gb}\right)\left(\frac{\sigma}{G}\right)^{\mathrm{n}} \tag{6.7}$$

where D_L is the diffusion coefficient, Φ means a function of (γ/Gb), which is usually expressed as[41]

$$\phi\left(\frac{\gamma}{Gb}\right) = \left(\frac{\gamma}{Gb}\right)^{\mathrm{m}} \tag{6.8}$$

m can be determined to be -2.3 by the relationship between $\ln(\dot{\varepsilon}_m \mathrm{kT}/\ D_L Gb\ )$ and $\ln\ (\gamma/Gb)$ under the stress of 240MPa, as shown in Fig.6-26(a). The negative value of m indicates the reciprocal variation trend for *SF* with increasing temperature. For the fcc metals, m is usually 2-3.5 [39,41,42]. The opposite sign in this research is related to the abnormal variation (i.e. *SFE* decreases with increasing temperature) of *SFE* with temperature for CCM alloy with ε-hcp phase. Assuming the effect of stacking fault on atom diffusion by can be express as

$$\left(\frac{\gamma}{Gb}\right)^{-2.3} = \mathrm{A}exp\left(-\frac{Q_{SF}}{\mathrm{R}T}\right) \tag{6.9}$$

where Q_{SF} is the increased activation energy for atom diffusion generated by stacking fault. Q_{SF} can be determined to be 86 kJ/mol by the relationship between $\ln\ (\gamma/Gb)^{-2.3}$ and ln(1/T), as shown in Fig.6-26(b).

6.5 Conclusions

High temperature mechanical properties of Co-Cr-Mo alloy fabricated by EBM have been investigated and the following conclusions have been obtained.

(1) The γ-fcc matrix phase could be wholly transformed into ε-hcp phase after aging treatment at 800 ℃ for 24 h. No significant preferential orientation was recognized in the ε grains of the aged samples. Also, lamellar colonies

composed of M_2N precipitates and the ε-hcp phase appeared in the matrix after aging treatment. M was determined to be Cr, Mo, or Si in M_2N nitride.

(2) In the rod with aging treatment at 800 ℃ for 24 h, the *ε*-hcp grain size increased along build height at first, then decreased gradually to the phase transformation position of *γ*-fcc to *ε*-hcp in the as-EBM-built rod, and maintained nearly constant in the initial single *γ*-fcc region. The reason for the grain size difference is that volume fraction of *ε*-hcp phase can increase more easily by the growth of preexisting *ε*-hcp grain than by the nucleation and growth of new ε-hcp grains.

(3) It is suggested that the conditions of heat treatment to homogenize the microstructure throughout the height of EBM-built object should be determined by taking into account the thermal history during the post-melt period of the EBM process especially when the solid-solid transformation is sluggish.

(4) The basal slip might be the unique deformation mode during high-temperature tensile deformation. The grain boundary slip did not occur at 700 ℃. The extremely low *SFE* and carbide array were the possible reasons for the poor ductility.

(5) All of the aged samples exhibited intergranular fracture. Voids were initiated around the precipitates and their growth and coalescence along grain boundaries led to final cracks.

(6) The sample built with 55° deviation from the *z* axis had the highest *UTS* of 806 MPa at 700 ℃ with a strain rate of 1.5×10^{-4} s^{-1}. The diffusive phase transformation does not weaken the anisotropic mechanical properties notably.

(7) In the rod with grain sizes varying along the build height, fracture in the creep process tended to occur in fine grain region which used to be single *γ*-fcc phase before aging treatment.

(8) Basal slip is main deformation mode in the course of creep at the temperature range of 650-800 ˚C because of the widely expanded Shockley partial dislocation pair.

(9) The creep curves exhibited typical three creep stages at all the investigated

temperature ranges (i.e. 650-800 ˚C) under the stress range of 240-330 MPa. The relation between minimum creep rate and applied stress could be described by the constitutive equation: $\dot{\varepsilon}_{\mathrm{m}} = \mathrm{A}\,\frac{\mathrm{G}\Omega}{\mathrm{b}^2\mathrm{k}T}\,(\frac{\sigma}{G})^{n} exp(-\frac{Q}{\mathrm{R}T})$. The stress exponent n and apparent activation energy Q were determined to be 5 and 365 kJ mol^{-1}, respectively.

(10) The decreased stacking fault energy with increasing temperature can keep Shockley partial dislocation pair expanding widely and inhibit dislocation climb at higher temperature. Therefore, the effect of stacking fault energy on minimum creep rate is recommended to express as: $\phi(\frac{\gamma}{Gb}) = (\frac{\gamma}{Gb})^{-2.3}$, and the increased activation energy for atom diffusion generated by stacking fault is 86 kJ/mol.

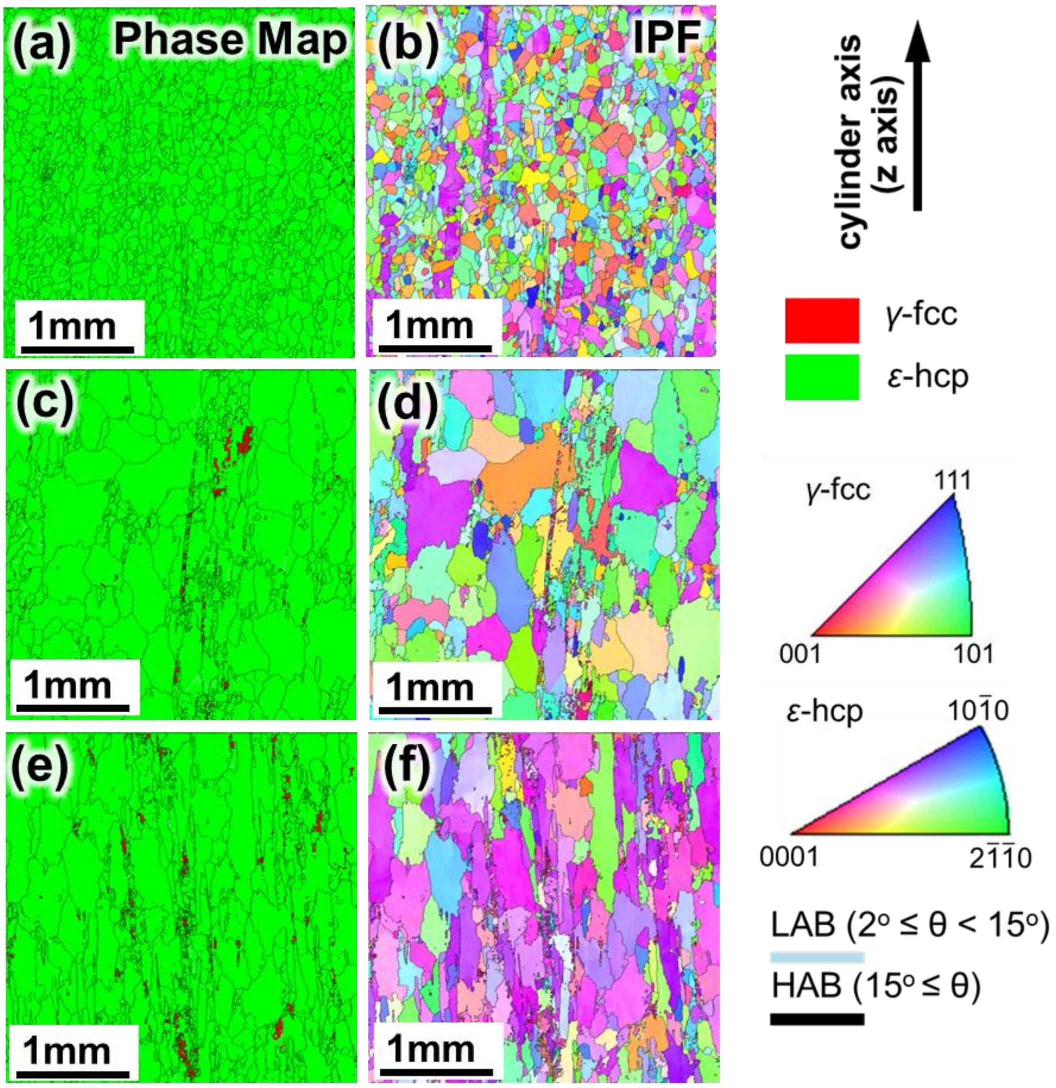

Fig.6-1. EBSD Phase maps (a,c,e) and (b,d,f) IPF maps on longitudinal cross section of different height of the rod after aging treatment at 800˚C, (a,b) top part, (c,d) center part, (e,f) bottom part.

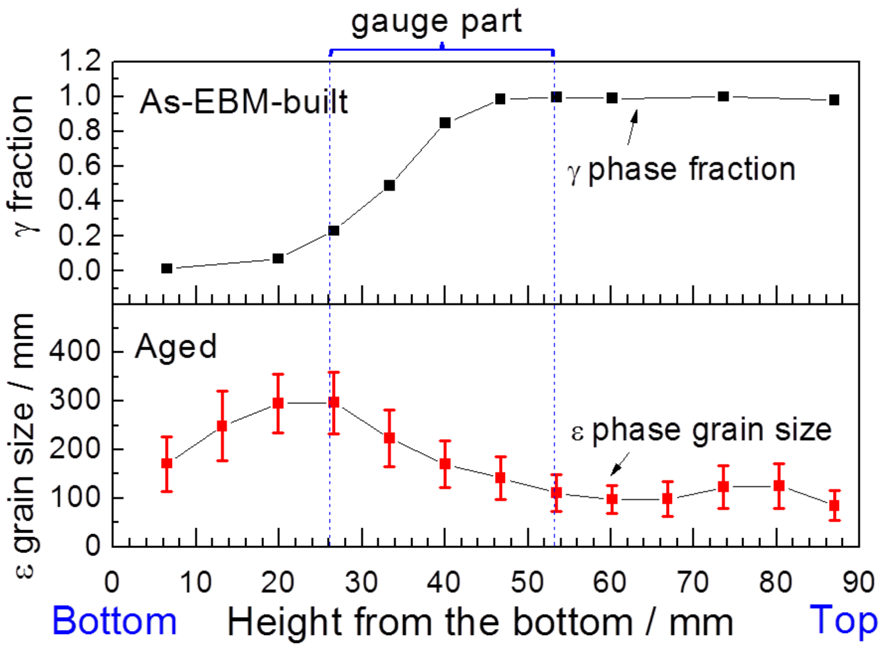

Fig.6-2. *γ* phase volume fraction variation in the as-EBM-built rod and *ε* phase grain size variation in the rod after aging treatment at 800˚C for 24 h.

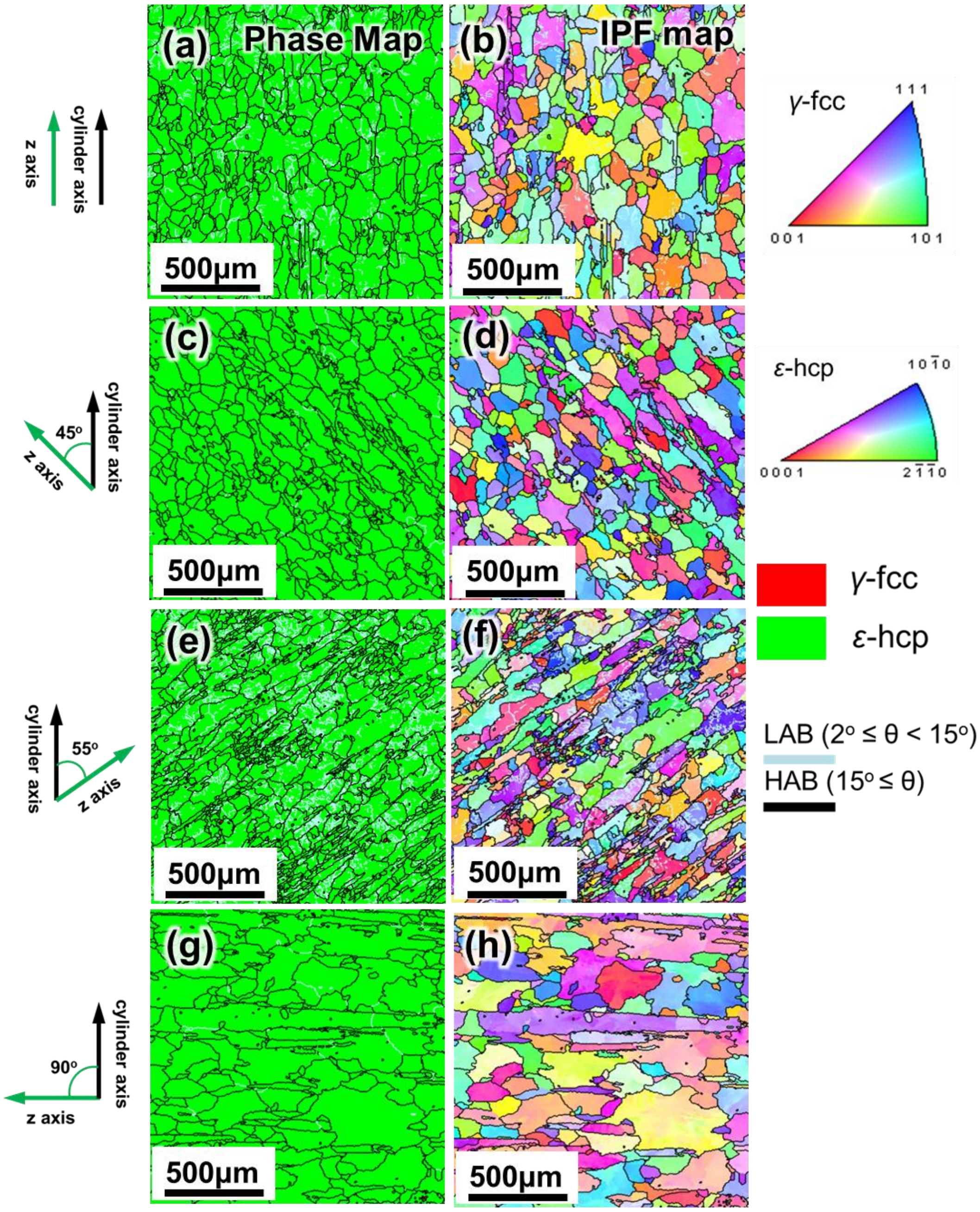

Fig.6-3. EBSD phase maps (a,c,e,g) and IPF maps (b,d,f,h) on the vertical cross section of top part of age-treated samples, (a,b) 0˚-sample, (c,d) 45˚-sample, (e, f) 55˚-sample, (g, h) 90˚-sample.

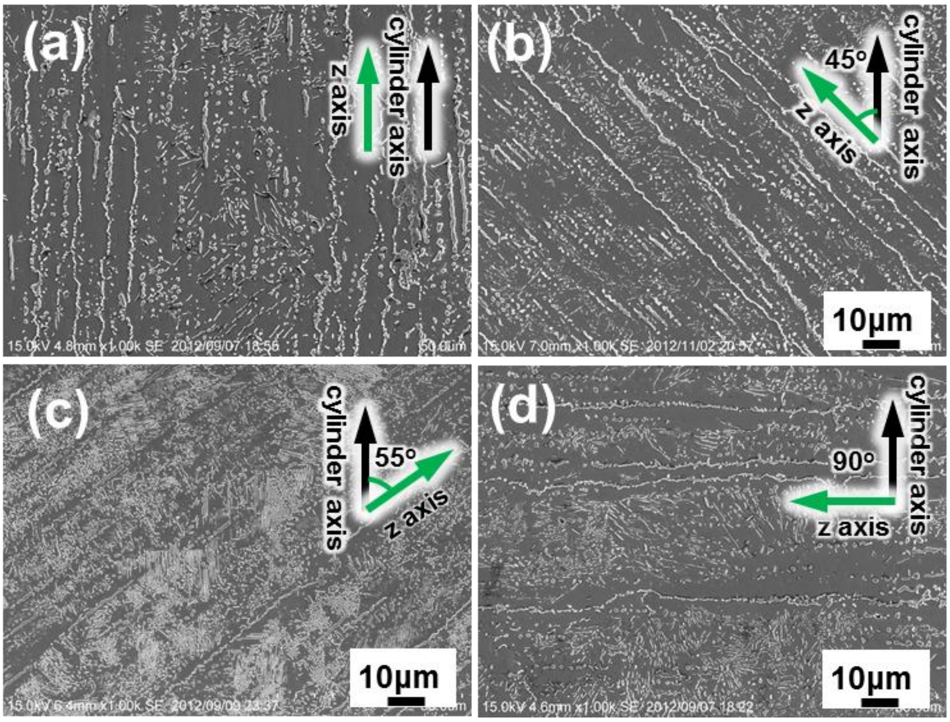

Fig. 6-4. SEM microstructures on the longitudinal cross-section of as-EBM-built samples (top part, about 75 mm from the bottom of the rods). (a) 0˚-sample, (b) 45˚-sample, (c) 55˚-sample, and (d) 90˚-sample.

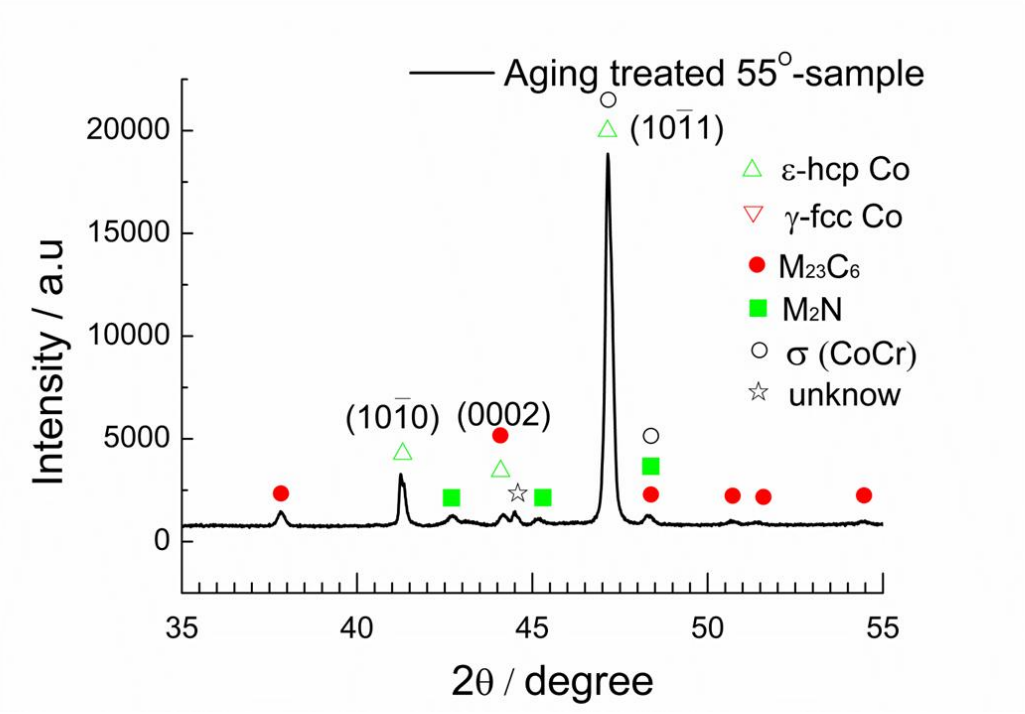

Fig. 6-5. XRD profiles on the vertical cross-section of 55˚-sample aged at 800˚C for 24 h.

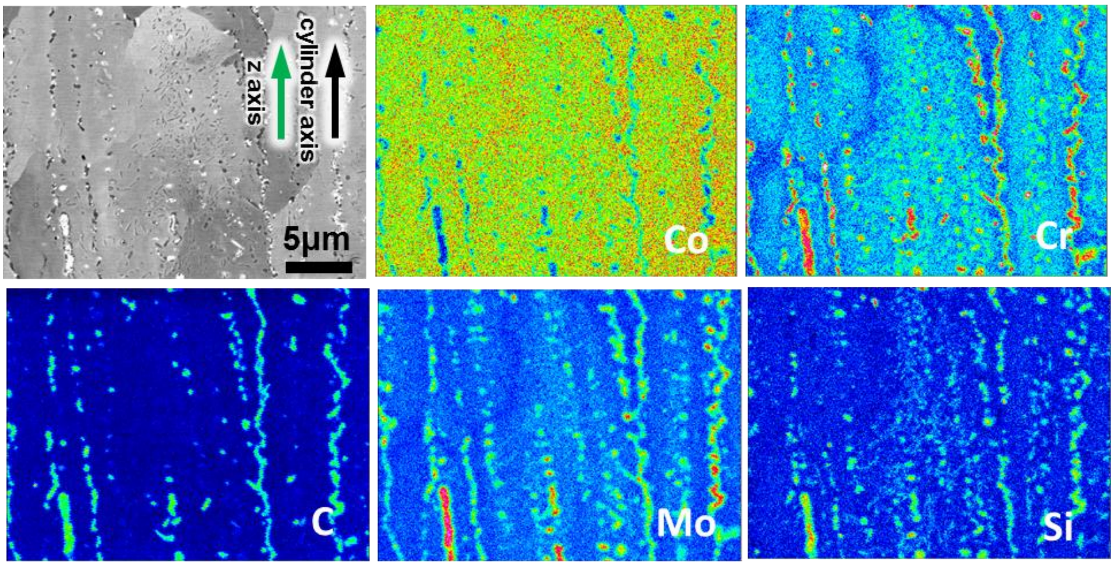

Fig. 6-6. EPMA element maps on the vertical cross section of 0˚-samples aged at 800˚C for 24 h.

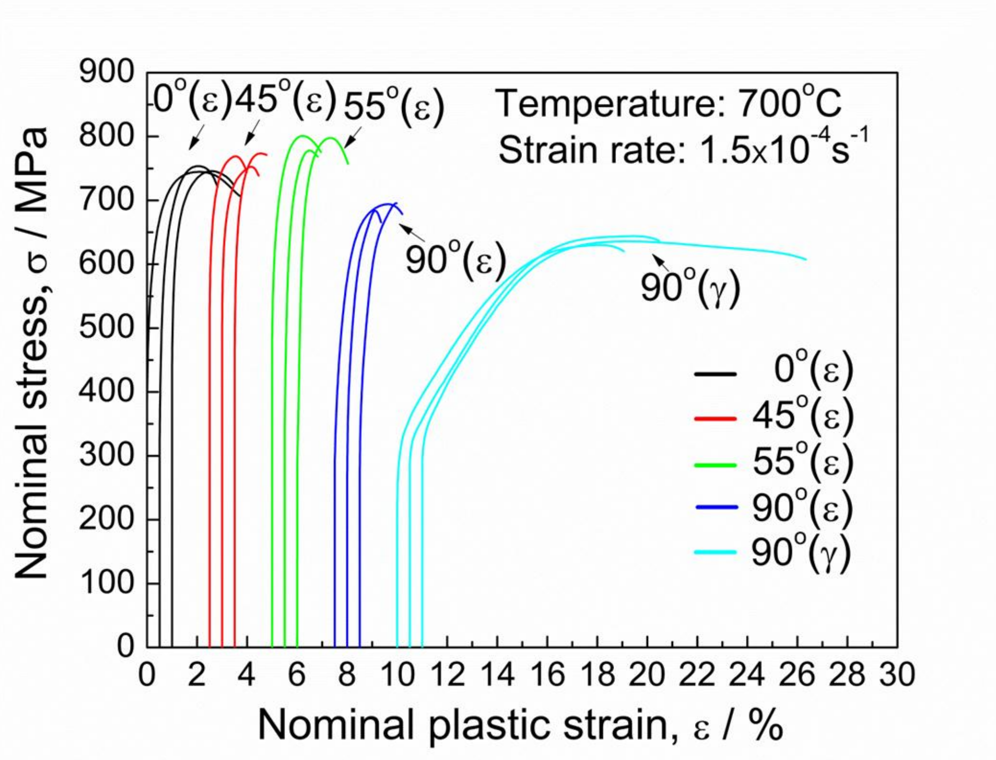

Fig. 6-7. Stress-strain curves of 0˚-, 45˚-, 55˚-, and 90˚-samples at 700 ˚C with strain rate of 1.5×10^{-4} s^{-1}.

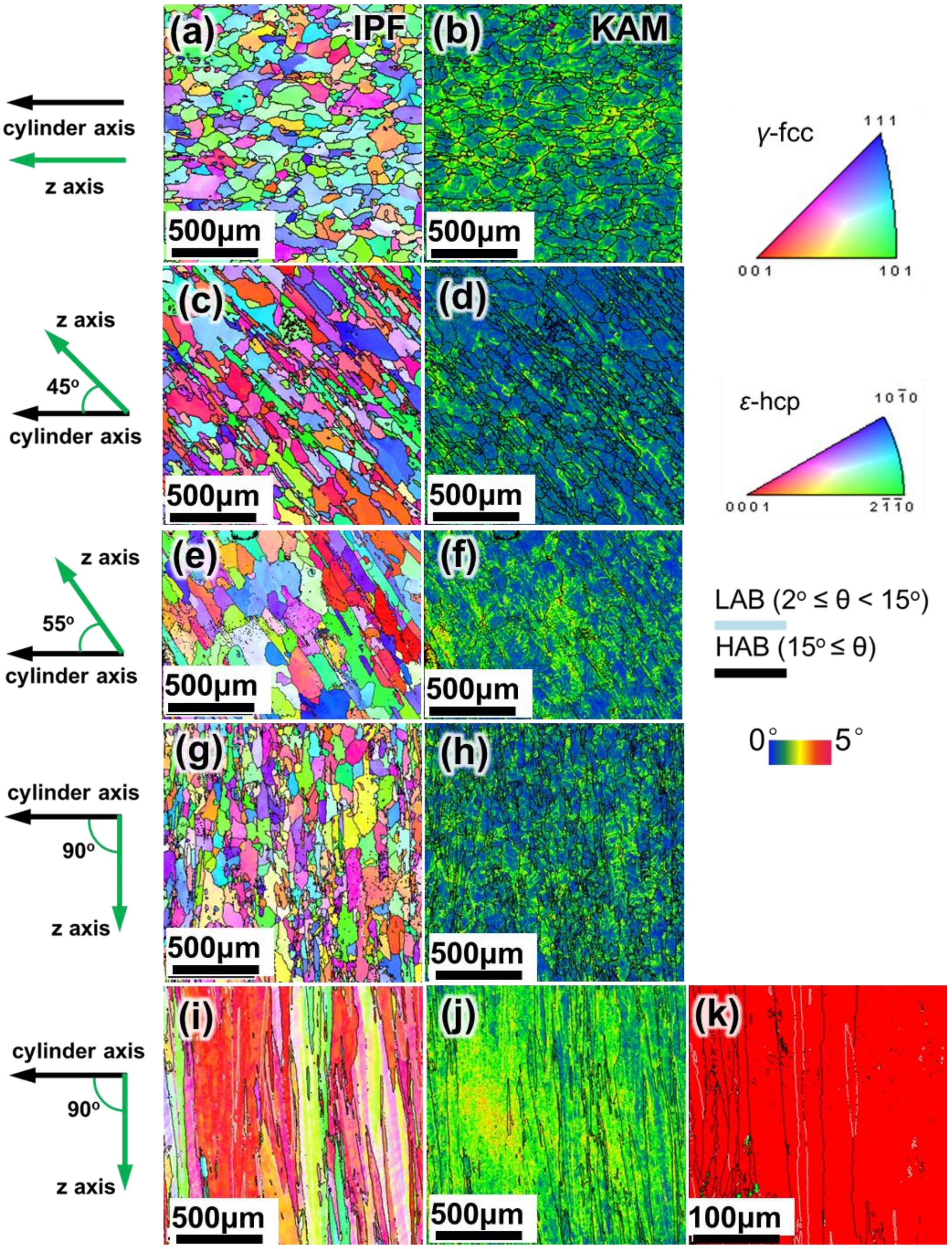

Fig. 6-8. EBSD IPF maps (a, c, e, g, and i), KAM maps (b, d, f, h, and j), and IQ + phase map (k) of samples after tensile test: (a, b) 0˚-sample; (c, d) 45˚-sample; (e, f) 55˚-sample; (g, h) 90˚-sample with ε matrix; (i, j, k) 90˚-sample with γ matrix.

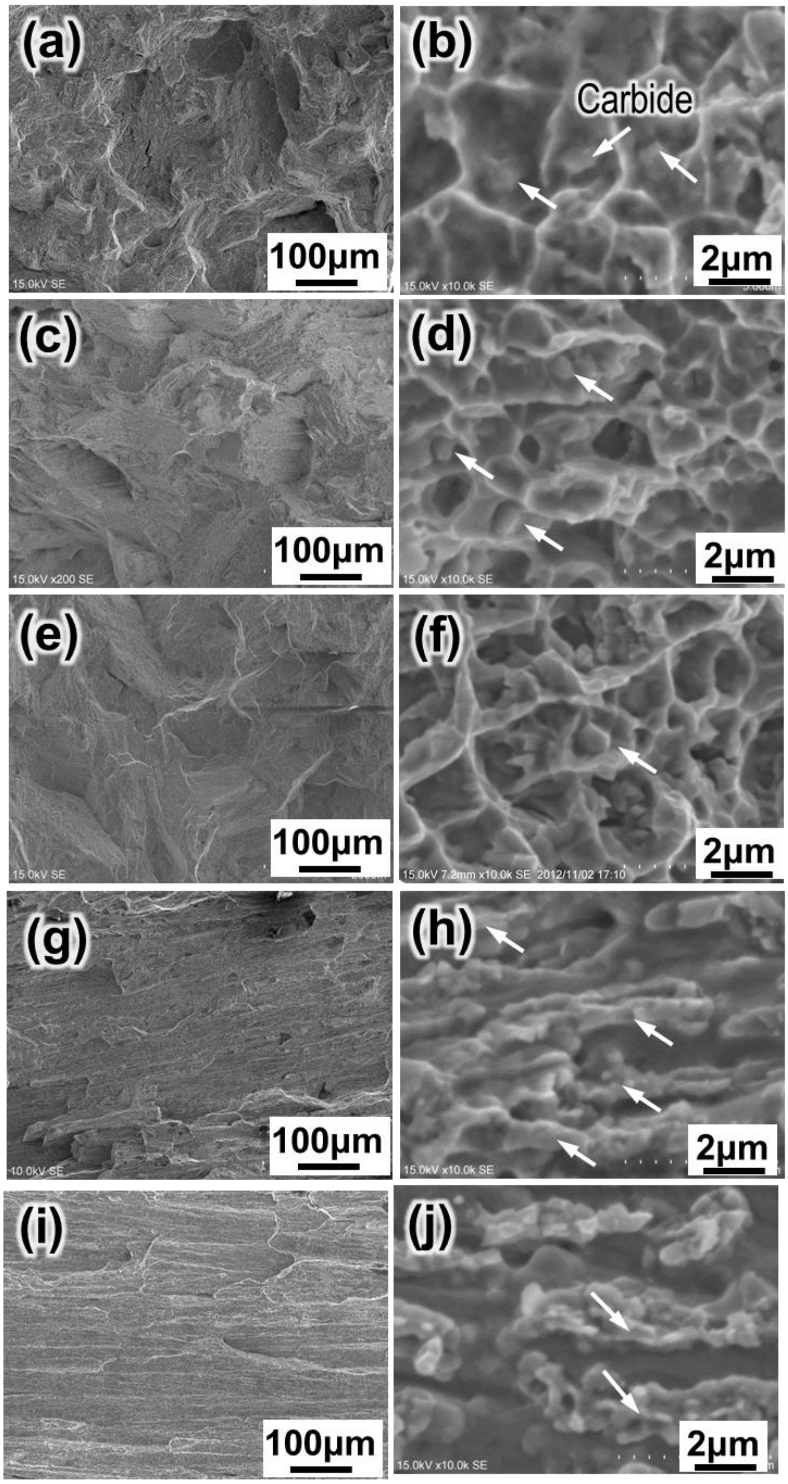

Fig. 6-9. Fracture surface morphology of samples after tensile test: (a, b) 0 °-sample; (c, d) 45 °-sample; (e, f) 55 °-sample; (g, h) 90 °-sample consisting of ε-phase; and (i, j) 90 °-sample consisting of γ phase.

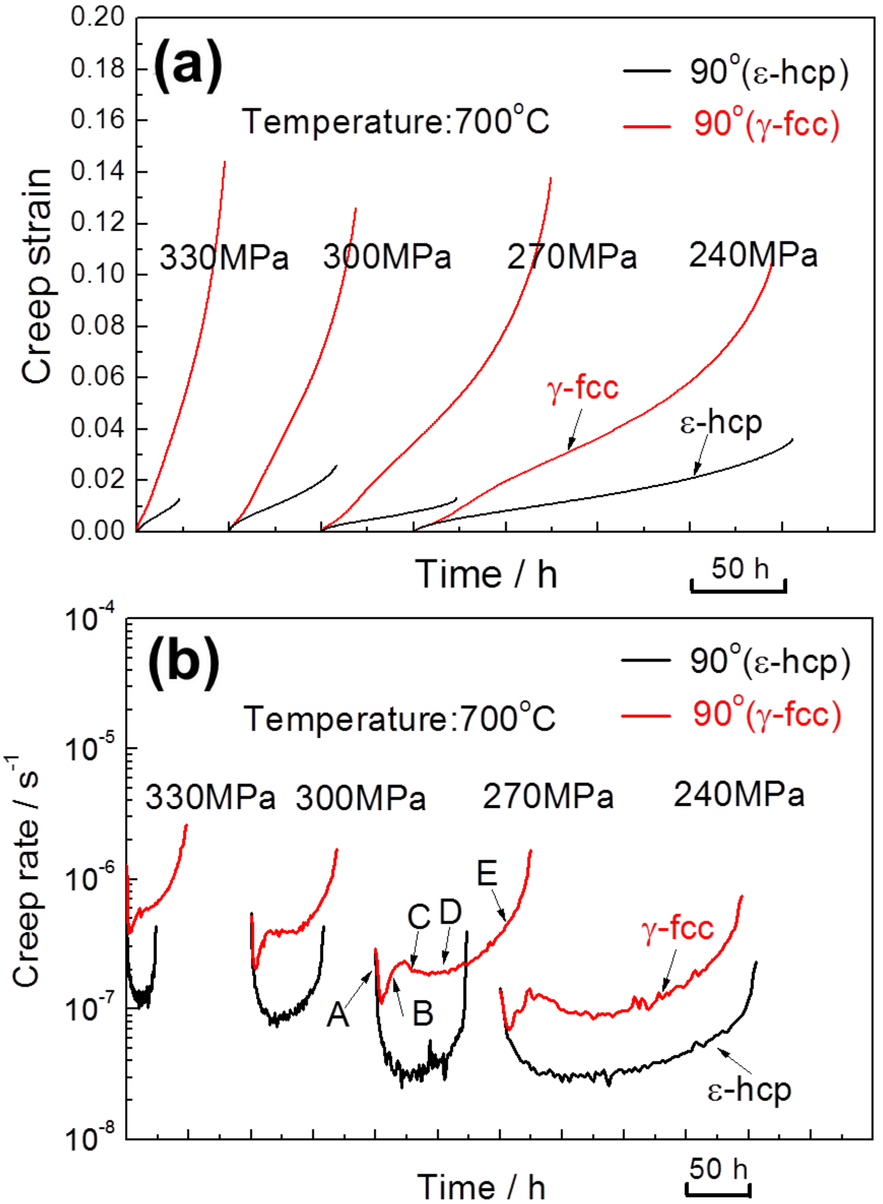

Fig. 6-10. Creep properties of 90 °-samples with different initial phases at 700˚C. (a) Creep curves at 700˚C with different stresses. (b) Creep rate variation with creep rupture time under different stresses.

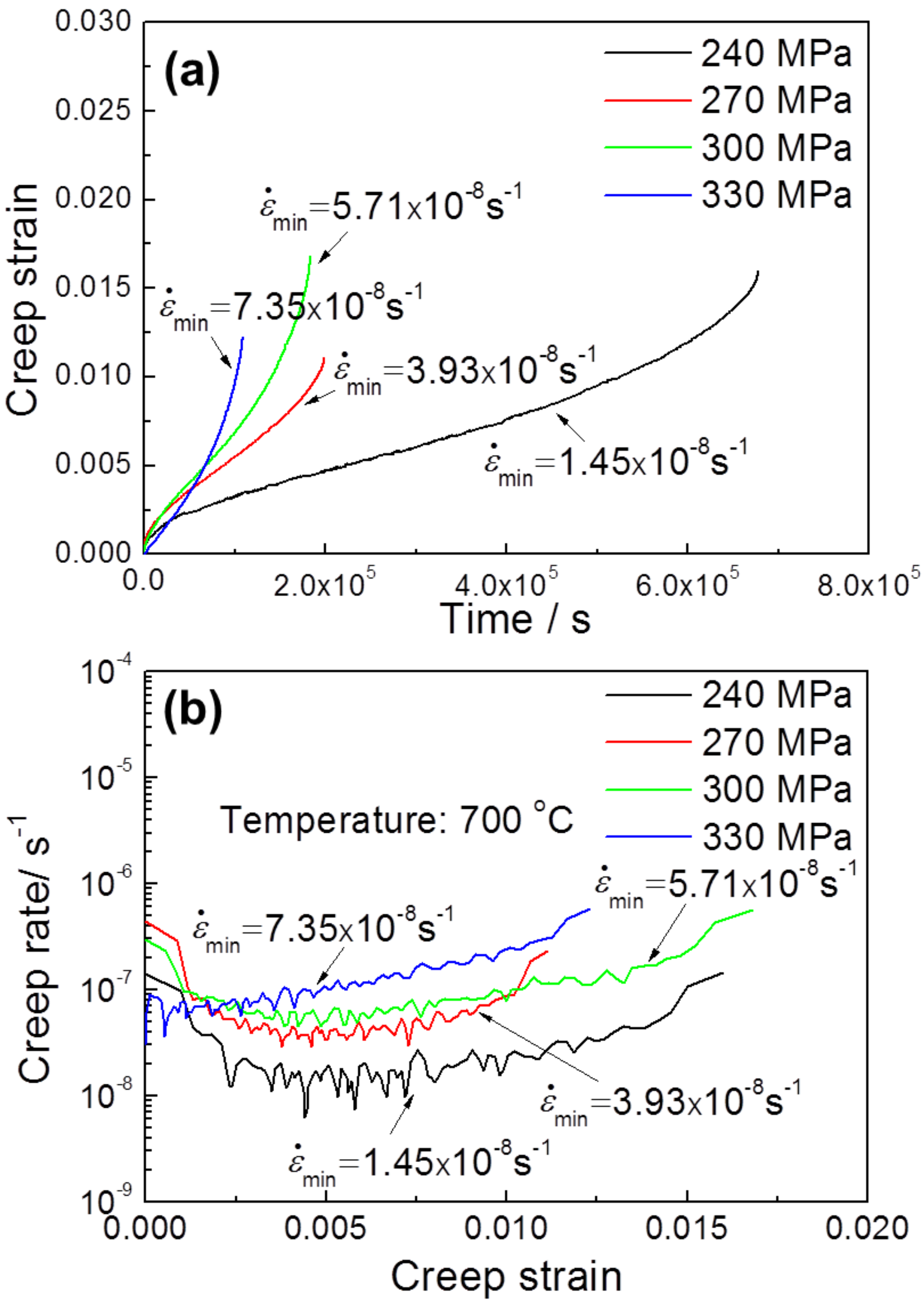

Fig. 6-11. (a) Creep curves of 0 °-sample crept at 700˚C with different stresses. (b) Creep rate variation with creep strain under different stresses.

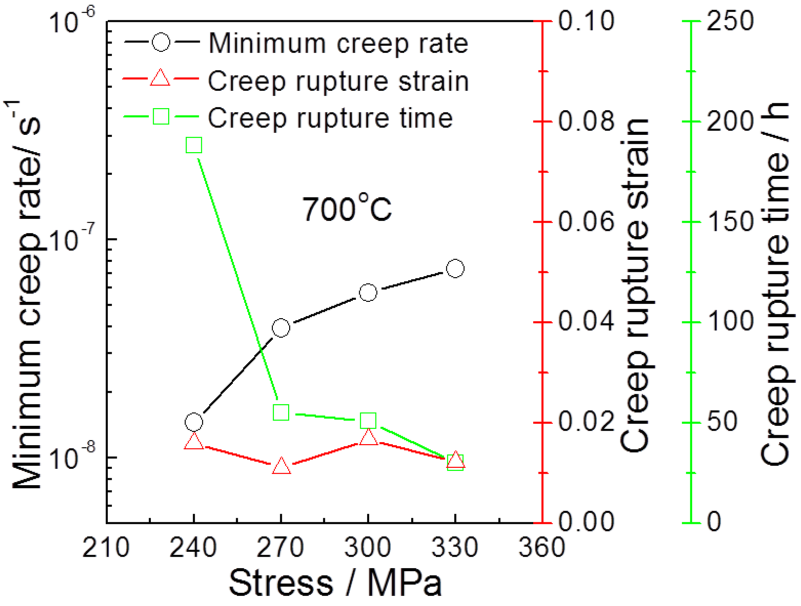

Fig. 6-12 Stress dependence of creep behavior of 0 °-sample at 700˚C

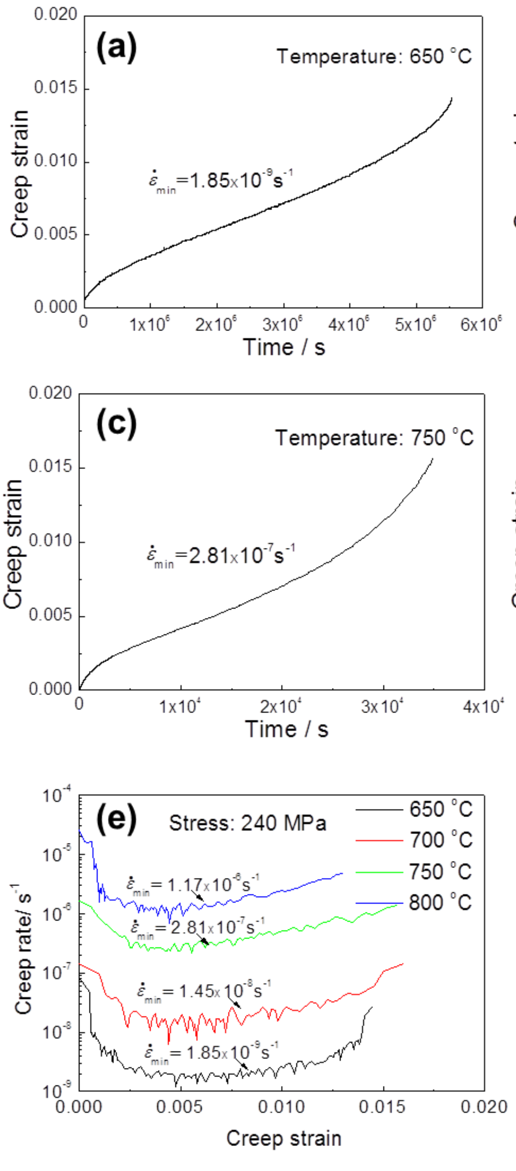

Fig.6-13. (a,b,c,d) Creep curves of 0 °-sample at 240 MPa with different temperatures, (a) 650˚C, (b) 700˚C, (c) 750˚C, and (d) 800˚C. (e) Creep rate variation with creep strain in different temperatures.

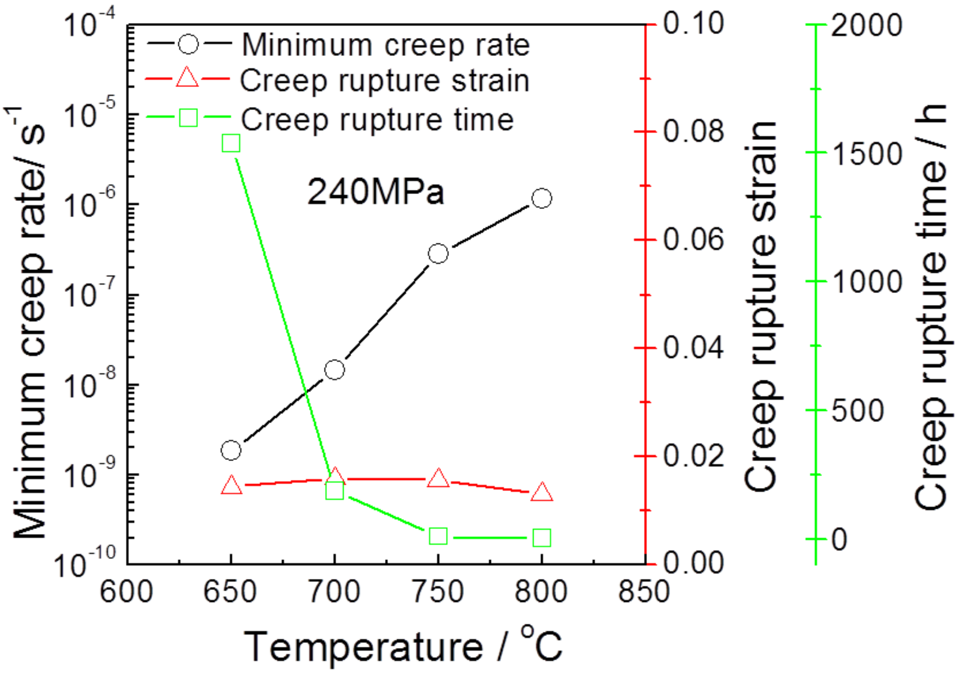

Fig. 6-14 Temperature dependence of creep behavior of 0 °-sample at 240MPa.

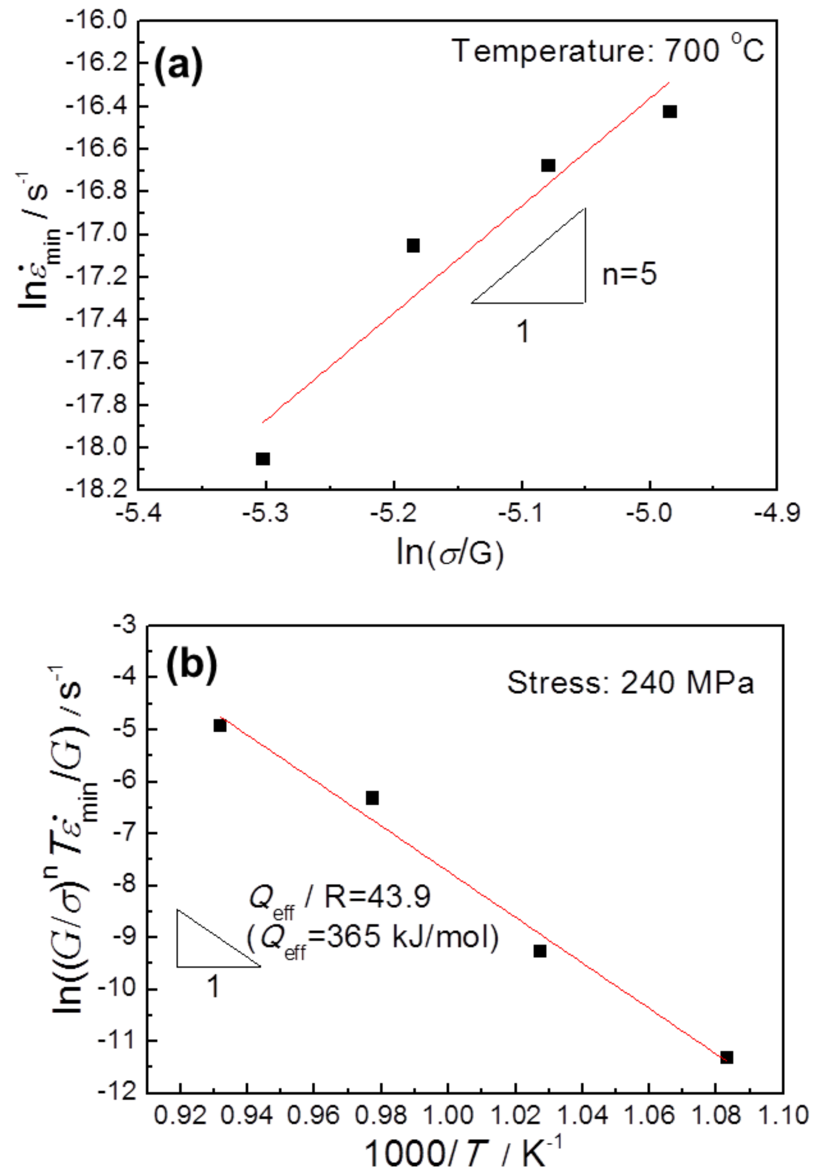

Fig.6-15. Variation of minimum creep rate with (a) applied stress and (b) temperature reciprocal.

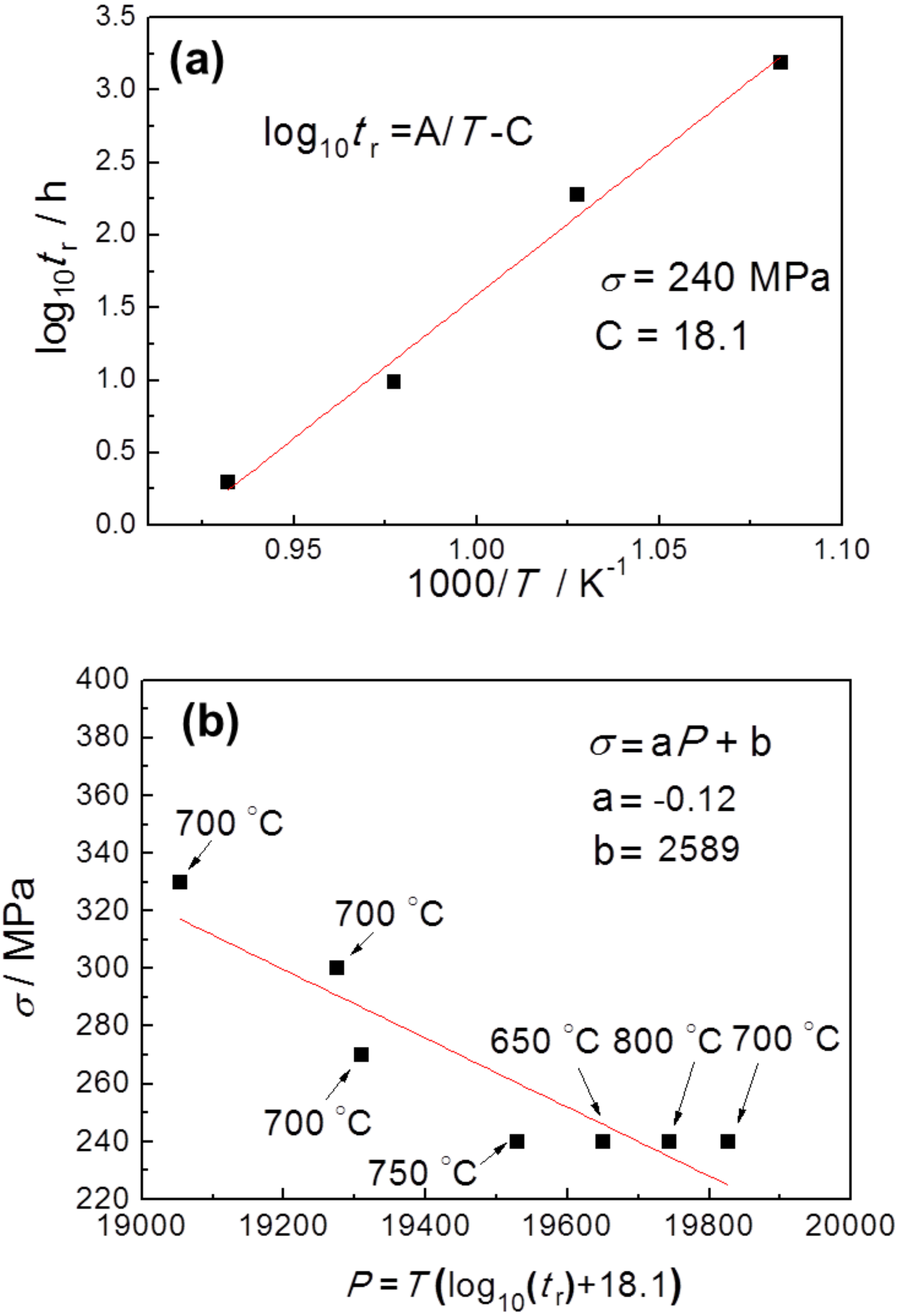

Fig.6-16. (a) Plots of creep rupture time (tr) and temperature reciprocal under stress of 240 MPa, (b) Relationship between experimental stress and Lason-miller parameter.

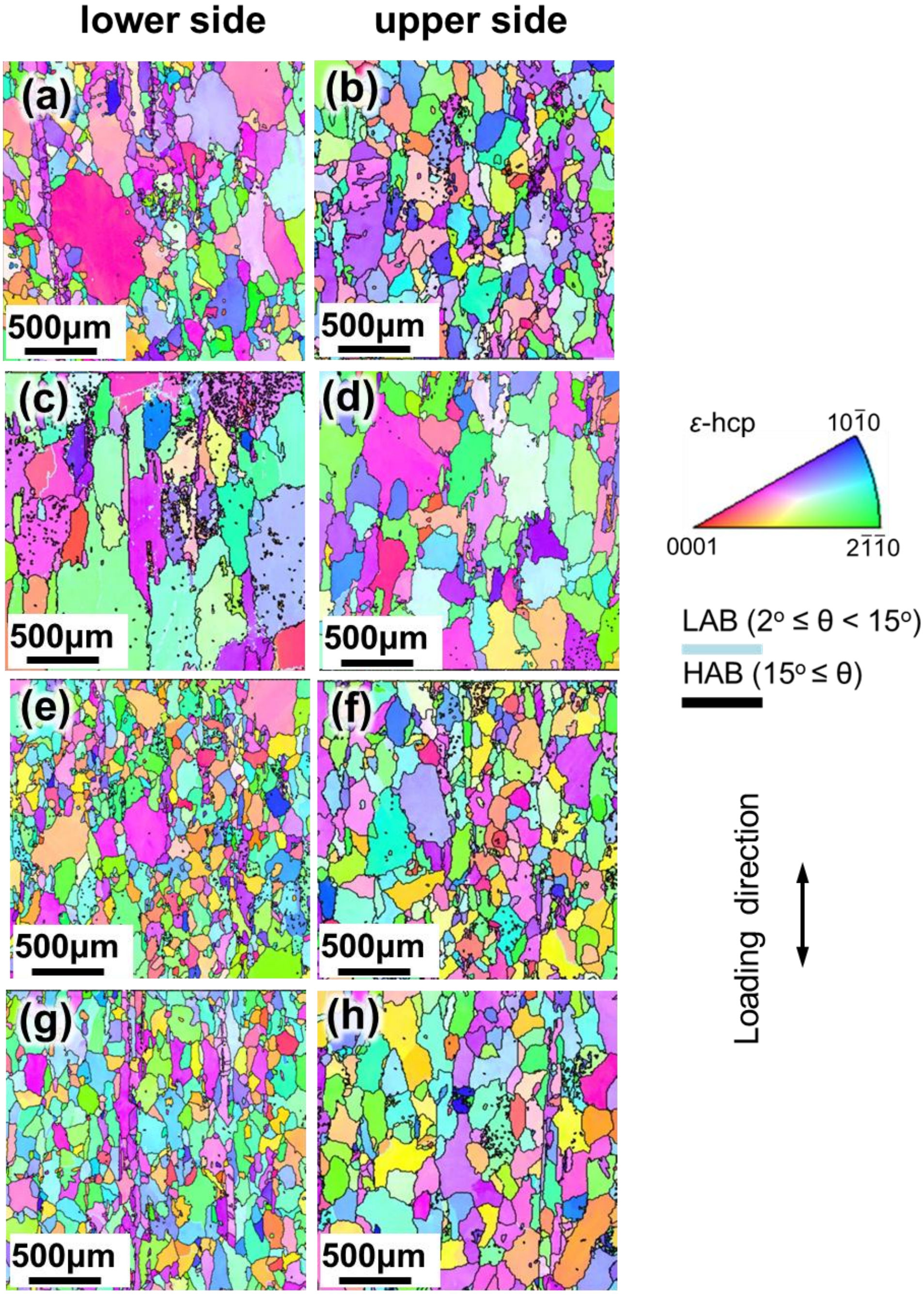

Fig.6-17. EBSD IPF maps of longitudinal cross-section microstructure on (a,c,e,g) upper sides and (b,d,f,h) lower sides of main cracks of 0 °-sample at 700˚C under different stresses, (a,b) 240MPa, (c,d) 270MPa, (e,f) 300MPa, (g,h) 330MPa

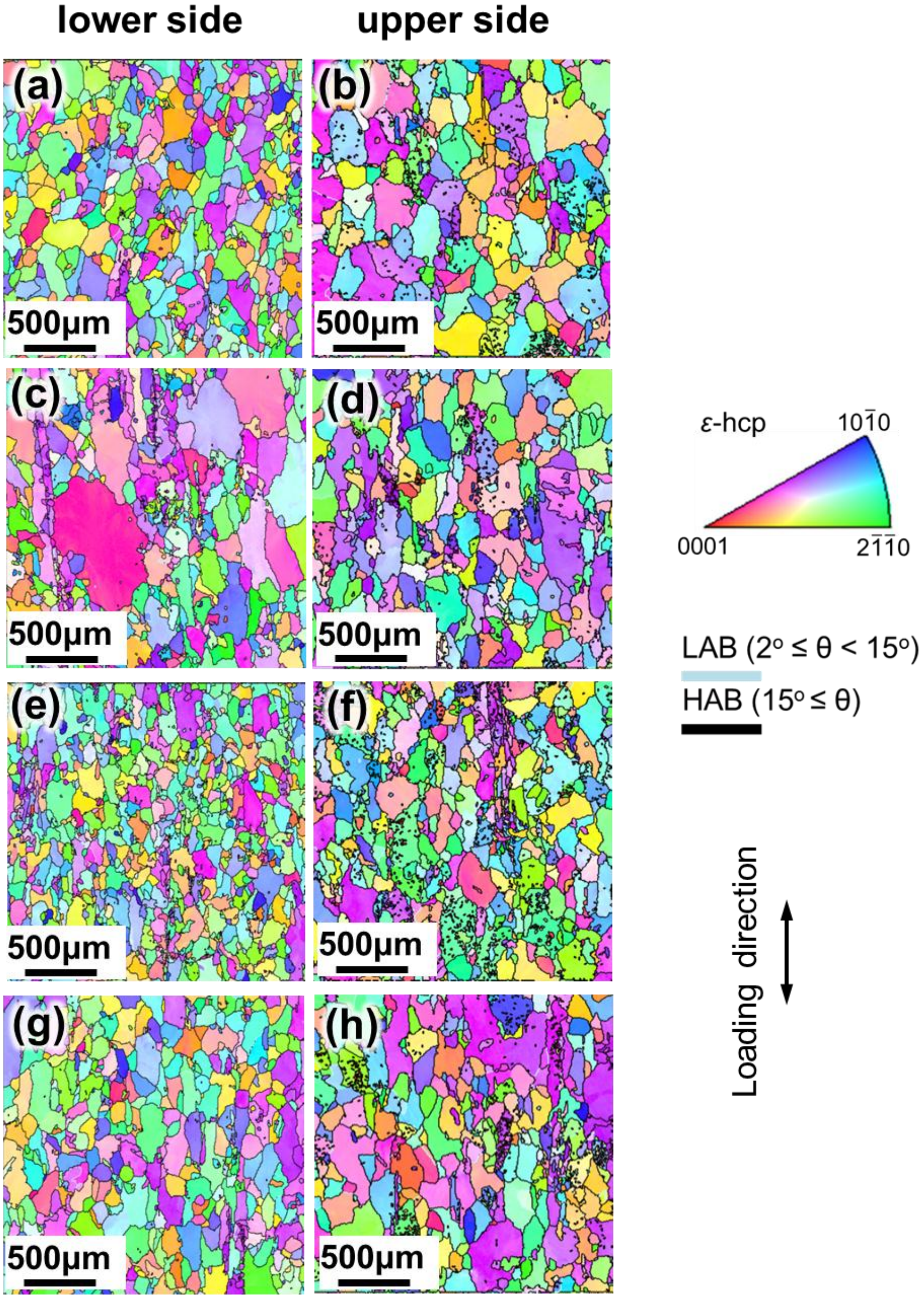

Fig.6-18. EBSD IPF maps of longitudinal cross section microstructure on (a,c,e,g) upper sides and (b,d,f,h) lower sides of main cracks of 0 º-sample under 240 MPa with different temperatures, (a,b) 650˚C, (c,d) 700˚C, (e,f) 750˚C, (g,h) 800˚C.

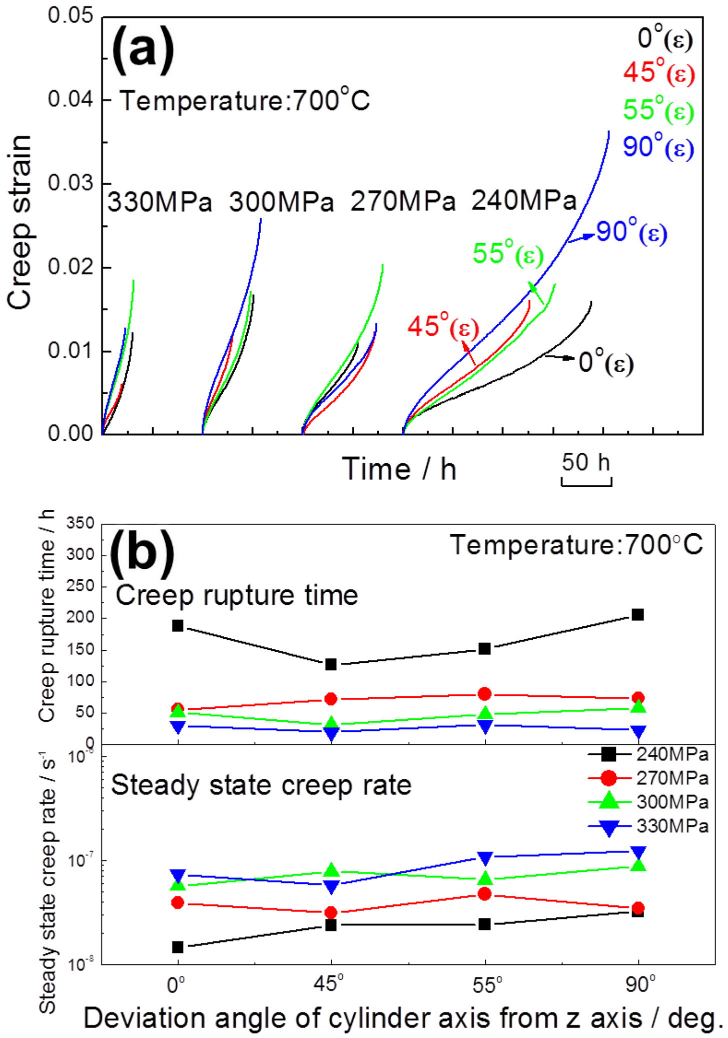

Fig. 6-19. (a) Creep curves of the samples with different build directions at 700˚C with different stresses. (b) Effect of build direction on creep rupture time and steady state creep rate.

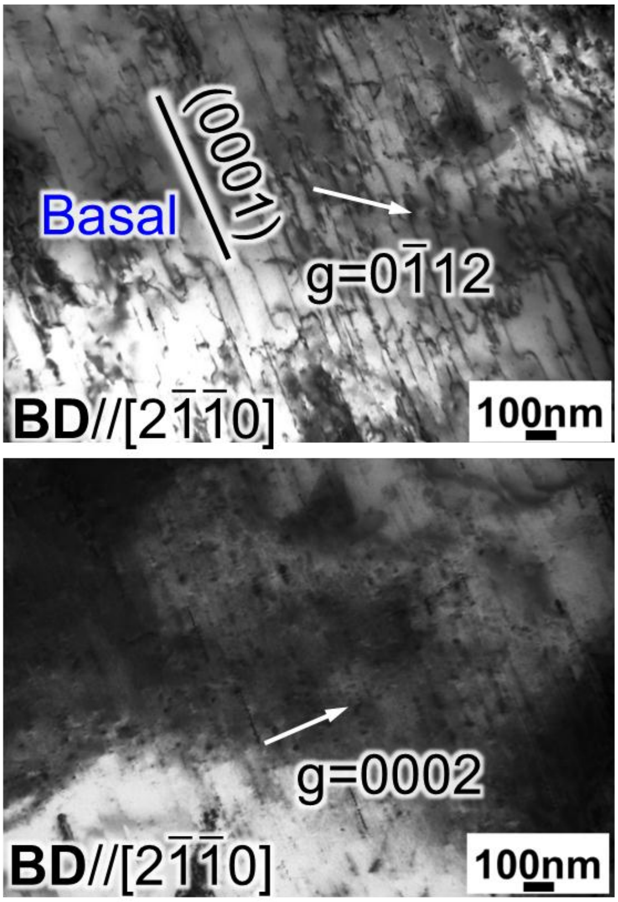

Fig. 6-20. TEM microstructures of 55˚-sample after tensile test. (a) BD // $[2\bar{1}\bar{1}0]$, (b) BD // $[2\bar{1}\bar{1}0]$.

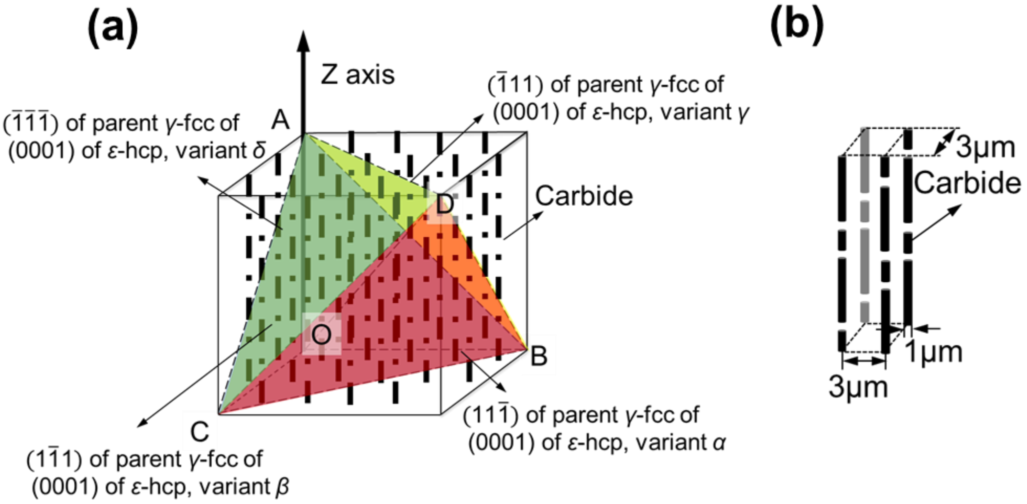

Fig. 6-21. (a) Phase transformation model from γ-fcc to ε-hcp with Shoji–Nishiyama orientation relationship. (b) Discontinuous carbide array with equal interval.

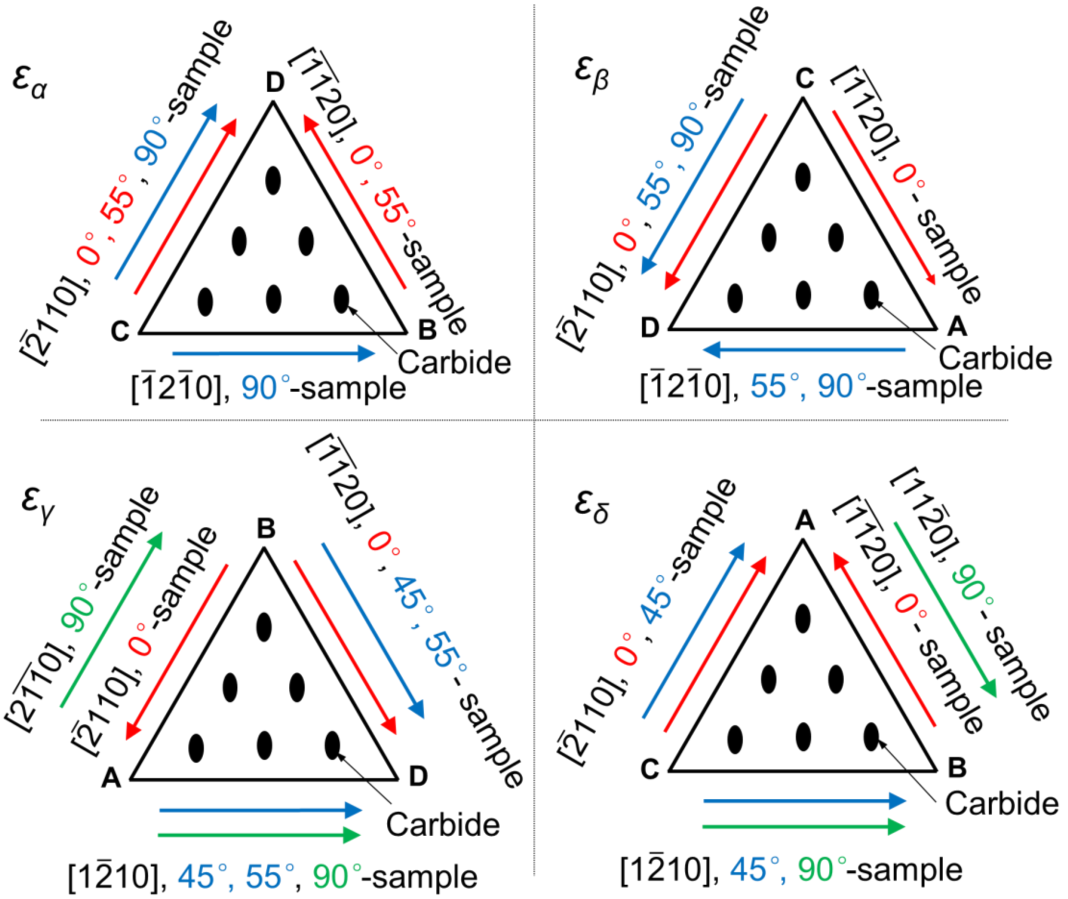

Fig. 6-22. Carbide array on the basal plane of ε_α, ε_β, ε_γ, and ε_δ. The color arrows correspond to the slip directions of perfect dislocations in 0˚-, 45˚-, 55˚-, and 90˚-samples with the same color in built angle.

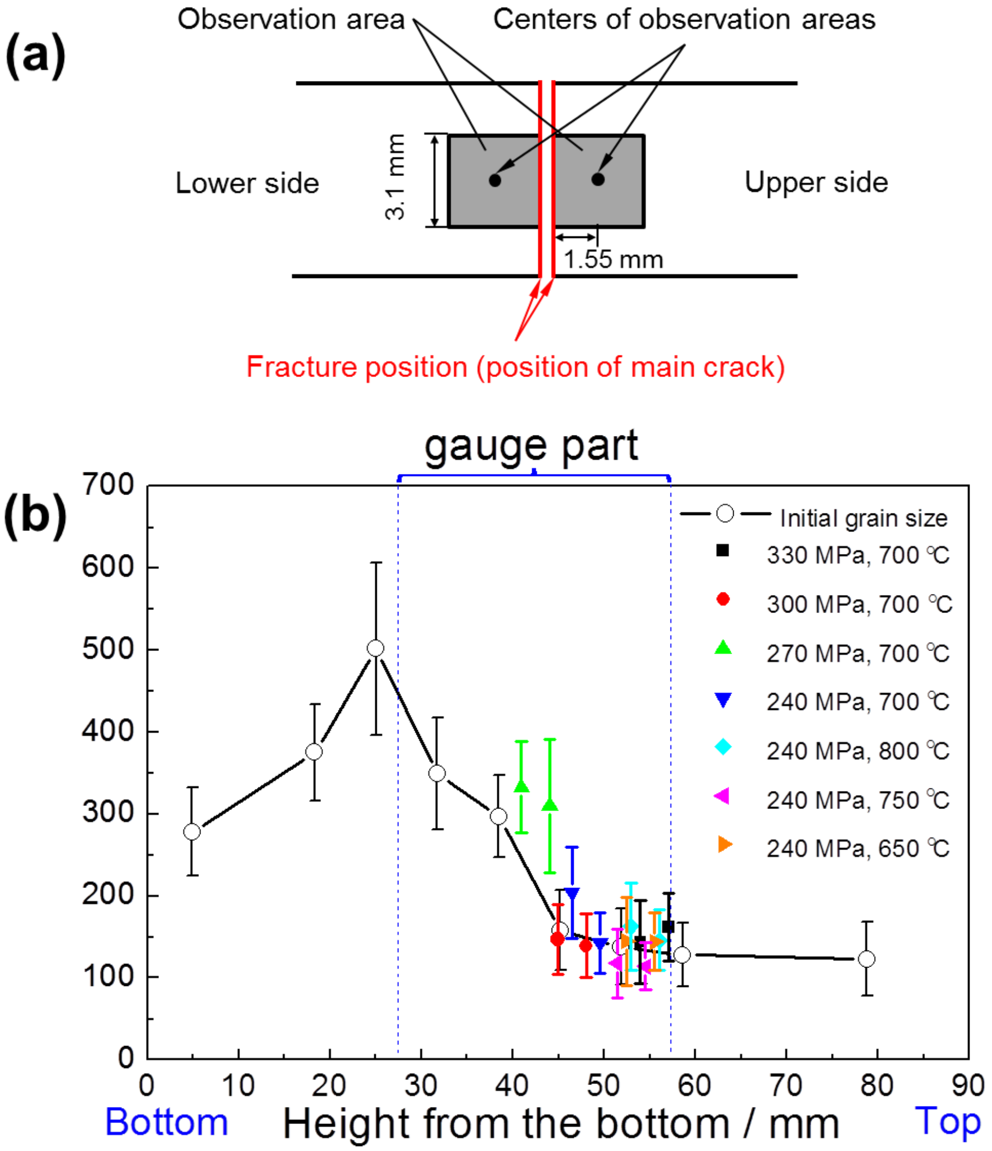

Fig.6-23. (a) Schematic of the positions for grain structure observation in the fracture specimens. (b) Grain size of longitudinal cross-section on both sides of the fracture position and grain size variation along the built height in the specimen before creep test.

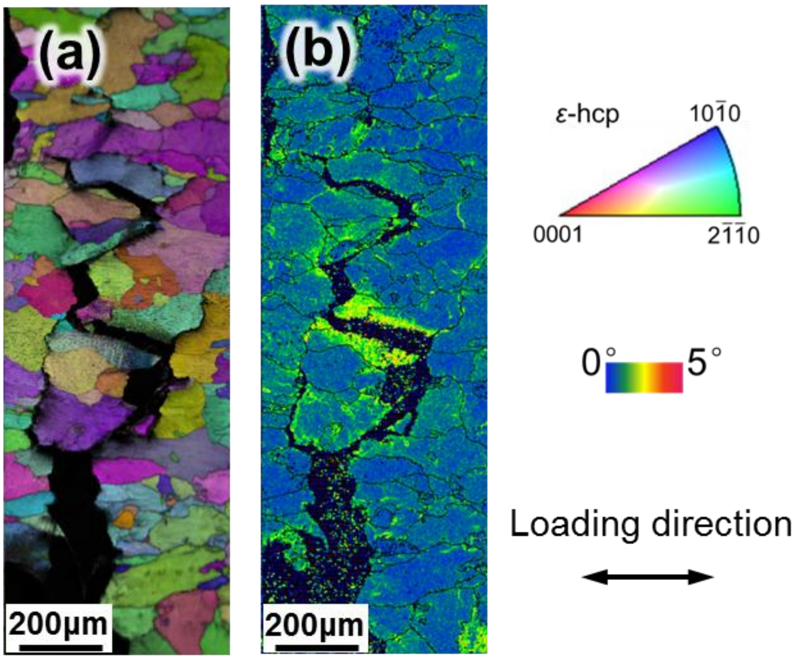

Fig.6-24. (a) EBSD IQ+IPF maps and (b) KAM map of longitudinal cross section near fracture of 0˚-sample crept at 650˚C under stress of 240 MPa.

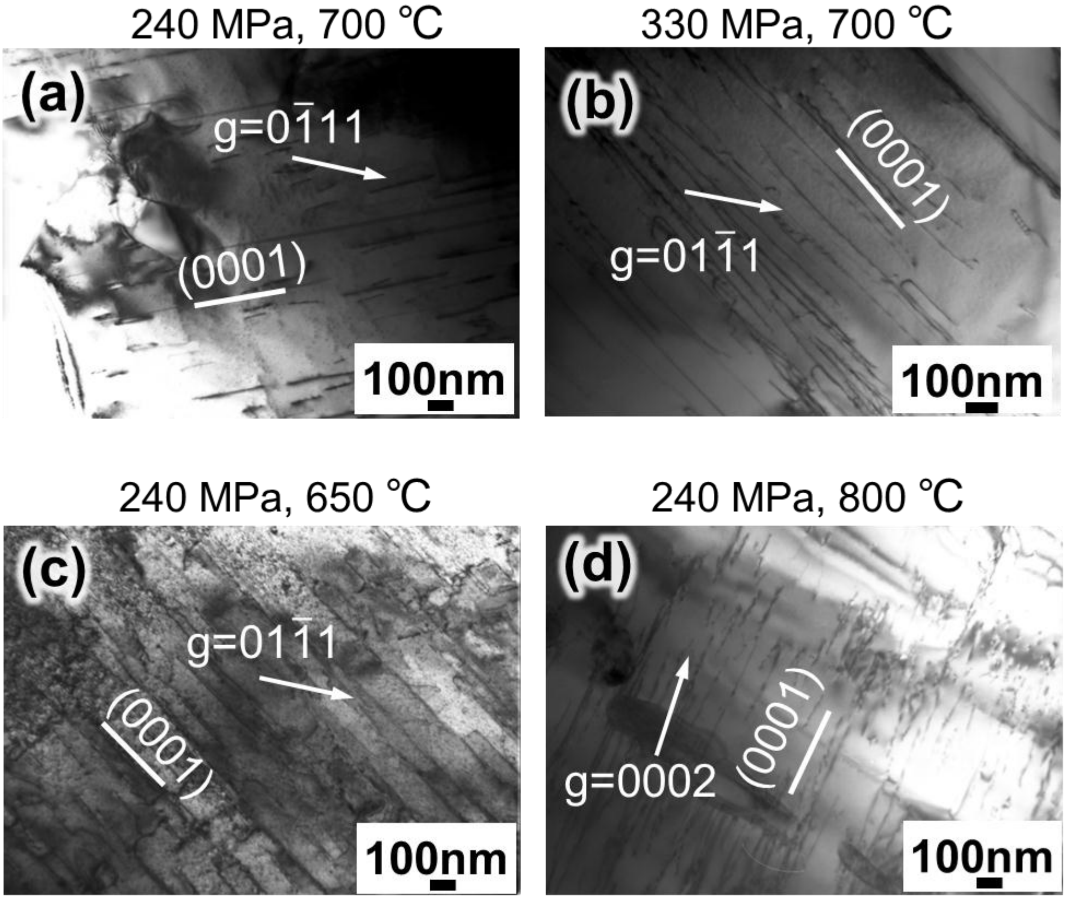

Fig.6-25. TEM bright-field image of 0˚-sample crept at (a) 240MPa, 700˚C, (b) 330MPa, 700˚C, (c) 240MPa, 650˚C, and (d) 240MPa, 800˚C, 330, with $[2\bar{1}\bar{1}0]$ incident beam direction.

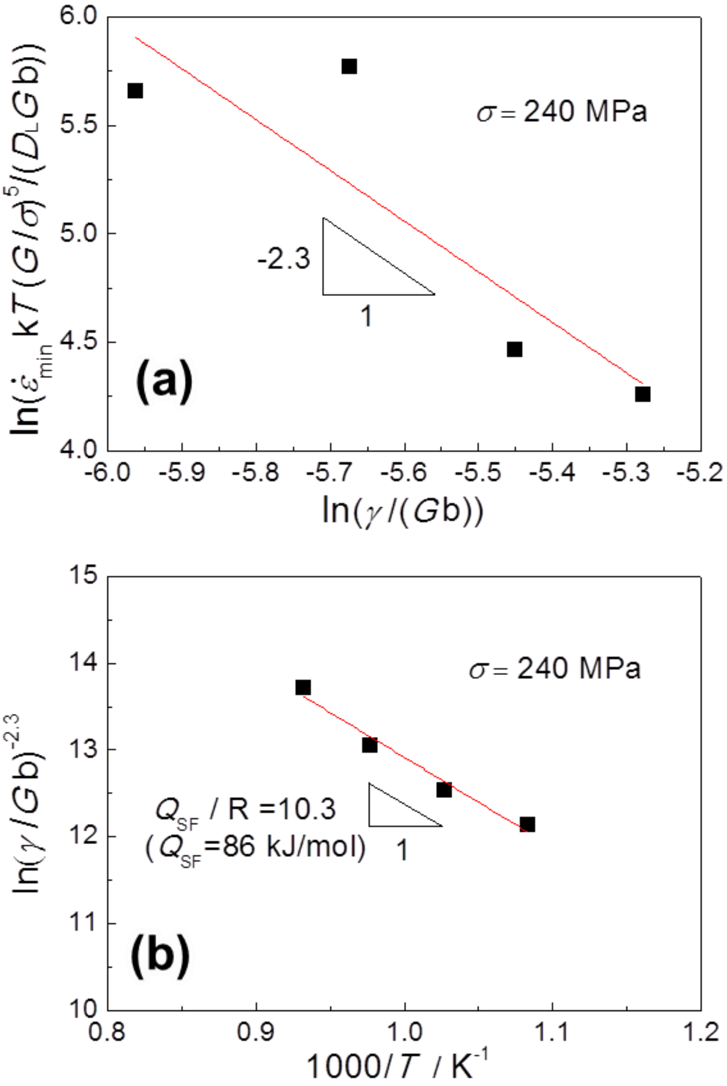

Fig. 6-26. (a) Effect of stacking fault energy on minimum creep rate of 0˚-sample under stress of 240MPa, and (b) effect of stacking fault on atom diffusion.

Table 6-1. Mechanical parameters at 700 ℃ with strain rate of 1.5 × $10^{-4}$$s^{-1}$

Sample	$\sigma_{0.2}$ (MPa)	UTS (MPa)	elongation (%)
0˚ (ε)	635 ± 13	754 ± 1.5	3.1 ± 0.7
45˚ (ε)	659 ± 30	765 ± 11	1.7 ± 0.1
55˚ (ε)	684 ± 14	796 ± 15	2.0 ± 0.5
90˚ (ε)	459 ± 4	693 ± 6.7	2.5 ± 0.7
90˚ (γ)	335 ± 6	643 ± 6.7	12.6 ± 3.0

Table 6-2. Young’s modulus measurement results for specimens with single ε phase.

Temperature / ˚C	650	700	750	800
Young’s modulus / GPa	162.4	157.5	151.3	144.3
Shear modulus / GPa	48.8	48.2	47.3	46.3
Poisson ratio	0.66	0.63	0.6	0.56

Table 6-3. Maximum Schmid factors (μ_{max}) for basal <**a**> slip system in variants ε_{α}, ε_{β}, ε_{γ}, and ε_{δ}.

Variants	Samples			
	0 °	45 °	55 °	90 °
ε_{α}	0.408	0	0.272	0.408
ε_{β}	0.408	0	0.272	0.408
ε_{γ}	0.408	0.408	0.272	0.408
ε_{δ}	0.408	0.408	0	0.408
All variants	0.408	0.408	0.272	0.408

Table 6-4. Stacking fault energy at different temperatures.

Temperature / ˚C	650	700	750	800	937.1
Stacking fault energy / mJ m^{-2}	37.8	31.2	24.6	18.0	0

Table 6-5 Width of stacking fault at different temperatures.

Temperature / ˚C	650	700	720	750	800
Edge dislocation / nm	9.23	10.03	10.56	11.41	13.63
Screw dislocation/ nm	0.07	0.42	0.56	0.87	1.70

References

[1] W. Betteridge, *Cobalt and Its Alloys*. Chichester, West Sussex: E. Horwood, 1982.

[2] F. G. Hodge and L. Dominey, *Cobalt and Cobalt Alloys.Kirk-Othmer Encyclopedia of Chemical Technology*. Hoboken, NJ, USA: John Wiley & Sons, Inc., 2000, pp. 1–22.

[3] C. T. Sims, N. S. Stoloff, and W. C. Hagel, *Superalloys II*. New York: John Wiley & Sons, Inc., 1987, pp. 1–640.

[4] B. Geddes, H. Leon, and X. Huang, *Superalloys: Alloying and Performance*. Materials Park: ASM International, 2010, pp. 1–184.

[5] W. H. Jiang, X. D. Yao, H. R. Guan, and Z. Q. Hu, “Secondary Carbide Precipitation in a Directionally Solidified Cobalt-Base Superalloy,” *Metallurgical and Materials Transactions A*, vol. 30, no. March, pp. 513–520, 1999.

[6] S. Pu, J. Zhang, Y. F. Shen, and L. H. Lou, “Recrystallization in a Directionally Solidified Cobalt-Base Superalloy,” *Materials Science & Engineering A*, vol. 480, pp. 428–433, 2008.

[7] Q. Wang, L. Zhang, and H. Shen, “Microstructure Analysis of Plasma Nitrided Cast / Forged CoCrMo alloys,” *Surface & Coatings Technology*, vol. 205, no. 7, pp. 2654–2660, 2010.

[8] S. Lee, N. Nomura, and A. Chiba, “Significant Improvement in Mechanical Properties of Biomedical Co-Cr-Mo Alloys with Combination of N Addition and Cr-Enrichment,” *Materials Transactions*, vol. 49, no. 2, pp. 260–264, 2008.

[9] S. Kurosu, H. Matsumoto, and A. Chiba, “Grain Refinement of Biomedical Co–27Cr–5Mo–0.16N Alloy by Reverse Transformation,” *Materials Letters*, vol. 64, no. 1, pp. 49–52, 2010.

[10] K. Yamanaka, M. Mori, and A. Chiba, “Mechanical Properties of As-Forged Ni-free Co–29Cr–6Mo Alloys with Ultrafine-Grained Microstructure,” *Materials Science & Engineering A*, vol. 528, no. 18, pp. 5961–5966, 2011.

[11] A. Chiba, K. Kumagai, N. Nomura, and S. Miyakawa, “Pin-on-Disk Wear Behavior in a like-on-like Configuration in a Biological Environment of High Carbon Cast and Low Carbon Forged Co–29Cr–6Mo Alloys,” *Acta Materialia*, vol. 55, no. 4, pp. 1309–1318, Feb. 2007.

[12] R. Juarez and A. S. Rodriguez, “Effect of Fcc-Hcp Phase Transformation Produced by Isothermal Aging on the Corrosion Resistance of a Co-27Cr-5Mo-0.05C alloy,” vol. 33, no. July, pp. 2229–2235, 2002.

[13] A. Mani, Salinas-Rodriguez, and H. F. Lopez, “Deformation Induced FCC to HCP Transformation in a Co–27Cr–5Mo–0.05C alloy,” *Materials Science & Engineering A*, vol. 528, pp. 3037–3043, 2011.

[14] K. Yamanaka, M. Mori, and A. Chiba, “Mechanical Properties of As-Forged Ni-Free Co–29Cr–6Mo Alloys with Ultrafine-Grained Microstructure,” *Materials Science and Engineering: A*, vol. 528, no. 18, pp. 5961–5966, Jul. 2011.

[15] M. Mori, K. Yamanaka, H. Matsumoto, and A. Chiba, “Evolution of Cold-Rolled Microstructures of Biomedical Co-Cr-Mo Alloys with and without N doping,” *Materials Science & Engineering A*, vol. 528, no. 2, pp. 614–621, 2010.

[16] H. Matsumoto, S. Kurosu, B. Lee, Y. Li, and A. Chiba, “Deformation Mode in Biomedical Co–27 % Cr–5 % Mo Alloy Consisting of a Single Hexagonal Close-Packed Structure,” *Scripta Materialia*, vol. 63, no. 11, pp. 1092–1095, 2010.

[17] K. Yamanaka, M. Mori, and A. Chiba, “Enhanced Mechanical Properties of As-Forged Co-Cr-Mo-N Alloys with Ultrafine-Grained Structures,” *Metallurgical and Materials Transactions A*, vol. 43A, pp. 5243–5257, 2012.

[18] K. Yamanaka, M. Mori, S. Kurosu, H. Matsumoto, and A. Chiba, “Ultrafine Grain Refinement of Biomedical Co-29Cr-6Mo Alloy during Conventional Hot-Compression Deformation,” *Metallurgical and Materials Transactions A*, vol. 40A, pp. 1980–1994, 2009.

[19] K. Yamanaka, M. Mori, and A. Chiba, “Origin of Significant Grain Refinement in Co-Cr-Mo Alloys Without Severe Plastic Deformation,” *Metallurgical and Materials Transactions A*, vol. 43, no. 12, pp. 4875–4887, Sep. 2012.

[20] S. M. Gaytan, L. E. Murr, E. Martinez, J. L. Martinez, B. I. Machado, D. A. Ramirez, F. Medina, S. Collins, and R. B. Wicker, “Comparison of Microstructures and Mechanical Properties for Solid and Mesh Cobalt-Base Alloy Prototypes Fabricated by Electron Beam Melting,” *Metallurgical and Materials Transactions A*, vol. 41, no. 12, pp. 3216–3227, Aug. 2010.

[21] R. S. Kircher, A. M. Christensen, and K. W. Wurth, “Electron Beam Melted (EBM) Co-Cr-Mo Alloy for Orthopaedic Implant Applications,” in *Solid Freeform Fabrication Proceedings*, 2009, pp. 428–436.

[22] Y. Birol, “A Novel C-free Co-Based Alloy for High Temperature Tooling Applications,” *Materials Science and Engineering: A*, vol. 528, no. 3, pp. 1117–1124, Jan. 2011.

[23] Y. Birol, “Thermal Fatigue Testing of Stellite 6-Coated Hot Work Tool Steel,” *Materials Science and Engineering: A*, vol. 527, no. 21–22, pp. 6091–6097, Aug. 2010.

[24] Y. Birol, “Thermal Fatigue Testing of Inconel 617 and Stellite 6 Alloys as Potential Tooling Materials for Thixoforming of Steels,” *Materials Science and Engineering: A*, vol. 527, no. 7–8, pp. 1938–1945, Mar. 2010.

[25] N. Tang, Y. P. Li, S. Kurosu, H. Matsumoto, Y. Koizumi, and A. Chiba, “Interfacial Reactions between Molten Al and a Co–Cr–Mo Alloy with and without Oxidation Treatment,” vol. 53, pp. 4324–4326, 2011.

[26] N. Tang, Y. Li, Y. Koizumi, S. Kurosu, and A. Chiba, “Interfacial Reaction between Co–Cr–Mo Alloy and Liquid Al,” *Corrosion Science*, vol. 75, pp. 262–268, Oct. 2013.

[27] M. Yan and Z. Fan, “Review Durability of Materials in Molten Aluminum Alloys,” *Journal of Materials Science*, vol. 36, no. 2, pp. 285–295, Jan. 2001.

[28] A. de J. Saldívar García, A. M. Medrano, and A. S. Rodríguez, “Formation of Hcp Martensite during the Isothermal Aging of an Fcc Co-27Cr-5Mo-0.05C Orthopedic Implant Alloy,” *Metallurgical and Materials Transactions A*, vol. 30, no. 5, pp. 1177–1184, May 1999.

[29] C. Montero-Ocampo, R. Juarez, and A. S. Rodriguez, “Effect of Fcc-Hcp Phase Transformation Produced by Isothermal Aging on the Corrosion Resistance of a Co-27Cr-5Mo-0.05C alloy,” *Metallurgical and Materials Transactions A*, vol. 33, no. 7, pp. 2229–2235, Jul. 2002.

[30] M. Calcagnotto, D. Ponge, E. Demir, and D. Raabe, “Orientation Gradients and Geometrically Necessary Dislocations in Ultrafine Grained Dual-Phase Steels Studied by 2D and 3D EBSD,” *Materials Science and Engineering: A*, vol. 527, no. 10–11, pp. 2738–2746, Apr. 2010.

[31] G. B. Olson and M. Cohen, “A General Mechanism of Martensitic Nucleation: Part I. General Concepts and the FCC → HCP Transformation,” *Metallurgical Transactions A*, vol. 7, no. 12, pp. 1897–1904, Dec. 1976.

[32] S. Allain, J. P. Chateau, O. Bouaziz, S. Migot, and N. Guelton, “Correlations between the Calculated Stacking Fault Energy and the Plasticity Mechanisms in Fe–Mn–C Alloys,” *Materials Science and Engineering: A*, vol. 387–389, pp. 158–162, Dec. 2004.

[33] T. Odahara, H. Matsumoto, and A. Chiba, “Mechanical Properties of Biomedical Co-33Cr-5Mo-0.3N Alloy at Elevated Temperatures,” *Materials Transactions*, vol. 49, no. 9, pp. 1963–1969, 2008.

[34] S. Kurosu, H. Matsumoto, A. Chiba, C. Landron, D. Fabregue, and E. Maire, “The Damage Process in a Biomedical Co–29Cr–6Mo–0.14N Alloy Analyzed by X-ray Tomography and Electron Backscattered Diffraction,” *Scripta Materialia*, vol. 64, no. 5, pp. 367–370, 2011.

[35] B. S. Lee, H. Matsumoto, and A. Chiba, “Fractures in Tensile Deformation of Biomedical Co–Cr–Mo–N alloys,” *Materials Letters*, vol. 65, no. 5, pp. 843–846, 2011.

[36] J. P. Hirth, *Theory of Dislocations*. New York : Wiley, 1982.

[37] Y. Han and M. C. Chaturvedi, “Steady State Creep Deformation of Superalloy Inconel 718,” *Materials Science and Engineering*, vol. 89, pp. 25–33, 1987.

[38] K. Hirano, R. P. Agarwala, B. L. Averbach, and M. Cohen, “Diffusion in Cobalt-Nickel Alloys,” *Journal of Applied Physics*, vol. 33, no. 10, p. 3049, Jun. 1962.

[39] A. S. Argon and W. C. Moffatt, “Climb of Extended Edge Dislocations,” *Acta Metallurgica*, vol. 29, no. 2, pp. 293–299, Feb. 1981.

[40] A. K. Mukherjee, J. E. Bird, and J. E. Dorn, “Experimental Correlations for High-Temperature Creep,” *Trans.ASM*, vol. 62, pp. 155, 1969.

[41] F. A. Mohamed and T. G. Langdon, “The Transition from Dislocation Climb to Viscous Glide in Creep of Solid Solution Alloys,” *Acta Metallurgica*, vol. 22, pp. 779, 1974.

[42] C. R. Barrett and S. O.D., “Influence of Stacking-Fault Energy on High-Temperature Creep of Pure Metals,” *Trans AIME*, vol. 233, pp. 1116, 1965.

Chapter 7

7. Conclusions

Microstructures and high temperature properties of Inconel 718 and Co-28Cr-6Mo alloys fabricated by electron beam melting with various build directions have been studied.

The main findings about microstructure and mechanical properties of EBM-built Inconel 718 alloy are as follows:

1) Single crystal-like structure of Inconel 718 alloy with <001> orientation in build direction can be obtained by the EBM process, which suggests crystal orientation can be controlled by selecting the oriented direction relative to the build direction, thus the mechanical properties can be controlled as a result.

2) Precipitate amount was dependent on the build height because the early-built part was kept at high temperature for longer time when waiting for the fabrication of the latter-built part, which would have more precipitates. However, inhomogeneous distribution of precipitates in the build height can be solved by subsequent solution treatment without changing the preferential crystal orientation.

3) 55 °-sample exhibited smaller minimum creep rate than the samples with other build directions, which suggests that creep resistance of component can be improved if the loading direction is parallel to the <111> orientation direction.

4) [001] variant of metastable γ''-Ni_3Nb ($D0_{22}$, bct) will dissolve into the matrix in 0 °- and 90 °-samples (<001> orientation) after creep deformation, but all the γ'' variants can be kept in 45 °- and 55 °-samples (<011> and <111> orientations) because the stress state difference for the γ'' variants in the samples with different build directions. This result can explain why the minimum creep rate in 0 °-sample is much higher than that in 55 °-sample in the same stress.

The main findings about microstructure and mechanical properties of Co-Cr-Mo alloy are as follows:

1) Single crystal-like structure of Co-Cr-Mo alloy with metastable γ-fcc phase can be obtained by the EBM process, whose <001> orientation was parallel to the build direction. This result demonstrates the ability of EBM used to produce single-crystal like structure of material with cubic structure.

2) Phase transformation from *γ*-fcc to *ε*-hcp may occur in bottom part of the sample with high build height in the EBM process because of long post-built time in the bottom part. The grain structure throughout the height of EBM-built object can not be homogenized by simple aging treatment. It is suggested that the conditions of heat treatment to homogenize the microstructure should be determined by taking into account the thermal history during the post-melt period of the EBM process especially when the solid-solid transformation is sluggish. The reverse phase transformation may be a possible way to solve the inhomogeneous microstructure problem in Co-Cr-Mo alloy.

3) Isothermal martensitic transformation or diffusive transformation from metastable γ-fcc to stable ε-hcp can be selected by choosing heat treatment temperature, by which the grain texture and resultant mechanical property can be controlled.

EBM is a newly developed technology, beside some obvious advantages, such as being able to produce 3D complex object, having high productivity and lower cost, the problems of the EBM in the practical use have also been found, which are listed in the follows, and expected to be solved in the future.

1) The microstructure of the object with high build height is not homogeneous because of the effect of post-built heating process on the early-built part. Heat treatment is necessary for the microstructure homogenization.

2) Large amount of experiments are necessary to find the proper build parameter when EBM is applied to a new material. Simulation model should be developed to predict the microstructure.

3) The stability of the build process should be improved to ensure the mechanical

property.

4) The surface roughness is not low enough, especially at the side surface, attached with numerical powders. This will affect the mechanical property of the porous object with thin strut part significantly.
5) The present process map for the EBM-built material should be improved because effect of preheating process on the microstructure is not considered.

Research prospect

Though the finding in the study about the microstructure and mechanical properties of Ni and Co based alloy fabricated by electron beam melting, further research is expected to promote the practical application of EBM-built products with high reliability, which are listed as follows:

1) Process map for Inconel 718 and Co-Cr-Mo alloy in EBM process should be developed to fabricate the part with the equiaxed grains or columnar grains according to the actual requirement of application. For example, equiaxed grains are preferred in application of orthopedic implant.
2) It is necessary to investigate how to obtain the homogeneous microstructure throughout the built part. Post-built heat treatment can be considered to remove the difference of phase, precipitate, grain size in the build height.
3) When the object with thin-wall shape is fabricated by EBM, the temperature gradient in the melt pool will increase significantly because the heat loss in the thin-wall part is much stronger than that of bulk one. Therefore the electron beam parameter for the bulk object is not suitable for the thin-wall object any more, and the beam parameter for the object with complex architecture should be selected differently from that for bulk object to obtain expected microstructure by considering the solidification process of the melt pool.
4) Single crystal-like microstructure of Co-Cr-Mo alloy with metastable γ-fcc phase can be obtained by EBM process. It will be very interesting to investigate how to obtain single oriented ε-hcp phase from the single crystal-like γ-fcc phase. The creep result of Co-Cr-Mo alloy with metastable γ-fcc phase implies that it may be possible to obtain single oriented ε-hcp phase by aging treatment at the loading condition.
5) The scanning strategy at present is to rotate the scanning direction by 90° on every layer, which is favorable to form the cubic texture. This would cause

mechanical difference of the EBM-built turbocharger at the blade part. The scanning strategy can be considered to change according to each blade part, while not be constant in the whole built object.

6) The mechanical property of Inconel 718 fabricated by EBM with the optimized condition (without Laves phase and unmelt particles) should be investigated further.
7) The mechanical properties of Inconel 718 and Co-Cr-Mo alloy with fine equiaxed grains should be investigated in the future.
8) The mechanical properties of cellular structures fabricated by EBM are dependent on the designed structure, build direction, build parameters and post-built heat treatment. Therefore, the mechanical properties of cellular structures fabricated by EBM still need to be investigated further by considering these influence factors.
9) Fatigue property of EBM-built Inconel 718 and Co-Cr-Mo alloy should be investigated to further understand the effect of anisotropic columnar grains, precipitate arrangement and crystal orientation on the mechanical properties. Then the build direction can be selected to control the mechanical based on result.

Acknowledgement

The financial support for this study was provided by the Ministry of Education, Culture, Sports, Science and Technology of Japan, which is gratefully acknowledged for relieving my fears for life.

I would first like to express my deepest gratitude to my main supervisor Prof. Akihiko Chiba, who provides me with the opportunity to do the cutting edge research (Additive manufacturing of the metals). Thanks for believing me and giving me the freedom to do the research according to my ideas.

Secondly, I would like to thank my second supervisor, Prof. Yuichiro Koizumi, who guided me through the entire doctoral study with his profound knowledge and rigorous scientific approach. I received constructive comments and subtle care from him. His enthusiasm for reach and rigorous attitude give me a deep impression, which will affect my future research.

A deep thank goes to Assistant Prof. Yunping Li, who gives me a lot of help in the research and daily life.

Assistant Prof. Kenta Yamanaka is specially thanked for raising me up to work hard with his crazy attitude for research. He always worked over the night, and has published over 20 papers in his Ph.D study.

A warm thank goes to Prof. Hiroaki Matsumoto, for teaching me how to use the XRD and high temperature tensile experiment and giving me beneficial suggestions.

Technician Shun Ito is deeply thanked for his patient direction for TEM operation.

All my past and present colleagues at Chiba lab are greatly thanked for accompanying me though the three year Ph.D study, giving me help and encourage. We have spent a lot of wonderful time, Hanami, drinking party and so on, which are good memory in my life.

My friends in China and Japan would be thanked for sharing their successful experiences and how to deal with tough times. I will always remember those wonderful moments we spent together.

At last, I want to express my deepest thanks to my parents, for loving me and always supporting me.

Publications

1. **Shi-Hai Sun**, Yuichiro Koizumi, Shingo Kurosu, Yun-Ping Li, Hiroaki Matsumoto, Akihiko Chiba, Build–direction dependence of microstructure and high-temperature tensile property of Co–Cr–Mo alloy fabricated by electron–beam melting (EBM), **Acta Materialia**, Vol.64, pp.154-168. Feb., 2014.[downloaded 888 times]
2. **Shi-Hai Sun**, Yuichiro Koizumi, Shingo Kurosu, Yun-Ping Li, Akihiko Chiba, Effect of phase transformation on tensile behavior of Co–Cr–Mo fabricated by electron–beam melting, **Journal of the Japan Society of Powder and Powder Metallurgy**, Vol.61, No.5, pp234-242, May, 2014.
3. Yuichiro Koizumi, **Shi-Hai Sun**, Tsuyoshi Saito, Shingo Kurosu, Akihiko Chiba, Prototyping of Co–Cr–Mo alloy flat spiral spring by electron beam melting, **Journal of the Japan Society of Powder and Powder Metallurgy**, Vol.61, No.5, pp243-249, May, 2014.
4. Yunping Li, Yujie Cui, Huakang Bian, **Shihai Sun**, Ning Tang, Yan Chen, Bin Liu, Yuichiro Koizumi, Akihiko Chiba, Detwining in Mg alloy with a high density of twin boundaries, **Science and Technology of Advanced Materials**, Vol.15, No.3, pp.1-8, 2014.
5. Yunping Li, Phacharaphon Tunthawiroon, Ning Tang, Huakang Bian, Fenglin Wang, **Shihai Sun**, Yan Chen, Kazuyo Omura, Yuichiro Koizumi, Akihiko Chiba, Effects of Al, Ti, and Zr doping on oxide film formation in Co–29Cr–6Mo alloy used as mould material for Al die-casting, **Corrosion Science**, Vol. 84, pp.147-158, July, 2014.
6. **Shi-Hai Sun**, Yuichiro Koizumi, Shingo Kurosu, Yun-Ping Li, Akihiko Chiba, Phase and grain size inhomogeneity and their influences on creep behavior of Co–Cr–Mo alloy additive manufactured by electron–beam melting, **Acta Materialia**, Vol.86, pp.305-318, Mar., 2015.
7. Yujie Cui, Yunping Li, **Shihai Sun**, Huakang Bian, Hua Huang, Zhongchang Wang, Yuichiro Koizumi, Akihiko Chiba, Enhanced Damping Capacity of Magnesium Alloys by Tensile Twin Boundaries, **Scripta Materialia**, In press.